

University of Wollongong - Research Online

Thesis Collection

Title: Mathematical modelling of gas separation and storage using advanced materials

Author: Aaron William Thornton

Year: 2009

Repository DOI:

Copyright Warning

You may print or download ONE copy of this document for the purpose of your own research or study. The University does not authorise you to copy, communicate or otherwise make available electronically to any other person any copyright material contained on this site.

You are reminded of the following: This work is copyright. Apart from any use permitted under the Copyright Act 1968, no part of this work may be reproduced by any process, nor may any other exclusive right be exercised, without the permission of the author. Copyright owners are entitled to take legal action against persons who infringe their copyright. A reproduction of material that is protected by copyright may be a copyright infringement. A court may impose penalties and award damages in relation to offences and infringements relating to copyright material.

Higher penalties may apply, and higher damages may be awarded, for offences and infringements involving the conversion of material into digital or electronic form.

Unless otherwise indicated, the views expressed in this thesis are those of the author and do not necessarily represent the views of the University of Wollongong.

Research Online is the open access repository for the University of Wollongong. For further information contact the UOW Library: research-pubs@uow.edu.au

University of Wollongong Thesis Collections

University of Wollongong Thesis Collection

University of Wollongong

Year 2009

Mathematical modelling of gas separation and storage using advanced materials

Aaron William Thornton
University of Wollongong

Thornton, Aaron William, Mathematical modelling of gas separation and storage using advanced materials, Doctor of Philosophy thesis, School of Mathematics and Applied Statistics, University of Wollongong, 2009. <http://ro.uow.edu.au/theses/3102>

This paper is posted at Research Online.

NOTE

This online version of the thesis may have different page formatting and pagination from the paper copy held in the University of Wollongong Library.

UNIVERSITY OF WOLLONGONG

COPYRIGHT WARNING

You may print or download ONE copy of this document for the purpose of your own research or study. The University does not authorise you to copy, communicate or otherwise make available electronically to any other person any copyright material contained on this site. You are reminded of the following:

Copyright owners are entitled to take legal action against persons who infringe their copyright. A reproduction of material that is protected by copyright may be a copyright infringement. A court may impose penalties and award damages in relation to offences and infringements relating to copyright material. Higher penalties may apply, and higher damages may be awarded, for offences and infringements involving the conversion of material into digital or electronic form.

Mathematical modelling of gas separation and storage using advanced materials

*A thesis submitted in fulfilment of the
requirements for the award of the degree of*

Doctor of Philosophy

from

University of Wollongong

by

Aaron William Thornton, B Math (Hons)

Nanomechanics Group, School of Mathematics and Applied Statistics,
University of Wollongong

2009

CERTIFICATION

I, Aaron W. Thornton, declare that this thesis, submitted in fulfilment of the requirements for the award of Doctor of Philosophy, in the School of Mathematics and Applied Statistics, University of Wollongong, is wholly my own work unless otherwise referenced or acknowledged. The document has not been submitted for qualifications at any other academic institution.

Aaron W. Thornton

28th August, 2009

Acknowledgements

The completion of this thesis would not have been possible without the ceaseless support of my supervisors, family, friends, and colleagues. To my primary supervisor Jim Hill, I extend my gratitude and respect for his total commitment in supporting me during this endeavour. His energetic personality and mathematical mind has provided me with the inspiration and encouragement to complete this thesis. I would also like to thank my secondary supervisor Anita Hill, for her tireless support, encouragement and contagious passion to solve these problems. Her superhuman energy, numerous contacts and insightful logic have been crucial factors in making this work possible. Special thanks also go to Kate Nairn for her patience, guidance and contributions.

I am extremely grateful for my wife and her unswerving faith, love and hope which has carried me throughout this time. I would also like to thank my parents and parents-in-law for their ongoing love and support for which I am in their debt. I also thank my colleagues and friends Matt, Barry, Tamsyn, Ivy, Brandon, Allan, Justin and Joe for their assistance and support.

Finally, I would like to acknowledge the interaction that I had with the Freeman group, Wessling group, Sarti group and MTR where I met many helpful researchers who provided me with feedback, friendship and facilities.

Abstract

Clean, sustainable and cost-efficient fuel alternatives are expected to replace conventional fossil fuel combustion systems as environmental and economic pressures rise. Alternative fuel candidates include synthetic gas, purified natural gas and hydrogen gas. The realization of an alternative fuel-based economy hinges on the efficient separation and storage of gases, for applications such as pollutant capture, synthetic fuel production, fuel purification and fuel storage. Membranes and adsorbents are materials characterized by an internal network of angstrom and nano-sized pores which are designed to separate and store gases, respectively. This thesis is concerned with the development of simple mathematical models to explain and predict gas transport and adsorption properties within advanced materials. Such models will guide the tailoring of porosity to optimize the desired properties. This thesis makes contributions to the following three areas:

- **Gas separation** Firstly, a new model that determines the transport properties of a gas within individual pores is presented. The model considers the interactions of the gas with the surface of the pore to characterize the various transport regimes within pores of different size, shape and composition. This is an entirely new approach to understanding and interpreting the various diffusion regimes known to occur within gas separation membranes. The new model can be used to determine the optimal pore characteristics that maximize the separation of gas mixtures. Secondly, a new empirical relationship between gas diffusion and the membrane free volume is introduced which is found to accurately describe known diffusion behaviour for a range of polymer membranes. This leads to a new method for determining the amount of free volume necessary to achieve a desired gas diffusion rate.

- **Gas storage** Based upon fundamental thermodynamic principles, a new model for gas storage within adsorbents is presented. The model incorporates the interactions between the gas and the internal surface area of the adsorbent, and proves to be an accurate and fast method for predicting storage performance within adsorbents of varying porosities. This novel approach can be used to determine the pore characteristics necessary to store the maximum amount of gas under the required operating conditions.
- **Physical aging** A new physical aging model based on the mechanism of vacancy diffusion is derived that accurately matches existing aging data. Using this model and the existing theory the mechanisms of physical aging are examined, particularly for thin polymer films. Specifically, the new approach provides new insights into the physical aging mechanisms responsible for polymer densification and can be used as a tool to predict the polymer's performance over time.

Finally, the new mathematical models that are presented here provide considerable insight into complex physical processes, and will serve to accelerate the development of alternative energy technologies by providing simple guidelines for material design.

Contents

I	Introduction	1
1	Overview	2
1.1	Aim of thesis	2
1.1.1	Gas separation	3
1.1.2	Gas storage	5
1.1.3	Physical aging in polymers	7
1.2	Thesis structure	8
II	Gas separation	11
2	Introduction to gas separation	12
2.1	Previous work	12
2.1.1	Fundamental theory	12
2.1.2	Transport (diffusion) mechanisms	14
2.1.2.1	Activation diffusion	15
2.1.2.2	Surface diffusion	15
2.1.2.3	Knudsen diffusion	17
2.1.3	Membranes: Porous structures	17
2.1.4	Transition State Theory (TST)	19
2.1.5	Transport models for ordered pore networks	21
2.1.5.1	Parallel transport model	21
2.1.5.2	Resistance in series transport model	21
2.1.6	Modelling approaches	22
2.1.6.1	Gas-pore interactions	22
2.1.6.2	Free volume theory within polymers	26
2.2	Thesis work overview	31

2.2.1	Nano-scale: Individual pore transport	31
2.2.2	Macro-scale: Bulk free volume transport	32
3	Gas transport regime within pores	41
3.1	Introduction	41
3.2	Mathematical formulation of gas-pore interactions	41
3.3	Transport mechanisms	49
3.3.1	Size-sieving activation diffusion	50
3.3.2	Surface diffusion	51
3.3.3	Suction diffusion	52
3.3.4	Knudsen diffusion	53
3.4	Enhanced separation by tailoring pore size	53
3.5	Determining diffusion regime from experimental flux	57
3.6	Comparison with experimental results	58
3.7	Predictions of the model	59
3.8	Conclusion	64
4	Free volume and gas transport	69
4.1	Introduction	69
4.2	Free volume, permeability, diffusivity and solubility	70
4.2.1	Transport properties vs fractional free volume ...	70
4.2.1.1	New classes of polymers	77
4.2.2	Permeability vs gas-specific free volume	79
4.2.3	Diffusivity vs simulated accessible volume	80
4.3	Physical interpretation of new relation	81
4.4	Parameter values related to gas diameter	82
4.5	Conclusion	83
III	Gas storage	89
5	Introduction to gas storage	90
5.1	Previous work	90
5.1.1	Storage methods	90

5.1.2	Physisorption	92
5.1.3	Modelling approaches	97
5.1.3.1	Geometry-based calculations	97
5.1.3.2	Molecular simulations	99
5.1.3.3	Ab-initio calculations	101
5.2	Thesis work overview	102
6	Gas adsorption model	110
6.1	Introduction	110
6.2	Gas adsorption model	110
6.3	Comparison with experimental results	116
6.4	Predictions of the model	121
6.5	Conclusion	127
7	Impregnated metal-organic frameworks	131
7.1	Introduction	131
7.2	Method	132
7.3	Comparison with experimental and simulation data	138
7.4	Model prediction of impregnated MOF structures	140
7.5	Conclusion	148
8	Nanotubes	153
8.1	Introduction	153
8.1.1	Hydrogen storage requirements	153
8.1.2	Storage methods	153
8.1.3	Nanotubes: Properties and synthesis	154
8.2	Method	155
8.3	Model prediction of nanotubes	161
8.4	Conclusion	165

IV	Physical aging of polymer membranes	171
9	Introduction to physical aging	172
9.1	Previous work	172
9.1.1	Kovacs model	174
9.1.2	Struik model	174
9.1.3	Constitutive kinetic equation	176
9.1.4	Kovacs, Aklonis, Hutchinson and Ramos model	177
9.1.5	Dorkenoo and Pfromm model	179
9.1.6	Zhou, Chung, Wang and Goh model	181
9.1.7	Curro, Lagasse and Simha (CLS) model	182
9.1.8	McCaig, Paul and Barlow (MPB) model	184
9.2	Thesis work overview	186
10	Vacancy diffusion model	192
10.1	Introduction	192
10.2	New empirically-derived vacancy diffusion model	193
10.3	Comparison with results in the literature	195
10.3.1	Comparison with MPB	195
10.3.2	Comparison with CLS	196
10.3.3	Comparison with constitutive kinetic equation	198
10.4	Model applied to thin film aging	199
10.5	Model predictions of transport in aging polymer	201
10.6	Conclusion	205
V	Conclusion	209
11	Concluding remarks and future directions	210
11.1	Summary	210
11.1.1	Gas separation	210
11.1.2	Gas storage	211
11.1.3	Physical aging in polymers	212
11.2	Final comments	212

11.3 Future directions	212
------------------------------	-----

Appendix

List of author's publications

List of Figures

1.1: Schematic of membrane-based gas separation	4
1.2: Schematic of gas storage within adsorbents	6
1.3: Schematic of physical aging in polymers	7
2.1: Gas separation membrane with constant concentration gradient	13
2.2: Dominant transport mechanism within pore size ranges	14
2.3: Porous structure within various types of membranes	18
2.4: Computer simulations for free volume clusters within glass and rubber	19
2.5: Transition state theory representations	20
2.6: Schematic models for parallel transport and resistance in series transport	22
2.7: Potential energy $\varepsilon_{\text{=}}(z)$ between two parallel planes and two parallel slabs	24
2.8: Potential energy minimum ε^* within cylindrical and slit-shaped pores	24
2.9: Separation regimes determined within pores of different sizes	25
2.10: Schematic model of the total flux components through membranes	26
2.11: O ₂ permeability for glassy PS, PC, PA, PE and LCP	28
2.12: Carbon dioxide permeability versus inverse <i>FFV</i> and modified <i>FFV</i>	30
3.1: Geometry of molecule entering a cylindrical and slit-shaped pore channel	45
3.2: Force profile about the entrance of a cylindrical pore	46
3.3: Molecule entering smaller pore from larger pore	48
3.4: Suction energy (<i>W</i>) of a single oxygen molecule at the entrance of a tube	50
3.5: Suction energies for light gases at the entrance of a carbon tube	54
3.6: Model prediction of permeability <i>P</i> as a function of pore size	60
3.7: Model prediction of permeability <i>P</i> as a function of temperature	62
3.8: Model prediction of CO ₂ /CH ₄ selectivity vs CO ₂ permeability for pore size	63
3.9: Model prediction of CO ₂ /CH ₄ selectivity vs CO ₂ permeability for temperature ...	64

4.1: Permeability of light gases vs inverse fractional free volume <i>FFV</i>	73
4.2: Diffusivity of light gases vs inverse fractional free volume <i>FFV</i>	75
4.3: Solubility of light gases vs inverse fractional free volume <i>FFV</i>	76
4.4: Permeability of oxygen vs inverse modified fractional free volume <i>FFV</i> _{O₂}	77
4.5: Schematic of different diffusion processes within polymers	79
4.6: Diffusivity of oxygen vs inverse accessible volume fraction <i>AVF</i>	81
4.7: The dependence of β values found from fits to permeability and diffusivity	83
5.1: Gas storage methods	91
5.2: Storage methods for hydrogen	92
5.3: Lennard-Jones potential energy between atom and infinite flat surface	93
5.4: Surface area of graphite elements	96
5.5: Density profiles for gas molecules upon the surface of a MOF	97
5.6: Stacking arrangements of spheres upon a graphite surface	98
5.7: Stacking arrangements of spheres within tubes of different diameters	98
5.8: Molecular simulations of hydrogen adsorption	100
5.9: Ab-initio calculations for the binding energy of hydrogen to fullerenes	102
5.10: Ab-initio calculations for the binding energy of hydrogen to nanotubes	102
6.1: Potential energy for adsorption, total volume and free volume within cavities ...	114
6.2: Schematic of the new adsorption model, TIMTAM	115
6.3: TIMTAM fit to simulation results for hydrogen uptake with pore size	117
6.4: TIMTAM fit to simulation results for hydrogen uptake with pressure	119
6.5: TIMTAM fit to experimental methane uptake within activated carbon	119
6.6: TIMTAM fit of hydrogen uptake to exp. and sim. results for IRMOF-1	120
6.7: TIMTAM results for H ₂ uptake in carbon slits, tubes and spheres with pressure	122
6.8: TIMTAM results for gravimetric H ₂ uptake in carbon slits, tubes and spheres ...	124
6.9: TIMTAM results for volumetric H ₂ uptake in carbon slits, tubes and spheres	126
7.1: Schematic representation for Mg-C ₆₀ @ MOF	132
7.2: Comparison of H ₂ uptake in sphere with centered C ₆₀ , offset C ₆₀ and empty	135
7.3: Potential energy for adsorption within Mg-C ₆₀ @ MOF	137
7.4: TIMTAM fit to experimental results for H ₂ uptake in IRMOF-1	138
7.5: TIMTAM fit to experimental results for H ₂ uptake in IRMOF-1, -8, -10 & -16	139
7.6: Profile of potential energy for adsorption within MOFs	142

7.7: Fractional free volume for adsorption of hydrogen and methane	143
7.8: Heat of adsorption within IRMOF-8 for hydrogen and methane	144
7.9: Modeling of total hydrogen uptake within IRMOF-8 and IRMOF-10	146
7.10: Modeling of total methane uptake within IRMOF-8 and IRMOF-10	147
7.11: Predicted methane uptake performance for impregnated MOFs	148
8.1: Potential energy for adsorption within carbon nanotubes	156
8.2: Contour potential energy for adsorption within carbon nanotubes	157
8.3: Fractional volume for adsorption within a carbon nanotube	158
8.4: Predictions of H ₂ uptake isotherms in a carbon nanotube	161
8.5: Predictions of H ₂ uptake in nanotubes with diameters 10, 15, and 20 Å	163
8.6: Predictions of H ₂ uptake in nanotubes with mass 10, 20, and 30 g/mol	163
8.7: Predictions of H ₂ uptake in nanotubes in DoE operating conditions	164
9.1: Diagrams of the physical aging process after a quench	173
9.2: The Struik model fitted to various aging data	175
9.3: Relationships between the parameters of Struik model and properties	176
9.4: Schematic example of each relaxation unit's contribution over time	178
9.5: KAHR model predictions of the relaxation process after quench	178
9.6: Schematic of the thickness-dependent glass transition temperature	180
9.7: The KAHR model fit to experimental N ₂ permeability results	181
9.8: The ZWCG model fit to experimental O ₂ permeability results	182
9.9: Schematic of the fractional free volume relaxation towards equilibrium	183
9.10: The CLS vacancy diffusion model and the KAHR model results	184
9.11: MPB dual vacancy diffusion and lattice contraction model	185
9.12: MPB dual mechanism model fitted to experimental O ₂ permeability	186
10.1: Experimental oxygen permeability data for BPA-BnzDCA	195
10.2: Free volume predicted by the KAHR, CLS and the new EVD model	197
10.3: Experimental oxygen permeability of PSF films as a function of time	200
10.4: Fractional free volume profile predictions within a polymer sample at times t ..	204
10.5: Gas uptake profile predictions within a polymer sample at times t	204
10.6: Gas release profile predictions within a polymer sample at times t	205
11.1: Membranes with identical pore size distributions but different arrangements ...	213

List of Tables

Table 3.1: Lennard-Jones constants, molecular mass and average velocity	49
Table 3.2: Model results for d_{min} , d_{opt} , W_{max} , v_{max} and d_K	55
Table 4.1: Gas permeability, diffusivity and solubility for high free volume polymers	71
Table 4.2: Best fit parameter values found from fits to experimental permeability	73
Table 4.3: Best fit parameter values found from fits to experimental diffusivity	75
Table 4.4: Comparison of CO ₂ solubility, diffusivity and permeability enhancement	78
Table 6.1: Parameter values used to reproduce the data	120
Table 7.1: Lennard-Jones parameter values for framework atoms	134
Table 7.2: Cavity atomic surface density	134
Table 7.3: Fullerene properties	134
Table 7.4: Adsorbent molecular mass per cavity and adsorbate molecular mass	135
Table 7.5: Parameter values for α and r_1 found from fits to data	140
Table 8.1: Parameter values used in this chapter	158

Part I

Introduction

Chapter 1

Overview

1.1 Aim of thesis

Currently there is a world-wide crisis rooted in two interrelated issues:

- the financial melt down of the world trading platform heavily based upon unregulated assets; and
- the realization that our planet earth is suffering from the atmospheric pollution caused by the overload of emissions from fossil fuel combustion systems.

An important contribution to the present crisis is to provide cost-effective and pollution-free energy alternatives to sustain the world-wide economy that survives upon energy consuming industries. There are three main research areas that have the potential to minimize the cost and pollution arising from energy sources:

- the post-combustion capture of pollutants to prevent current fossil fuel power plants from further harming the atmosphere;
- the formation of cleaner combustion fuel alternatives including synthetic gas (from gasified coal) and purified natural gas (with carbon dioxide removed); and
- the complete replacement of fossil fuel systems with renewable energy technologies, such as the hydrogen electro-chemical fuel cell that produces electricity with pure steam as the exhaust product.

These solutions depend heavily on the ability to both separate and store gases. Membranes and adsorbents are materials composed of angstrom and nanometre-sized pores that can be designed to efficiently separate and store gas mixtures. The aim of this thesis is to provide simple mathematical models and conceptual frameworks that will guide the design of these materials to achieve maximum performance. The three specific areas addressed in this thesis are:

- (i) **gas separation** process using membranes;
- (ii) **gas storage** process using adsorbents; and
- (iii) **physical aging** in polymers.

1.1.1 Gas separation

Problem

Gas separation using membranes is an important operation critical to sustain today's energy consuming world without further polluting the environment. The basic concept of membrane-based gas separation is demonstrated in Figure 1.1. The membrane must be designed in such a way that it allows only the desired gas molecules to pass through and consequently separates the mixture. Membranes may be created from a variety of different materials including carbon, silica, polymer, zeolite and composites. Each material contains a porous network comprising pores of a particular size, shape, composition and distribution. The optimal membrane structure depends on the proposed application. In clean fuel technologies some gas separation applications include:

- pollutants from exhaust mixtures;
- carbon dioxide from natural gas;
- carbon monoxide from gasified coal; and
- hydrogen from various mixtures.

Since gas separation occurs as a result of significant differences in the gas transport properties of each gas, the goal is to understand the gas transport behaviour within a range of competing membrane materials. Simple models and conceptual frameworks are needed that describe and predict the transport properties of each gas within the different porous systems, which can then be used to design membranes that separate mixtures faster and more efficiently.

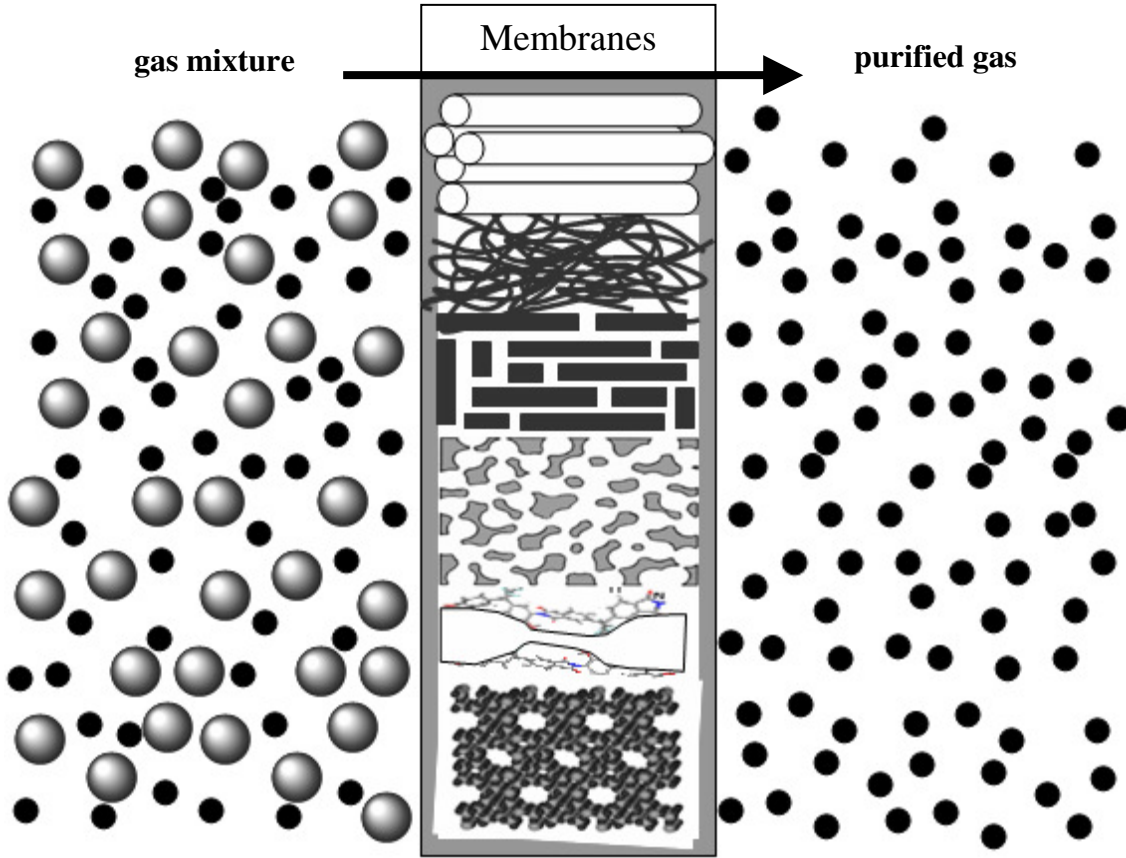


Figure 1.1: Schematic of membrane-based gas separation.

Solution

This thesis provides new mathematical models for the gas transport within the various porous networks. Two approaches are taken:

- a nano-scale investigation into the behaviour of each gas within individual pores; and
- a macro-scale investigation into the relationship between gas transport and the bulk material property, free volume.

Nano-scale investigation

By employing mathematical modelling, using the Lennard-Jones interaction potential for the gas molecule and the pore wall, the various gas diffusion regimes occurring within pores of different size, shape and composition are determined. Existing transport mechanism theory is combined with the new approach to predict the transport of the gases He, H₂, CO₂, O₂, N₂, CH₄, CO, Ar, C₂H₆, n-C₅H₁₂ and SF₆ through carbon tubes, carbon slits, silica tubes and silica slits. The minimum pore size for barrier-free transport (d_{min}) and the minimum pore size for Knudsen diffusion (d_K) are calculated for

each gas and a mechanism for the intermediate region (alternative to surface diffusion) is suggested in which the attractive van der Waals forces cause an accelerated entrance velocity of the gas at the pore opening. Experimental results for gas transport in carbon nanotube (CNT), carbon molecular sieving (CMS) and molecular sieving silica (MSS) membranes are explained well by this model. Another application of the model is demonstrated in which the porous structure and corresponding transport mechanisms are determined from experimental flux. Additionally, separation performance (selectivity vs permeability) is predicted by the model as a function of pore size and temperature. This approach provides guidelines for tailoring porosity in membranes, such that desired separations can be achieved.

Macro-scale investigation

Glassy polymer membranes comprise moveable and amorphous porous networks which make it difficult to study individual gas transport. An alternative approach from the macro-scale is to relate gas diffusion with bulk material properties. It has been widely accepted that gas diffusion can be related to the fractional free volume of the polymer through the Doolittle relation $D = A \exp(-B/f)$, where f is the fractional free volume and A and B are certain constants. As the free volume increases and the pores become connected and bi-continuous, the Doolittle relation does not adequately model the experimental data. By collecting and analysing an extensive database of conventional and high free volume polymers, an empirically determined relation of the form $D = \alpha \exp(\beta f)$, where α and β are constants, is shown to fit the experimental and computer simulation data well. Plausible reasons for the improved fit of this new relation over a wide range of f are postulated. In practise the new relation is an efficient tool for predicting transport properties for a wider range of available polymers, based on one readily obtainable material characteristic, the fractional free volume.

1.1.2 Gas storage

Problem

Gas storage materials are needed for the capture of carbon dioxide from post-combustion exhaust products and pre-combustion gas purifying stages, in addition to the storage of bulk natural, synthetic and hydrogen gas for large-scale exporting and for on-board vehicular transportation. Gas can be liquified at cryogenic temperatures or compressed at ultra high pressures. Both methods require a great deal of energy and

engineering. Alternatively, physisorption is a physical mechanism by which gases bind (or adsorb) onto a surface, forming highly dense and stable layers of gas molecules. Adsorbents are materials with high surface areas capable of storing large amounts of gas at close to ambient conditions, and therefore removing the need for freezers and compressors. Various materials can be used as adsorbents including zeolites, metal-organic frameworks, graphite, nanotubes, fullerenes and other nanostructures. There is a need for simple models and conceptual frameworks that describe and predict the adsorption properties of each gas within the different porous networks, which can then be used in the design of adsorbents to store large amounts of gas at close to ambient conditions.

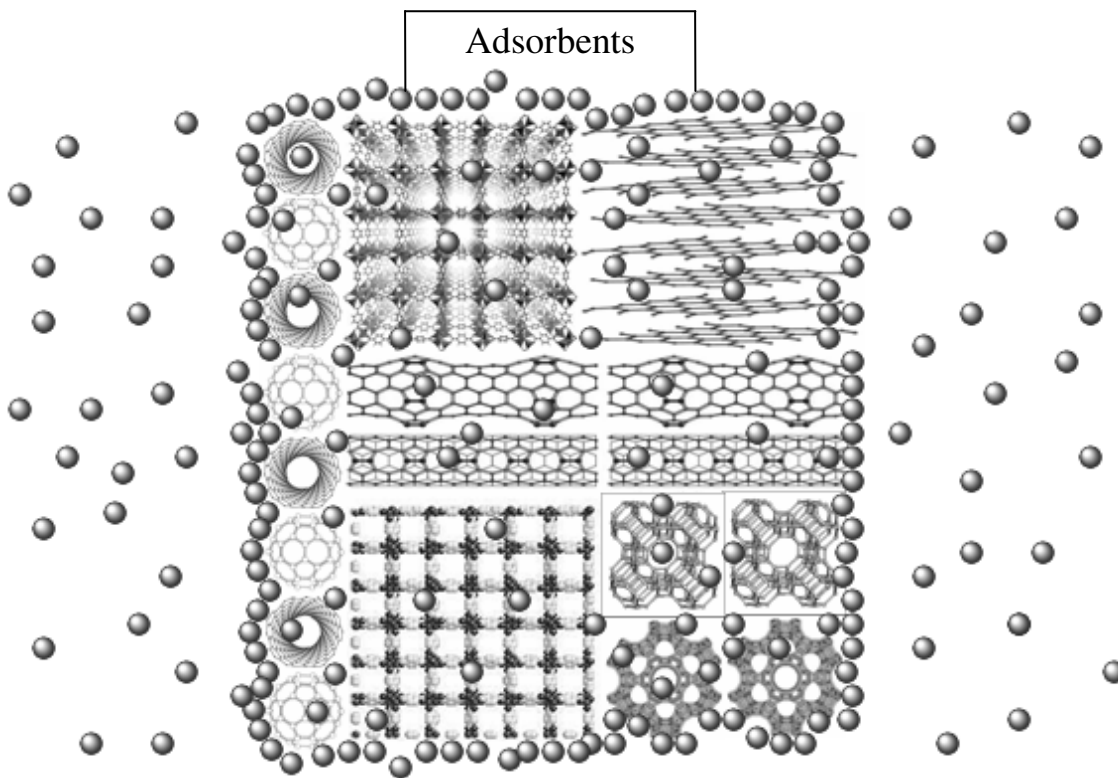


Figure 1.2: Schematic of gas storage within adsorbents.

Solution

This thesis provides a novel modelling framework, which has been called the Topologically Integrated Mathematical Thermodynamic Adsorption Model (TIMTAM), for understanding, describing and predicting gas storage outcomes within high surface area materials that utilize the physisorption mechanism. The key factors influencing gas uptake are adsorption potential (heat of adsorption), surface area, pore size (free volume) and pore shape, and each factor can be tuned to optimize the storage

performance for a particular application. The model presented here incorporates each factor and provides a fast and accurate method of predicting storage properties that consequently guide the material design. Experimental and simulation results in the literature for gas adsorption in metal-organic frameworks, nanotubes and activated carbon are used to verify the reliability of the model and excellent agreement is obtained with the model predictions. Further, the model is used to investigate recently proposed adsorbents namely, metal-organic frameworks impregnated with metal-decorated fullerenes and inorganic nanotubes.

1.1.3 Physical aging in polymers

Problem

Currently polymers are the leading membranes in the gas separation industry as well as excellent barriers for food packaging, coatings for corrosion protection and gas adsorbents. One of their drawbacks is their change in properties with time due to a process termed physical aging. Over time the porous network within the polymer collapses due to A) the migration of free volume elements to the external surface and/or B) the shrinking of free volume elements, see Figure 1.3. There is a need for simple models and frameworks that accurately describe and predict the physical aging process so that performance over time can be predicted and managed.

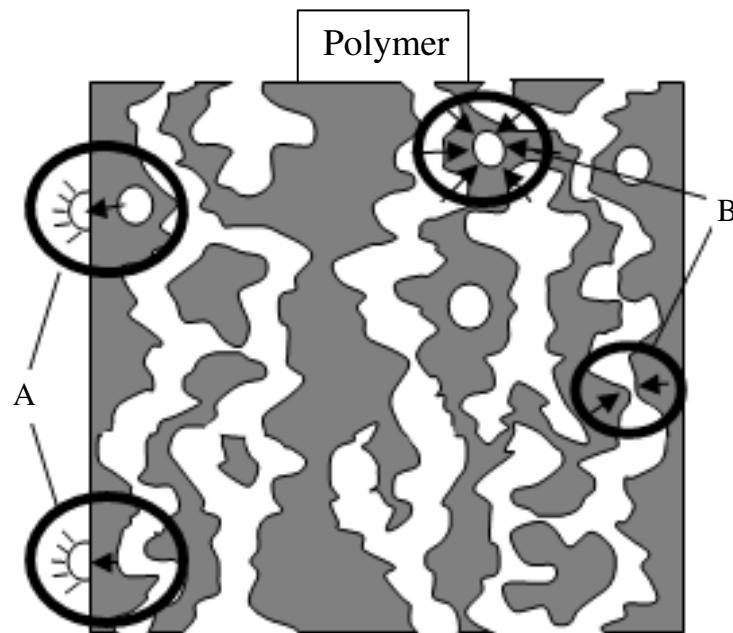


Figure 1.3: Schematic of physical aging in a polymer by A) disappearance of free volume elements at the external surfaces and B) shrinking of free volume elements.

Solution

A new physical aging model is presented which is based on the mechanism of vacancy diffusion. The advantage of the model is that it provides users with a simple analytical equation that can readily predict the membrane performance. The model agrees with the experimental data and is found to be in similar form to an early established constitutive kinetic equation. Some applications of the model are demonstrated including the analysis of ultra thin film aging and the prediction of gas transport, storage and delivery within an aging polymer.

1.2 Thesis structure

This thesis is presented as five parts and eleven chapters where each chapter ends with its own list of references and symbols. Details of the contents in each chapter are given below.

PART I INTRODUCTION

Chapter 1: Overview

This chapter outlines the aim of the thesis, the main problems to be addressed, and the solutions to be presented.

PART II GAS SEPARATION

Chapter 2: Introduction to gas separation

In this chapter fundamental gas separation theory is detailed, porous structures within various membranes are compared and the previous work in gas separation modelling is reviewed. Finally, an overview of the thesis work is given that focuses on the issue of how the thesis work extends and builds upon the previous work.

Chapter 3: Gas transport regime within pores

In this chapter a new nano-scale gas transport model is established. First the methodology is outlined in detail. Second some fundamental results of the model are presented including the critical pore sizes that distinguish between the various transport regimes for light gases, hydrocarbons, and sulphurs, within pores of different shape and composition. Then a method for determining the transport mechanism from experimental flux according to the framework of the model is provided. The model results are shown to agree with the experimental data. The model is then used to predict

separation performance (selectivity versus permeability) as a function of pore size and temperature, followed by conclusions.

Chapter 4: Free volume and gas transport

In this chapter a new macro-scale gas transport model is established. An extensive collection of experimental data for permeability, diffusivity, solubility, and free volume is analyzed and a new empirical relationship is shown to describe all the data. The new model is related to percolation theory and is used to analyze new classes of polymers in terms of their free volume and transport properties. Finally, the results are summarized in the conclusion section.

PART III GAS STORAGE

Chapter 5: Introduction to gas storage

In this chapter various methods for gas storage are compared, the theory of the physisorption mechanism is outlined in detail and three main modelling techniques are reviewed: geometry-based calculations, molecular simulations and ab-initio calculations. Finally an overview of the thesis work is given which is shown to incorporate parts of the current modelling approaches for gas adsorption.

Chapter 6: Gas adsorption model

Here a new gas adsorption model is established, the methodology is explained, and the model is shown to accurately describe gas uptake results within carbon nanotubes, carbon slits and metal-organic frameworks. The versatility of the model is demonstrated by comparing the model predictions within spherical, cylindrical and slit-shaped pores, followed by conclusions.

Chapter 7: Impregnated metal-organic frameworks

This chapter is dedicated to using the new adsorption model (presented in Chapter 6) to predict the gas storage potential of a new class of adsorbents, metal-organic frameworks impregnated with various nanostructures.

Chapter 8: Nanotubes

Similar to Chapter 7, this chapter presents the model predictions for gas adsorption within nanotubes composed of various elements. The model predictions are compared with the targets set by the U.S. Department of Energy and various factors are explored

which should be considered when creating nanotubes for gas adsorption such as heat of adsorption, mass and tube size.

PART IV PHYSICAL AGING IN POLYMERS

Chapter 9: Introduction to physical aging

This chapter contains the theory of physical aging and a review of various physical aging models, followed by a thesis work overview which relates to the previous work.

Chapter 10: Vacancy diffusion model

A new physical aging model is presented in this chapter which is based on the mechanism of vacancy diffusion. The new model is compared with experimental data and other aging models. Model predictions are also presented for the gas storage and release process demonstrating the transport behaviour within an aging polymer. Finally conclusions are given.

PART V CONCLUSION

Chapter 11: Concluding remarks and future directions

The final chapter summarizes the work presented within the thesis and gives some concluding comments on the major contributions of this work. Finally, potential future research directions are presented.

Part II

Gas separation

Chapter 2

Introduction to gas separation

2.1 Previous work

Rather than adopting an Edisonian trial-and-error approach to membrane development, it is more efficient to have an understanding of the separation phenomena to guide membrane design. For example, relationships have been found between experimental separation results and pore sizes determined from Positron Annihilation Lifetime Spectroscopy (PALS) [1, 2] and Small Angle X-ray Scattering (SAXS) [3, 4], which are used to guide the tailoring of pore sizes to enhance separation performance. Similarly, methods such as Monte Carlo (MC) simulations [5] and Molecular Dynamics (MD) [6, 7] improve the understanding of the relationships between membrane characteristics and separation properties. In addition to these experimental inputs, it is beneficial to have simple models and theories that provide an overall understanding of separation performance. In this chapter current models and conceptual frameworks are reviewed that contribute insight into the gas separation phenomenon and therefore help guide the optimization of material design.

2.1.1 Fundamental theory

A quantitative measure of gas transport is the flux (or permeation rate) which is defined as the number of molecules that pass through a unit area per unit time. Assuming no chemical activity, it is believed that molecular flux is in accordance with Fick's first law, in that the flux J is proportional to the concentration gradient through the membrane i.e. the flux goes from regions of high concentration to regions of low concentration, expressed in the form

$$J = -D \frac{dc}{dx}, \quad (2.1)$$

where D is the diffusivity (or diffusion coefficient), $c(x)$ is the concentration and x is the position across the membrane. This is the classical mass flux equation, which will be used throughout this work to describe gas transport. By assuming a constant concentration gradient across the membrane, the flux can be approximated as

$$J = D \frac{C_2 - C_1}{L}, \quad (2.2)$$

where C_1 ($= c(0)$) and C_2 ($= c(L)$) are the downstream and upstream concentrations (corresponding to the pressures p_1 and p_2), respectively, and L is the membrane thickness, labelled in Figure 2.1.

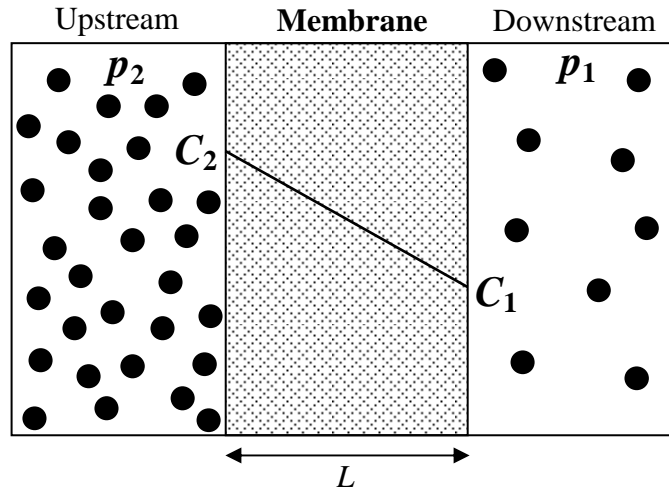


Figure 2.1: Gas separation membrane with a constant concentration gradient across membrane thickness L .

The membrane performance of various materials is commonly compared by the thickness-independent material property, permeability P , which is related to the flux J in the following way

$$P = \frac{J L}{p_2 - p_1} = \left(\frac{C_2 - C_1}{p_2 - p_1} \right) D. \quad (2.3)$$

In the case where the upstream pressure is much greater than the downstream pressure ($p_2 \gg p_1$ and $C_2 \gg C_1$) the permeability can be simplified to give

$$P = \frac{C_2}{p_2} D. \quad (2.4)$$

By introducing a solubility coefficient S , that is, the ratio of concentration over pressure C_2/p_2 , the permeability is expressed simply as

$$P = S D. \quad (2.5)$$

This form is useful as it assists the understanding of this property by representing it as two components:

- Solubility, S , an equilibrium component describing the amount of gas molecules within the membrane; and
- Diffusivity, D , a dynamic component describing the mobility of the gas molecules within the membrane.

The separation of a mixture of molecules A and B is characterised by the selectivity factor $\alpha_{A/B} = P_A / P_B$ i.e. the permeability of molecules A over the permeability of molecules B. According to Equation 2.5, it is possible to make separations by diffusivity selectivity D_A / D_B or solubility selectivity S_A / S_B .

2.1.2 Transport (diffusion) mechanisms

Gases are known to diffuse within membranes according to various transport mechanisms, illustrated in Figure 2.2. In this section three mechanisms of transport are discussed, namely:

- Activation diffusion (size sieving);
- Surface diffusion (also an activation process); and
- Knudsen diffusion.

Quantitative expressions are given for the diffusivity D and solubility S , and their product, permeability P .

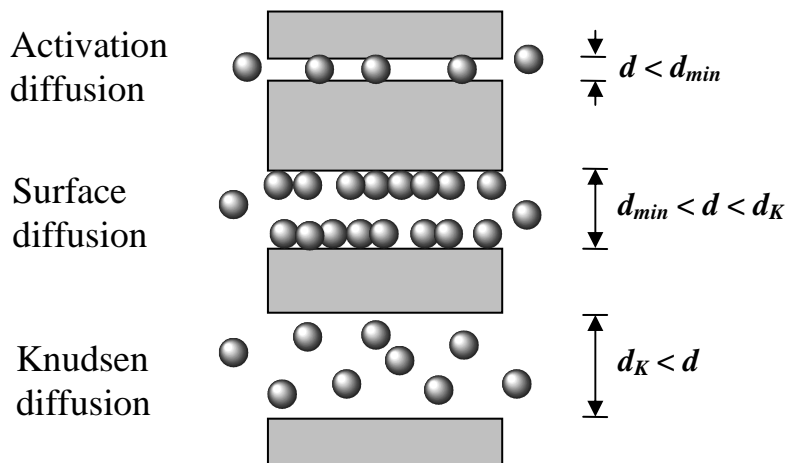


Figure 2.2: Dominant transport mechanism within pores of size d .

2.1.2.1 Activation diffusion ($d < d_{min}$)

Diffusivity

Gas molecules attempting to enter pores of diameters less than d_{min} will need to have sufficient initial kinetic energy to overcome the energy barrier experienced at the entrance of the pore in order to make a successful diffusive jump, which is indicative of transport generally known as activation diffusion. With an average kinetic energy of RT , the Arrhenius expression represents the probability that a gas molecule will have a kinetic energy greater than the energy barrier E_A (> 0). In view of this, the activated diffusion coefficient can be expressed as

$$D_A = D_{A*} \exp\left(\frac{-E_A}{RT}\right), \quad (2.6)$$

where D_{A*} is a pre-exponential coefficient depending on the average length of each diffusive jump, the frequency of the gas molecule encountering the pore entrance and the average velocity of each diffusive jump.

Solubility

The gas concentration within the membrane depends on the pore free volume v_f and is assumed to not significantly depend on temperature or gas-gas interactions, so that the solubility may be expressed as

$$S_A = S_{A*} v_f, \quad (2.7)$$

where S_{A*} is a proportionality constant.

Permeability

The permeability is dominated by the activated diffusion coefficient D_A , which is an increasing function of temperature, expressed as

$$P_A = D_{A*} S_{A*} v_f \exp\left(\frac{-E_A}{RT}\right). \quad (2.8)$$

2.1.2.2 Surface diffusion ($d_{min} < d < d_K$)

Diffusivity

Surface diffusion is the diffusion mechanism which dominates in the pore size region between activation diffusion and Knudsen diffusion [8]. Note that surface diffusion occurs in all pores larger than d_{min} but is only the dominant mechanism within the

region between d_{min} and d_K . Surface diffusion is also a form of activation diffusion; the energy barrier is the energy required for the molecule to jump from one adsorption site to another across the surface of the pore. Gilliland et al. [9] established an equation for the surface diffusion coefficient expressed here as

$$D_s = D_{s*} \exp\left(\frac{-aq}{RT}\right), \quad (2.9)$$

where D_{s*} is a pre-exponential coefficient depending on the frequency of vibration of the adsorbed molecule normal to the surface and the distance from one adsorption site to the next. q (> 0) is the heat of adsorption and a is a proportionality constant ($0 < a < 1$) such that aq is the energy barrier which separates the adjacent adsorption sites. An important observation is that more strongly adsorbed molecules are less mobile than weakly adsorbed molecules [10].

Solubility

In the region of surface diffusion, the gas concentration has been well described by Henry's Law $c = Kp$, with the temperature dependent Henry's Law coefficient $K = K_0 \exp(q/RT)$, where K_0 is a proportionality constant and p is pressure [10, 11]. Since solubility is the ratio of the equilibrium concentration over pressure, the solubility is equivalent to the Henry's Law coefficient,

$$S_s = K_0 \exp\left(\frac{q}{RT}\right), \quad (2.10)$$

which implies that solubility is a decreasing function with temperature.

Permeability

The product of diffusivity and solubility gives

$$P_s = K_0 D_{s*} \exp\left(\frac{(1-a)q}{RT}\right), \quad (2.11)$$

and since $0 < a < 1$, the total permeability will decrease with increased temperature meaning that the increased diffusivity is overruled by the decrease in surface concentration [10].

2.1.2.3 Knudsen diffusion ($d_K < d$)

Diffusivity

Knudsen diffusion [12-14] applies to pores between 10 Å and 500 Å in size where the majority of gas molecules travel in the free space, frequently bumping into the walls and each other. Here d_K is defined as the pore diameter such that Knudsen diffusion is the dominant transport mechanism within pores larger than d_K . The Knudsen diffusivity coefficient can be expressed in the following form

$$D_K = \frac{d}{3\tau} \bar{v}, \quad (2.12)$$

where d is the pore diameter, τ is the pore tortuosity and \bar{v} is the average molecular speed. This expression shows that the separation outcome depends on the differences in molecular speeds (or molecular mass). The average molecular speed \bar{v} is calculated using the Maxwell speed distribution,

$$\bar{v} = \sqrt{\frac{8RT}{\pi m}}, \quad (2.13)$$

where m is the molecular mass.

Solubility

The simplest expression for the solubility comes from the ideal gas law,

$$S_K = \frac{v_f}{RT}. \quad (2.14)$$

Permeability

Finally, the total permeability for Knudsen transport is a decreasing function of temperature and molecular mass and takes the form [10]

$$P_K = \frac{d}{3\tau} v_f \sqrt{\frac{8}{mRT\pi}}. \quad (2.15)$$

2.1.3 Membranes: Porous structures

The available range of membrane materials includes polymeric, carbon, silica, zeolite and composite. Each type of membrane has a different porous structure, as illustrated in Figure 2.3. Membranes can be thought of as having a fixed (immovable) network of pores in which the gas molecule travels, with the exception of polymeric membranes.

Polymeric membranes are composed of an amorphous mix of polymer chains

bound together mostly by van der Waals forces. This arrangement allows polymers to vary in their flexibility, ranging from very stiff polymers known as “glasses” to very flexible polymers known as “rubbers”, distinguished by the mobility of the chains. Although polymeric membranes have often been branded as non-porous, in this modelling framework it is convenient to consider them as porous. Glassy polymers have pores that can be considered as “frozen” over short times scales, as demonstrated in Figure 2.4a, while rubbery polymers have dynamic pores that move, shrink, expand and disappear, as demonstrated in Figure 2.4b [5].

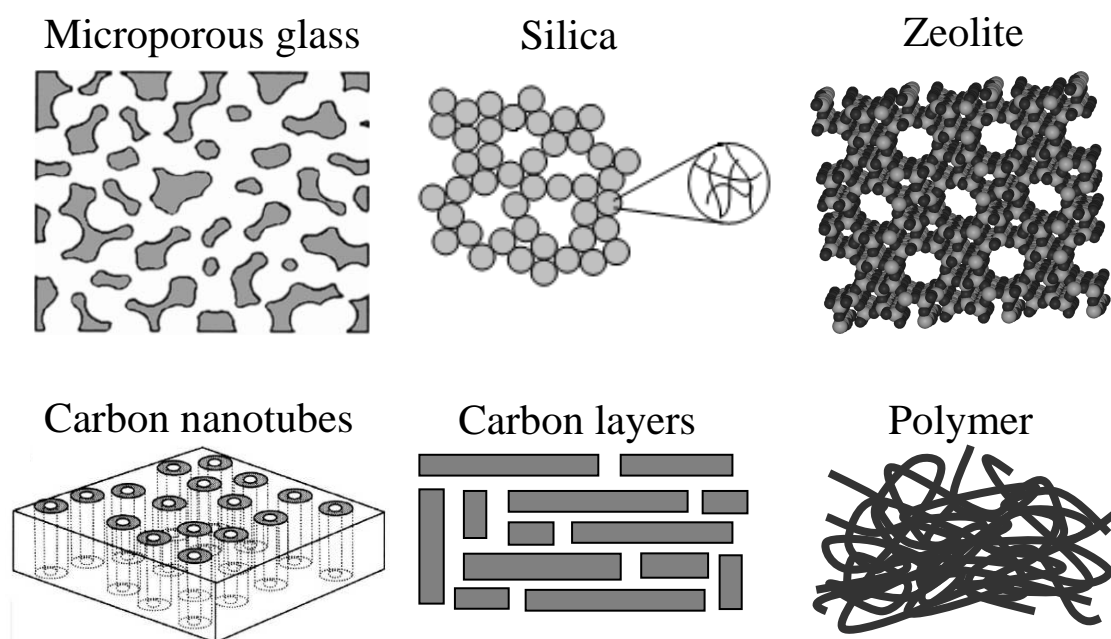


Figure 2.3: Porous structure within various types of membranes [12, 15, 16].

a) Glassy polymer

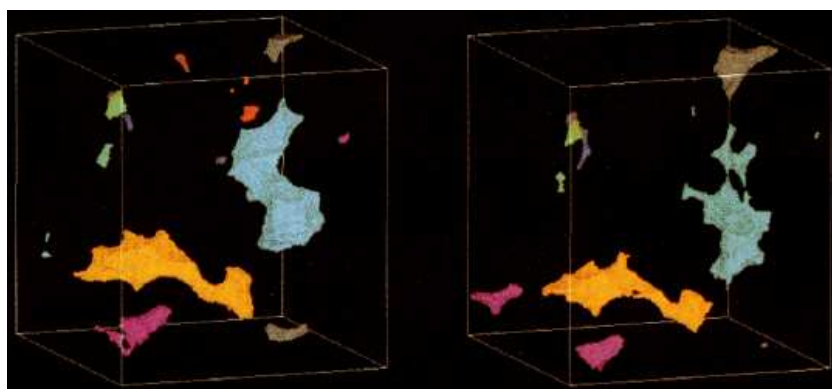


Figure 2.4 (continued to next page)

b) Rubbery polymer

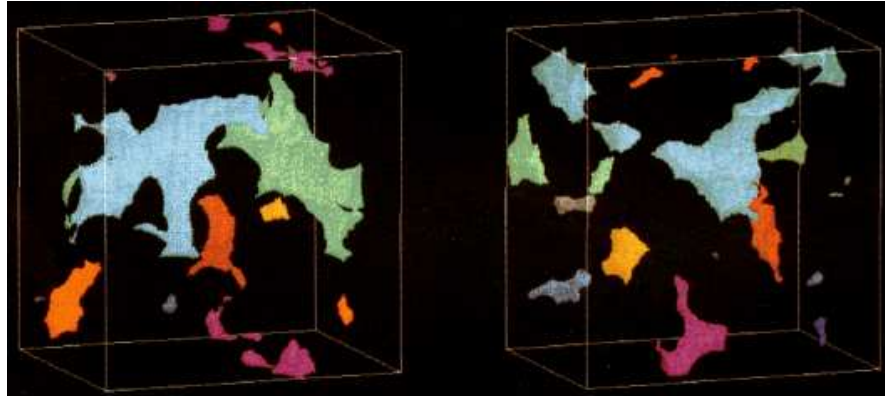


Figure 2.4: Computer simulations performed by Greenfield and Theodorou [5] for free volume clusters before and after 10^7 Monte Carlo steps within a) glassy polymer and b) rubbery polymer.

2.1.4 Transition State Theory (TST)

The diffusion of molecules within porous networks similar to that of microporous silica and glassy polymers can be modelled within the framework of Transition State Theory (TST) [16, 17]. A gas molecule bounces around in the reactant cavity eventually bouncing towards the transition state by which it transports through to the product cavity and therefore successfully makes a diffusive jump, demonstrated in Figure 2.5a. Within glassy polymers, see Figure 2.5b, the transition state is a dynamical section that becomes available through polymer chain motions. Within microporous silica, see Figure 2.5c, the transition state is a permanent pathway for the transport of the gas molecule. The transition state theory offers a method to express the rate of diffusion D (or diffusivity) within these porous networks in the following way:

D = the probability that the molecule will travel towards a transition (ρ_g)

X the probability that the molecule will pass through the transition (ρ_E)

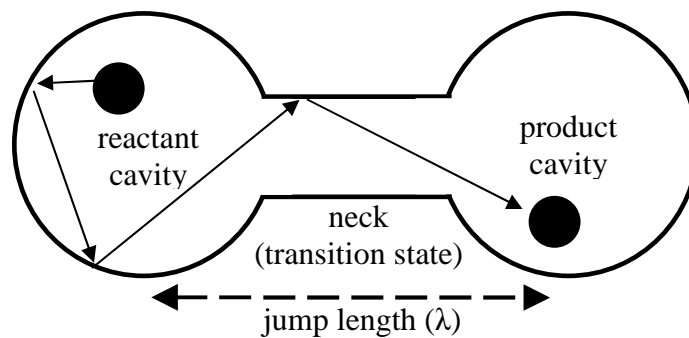
X the velocity of the molecule through the transition (u)

X the jump length from the reactant cavity to the product cavity (λ).

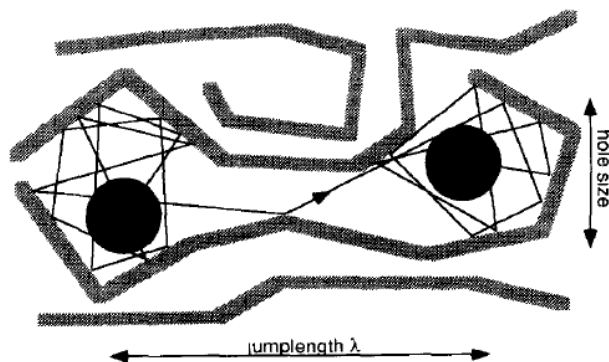
This formula, $D = \rho_g \rho_E u \lambda$, provides some insight into the factors contributing to the separation of particular molecules. If the transition state has the form of a narrow constriction then the smaller molecules are more likely to pass through and therefore have a higher rate of diffusion than their larger counterparts. On the other hand, if the

transition state is wide enough for both molecules to freely pass through then the velocity at which they travel may be the dominant factor in determining the rate of diffusion. Further, within glassy polymers the rate of diffusion could be dominated by the rate of polymer chain movements which occasionally provide a transition pathway for the molecules.

a) Demonstration of the transition state theory.



b) Diffusive jump in glassy polymer. Taken from Smit et al. [18].



c) Diffusive jump in microporous silica. Taken from Shelekhin et al. [16].

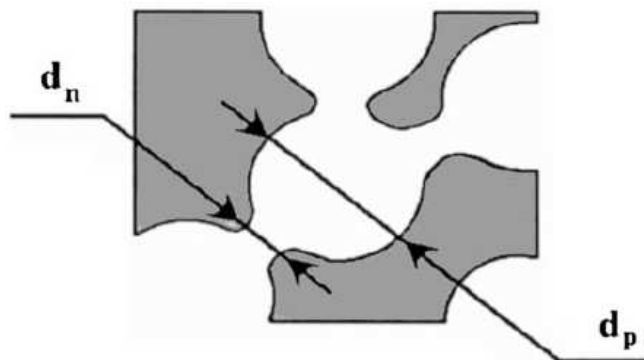


Figure 2.5: Transition State Theory.

2.1.5 Transport models for ordered pore networks

Membranes with ordered structures such as zeolites, nanotubes and graphene have great potential as gas separation membranes. In addition to having thermal and chemical stability, the porosity of these structures is ordered and therefore there is usually more control over separation properties. The pores within these structures are such that gas transport can not be completely explained by the Transition State Theory. This is because, in nanotubes for example, there is only one transition, from outside of the tube to inside of the tube and similarly with graphene based structures. Two alternative models are outlined here, which are illustrated in Figure 2.6, and which are explained in depth by the work of Gilron and Soffer [19].

2.1.5.1 Parallel transport model

The parallel transport model considers the total flux as the contribution from the molecules travelling via surface diffusion and from the molecules travelling via Knudsen diffusion. This model does not consider transition stages and is applicable to straight pores that continue throughout the entire membrane such as nanotube-based membranes. Gilron and Soffer presented the following expression,

$$P_{tot} = P_S + P_K, \quad (2.16)$$

where P_S is the surface diffusion permeability and P_K is the Knudsen diffusion permeability, defined by Equations 2.11 and 2.15, respectively.

2.1.5.2 Resistance in series transport model

The resistance in series model assumes that the gas molecules encounter constrictions at certain positions throughout the pore which control the rate of diffusion. For this scenario the total permeability is inversely related to the total resistance

$$R_{tot} = \frac{l}{P_{tot}} = \frac{x_K l \tau}{P_K} + \frac{(1-x_K) l \tau}{P_A}, \quad (2.17)$$

where x_K is the fraction of the total pore length l with pore size d_{p2} in which Knudsen diffusion dominates while $(1-x_K)$ is the fraction of the total pore length l with pore size d_{p1} in which activation diffusion dominates and τ is the pore tortuosity, see Figure 2.6b. Total permeability simplifies to

$$P_{tot} = \frac{P_A P_K}{\tau(x_K P_A + (1-x_K) P_K)}. \quad (2.18)$$

where P_A is the activation diffusion permeability and P_K is the Knudsen diffusion permeability, defined by Equations 2.8 and 2.15, respectively.

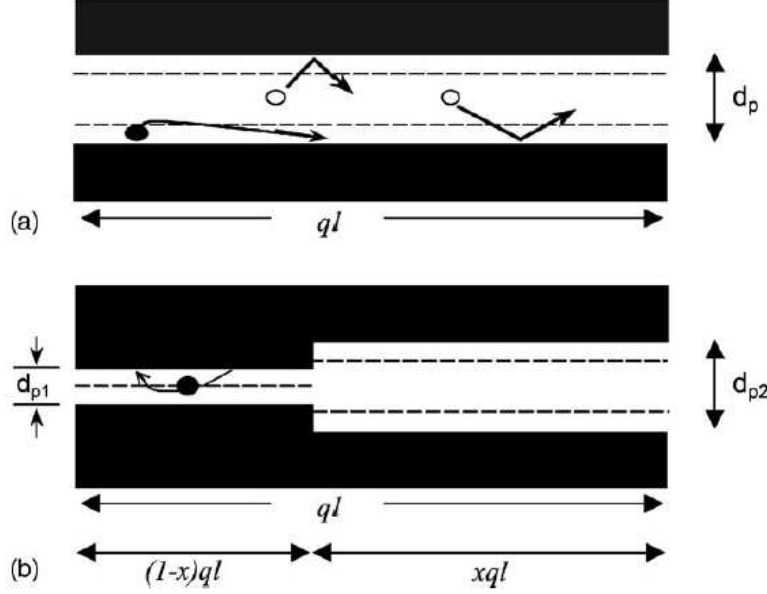


Figure 2.6: Schematic models for a) parallel transport and b) resistance in series transport. Taken from Gilron and Soffer [19].

2.1.6 Modelling approaches

There are many material properties that relate to permeability which can be used to predict and enhance separation performance. Here two approaches are reviewed:

- investigations into the transport mechanisms within individual pores at the nano-scale where pore size, shape and composition are considered (Section 2.1.6.1); and
- investigations into the relationship between permeability and the bulk free volume at the macro-scale (Section 2.1.6.2).

2.1.6.1 Gas-pore interactions

Particles at the nano-scale are attracted at large distances and repelled at short distances due to van der Waals forces. These forces caused by interactions between particles have become crucial in understanding molecular motion. One particular case of interest is the C_{60} -nanotube oscillator device which has been modelled from two approaches: 1) a MD computer simulation approach and 2) a mathematical continuum modelling approach. According to the MD simulations [20, 21] of this device, the C_{60} fullerene positioned at the opening of the CNT is either repelled away from the tube or sucked inside the tube

where it begins to oscillate back and forth between both openings due to van der Waals forces. The MD approach is limited to the investigation of a single case at one time and is incapable of considering the infinite variations of tube size, length and composition. The mathematical modelling approach for the oscillator device treats the tube and fullerene as continuous surfaces where the interactions between them are found by integrating the van der Waals potentials across each surface [22, 23]. This approach allows the various tube properties to be studied and was found to deliver important information such as the minimum size of a CNT to accept a fullerene and the size of a CNT that provides the maximum suction energy, which compares well with the MD simulations [21, 22]. The method has since been used to successfully model nanoscale gigahertz oscillators [23], drug acceptance into CNT's for "golden bullet" drug delivery [24, 25], water transport through CNT's [26] and other applications [27, 28].

The van der Waals interactions between particles are modelled well by the Lennard-Jones function containing two parameters, the kinetic diameter σ (the distance where the potential energy between the particles is zero) and the well depth ε (the greatest potential minimum between the particles), explained in further detail in Section 5.1.2. These parameters were used by Freeman [29] to establish a theoretical basis for the upper-bound relationship (empirically determined by Robeson [30]) between selectivity and permeability for a range of polymers and gases. The diffusion of a gas is dependent on its kinetic diameter while its solubility mainly depends on the condensability of the gas and consequently on the well depth for gas-gas interactions. It is noted by Freeman [29] that gas-polymer interactions are also an important factor but the dependence was not determined.

Gas-pore wall interactions have been considered to identify different pore size regimes for gas adsorption by Everett and Powl [31] and later modified to determine gas separation scenarios by de Lange et al. [10]. Figure 2.7 shows the potential energy within slit-shaped pores. A deep single minimum occurs within small pores and the shallower double minimum occurs in larger pores, calculated by Everett and Powl. This potential energy is thought of as the adsorption energy which is enhanced at an optimal pore size, indicated by the peaks in Figure 2.8 for cylindrical and slit-shaped pores. Everett and Powl used these calculations to further understand adsorption of noble gases within microporous carbons. One of the key points outlined in Everett and Powl's work is that the separation outcomes may be predicted by comparing the potential energy curves of particular gases.

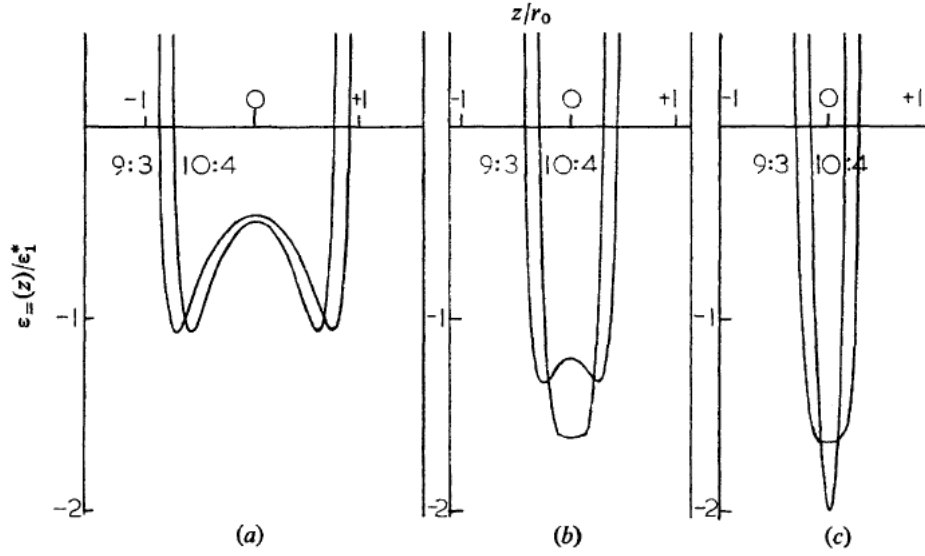


Figure 2.7: Potential energy $\varepsilon_-(z)$ between two parallel planes (10:4) and two parallel slabs (9:3) at a distance apart of $2d$ for (a) $d/r_0 = 1.60$, (b) $d/r_0 = 1.14$ and (c) $d/r_0 = 1.00$, normalized by the energy minimum ε_1^* located at a distance of r_0 from a single slab. Taken from Everett and Powl [31].

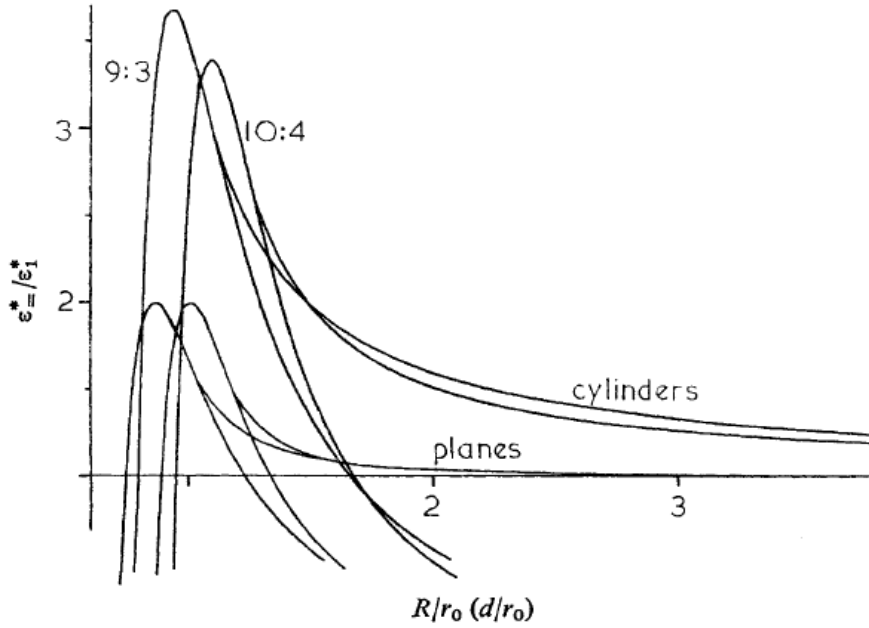


Figure 2.8: Scaled potential energy minima $\varepsilon^* / \varepsilon_1^*$ within cylindrical and slit-shaped pores with varying radius R and slit size $2d$, respectively, where ε^* is the minimum potential within the pore and ε_1^* is the minimum potential with a single flat surface. Curves that go below the horizontal axis are the scaled potentials within the centre of the pore $\varepsilon(0) / \varepsilon_1^*$ where the potential in the centre $\varepsilon(0)$ becomes less than the minimum potential with a single flat surface ε_1^* , i.e. $\varepsilon(0)/\varepsilon_1^* < 1$, within larger pores. Taken from Everett and Powl [31].

de Lange, Keizer and Burggraaf [10] later extended the work of Everett and Powl by relating transport mechanisms to potential energy calculations. Figure 2.9 demonstrates the separation scenarios within cylindrical shaped pores. Situation 'a' is where molecule A is accepted within the pore while molecule B is rejected by the repulsive forces experienced. This refers to true molecular sieving or size-sieving. Situations 'b1' and 'b2' are where both molecules are accepted within the pore but molecule A has a much deeper potential than molecule B. Since the pore is cylindrical, molecules may not pass each other and therefore the rate of diffusion is governed by the slowest component. Situations 'c1' and 'c2' are where molecules may pass each other and the potential energy becomes weaker having less influence on transport. These scenarios are combined with an extensive model that incorporates different stages of transport through the membrane and existing transport equations.

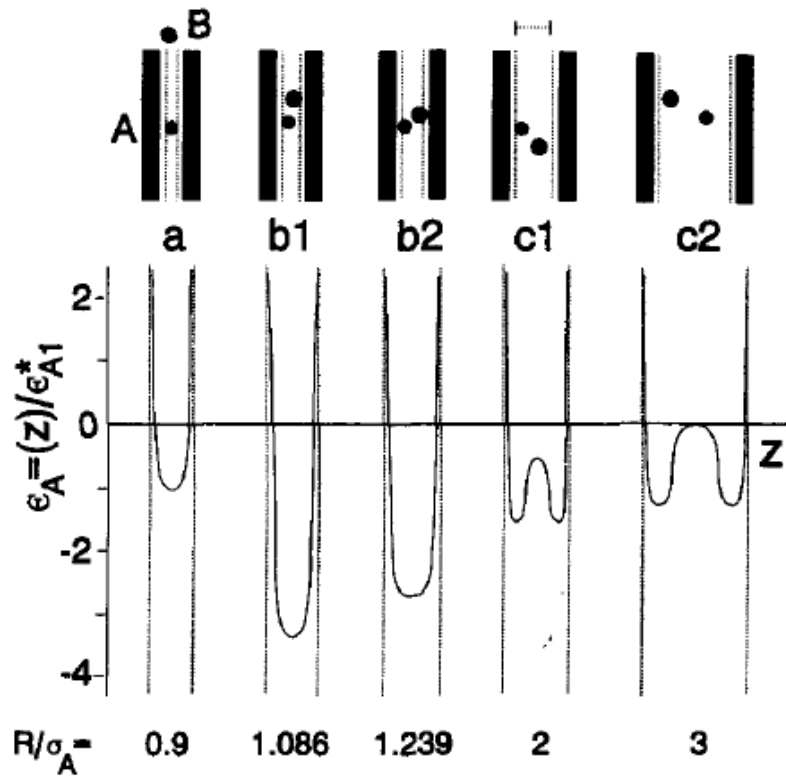


Figure 2.9: Separation regimes determined by the potential energies within pores of different sizes. Potential energy $\varepsilon_A(z)$ for molecule A within cylindrical pores with radius R , scaled by the potential minimum ε_1^* for molecule A with a single free surface and the Lennard-Jones kinetic diameter parameter σ_A . Taken from de Lange et al. [10].

The extensive model considers the total flux as the contribution of the flux at different stages, indicated schematically in Figure 2.10: 1) Adsorption onto surface and flux from position $\theta_{0,\text{surf}}$ to θ_0 at the pore entrance via surface diffusion ($f2.J$); 2) Adsorption directly at the pore entrance at position θ_0 ($f1.J$); 3) Flux directly to pore entrance with no adsorption taking place ($F1.J$); 4) Entrance of adsorbed molecules at position θ_0 to position θ_1 within the pore ($F2.J$); 5) Micropore diffusion through the pores (J); 6) Desorption of the molecules from within the pore to the external surface or directly to the gas phase; 7) Desorption from the external surface to the gas phase.

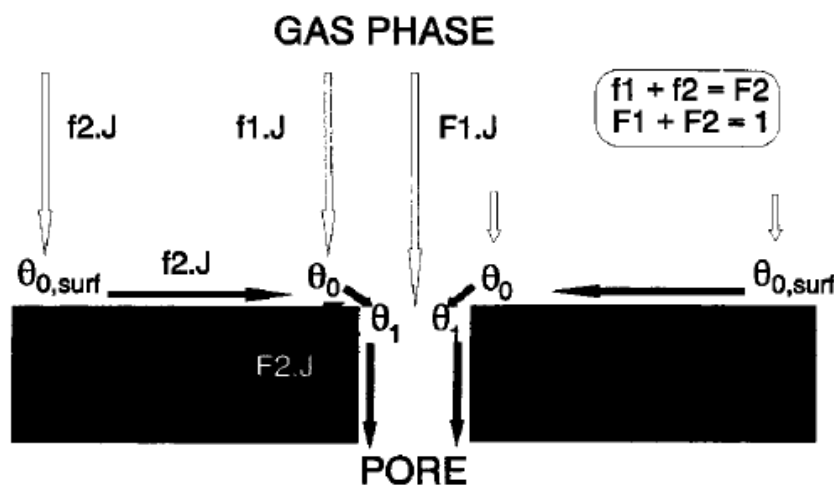


Figure 2.10: Schematic model of the total flux components through microporous membranes. Taken from de Lange et al. [10].

2.1.6.2 Free volume within polymers

There is a wide range of polymers available for use as membranes which differ greatly in their structure, mobility, and packing, all of which influence transport properties. In glassy polymer membranes, the study of the transport of an individual gas molecule provides insufficient information to form a complete model for the total flux outcome throughout the entire membrane. Factors at the macro-scale that have a significant effect on gas transport are free space, pore connectivity and pore size distribution. Fundamental equations, molecular simulation procedures and Positron Annihilation Lifetime Spectroscopy (PALS) techniques for analysing the macro-scale properties are discussed here.

Free space can be quantified by various methods. Doolittle [32] originally showed that the viscosities of liquid normal paraffins are related to the relative free space of the liquid. Relative free space was defined as v_f / v_0 where v_f is the volume of free-space per gram of liquid at any temperature and v_0 is the volume of 1 gram of liquid extrapolated to absolute zero without a change of phase. Viscosity was then related to relative free space by this expression, $\eta = A \exp(B v_0 / v_f)$. The relative free space of the liquids ranged from 0.2178 to 0.6868 or in other words 18% to 40% free volume. The relation applies to simple liquids at high enough temperatures so that the proportion of free volume is relatively high.

Williams, Landel and Ferry (WLF) [33] then used a modified Doolittle expression to relate the shift factor (a factor characterising the time shifts of various properties at different temperatures) of amorphous polymers to the amount of free space. They assumed that for supercooled systems Doolittle's equation could be modified by noting that v_f is small and v_0 is practically equal to the specific volume ($v_0 + v_f$), so v_f / v_0 can be replaced by the fractional free volume, $v_f / (v_0 + v_f) = FFV$. For decades this assumption was valid when applied to glassy polymers with a typical v_f of 10% (for example polysulfone PSF, polycarbonate PC, polymethylmethacrylate PMMA, and polyvinylacetate PVAc) [34]. The advent of very high free volume glassy polymers [6, 7, 35-39] has meant that now there are supercooled systems with fractional free volumes of up to about 35% (for example polytrimethylsilylpropene PTMSP, polymethylpentene PMP, and polytetrafluoroethylenebistrifluoromethyldifluorodioxole AF2400) which make the WLF assumption invalid. However, replacing relative free space with fractional free volume does not change the basic form of the equation as shown here,

$$A \exp\left(B \frac{v_0 + v_f}{v_f}\right) = A \exp\left(B \frac{v_0}{v_f} + B\right) = A \exp(B) \exp\left(B \frac{v_0}{v_f}\right) = A_1 \exp\left(B \frac{v_0}{v_f}\right). \quad (2.19)$$

Therefore even though the WLF assumption does not apply to newly available high free volume polymers, the Doolittle relation remains the same, with a different constant $A_1 = A \exp(B)$. Today the Doolittle relation is most frequently expressed in terms of fractional free volume, FFV , which is $v_f / (v_0 + v_f)$ rather than the ratio v_f / v_0 .

Cohen and Turnbull [40] later provided a theoretical explanation for the Doolittle equation by considering the transport in a liquid of hard spheres where a molecule can not diffuse unless there is a critical amount of space available for it to move (usually equal to its occupied space). Subsequently Cohen and Turnbull combined Doolittle's

expression with the Stokes-Einstein relation to create an expression for the diffusion coefficient D within liquids and glasses. The result was of the form

$$D = A \exp\left[-\frac{B}{FFV}\right], \quad (2.20)$$

where the constant A depends on the system's temperature and the gas molecule's volume and shape and B , while originally labelled as a material constant, was later found to depend on the gas molecule's kinetic diameter [41]. Equation 2.20 will be used throughout this thesis as the Doolittle relation.

In previous work [42-44] the permeabilities of polymers approximately obey this Doolittle expression where a linear relationship is observed when viewed on logarithmic permeability versus inverse free volume axes, see Figure 2.11. This approximation is valid for families of polymers but breaks down when polymers are compared that have widely varying free volume [7, 45, 46].

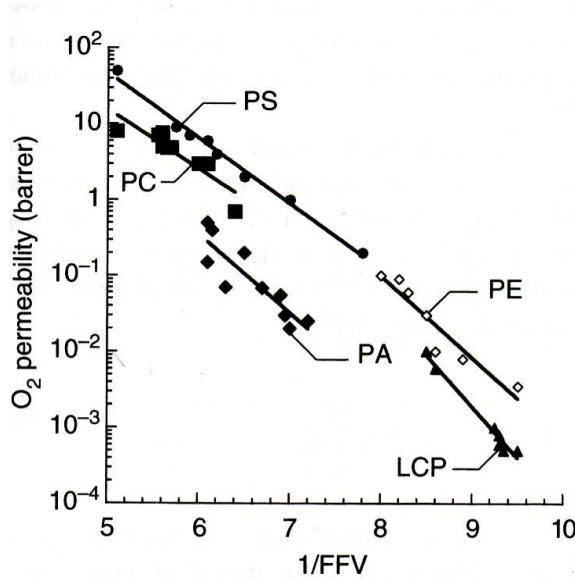


Figure 2.11: O_2 permeability for glassy polystyrenes (PS) at 35°C [47], polycarbonates (PC) at 35°C [48, 49], polyamides (PA) at 25°C [50], polyesters (PE) at 30°C [51] and liquid crystalline polyesters (LCP) at 35°C [52, 53]. Taken from Yampolskii et al. [44].

An alternative relation has been used in the past by Jia and Xu [54], to fit the permeability of sixty homopolymers, expressed in the following form

$$P = a \exp(b FFV / CED), \quad (2.21)$$

where a and b are parameters found to be related to the square of the gas kinetic diameter, and CED is the cohesive energy density calculated from Bondi's group contribution method [55, 56]. This relation was later found to be a poor predictor when tested against a different dataset, carried out by Thran et al. [43].

A more complex version of the Doolittle equation, established by Vrentas and Duda [57], is capable of predicting permeability behaviour in polymers, taking into account that the free volume is dependent on gas concentration, and therefore gas sorption data is required to make the prediction. Once gas sorption data is collected an extensive prediction can be made for gas permeability at different temperature, pressure and molecular weight [58]. Thran et al. [43] have investigated six gases and seventy-one polymers from the Landolt Bornstein database and found significant deviations to the $\log(D)$ versus FFV^{-1} relationship that are not predicted by the theory of Vrentas and Duda. Thran et al. [43] suggested that the substantial deviations from linearity are due to the influence of an additional polymer property, for example cohesive energy density and/or glass transition temperature. For a comprehensive review of models for diffusion in polymers see Frisch and Stern [59].

The definition of occupied volume v_0 is different throughout the literature. As stated earlier, Doolittle defined occupied volume as the volume of 1 gram of liquid extrapolated to absolute zero without a change of phase. Over time the most popular definition of occupied volume for polymers has come from using Bondi's group contribution method [55, 56] which is based on the packing densities of molecular crystals at absolute zero and the van der Waals volume of each of the various groups in the polymer structure,

$$v_0 = 1.3 \sum_{k=1}^K (v_w)_k, \quad (2.22)$$

where K is the total number of groups into which the repeat unit structure of the polymer is divided and $(v_w)_k$ is the van der Waals volume of each group k . The factor of 1.3 was estimated by Bondi and is assumed to be applicable to all groups and structures.

Park and Paul [60] modified Bondi's group contribution method by allowing the occupied volume to vary depending on the gas used for permeation and on each group within the polymer structure. In this way fractional free volume becomes more of an accessible fractional free volume for the particular gas being used [5],

$$(FFV)_n = [v - (v_0)_n] / v, \quad (2.23)$$

$$(v_0)_n = \sum_{k=1}^K \gamma_{nk} (v_w)_k, \quad (2.24)$$

where $(FFV)_n$ is the fractional free volume accessible for a gas n , v is the total specific volume and γ_{nk} is an empirical parameter for a gas n and group k . Park and Paul used a comprehensive database of polymers and their γ_{nk} values were chosen so that the new $(FFV)_n$ values had the best possible fit to the Doolittle relation $P = A^* \exp(-B/(FFV)_n)$, where A^* is the product of A and a solubility constant S . As shown in Figure 2.12 the spread of the data is reduced when comparing the modified fractional free volume $(FFV)_{CO_2}$ with the conventional fractional free volume FFV .

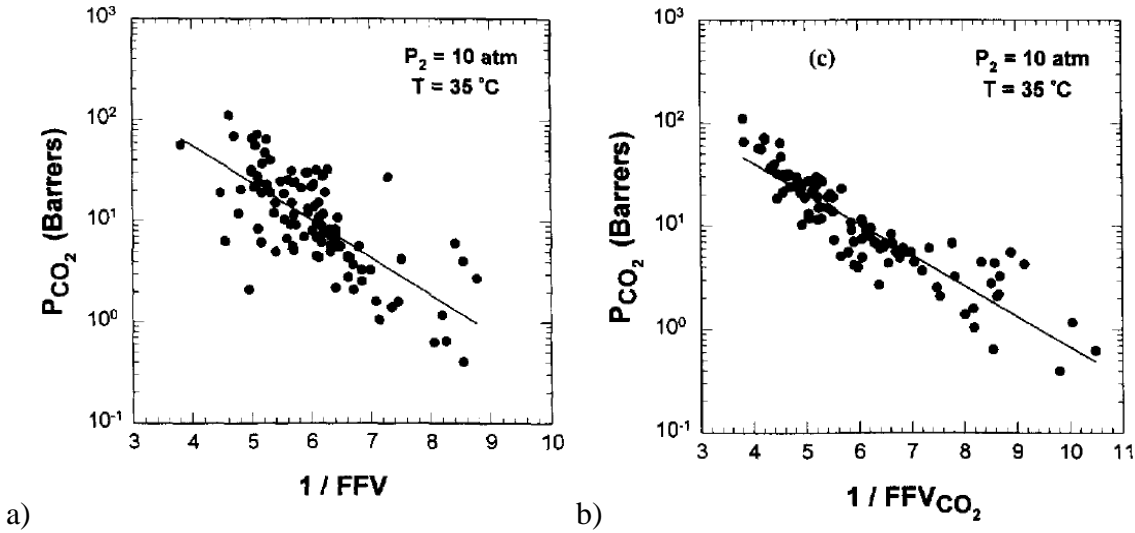


Figure 2.12: Carbon dioxide permeability versus inverse a) fractional free volume and b) modified fractional free volume. Taken from Park and Paul [60].

The amount of free volume alone does not provide information about the connectivity and tortuosity of the pores. This presents a problem when searching for a model that explains transport data for the wide range of polymers using the amount of free volume as the determining factor. Percolation theory sheds light on this problem by suggesting that once a certain amount of randomly placed free volume elements is added to a system a percolation threshold will be reached and there will exist a connected pathway from one side of the system to the other. Since glassy polymers consist of randomly placed free volume elements, a percolation threshold exists and has been determined by Greenfield and Theodorou [5] via computer simulations and

Hedstrom et al. [3] via molecular dynamics (MD) simulations guided by small angle X-ray scattering (SAXS) experimental results. It seems plausible that a relation between permeability and free volume should have the ability to predict the increase in permeability due to pores becoming interconnected, i.e. connected channels forming a percolation pathway.

2.2 Thesis work overview

The new models presented in this thesis are built upon the previous work reviewed above. First in Chapter 3 a nano-scale approach is taken by considering gas-pore interactions, similar to the works by Cox et al. [22, 23], Hilder and Hill [61], Everett and Powl [31], de Lange et al. [10] and Freeman [29]. Second in Chapter 4 a macro-scale approach is taken by considering the bulk free volume, similar to works by Doolittle [32], Williams et al. [33], Park and Paul [60], Ventras and Duda [57], Jia and Xu [54], and Thran et al. [43]. More details are found below.

2.2.1 Nano-scale: Individual pore transport

A key investigation that has not been explored in the previous work is the development of a method to determine the pore size regions in which different transport mechanisms dominate. This thesis provides a method by combining and extending upon the previous work. Mathematical formulations for the interactions between the gas molecule and the pore are developed following the work of Cox et al. [22, 23] who investigated the interactions between the fullerene and the nanotube. The formulations are then used to provide insight into the transport behaviour of each gas within differently shaped pores similar to the work of Everett and Powl [31] who determined adsorption scenarios within microporous silica and the work of de Lange et al. [10, 62] who investigated the separation scenarios within ceramics. By combining these results with the existing transport theory, pore size regions are distinguished in which different transport mechanisms dominate and quantitative expressions for the permeability are given. The main features that the model predicts are minimum pore size for barrier-free transport, pore size that maximizes the suction force at the entrance, and minimum pore size for Knudsen-type transport. Experimental results match the model predictions well and provide insight into the separation properties observed [15, 19, 63, 64].

2.2.2 Macro-scale: Bulk free volume transport

The previous Doolittle-derived free volume based models [32, 33, 57] have had great success in modelling transport properties in polymers having free volume within a certain range. Yet a global model is highly sought after that can describe gas diffusion in the wide range of polymers currently available, with fractional free volumes ranging from 10 to 35 %, and has hitherto not been available. By using an extensive collection of data for conventional and high free volume polymers [6, 7, 36, 37] a new relation is proposed of the form

$$D = \alpha \exp(\beta FFV). \quad (2.25)$$

This is in similar form to the expression from Jia and Xu [54] and is a reasonable predictor without the need for calculating the cohesive energy density or measuring the sorption data for each polymer, and is based only on the structural parameter, fractional free volume. This new relation fits, much better than the Doolittle relation, this wider range of polymers and also shows the increase in permeability/diffusivity at the critical free volume where pores are predicted to become bi-continuous by the work of Hedstrom et al. [3]. Equation 2.25 also fits the experimental diffusion coefficients and MD simulated accessible volume fraction (AVF) data of Hofmann et al. [7] for oxygen in a range of polymers, which display the percolation induced increase in the rate of molecular transport at the critical accessible free volume predicted by Greenfield and Theodorou [5].

References

- [1] F. Peng, L. Lu, H. Sun, Y. Wang, J. Liu and Z. Jiang, Hybrid organic-inorganic membrane: solving the tradeoff between permeability and selectivity, *Chem. Mater.*, 17 (2005) 6790.
- [2] Y. Yampol'skii, N. B. Beshpalova, E. S. Finkel'shtein, V. I. Bondar and A. V. Popov, Synthesis, gas permeability, and gas sorption properties of fluorine containing norbornene polymers, *Macromolecules*, 27 (1994) 2872.
- [3] J. A. Hedstrom, M. F. Toney, E. Huang, H. C. Kim, W. Volksen, T. Magbitang and R. D. Miller, Pore morphologies in disordered nanoporous thin films, *Langmuir*, 20 (2004) 1535.

- [4] H. Jinnai, Y. Nishikawa, S.-H. Chen, S. Koizumi and T. Hashimoto, Morphological characterization of bicontinuous structures in polymer blends and microemulsions by the inverse-clipping method in the context of the clipped-random-wave model, *Phys. Rev. E*, 61 (2000) 6773.
- [5] M. L. Greenfield and D. N. Theodorou, Geometric analysis of diffusion pathways in glassy and melt atactic polypropylene, *Macromolecules*, 26 (1993) 5461.
- [6] X. Y. Wang, K. M. Lee, Y. Lu, M. T. Stone, I. C. Sanchez and B. D. Freeman, Cavity size distributions in high free volume glassy polymers by molecular simulation, *Polymer*, 45 (2004) 3907.
- [7] D. Hofmann, M. Entrialgo-Castano, A. Lerbret, M. Heuchel and Y. Yampolskii, Molecular modeling investigation of free volume distributions in stiff chain polymers with conventional and ultrahigh free volume: Comparison between molecular modeling and positron lifetime studies, *Macromolecules*, 36 (2003) 8528.
- [8] Y. Yampolskii, I. Pinnau and B. D. Freeman, *Materials Science of Membranes for Gas and Vapor Separation*, John Wiley & Sons, Ltd, 2006.
- [9] E. R. Gilliland, R. F. Baddour, G. P. Perkinson and K. J. Sladek, Diffusion on surfaces. I. Effect of concentration on the diffusivity of physically adsorbed gases, *Ind. Eng. Chem. Fundam.*, 13 (1974) 95.
- [10] R. S. A. de Lange, K. Keizer and A. J. Burggraaf, Analysis and theory of gas transport in microporous sol-gel derived ceramic membranes, *J. Membr. Sci.*, 104 (1995) 81.
- [11] R. M. de Vos and H. Verweij, Improved performance of silica membranes for gas separation, *J. Membr. Sci.*, 143 (1998) 37.
- [12] B. J. Hinds, N. Chopra, T. Rantell, R. Andrews, V. Gavalas and L. G. Bachas, Aligned multiwalled carbon nanotube membranes, *Science*, 303 (2004) 62.

- [13] M. Knudsen, Die Gesetze der Molekularströmung und der inneren Reibungsströmung der Gase durch Röhren, *Ann. Phys.*, 28 (1909) 75.
- [14] S. T. Hwang and K. Kammermeyer, *Membranes in Separations*, Krieger, Malabar, Florida, 1984.
- [15] M. C. Duke, S. J. Pas, A. J. Hill, Y. S. Lin and J. C. Diniz da Costa, Exposing the molecular sieving architecture of amorphous silica using positron annihilation spectroscopy, *Adv. Funct. Mater.*, 18 (2008) 1.
- [16] A. B. Shelekhin, A. G. Dixon and Y. H. Ma, Theory of gas diffusion and permeation in inorganic molecular-sieve membranes, *AIChE*, 41 (1995) 58.
- [17] A. A. Gray-Weale, R. H. Henchman, R. G. Gilbert, M. L. Greenfield and D. N. Theodorou, Transition-state theory model for the diffusion coefficients of small penetrants in glassy polymers, *Macromolecules*, 30 (1997) 7296.
- [18] E. Smit, M. H. V. Mulder, C. A. Smolders, H. Karrenbeld, J. van Eerden and D. Feil, Modelling of the diffusion of carbon dioxide in polyimide matrices by computer simulation, *J. Membr. Sci.*, 73 (1992) 247.
- [19] J. Gilron and A. Soffer, Knudsen diffusion in microporous carbon membranes with molecular sieving character, *J. Membr. Sci.*, 209 (2002) 339.
- [20] D. Qian, W. K. Liu and R. S. Ruoff, Mechanics of C60 in nanotubes, *J. Phys. Chem. B.*, 105 (2001) 10753.
- [21] P. Liu, Y. W. Zhang and C. Lu, Oscillatory behavior of C60-nanotube oscillators: A molecular-dynamics study, *J. Appl. Phys.*, 97 (2005) 094313.
- [22] B. J. Cox, N. Thamwattana and J. M. Hill, Mechanics of atoms and fullerenes in single-walled carbon nanotubes. I. Acceptance and suction energies, *Proc. R. Soc. A*, 463 (2007) 461.
- [23] B. J. Cox, N. Thamwattana and J. M. Hill, Mechanics of atoms and fullerenes in single-walled carbon nanotubes. II. Oscillatory behaviour, *Proc. R. Soc. A*, 463 (2007) 477.

- [24] T. A. Hilder and J. M. Hill, Modelling the encapsulation of the anticancer drug cisplatin into carbon nanotubes, *Nanotechnology*, 18 (2007) 275704.
- [25] B. J. Cox, N. Thamwattana and J. M. Hill, Mechanics of spheroidal fullerenes and carbon nanotubes for drug and gene delivery, *Q. J. Mech. Appl. Mech.*, 60 (2007) 231.
- [26] T. A. Hilder and J. M. Hill, Maximum velocity for a single water molecule entering a carbon nanotube, *J. Nanosci. Nanotechnol.*, 9 (2009) 1403.
- [27] T. A. Hilder and J. M. Hill, Oscillating carbon nanotori along carbon nanotubes, *Phys. Rev. B: Condens. Matter*, 75 (2007) 125415.
- [28] B. J. Cox, N. Thamwattana and J. M. Hill, Mechanics of fullerenes oscillating in carbon nanotube bundles, *J. Phys. A: Math. Theor.*, 40 (2007) 13197.
- [29] B. D. Freeman, Basis of permeability/selectivity tradeoff relations in polymeric gas separation membranes, *Macromolecules*, 32 (1999) 375.
- [30] L. M. Robeson, Correlation of separation factor versus permeability for polymeric membranes, *J. Membr. Sci.*, 62 (1991) 165.
- [31] D. H. Everett and J. C. Powl, Adsorption in slit-like and cylindrical micropores in the henry's law region. A model for the microporosity of carbons, *J. Chem. Soc., Faraday Trans. 1*, 72 (1976) 619.
- [32] A. K. Doolittle, Studies in newtonian flow. II. The dependence of the viscosity of liquids on free-space, *J. Appl. Phys.*, 22 (1951) 1471.
- [33] M. L. Williams, R. F. Landel and J. D. Ferry, The temperature dependence of relaxation mechanisms in amorphous polymers and other glass-forming liquids, *J. Am. Chem. Soc.*, 77 (1955) 3701.
- [34] A. J. Hill, M. R. Tant, R. L. McGill, R. R. Shang, D. L. Stockl, D. L. Murray and J. D. Cloyd, Free volume distribution during consolidation and coalescence of latex films, *J. Coat. Technol.*, 73 (2001) 115.

- [35] T. C. Merkel, V. Bondar, K. Nagai and B. D. Freeman, Hydrocarbon and perfluorocarbon gas sorption in poly(dimethylsiloxane), poly(1-trimethylsilyl-1-propyne), and copolymers of tetrafluoroethylene and 2,2-bis(trifluoromethyl)-4,5-difluoro-1,3-dioxole, *Macromolecules*, 32 (1999) 370.
- [36] L. G. Toy, K. Nagai, B. D. Freeman, I. Pinnau, Z. He, T. Masuda, M. Teraguchi and Y. P. Yampolskii, Pure-gas and vapor permeation and sorption properties of poly[1-phenyl-2-[p-(trimethylsilyl)phenyl]acetylene] (PTMSDPA), *Macromolecules*, 33 (2000) 2516.
- [37] C. L. Staiger, S. J. Pas, A. J. Hill and C. J. Cornelius, Gas separation, free volume distribution, and physical aging of a highly microporous spirobisindane polymer, *Chem. Mater.*, 20 (2008) 2606.
- [38] T. C. Merkel, V. Bondar, K. Nagai and B. D. Freeman, Sorption and transport of hydrocarbon and perfluorocarbon gases in poly(1-trimethylsilyl-1-propyne), *J. Polym. Sci., Part B: Polym. Phys.*, 38 (2000) 273.
- [39] A. Y. Alentiev, V. P. Shantarovich, T. C. Merkel, V. I. Bondar, B. D. Freeman and Y. P. Yampolskii, Gas and vapor sorption, permeation, and diffusion in glassy amorphous teflon AF1600, *Macromolecules*, 35 (2002) 9513.
- [40] M. H. Cohen and D. Turnbull, Molecular transport in liquids and glasses, *J. Chem. Phys.*, 31 (1959) 1164.
- [41] H. Lin and B. D. Freeman, Gas permeation and diffusion in cross-linked poly(ethylene glycol diacrylate), *Macromolecules*, 39 (2006) 3568.
- [42] Y. Huang, X. Wang and D. R. Paul, Physical aging of thin glassy polymer films: Free volume interpretation, *J. Membr. Sci.*, 277 (2006) 219.
- [43] A. Thran, G. Kroll and F. Faupel, Correlation between fractional free volume and diffusivity of gas molecules in glassy polymers, *J. Polym. Sci., Part B: Polym. Phys.*, 37 (1999) 3344.
- [44] Y. Yampol'skii, I. Pinnau and B. D. Freeman, *Materials Science of Membranes for Gas and Vapor Separation*, John Wiley & Sons, Ltd, 2006.

- [45] R. K. Bharadwaj and R. H. Boyd, Small molecule penetrant diffusion in aromatic polyesters: a molecular dynamics simulation study, *Polymer*, 40 (1999) 4229.
- [46] K. Haraya and S. T. Hwang, Permeation of oxygen, argon and nitrogen through polymer membranes, *J. Membr. Sci.*, 71 (1992) 13.
- [47] A. Puleo, N. Muruganandam and D. R. Paul, Gas sorption and transport in substituted polystyrenes, *J. Polym. Sci., Part B: Polym. Phys.*, 27 (1989) 2385.
- [48] D. H. Weinkauf and D. R. Paul, Gas transport properties of thermotropic liquid-crystalline copolyesters. II. The effects of copolymer composition, *J. Polym. Sci., Part B: Polym. Phys.*, 30 (1992) 837.
- [49] M. Salame and S. Steingiser, Barrier polymers, *Polym. Plast. Technol. Eng.*, 8 (1977) 155.
- [50] W. M. Lee, Selection of barrier materials from molecular structure, *Polym. Eng. Sci.*, 20 (1980) 65.
- [51] R. R. Light and R. W. Seymour, Effect of sub-T_g relaxations on the gas transport properties of polyesters, *Polym. Eng. Sci.*, 22 (1982) 857.
- [52] D. H. Weinkauf and D. R. Paul, Gas transport properties of thermotropic liquid-crystalline copolyesters. I. The effects of orientation and annealing, *J. Polym. Sci., Part B: Polym. Phys.*, 30 (1992) 813.
- [53] D. H. Weinkauf and D. R. Paul, Gas transport properties of liquid crystalline poly(ethylene ter-ephthalate-co-p-pxybenzoate), *J. Polym. Sci., Part B: Polym. Phys.*, 29 (1991) 329.
- [54] L. Jia and J. Xu, A simple method for prediction of gas permeability of polymer from their molecular structure, *Polym. J.*, 23 (1991) 417.
- [55] D. VanKrevelen, *Properties of Polymers*, Elsevier, Amsterdam, The Netherlands, 1990.
- [56] A. Bondi, van der Waals volumes and radii, *J. Phys. Chem.*, 68 (1964) 441.

- [57] J. S. Vrentas and J. L. Duda, Diffusion in polymer-solvent systems. I. Reexamination of the free-volume theory, *J. Polym. Sci: Polym. Phys. Ed.*, 15 (1977) 403.
- [58] K. Ganesh, R. Nagarajan and J. L. Duda, Rate of gas transport in glassy polymers: A free volume based predictive model, *Ind. Eng. Chem. Res.*, 31 (1992) 746
- [59] H. L. Frisch and S. A. Stern, Diffusion of small molecules in polymers, *CRC Critical Reviews in Solid State Materials*, 11 (1983) 123.
- [60] J. Y. Park and D. R. Paul, Correlation and prediction of gas permeability in glassy polymer membrane materials via a modified free volume based group contribution method, *J. Membr. Sci.*, 125 (1997) 23.
- [61] T. A. Hilder and J. M. Hill, Continuous versus discrete for interacting carbon nanostructures, *J. Phys. A: Math. Theor.*, 40 (2007) 3851.
- [62] A. J. Burggraaf, Single gas permeation of thin zeolite (MFI) membranes: theory and analysis of experimental observations, *J. Membr. Sci.*, 155 (1999) 45.
- [63] J. K. Holt, H. G. Park, Y. Wang, M. Stadermann, A. B. Artyukhin, C. P. Grigoropoulos, A. Noy and O. Bakajin, Fast mass transport through sub-2-nanometer carbon nanotubes, *Science*, 312 (2006) 1034.
- [64] H. Chen and D. S. Sholl, Predictions of selectivity and flux for CH₄/H₂ separations using single walled carbon nanotubes as membranes, *J. Membr. Sci.*, 269 (2006) 152.

List of symbols used in Chapter 2

J	flux or permeation rate
D	diffusivity
C	gas concentration
C_2, C_1	upstream and downstream gas concentration
p_2, p_1	upstream and downstream pressure

x	position across membrane
L	membrane thickness
P	permeability
S	solubility
d	pore size (between surface nuclei)
d_{min}	minimum pore size for barrier-free transport
d_K	minimum pore size for dominant Knudsen transport
E_A	activation energy
T	temperature
v_f	free volume
q	heat of adsorption
K	Henry's law coefficient, $K = K_0 \exp(q/RT)$, where K_0 is a constant
m	mass of gas molecule
τ	pore tortuosity
\bar{v}	average molecular gas speed
ρ_g	probability that the molecule will travel towards a transition
ρ_E	probability that the molecule will pass through the transition
u	velocity of the molecule through the transition
λ	jump length from the reactant cavity to the product cavity
R	resistance ($= L / P$)
l	pore length
x_K	fraction of pore length in which Knudsen dominates
$\varepsilon_-(z)$	potential energy between two parallel planes
FFV	fractional free volume
FFV_n	gas-specific fractional free volume

<i>CED</i>	cohesive energy density
v_0	occupied volume
v_w	van der Waals volume
v	total specific volume ($v_0 + v_f$)

Chapter 3

Gas transport regime within pores

3.1 Introduction

This chapter outlines the mathematical details used to investigate the kinetics of a gas molecule entering a pore. Subsequently, the results are combined with existing transport theory to determine new critical pore sizes for the transition between diffusion mechanisms and their corresponding equations for permeability. The results are compared with experimental data for gas flow rates in carbon nanotube (CNT)-based, carbon molecular sieve (CMS) and molecular sieving silica (MSS) membranes. Possible applications of the model are presented and separation predictions are calculated. As the ability to tailor the porosity of membranes develops, results such as these will guide the material designer.

3.2 Mathematical formulation of gas-pore interactions

The entrance of a pore can be at the surface of the membrane or at a transition region from a larger section within the membrane. The rate of diffusion is believed to be controlled at these pore openings where the gas molecule experiences either an energy barrier, a suction energy or no energy, resulting in a decrease, an increase or no change in the rate of diffusion, respectively [1, 2]. The quantity and nature of these pore openings depend on the material, illustrated in Figure 2.3. Here the van der Waals interactions between the gas and the pore wall are integrated throughout the transition state at the opening of the pore resulting in the work done by the van der Waals forces. Assuming that the amount of energy is converted to kinetic energy this work done can be understood in terms of suction energy, in which a negative suction energy means a

repulsive force (or energy barrier) while a positive suction energy means an attractive force (or acceptance energy) for the gas molecule.

As a molecule approaches a pore opening each atom in the gas molecule will interact with every atom making up the pore wall through van der Waals forces. If the pore opening is too small then the attractive van der Waals forces will not be strong enough to suck the molecule inside and so the molecule will need to have a certain amount of kinetic energy to enter the pore. Therefore, by calculating the total work done by the forces between the gas molecule and the pore wall a minimum pore size for barrier-free transport (d_{min}), and an optimal pore size (d_{opt}) which provides a maximum suction energy, and a minimum pore size for Knudsen transport (d_K) can be determined. By assuming an even distribution of atoms on the pore wall a hybrid discrete-continuum formulation [3] is employed, such that the total interaction potential energy is given by

$$PE = \sum_i \eta \int \Phi(\rho_i) dS, \quad (3.1)$$

where $\Phi(\rho_i)$ is the potential function for atom i of the gas molecule interacting with a surface element dS on the pore wall at a distance of ρ_i away as shown in Figure 3.1, and η is the mean atomic surface density of the atoms making up the pore wall. Here the Lennard-Jones inverse power model is used to represent the interaction potential function between two species

$$\Phi(\rho) = 4\varepsilon \left[-\left(\frac{\sigma}{\rho}\right)^6 + \left(\frac{\sigma}{\rho}\right)^{12} \right], \quad (3.2)$$

where ε is the well depth and σ is the kinetic diameter. Alternatively, this can also be written as

$$\Phi(\rho) = -C_6\rho^{-6} + C_{12}\rho^{-12}, \quad (3.3)$$

where $C_n = 4\varepsilon\sigma^n$. This study is only concerned with the force in the axial direction and therefore the total interaction force, assuming a cylindrical pore shape with the center of the molecule at position Z on the z -axis, is given by

$$F_{cyl}^{tot}(Z) = -\pi\eta d \sum_{i=1}^N \int_0^{2\pi} \int_0^\infty \frac{d\Phi(\rho_i)}{d\rho_i} \frac{(Z + z_i - z)}{\rho_i} dz d\theta, \quad (3.4)$$

and assuming a slit-shaped pore, is given by

$$F_{slit}^{tot}(Z) = -\pi \eta d \sum_{i=1}^N \left[\int_{-\infty}^{\infty} \int_0^{\infty} \frac{d\Phi(\rho_{1,i})}{d\rho_{1,i}} \frac{(Z + z_i - z)}{\rho_{1,i}} dz dy \right. \\ \left. + \int_{-\infty}^{\infty} \int_0^{\infty} \frac{d\Phi(\rho_{2,i})}{d\rho_{2,i}} \frac{(Z + z_i - z)}{\rho_{2,i}} dz dy \right], \quad (3.5)$$

where d is the theoretical pore size which represents the distance between the atom centers making up the pore wall, N is the number of atoms in the discretely modelled molecule, z_i is the offset distance of atom i from the center of the molecule and, $\rho_{1,i}$ and $\rho_{2,i}$ are the distances of atom i from the two parallel slit surfaces. Note that the final results of the model will be expressed in terms of the experimental pore diameter d^* (or effective pore size), defined as $d^* = d - \delta d$, where δd represents the electron cloud thickness, as shown in Figure 3.1. The general definition of “pore diameter” is not agreed upon and usually depends on the characterization method used (for example PALS, SAXS or Neutron reflectometry etc.). In this study δd is set as 3.32 Å for both carbon and silica systems which is the constant used in PALS analysis originally derived from fitting a quantum mechanics expression to observed lifetimes of porous materials with known mean pore diameters [4, 5]. If the material under consideration is an ordered structure with known atom positions then the theoretical pore diameter can be used for predictions, avoiding the potential error in δd representing the difference between the experimentally determined pore diameter (whatever that may be) and the theoretical pore diameter (distance from atom centers). An example of the force profile about the entrance of a cylindrical pore is shown in Figure 3.2.

By using previous results from Cox et al. [6] and Hilder and Hill [3] analytical expressions can be determined for the total interaction force for every gas considered in this work. The centers of mass of all the atoms in the gas molecules He, H₂, CO₂, O₂, N₂ and CO are assumed to be situated on the z -axis for convenience. The total interaction force for these molecules around the entrance of a cylindrical shaped pore takes the form

$$F_{cyl}^{tot}(Z) = \sum_{i=1}^n \pi d \eta \left[\left(\frac{C_{6,i}}{\left((d/2)^2 + (Z + z_i)^2 \right)^3} \right) - \left(\frac{C_{12,i}}{\left((d/2)^2 + (Z + z_i)^2 \right)^6} \right) \right]. \quad (3.6)$$

Similarly, the total interaction force around the entrance of a slit-shaped pore takes the following form

$$F_{slit}^{tot}(Z) = \sum_{i=1}^n \frac{3}{4} \pi \eta \left[\left(\frac{C_{6,i}}{\left((d/2)^2 + (Z + z_i)^2 \right)^{5/2}} \right) - \frac{21}{32} \left(\frac{C_{12,i}}{\left((d/2)^2 + (Z + z_i)^2 \right)^{11/2}} \right) \right], \quad (3.7)$$

where $C_{6,i}$ and $C_{12,i}$ are the attractive and repulsive Lennard-Jones parameters, respectively between an atom i of a particular gas molecule and the pore wall. The parameter values for each individual atom are taken from the Universal Force Field (UFF) values [7] summarized in Table 3.1, where each combination can be approximated by using the Lorentz-Berthelot mixing rules. These parameter values have been widely used by the molecular simulation community to successfully model adsorption and diffusion in porous systems [8-10]. Note that the parameter values can be chosen for any pore wall composition, and here the values for carbon and silica are used, corresponding to CNT-based, CMS and MSS membranes.

The atoms in methane do not align along the z -axis as with the other gas molecules and therefore a different total interaction force expression is used for methane (CH_4) entering a cylindrical pore, thus

$$F_{cyl}^{tot}(Z) = \sum_{i=1}^5 \pi d \eta \left[\frac{C_{6,i}}{\alpha_1^6} F(3, 1/2; 1; 1 - \alpha_2^2 / \alpha_1^2) - \frac{C_{12,i}}{\alpha_1^{12}} F(6, 1/2; 1; 1 - \alpha_2^2 / \alpha_1^2) \right], \quad (3.8)$$

where $\alpha_1^2 = (d/2 + r_i)^2 + (Z + z_i)^2$, $\alpha_2^2 = (d/2 - r_i)^2 + (Z + z_i)^2$, $F(a, b; c; x)$ denotes the usual hypergeometric function [11] and r_i is the offset position of atom i in the radial direction, as shown in Figure 3.1. Accordingly the total interaction force for a methane molecule entering a slit-shaped pore is given as

$$F_{slit}^{tot}(Z) = \sum_{i=1}^5 \frac{3}{4} \pi \eta \left[\frac{C_{6,i}}{\left((Z + z_i)^2 + ((d/2) + x_i)^2 \right)^{5/2}} - \frac{21}{32} \frac{C_{12,i}}{\left((Z + z_i)^2 + ((d/2) + x_i)^2 \right)^{11/2}} + \frac{C_{6,i}}{\left((Z + z_i)^2 + ((d/2) - x_i)^2 \right)^{5/2}} - \frac{21}{32} \frac{C_{12,i}}{\left((Z + z_i)^2 + ((d/2) - x_i)^2 \right)^{11/2}} \right], \quad (3.9)$$

where z_i and x_i are the offset distances from center of molecule $((x,y,z) = (0,0,Z))$ in the z and x direction, respectively, as shown in Figure 3.1. Since there are any number of possible orientations that a methane molecule can enter a pore an average of four distinct orientations is given.

Since the model does not consider gas-gas interactions, the results become less meaningful when the pore size is much larger than the mean free path of the gas molecules.

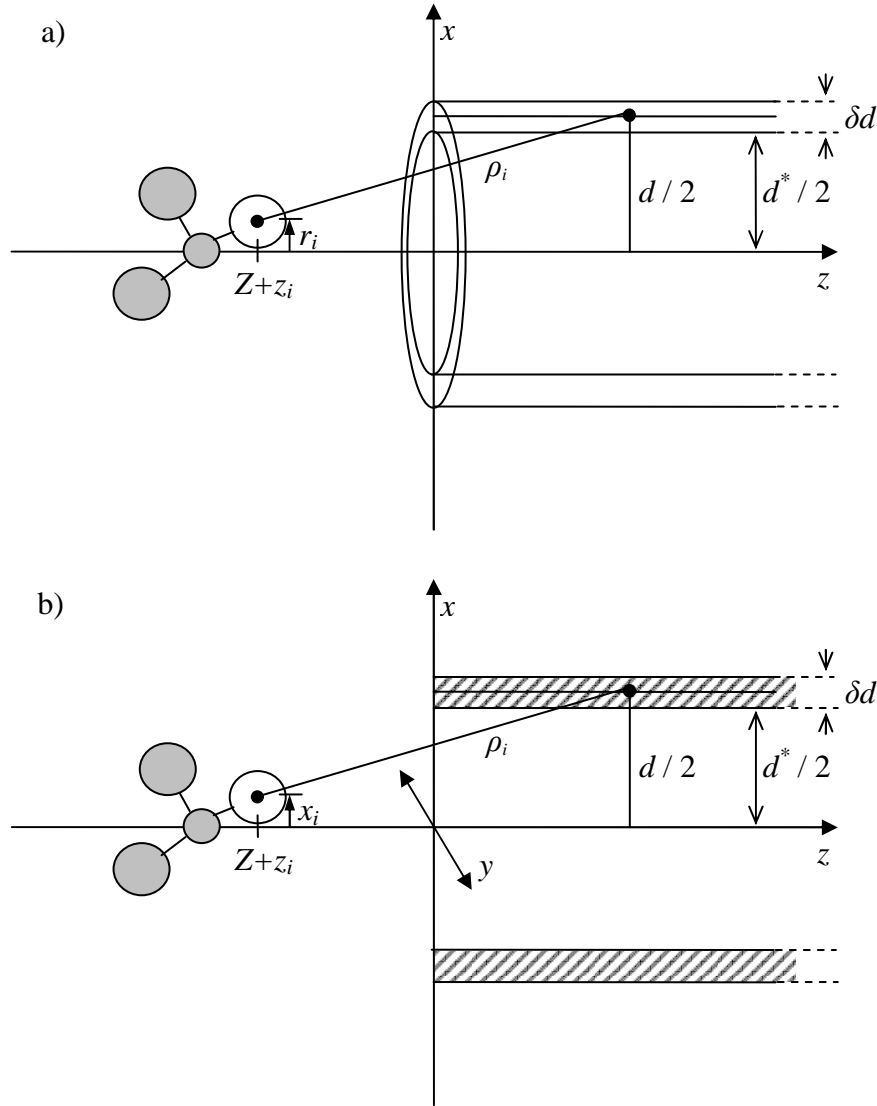


Figure 3.1: Geometry of molecule entering a) a cylindrical pore channel and b) a slit-shaped pore channel. Experimental pore diameter d^* is equivalent to the theoretical pore diameter d minus the electron cloud thickness δd of the wall atoms, i.e. $d^* = d - \delta d$.

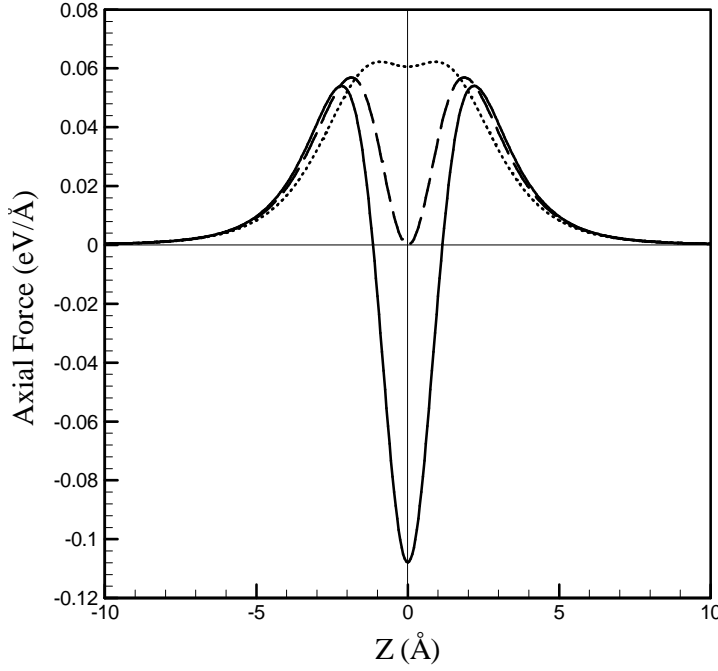


Figure 3.2: Force profile for an oxygen molecule about the entrance ($Z = 0$) of a cylindrical pore with diameter $d = 3.47$ (solid), 3.66 (dashed) and 3.40 (dotted) Å.

The minimum pore size for barrier-free transport d_{min} is found by integrating the attractive and repulsive forces at the pore opening and thus obtaining the acceptance energy

$$W_a = \int_{-\infty}^{Z_0} F^{tot}(Z) dZ, \quad (3.10)$$

where the interaction force $F^{tot}(Z)$ is attractive between $-\infty$ and $-Z_0$ and repulsive between $-Z_0$ and Z_0 . Note that $Z_0 (> 0)$ is a distance which depends upon the gas under consideration. This represents the work done by the van der Waals forces which are imparted onto the molecule in the form of kinetic energy. This acceptance energy calculation enables us to find d_{min} which indicates the critical pore size distinguishing barrier transport from barrier-free transport, found by solving the condition $W_a = 0$.

The total suction energy (W) is obtained by integrating over the molecule's entire travelling distance $-\infty$ to ∞ , which is numerically equivalent to approximately -10 Å to 10 Å since the interactions become significantly weak beyond 10 Å from the tube and axially neutral beyond 10 Å within the tube,

$$W = \int_{-\infty}^{\infty} F^{tot}(Z) dZ. \quad (3.11)$$

This expression is solved numerically when treating the gas molecule discretely as an orientation of individual atoms. Alternatively, if a molecule is treated as one spherical entity with an interaction point at its center then the total suction can be expressed analytically for cylindrical pores as [6]

$$W_{cyl} = \frac{12\pi^2\eta}{(d^* + \delta d)^4} \left(C_6 - \frac{42C_{12}}{(d^* + \delta d)^6} \right). \quad (3.12)$$

and for slit-shaped pores as

$$W_{slit} = 8\pi\eta\epsilon\sigma^2 \left[\frac{1}{2} \left(\frac{2\sigma}{d^* + \delta d} \right)^4 - \frac{1}{5} \left(\frac{2\sigma}{d^* + \delta d} \right)^{10} \right]. \quad (3.13)$$

Equations 3.12 and 3.13 will be the most useful equations for readers to use for their own research and therefore are expressed using the experimental pore size d^* , as this dimension is more available than the theoretical pore size. Equation 3.12 is identical to the adsorption potential energy function at the center of a cylindrical pore used by Everett and Powl [12] to determine the pore sizes and internal surface area in microporous carbons. In this chapter these expressions are used to understand diffusion rather than adsorption. The parameter values utilized for this approach are from Breck [13] for the gases He, H₂, CO₂, O₂, N₂ and CH₄, and Poling [14] for the gases CO, Ar, C₂H₆, n-C₅H₁₂ and SF₆, listed in Table 3.1.

Solving $W = 0$ for d^* is a good approximation for finding d_{min} instead of solving the more complicated $W_a = 0$. In this study the results for d_{min} are presented by using the more accurate method of solving $W_a = 0$ for the discrete cases. The optimal pore size d_{opt} that provides the maximum suction energy (W_{max}) is obtained by locating the maximum at $dW/dd = 0$.

Finally, the minimum pore size for Knudsen-type transport d_K is found when the gas molecules' initial kinetic energy W_0 is greater than the kinetic energy due to the gas-pore wall interactions. In other words, the interactions with the pore wall become weak and insignificant. This can be determined by satisfying the condition, $W_0 > W$. The concept of a minimum pore size for Knudsen transport is new as the current method for determining the occurrence of Knudsen transport is by finding the pore size region for which the Knudsen number ($Kn = \lambda/d$, where λ is the mean free path) is greater than or equal to 10 [15]. Note that the current method ignores penetrant-wall interactions and only gives a "maximum" pore size for Knudsen transport, and is therefore incapable of

determining a critical “minimum” pore size for Knudsen transport as opposed to activation diffusion and surface diffusion.

These results apply to a molecule entering a cylindrical pore at the exterior surface of the membrane but can also apply to a molecule entering a pore from a larger pore within the material or a section inside the bulk of the material as shown in Figure 3.3. The only difference is that the suction energy is reduced due to the molecule’s interaction with the surface of the larger section. This means that d_{min} increases slightly but the optimal pore size d_{opt} remains the same.

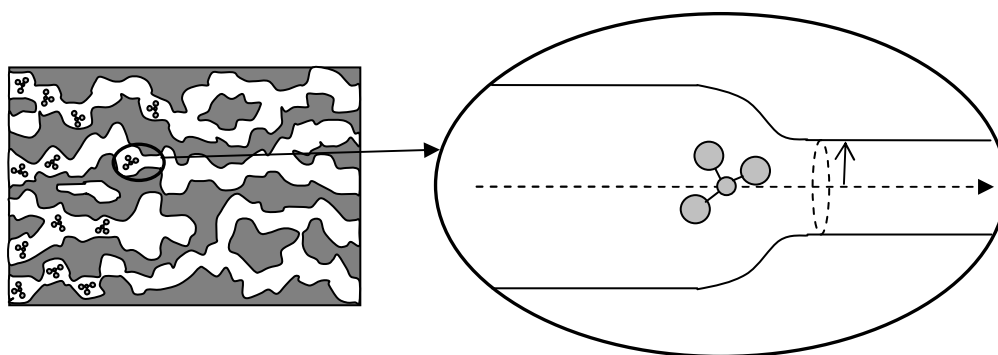


Figure 3.3: Molecule entering smaller pore from larger pore.

In a system of long symmetrical and frictionless pores, like a CNT-based membrane, the model predicts that the suction energy could cause an accelerated velocity which continues throughout the frictionless environment until the end of the tube, where an identical opposing suction force reduces the velocity back to the gas’ original velocity before entering the tube. This newly proposed diffusion mechanism, termed “suction diffusion”, and an expression for the diffusivity are described in Section 3.3.3. In systems with pores of short length this accelerated velocity is of little advantage and the rate of diffusion is dominated by effects such as surface adsorption, number of transitions, tortuosity and connectivity etc.

In amorphous membranes, for a molecule to successfully reach the downstream side of a membrane it is required to travel through a variety of differently sized pore channels within the membrane. These energy calculations determine the efficiency of transport through the different pore regions and therefore are useful in determining separation outcomes, especially when chemical interactions other than van der Waals are assumed to be negligible.

Table 3.1: Lennard-Jones constants, molecular masses and average velocities at room temperature used throughout this chapter [7, 13].

Gas / Pore atoms	σ (Å)	ϵ / k_B (K)	m (g/mol)	\bar{v} (m/s)
from UFF [7]				
C	3.43	53	12.01	-
H	2.57	22	1.01	-
O	3.12	30	16.00	-
N	3.26	35	14.01	-
Si	3.83	202	28.09	-
from Breck [13]				
He	2.60	10	4.00	1277
H ₂	2.89	60	2.02	1800
CO ₂	3.30	195	44.01	385
O ₂	3.46	107	32.00	452
N ₂	3.64	71	28.01	483
CH ₄	3.87	149	16.04	638
from Poling [14]				
CO	3.69	92	25.01	476
Ar	3.54	93	39.95	399
n-C ₅ H ₁₂	5.78	341	72.15	297
C ₂ H ₆	4.44	216	30.07	455
SF ₆	5.13	222	146.06	209

3.3 Transport mechanisms

An example of the above approach is demonstrated in Figure 3.4 for a single oxygen molecule entering a carbon tube. The critical pore sizes d_{min} and d_K distinguish between the regions where three different diffusion mechanisms dominate the transport, namely, (a) Activation diffusion (size sieving), (b) Surface diffusion (or possibly suction diffusion) and (c) Knudsen diffusion. The diffusion mechanisms are described below

and quantitative expressions are suggested for the permeability. Further details of the existing transport mechanisms are given in Section 2.1.2.

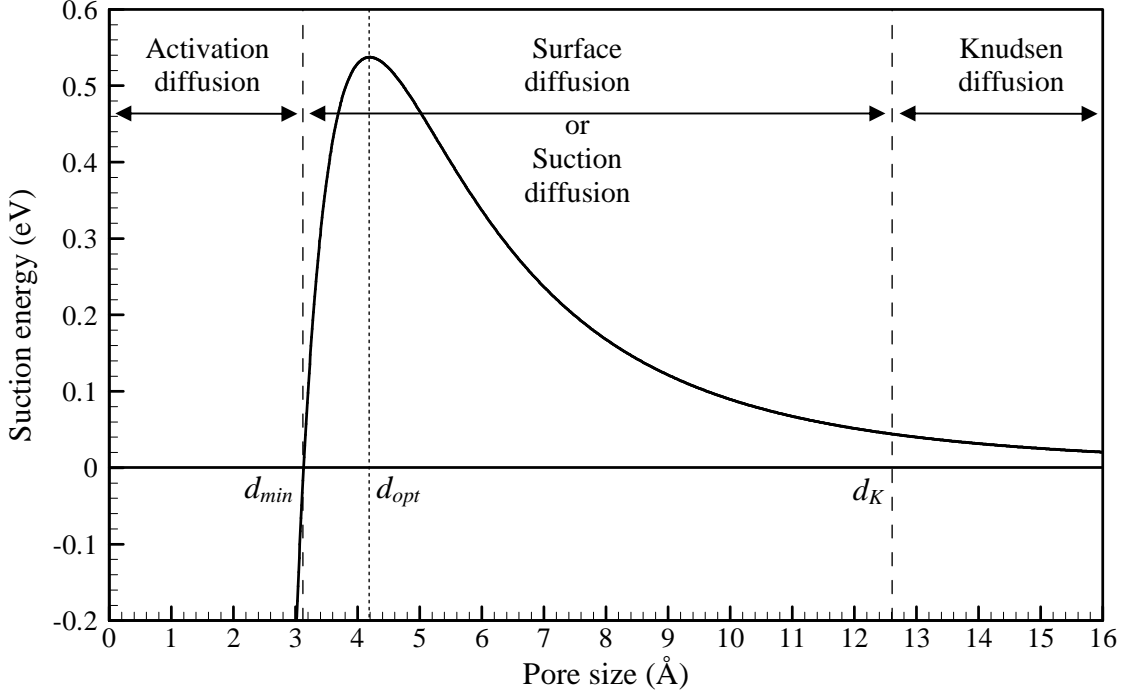


Figure 3.4: Suction energy (W) of a single oxygen molecule at the entrance of a carbon tube with pore size d^* . The pore regions where the diffusion mechanisms (activation, surface, suction and Knudsen) dominate are separated by the critical pore sizes d_{min} (where $W = 0$) and d_K (where $W = W_0 = 0.04$ eV), indicated by dashed lines. Maximum suction energy occurs at pore size d_{opt} , indicated by a dotted line.

The total permeability P according to the solution-diffusion model is the product of the diffusivity D and the solubility S ,

$$P = DS, \quad (3.14)$$

where S may be approximated as the ratio c/p (where c is the equilibrium concentration within the sample at an upstream pressure of p) assuming that the upstream pressure is much higher than the downstream pressure.

3.3.1 Size-sieving activation diffusion ($d^* < d_{min}$)

Diffusivity

In view of the existing theory for size-sieving activation diffusion, the model results suggest that the energy barrier is the magnitude of W for $d^* < d_{min}$. Thus the activation

diffusion coefficient can be expressed as

$$D_A = D_{A^*} \exp\left(\frac{-|W|}{RT}\right), \quad (3.15)$$

where D_{A^*} is a pre-exponential coefficient dependent on length of the diffusive jump, frequency of the gas molecule encountering the pore entrance and the velocity of the diffusive jump.

Permeability

In the region of size sieving activation diffusion, the solubility ratio is known to vary much less with temperature than the diffusivity. Therefore the permeability is governed mainly by the diffusivity, thus

$$P_A = D_{A^*} S_A \exp\left(\frac{-|W|}{RT}\right), \quad (3.16)$$

where S_A is the constant solubility coefficient.

3.3.2 Surface diffusion ($d_{min} < d^* < d_K$)

Diffusivity

As explained in Section 2.1.2.2, surface diffusion is the dominant transport mechanism in the pore size range between d_{min} and d_K with diffusivity expressed as a function of the heat of adsorption q as follows

$$D_S = D_{S^*} \exp\left(\frac{-aq}{RT}\right), \quad (3.17)$$

where D_{S^*} is a pre-exponential coefficient dependent on the frequency of vibration of the adsorbed molecule normal to the surface and distance from one adsorption site to the other. q is the heat of adsorption and a is a proportionality constant ($0 < a < 1$) such that aq is the energy barrier which separates the adjacent adsorption sites. It has been suggested by Everett and Powl [12] that a good approximation for the heat of adsorption is the minimum potential adsorption energy plus half of the average kinetic energy in the bulk gas phase, $q = W + RT/2$. Therefore the surface diffusion coefficient may be expressed as

$$D_S = D_{S^*} a^* \exp\left(\frac{-aW}{RT}\right), \quad (3.18)$$

where $a^* = \exp(-a/2)$.

Permeability

The combination of the solubility coefficient, in this case given by Henry's Law coefficient $K = K_0 \exp(q/RT)$, with the surface diffusion coefficient results in the following expression for permeability

$$P_S = P_{S*} \exp\left(\frac{(1-a)W}{RT}\right), \quad (3.19)$$

where P_{S*} is a constant that depends on D_{S*} , K_0 , a^* and porosity. Since $0 < a < 1$, the permeability will decrease with increased temperature meaning that the increased diffusivity is overruled by the decrease in surface concentration [16].

3.3.3 Suction diffusion ($d_{min} < d^* < d_K$)

Diffusivity

Alternatively, if the pores have a frictionless surface where the surface is a seamless array of closely packed atoms such that there are no discrete adsorption sites, another expression for diffusivity may be derived using the concept of suction. Shelekhin et al. [1] described diffusion by considering Transition State Theory (TST, outlined in Section 2.1.4) in the following way:

Diffusivity = probability that the molecule makes a jump (ρ)

× length of diffusive jump (λ)

× velocity of molecule throughout the jump (u)

By following this principle, an expression for the suction diffusion coefficient can be derived based on the suction energy

$$D_{Suc} = D_{Suc*} \lambda \sqrt{\frac{2(W + RT)}{m}}, \quad (3.20)$$

where D_{Suc*} is a coefficient dependent on the probability of a molecule entering the pore (related to travelling direction), m is the molecular mass of the gas molecule, λ is the diffusive jump length and RT is the additional kinetic energy originally present in the molecule before its interaction with the pore.

Permeability

In a frictionless system the suction diffusion coefficient determined previously can be combined with a term for the solubility ratio from the ideal gas law, resulting in total permeability

$$P_{Suc} = P_{Suc*} \frac{v_f}{RT} \sqrt{\frac{2(W + RT)}{m}}, \quad (3.21)$$

where P_{Suc*} is a constant that depends on D_{Suc*} , porosity and jump length, and v_f is the amount of free volume.

3.3.4 Knudsen diffusion ($d_K < d^*$)

Diffusivity

Knudsen diffusion [17-19] is known to apply to pores between 10 Å and 500 Å in size. The Knudsen diffusion coefficient can be expressed in the following form

$$D_K = \frac{d}{3} \bar{v}, \quad (3.22)$$

where \bar{v} is the average molecular speed. The average molecular speed \bar{v} is calculated using the Maxwell speed distribution,

$$\bar{v} = \sqrt{\frac{8RT}{\pi m}}, \quad (3.23)$$

where m is the molecular mass. Speeds for each gas are given in Table 3.1.

Permeability

Finally, the total permeability for Knudsen transport is a decreasing function of temperature and molecular mass of the form [16]

$$P_K = P_{K*} v_f \sqrt{\frac{8}{\pi m RT}}, \quad (3.24)$$

where P_{K*} is a constant that depends on D_{K*} , tortuosity and porosity.

3.4 Enhanced separation by tailoring pore size

The most common diffusion mechanisms known as activation diffusion, surface diffusion and Knudsen diffusion, usually dominate in small pores ($d^* < 3$ Å), medium pores (3 Å $< d^* < 10$ Å) and large pores (10 Å $< d^* < 500$ Å) for light gases, respectively [20, 21]. Separation by differences in diffusivity and/or differences in solubility can be enhanced by tailoring the pore size such that the differences are maximized. The greatest separations are usually achieved when the competing gases are in different modes of transport. Thus it is important to know the critical pore sizes that distinguish the different diffusion mechanisms for each gas.

Figure 3.5 is a graph of the suction energy for the light gases, He, H₂, CO₂, O₂, N₂ and CH₄, entering a carbon tube and the key features are summarized in Table 3.2 A), along with results for silica tubes B), carbon slits C), and silica slits D). Additionally, Table 3.2 includes the results for carbon monoxide (a key element of synthetic gas), argon (inert gas frequently used in industrial processes), n-pentane (a hydrocarbon found in fossil fuels), ethane (another hydrocarbon found in fossil fuels) and sulfur hexafluoride (the most potent greenhouse gas according to the Intergovernmental Panel on Climate Change [22]). The results can be used as a guide to tailor the pore size of a membrane according to the desired gas separation application. For example, if the application was natural gas purification (separation of CO₂ from CH₄) then the pore size range that allows CO₂ through while rejecting CH₄ can be found from Table 3.2 (carbon tube: 3.40-3.88 Å; silica tube: 3.42-4.30 Å; carbon slit: 2.74-4.30 Å; silica slit: 2.90-4.30 Å). Further, by using the transport equations (outlined in Section 3.3) it is possible to determine the pore size necessary to achieve a desired permeability and selectivity at the specified operating temperature, demonstrated in Section 3.7.

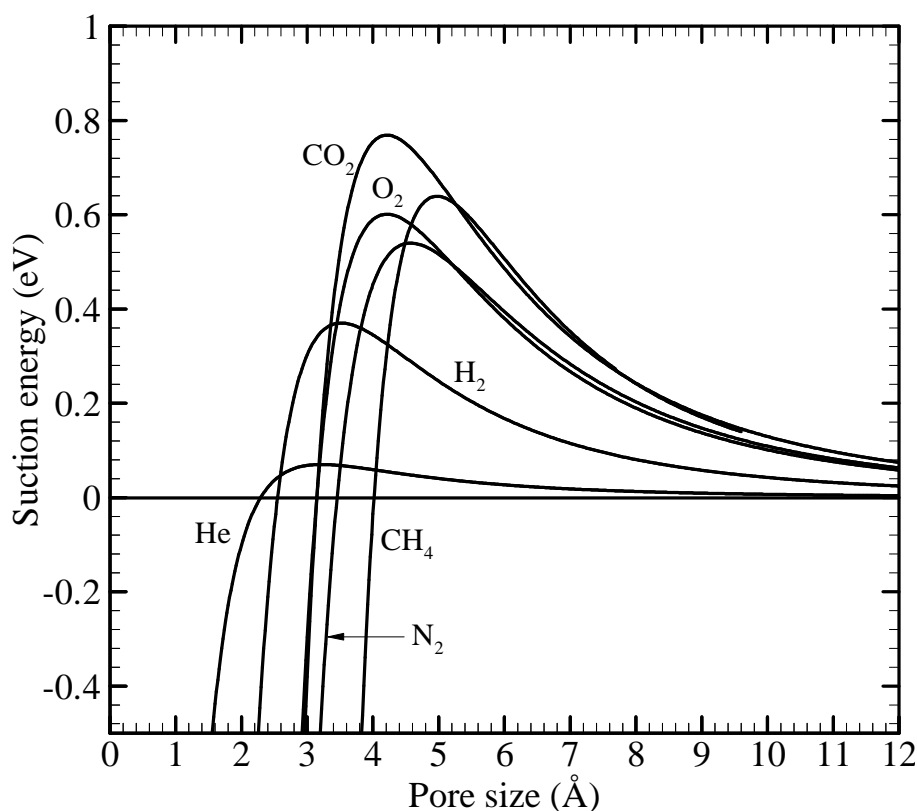


Figure 3.5: Suction energies for light gases at the entrance of a carbon tube with pore size d^* .

Table 3.2: Minimum pore size for barrier-free transport (d_{min}), optimal pore size (d_{opt}), maximum suction energy (W_{max}), maximum enhanced entrance velocity ($v_{max} = \sqrt{2W_{max}/m}$) and minimum pore size for Knudsen diffusion (d_K) at room temperature 298 K. All pore sizes are given as the experimental pore size d^* .

A) Carbon tube

Gas	d_{min} (Å)	d_{opt} (Å)	W_{max} (eV)	v_{max} (m/s)	d_K (Å)
He	2.40	3.22	0.07	1837	5.40
H ₂	2.68	3.52	0.37	5951	10.38
CO ₂	3.4	4.22	0.77	1837	14.82
O ₂	3.26	4.22	0.60	1902	13.72
N ₂	3.58	4.58	0.54	1929	14.06
CH ₄	3.88	4.98	0.67	2839	14.88
CO	3.26	4.21	0.47	1798	8.01
Ar	3.71	4.71	0.40	1400	13.13
n-C ₅ H ₁₂	5.85	7.14	1.31	1873	25.49
C ₂ H ₆	4.57	5.67	0.77	2227	18.40
SF ₆	5.22	6.43	0.92	1102	21.24

B) Silica tube

Gas	d_{min} (Å)	d_{opt} (Å)	W_{max} (eV)	v_{max} (m/s)	d_K (Å)
He	2.58	3.42	0.15	2649	7.32
H ₂	2.84	3.72	0.77	8588	13.64
CO ₂	3.42	4.42	1.32	2406	18.00
O ₂	3.44	4.42	1.25	2744	17.70
N ₂	3.74	4.76	1.10	2752	17.98
CH ₄	4.30	5.16	1.35	4036	18.56
CO	3.44	4.41	0.97	2591	16.43
Ar	3.96	4.99	0.46	1487	14.25
n-C ₅ H ₁₂	6.06	7.39	1.5	2004	27.19
C ₂ H ₆	4.80	5.95	0.88	2377	19.79
SF ₆	5.45	6.69	1.05	1178	22.73

C) Carbon slit

Gas	d_{min} (Å)	d_{opt} (Å)	W_{max} (eV)	v_{max} (m/s)	d_K (Å)
He	1.98	2.70	0.04	1412	3.17
H ₂	2.18	2.98	0.22	4578	7.72
CO ₂	2.74	3.62	0.45	1412	11.32
O ₂	2.72	3.62	0.36	1464	10.44
N ₂	3.02	3.94	0.32	1483	10.71
CH ₄	4.30	5.16	0.44	2306	11.04
CO	2.77	3.62	0.28	1381	9.60
Ar	3.18	4.08	0.24	1073	9.93
n-C ₅ H ₁₂	5.31	6.31	0.77	1439	19.92
C ₂ H ₆	3.96	4.97	0.46	1711	14.20
SF ₆	4.92	6.03	0.59	882	21.73

D) Silica slit

Gas	d_{min} (Å)	d_{opt} (Å)	W_{max} (eV)	v_{max} (m/s)	d_K (Å)
He	2.14	2.88	0.07	1875	5.51
H ₂	2.34	3.16	0.46	6605	10.37
CO ₂	2.90	3.80	0.78	1850	13.89
O ₂	2.88	3.80	0.74	2110	13.64
N ₂	3.18	4.12	0.65	2116	13.87
CH ₄	4.30	5.16	0.84	3188	14.34
CO	2.92	3.80	0.58	1990	12.62
Ar	3.41	4.33	0.27	1143	10.84
n-C ₅ H ₁₂	5.35	6.54	0.89	1540	12.30
C ₂ H ₆	4.19	5.22	0.52	1826	15.32
SF ₆	4.78	5.89	0.62	905	17.70

The first observation made from the results in Table 3.2 is that the minimum pore sizes for barrier-free transport d_{min} of each gas are in the same order as the kinetic diameter with slightly different values because the model takes into account the interaction with the pore wall and not kinetic size only. This means that the model is a

more accurate method for predicting whether a gas molecule will experience an energy barrier or not, consequently predicting the mode of transport. Another important observation is that the model predicts that Knudsen diffusion occurs in different pore size regions for each gas. For example, within a 12 Å sized pore, the model predicts that helium and hydrogen will be in Knudsen flow while all the other light gases will not. As mentioned earlier, the maximized suction energy is only beneficial for transport if the suction energy is converted to kinetic energy, without any thermal dissipation effects, and that the resultant enhanced entrance velocity v_{max} can be maintained through a frictionless environment for a substantial distance. The only system satisfying these details is that of the CNT-based membranes which are believed to have long and essentially frictionless pores. Hence, in other systems the suction energy at the entrance of the pores may not have significant influence on the overall diffusivity. However, the other results that the model predicts, such as, d_{min} and d_K , are of great importance in all membrane systems.

3.5 Determining diffusion regime from experimental flux

A widely used experimental data fitting technique that determines the mode of transport is performed by fitting permeance data to the Arrhenius function $J = J_0 \exp(-E/RT)$. With the relationship between flux J and permeability P , defined as $J = P\Delta p/L$, the above permeability expressions in the previous section provide the decision criteria, where Δp is the pressure gradient and L is the membrane thickness. If E is positive then the dominant transport mechanism is size-sieving activation diffusion with E representing the energy barrier $|W|$ for $d^* < d_{min}$. If E is negative then the dominant transport mechanism is surface diffusion with E representing the weighted contribution of suction energy (or adsorption energy) for the energy barrier and surface concentration $(a-1)W$. If E is zero, i.e. no change in permeability with varying temperature, then either the size-sieving energy barrier and heat of adsorption are equal to zero ($W = 0$) or the surface diffusion energy barrier and heat of adsorption are both equal ($a = 1$). If the Arrhenius function does not fit the data then the mode of transport could be Knudsen flow, the newly proposed suction diffusion or a combination of all mechanisms since the dominant mode of transport can change as temperature is varied. The above criteria will be a useful tool in understanding the mode of transport for each gas in a range of membrane materials.

3.6 Comparison with experimental results

As with all models, it is important to test the predictions against experimental results. The difficulty with testing these predictions is that there exists no membrane system with a single uniform pore size. Even within membranes with a narrow pore size distribution, such as CNT-based membranes, there is still a variation of about 2 Å. Therefore, it is almost impossible to test the critical pore sizes d_{min} and d_K calculated within an accuracy of 0.01 Å. Nevertheless, the model's predictions will be tested within the range of the available data and are shown to reasonably agree.

Experimental gas selectivity data for CNT-based membranes, with an average pore size of 16 Å, show that all light gases (He, H₂, O₂, N₂, CO₂ and CH₄) follow Knudsen diffusion [23]. This agrees excellently with the model prediction that all light gases travel by Knudsen diffusion in pores larger than 15 Å. In addition, the model also predicts that the hydrocarbon C₂H₆ exhibits Knudsen diffusion in pores larger than 25 Å (using Equation 3.12 with $\sigma = 4.443$ Å and $\varepsilon/k_B = 215.7$ K [14]), which explains why Knudsen diffusion is not observed for C₂H₆ along with the heavier hydrocarbons. To-date there are no CNT-based membranes available with smaller pore sizes, and so the testing of the model predictions with experimental results for d_{min} and W_{max} is not possible. However there has been some simulation work, in particular by Chen and Sholl [24] that predicted the selection of CH₄ over H₂ in a (10,10) nanotube with diameter equal to 10.3 Å. Remarkably, the model predicts that within a nanotube of this size H₂ will be in Knudsen flow while CH₄ will be in modes of surface diffusion or suction diffusion with a much higher concentration than H₂ and therefore higher flux. Additionally, the model predicts that the (5,5) CNT with a pore size of 3.48 Å has a pore size in between the d_{min} 's for some light gases, and is consequently theoretically capable of making the following size sieving separations : He/CH₄, He/N₂, H₂/CH₄, H₂/N₂, CO₂/CH₄, CO₂/N₂, O₂/CH₄ and O₂/N₂. These predicted separations (gas A / gas B) occur because gas B is restricted to activation diffusion while gas A is not. Other separations may occur possibly by differences in enhanced velocity v_{max} , as a result of suction energy converted to kinetic energy, but this is yet to be confirmed by experiment. The enhanced water flux reported in these CNT-based membranes [23, 25, 26] could possibly be a result of this suction energy at the entrance and will be of great interest in future work.

Permeation measurements in CMS membranes by Gilron and Soffer [27] demonstrate molecular sieving and Knudsen characteristics between 25 and 500 °C. *n*-pentane permeated through the membrane while sulfur hexafluoride did not. For these gases, the model estimates that the pore sizes must be in the range of 4.24 - 6.36 Å, which agrees well with the pore sizes estimated by Gilron and Soffer, 4.3 - 5.8 Å using permeation cutoff measurements. Within pores of this size the model predicts that only helium is in true Knudsen diffusion while the other light gases tend towards Knudsen diffusion as temperature increases. This behaviour is demonstrated well in figure 7 of reference [27] where all curves tend towards a Knudsen type flow with increasing temperature. More specifically, CO₂ reaches this transport mode at much higher temperatures than the other gases, agreeing with the model prediction, since CO₂ has the greatest interaction energy with the wall and thus remains in surface diffusion mode until much higher temperatures.

Recent investigations into MSS membranes have elucidated the influence that small changes in pore sizes can have on permeation results [28]. It has been shown that a change in pore size from 2.2 to 2.9 Å translates to a change in the separation mechanism between hydrogen and helium from size-sieving to Knudsen. The model predicts that hydrogen and helium compete by the size-sieving mechanism (activation diffusion) in pores smaller than 2.34 or 2.84 Å (within slit or tube pores, respectively) and hence agrees well with the experimental results. The reason for the immediate jump from size-sieving to Knudsen type separation is because the pore morphology in this membrane system is tri-modal (having three pore size distributions), in which the 2.9 Å pores are the smaller pores and hence the intermediate and larger pores determine the separation outcome as a result of the smaller pores losing size-sieving ability. Conveniently, the model also predicts that hydrogen and helium are in Knudsen flow within the range of the large pores found by PALS in this sample. Therefore the model agrees well and assists in the interpretation of the separation outcomes using these MSS membranes.

3.7 Predictions of the model

In this section predictions are made using the model to demonstrate the different transport behaviours with varying pore size and temperature for light gases (He, H₂, O₂, N₂, CO₂ and CH₄).

Figure 3.6 predicts the permeability P as a function of pore size d for the different transport mechanisms, described above in Section 3.3, with Equation 3.12 as the definition for W . The results represent the permeability within a single pore. In reality there will be a distribution of pore sizes therefore the transition between activation diffusion and the other modes of transport will be smooth. Each mode of transport is scaled arbitrarily such that the trends may be clearly seen and therefore the magnitude is insignificant. The permeability for activation diffusion is a sharply increasing function of pore size as the energy barrier changes dramatically with pore size. The newly

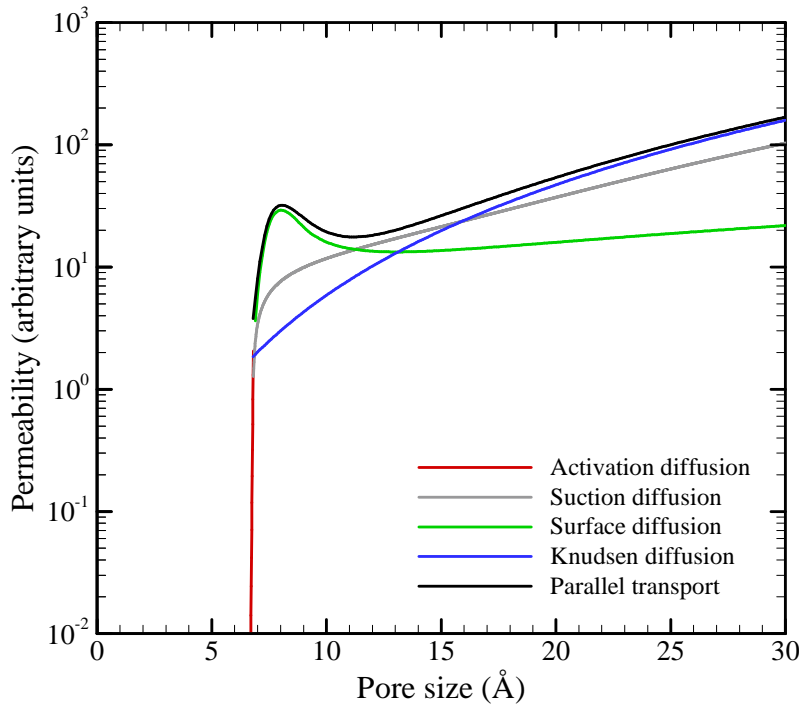


Figure 3.6: Model prediction of normalized permeability P as a function of pore size (distance between surface nuclei, d). Modes of transport are indicated: Activation diffusion (Equation 3.16), Suction diffusion (Equation 3.21), Surface diffusion ($a = 0.85$, Equation 3.19), Knudsen diffusion (Equation 3.24) and Parallel transport (Equation 3.25).

proposed suction diffusion predicts the permeability to sharply increase at the optimal pore size d_{opt} where the suction energy is maximized, followed by a gradual increase at larger pore sizes where the suction energy becomes weak and the permeability is dominated by a Knudsen-type transport. As explained earlier, the permeability for surface diffusion is dominated by the surface concentration and therefore the model predicts a peak at which the heat of adsorption is maximized. The permeability for

Knudsen diffusion increases as a cubic function of pore size as the diffusivity depends linearly on the pore size d and the concentration depends on the volume of the pore d^2 (assuming cylindrical pores). The parallel transport model assumes that surface diffusion and Knudsen diffusion are occurring simultaneously such that the total permeability is given by,

$$P_{tot} = P_S + P_K. \quad (3.25)$$

This model is explained in further detail in Section 2.1.5.1 and has been used by various groups [27, 29, 30]. Parallel transport is initially dominated by surface diffusion within the smaller pores where the surface concentration is high while the mode of Knudsen diffusion dominates within the larger pores where bulk gas molecules dominate the larger free space.

Permeability varies with temperature for each transport mechanism as demonstrated in Figure 3.7. The permeability for activation diffusion is the only increasing function with respect to temperature. Surface diffusion takes advantage of the interactions with the pore wall which become insignificant at high temperatures resulting in a high permeability at low temperatures and Knudsen-type transport at high temperatures. When gases are in the mode of surface diffusion the surface concentration decreases more than the increase in surface mobility resulting in an overall decrease in permeability with increasing temperature. Knudsen diffusion displays decreasing permeability with raising temperature as the concentration loss overrules the increase in diffusivity. As temperature increases, the surface diffusion part of the parallel transport model has less influence causing the permeability to tend towards a Knudsen-type transport at high temperatures. The resistance in series transport model, detailed in Section 2.1.5.2, assumes that the diffusing molecules travel through pores in the mode of Knudsen diffusion while occasionally encountering constrictions where activation diffusion occurs. The total permeability is therefore expressed as

$$P_{tot} = \frac{P_A P_K}{P_K (1-x) + P_A x}, \quad (3.26)$$

where x is the fraction of the pore length where Knudsen diffusion occurs. As shown in Figure 3.7, the total permeability predicted by the resistance in series model behaves mostly according to the mode of activation diffusion even with a small fraction of constrictions $(1-x)$.

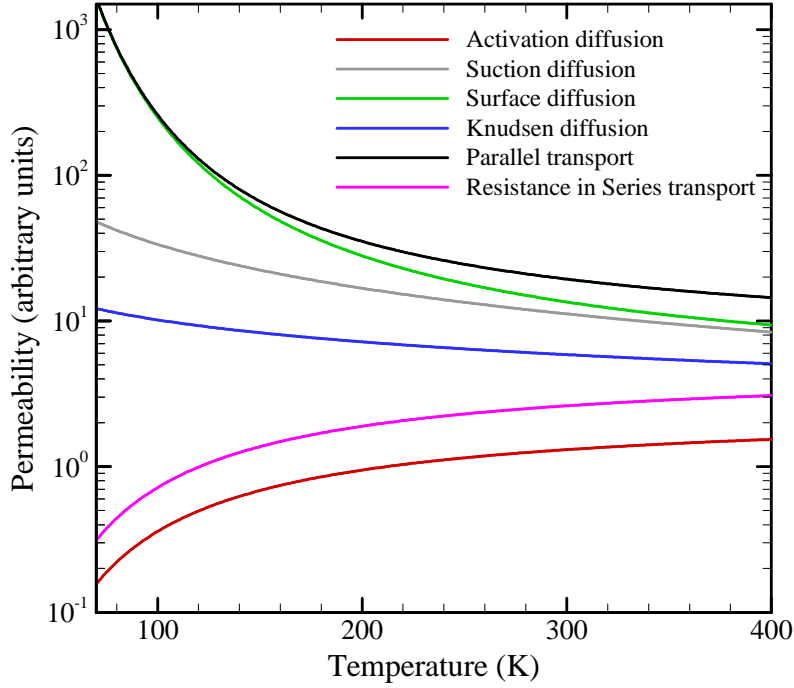


Figure 3.7: Model prediction of permeability as a function of temperature. Modes of transport are indicated: Activation diffusion ($d = 6.8 \text{ \AA}$, Equation 3.16), Suction diffusion ($d = 10 \text{ \AA}$, Equation 3.21), Surface diffusion ($d = 10 \text{ \AA}$, Equation 3.19), Knudsen diffusion ($d = 10 \text{ \AA}$, Equation 3.24), Parallel transport ($d = 10 \text{ \AA}$, Equation 3.25) and Resistance in series transport ($d_{small} = 6.8 \text{ \AA}$, $d_{large} = 10 \text{ \AA}$, $x = 0.8$, Equation 3.26).

In the interest of gas separation the model prediction for CO_2/CH_4 selectivity versus CO_2 permeability has been calculated with varying pore size and temperature, in Figure 3.8 and Figure 3.9, respectively. Equation 3.12 was used for the suction energy W with the parameter values taken from Table 3.1. The selectivity for CO_2/CH_4 with both gases in the mode of activation diffusion was calculated to be on the order of 10^{20} because only a single pore is considered and therefore has been omitted from the plot. Since CO_2 has a stronger van der Waals well depth than CH_4 , the suction diffusion model predicts at small pore sizes that the CO_2 permeability is higher than CH_4 resulting in a CO_2/CH_4 selectivity greater than 1. As pores become larger the pore interactions become less significant and selectivity tends toward the constant selectivity for Knudsen diffusion. The selectivity is high for small pores with surface diffusion as the transport mechanism where permeability is dominated by the concentration component for which CO_2 forms denser surface layers than CH_4 . As pores become larger, the heat of adsorption peaks reach a maximum CO_2 permeability, followed by a decrease in the heat of adsorption

resulting in a surface concentration loss. In this case, a single pore is considered and therefore the surface concentration eventually increases with increasing pore size according to the surface area of the cylindrical pore with the density of both gases tending toward that on a flat surface. The Knudsen diffusion selectivity favours CH_4 because of its lighter mass resulting in a higher molecular velocity and does not change with pore size. Finally, the parallel transport follows the same trend as surface diffusion in small pores and tends toward Knudsen behaviour as pore sizes increase.

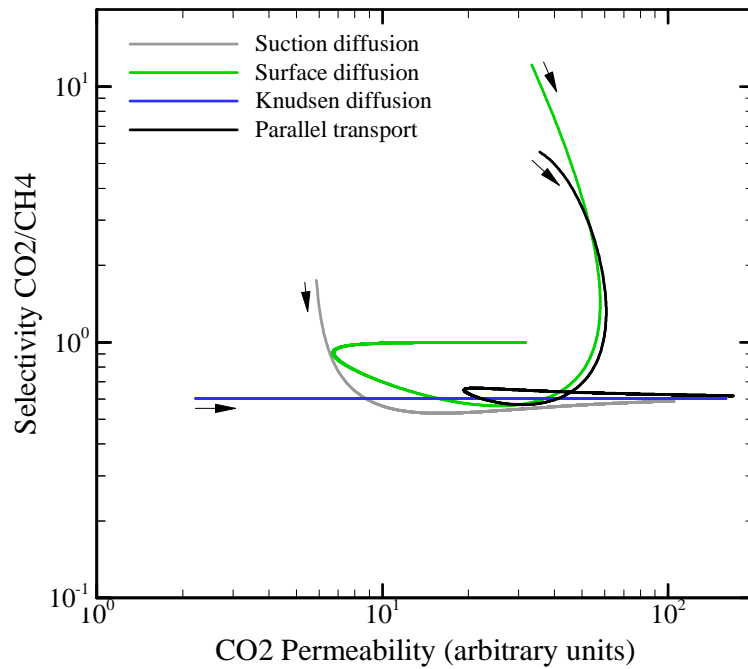


Figure 3.8: Model predictions of CO_2/CH_4 selectivity versus CO_2 permeability for varying pore size d . Arrows indicate the direction of increasing pore size. The pore size range, $7.22 > d > 30 \text{ \AA}$, was chosen such that both gases were in the same mode of transport.

The model prediction for varying temperature is given in Figure 3.9. The selectivity is predicted to slightly increase with increasing temperature when gases are in the mode of suction diffusion. This is caused as a result of the larger suction energy that CH_4 experiences over CO_2 for this particular pore size. Similarly when the mode of surface diffusion is assumed the heat of adsorption is higher for CH_4 than for CO_2 due to the pore size chosen and therefore the selectivity will increase with increasing temperature. Knudsen selectivity does not depend on temperature. Parallel transport is dominated by the surface diffusion component at low temperatures and gradually becomes more

dependent on the Knudsen diffusion component at high temperatures. Note that the trends will be different depending on the pore size. For example, in the case of $d = 8 \text{ \AA}$, the selectivity was predicted to decrease as temperature increased.

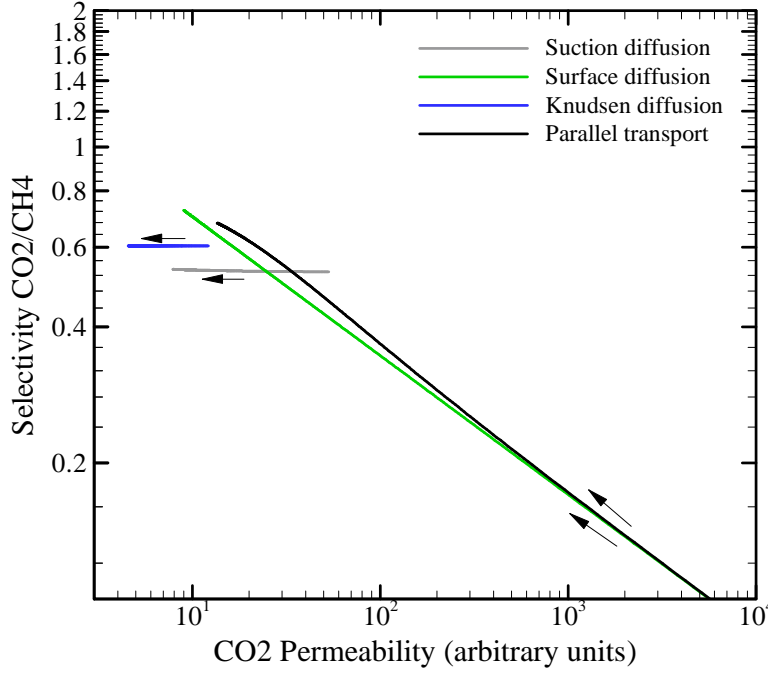


Figure 3.9: Model predictions of CO_2/CH_4 selectivity versus CO_2 permeability for varying temperature T , within a pore of size $d = 10 \text{ \AA}$. Arrows indicate the direction of increasing temperature, from 70 to 500 K.

3.8 Conclusion

Tailoring the pore size distribution of materials has been suggested as a means of tuning the transport properties in membranes [31, 32]. To enhance the development of gas separation membranes the modelling of the transport of individual gas molecules through pores has been undertaken. The interactions between the gas molecules and the pore wall at the pore opening have been considered and integrated to determine a suction energy from which certain information about the gas kinetics can be obtained. This novel approach provides a theoretical determination of the size of pores in which different modes of diffusion occur for each gas. Critical pore sizes d_{min} and d_K indicate the division of the three diffusion regimes, namely, activation diffusion, surface diffusion and Knudsen diffusion. By using this model one can predict the separation outcome of a variety of membranes in which the pore shape, size and composition are known, and conversely predict pore characteristics with known permeation rates.

Further, one can also have a desired separation in mind and use this model to guide the design of the membrane material.

The predictions of the model have been tested and agree well with experimental gas selectivities in CNT-based, CMS and MSS membranes.

This novel approach provides the opportunity for many further applications including (i) quantitatively predicting separation outcomes based on known pore size distributions of polymers, silicas, and other materials, (ii) predicting the effect of physical aging on separation performance and (iii) testing a variety of pore shapes and/or molecules that are larger and non spherical.

References

- [1] A. B. Shelekhin, A. G. Dixon and Y. H. Ma, Theory of gas diffusion and permeation in inorganic molecular-sieve membranes, *AIChE*, 41 (1995) 58.
- [2] M. Acharya and H. C. Foley, Transport in nanoporous carbon membranes: Experiments and analysis, *AIChE*, 46 (2000) 911.
- [3] T. A. Hilder and J. M. Hill, Continuous versus discrete for interacting carbon nanostructures, *J. Phys. A: Math. Theor.*, 40 (2007) 3851.
- [4] G. Dlubek, A. P. Clarke, H. M. Fretwell, S. B. Dugdale and M. A. Alam, Positron lifetime studies of free volume hole size distribution in glassy polycarbonate and polystyrene, *Phys. Status Solidi A*, 157 (1996) 351.
- [5] D. M. Schrader and Y. C. Jean, Positron and positronium chemistry, studies in physical and theoretical chemistry, Elsevier Sci. Publ. Co., Amsterdam, 1988.
- [6] B. J. Cox, N. Thamwattana and J. M. Hill, Mechanics of atoms and fullerenes in single-walled carbon nanotubes. I. Acceptance and suction energies, *Proc. R. Soc. A*, 463 (2007) 461.
- [7] A. K. Rappe, C. J. Casewit, K. S. Colwell, W. A. Goddard and W. M. Skiff, Uff, a full periodic-table force-field for molecular mechanics and molecular-dynamics simulations, *J. Am. Chem. Soc.*, 114 (1992) 10024.

- [8] C. W. Bauschlicher, Hydrogen and fluorine binding to the sidewalls of a (10,0) carbon nanotube, *Chem. Phys. Lett.*, 322 (2000) 237.
- [9] T. Duren, L. Sarkisov, O. M. Yaghi and R. Q. Snurr, Design of new materials for methane storage, *Langmuir*, 20 (2004) 2683.
- [10] G. Garberoglio, A. I. Skoulidas and J. K. Johnson, Adsorption of gases in metal organic materials: Comparison of simulations and experiments, *J. Phys. Chem. B.*, 109 (2005) 13094.
- [11] I. S. Gradshteyn and I. M. Ryzhik, *Table of Integrals, Series and Products*, Academic Press, San Diego, 2000.
- [12] D. H. Everett and J. C. Powl, Adsorption in slit-like and cylindrical micropores in the henry's law region. A model for the microporosity of carbons, *J. Chem. Soc., Faraday Trans. 1*, 72 (1976) 619.
- [13] D. W. Breck, *Zeolite Molecular Sieves: Structure, Chemistry, and Use*, John Wiley & Sons, New York, 1973.
- [14] B. E. Poling, J. M. Prausnitz and J. O. O'Connell, *The Properties of Gases and Liquids*, McGraw-Hill, New York, 2001.
- [15] A. F. Mills, *Mass Transfer*, Prentice-Hall, Upper Saddle River, NJ, 2001.
- [16] R. S. A. de Lange, K. Keizer and A. J. Burggraaf, Analysis and theory of gas transport in microporous sol-gel derived ceramic membranes, *J. Membr. Sci.*, 104 (1995) 81.
- [17] B. J. Hinds, N. Chopra, T. Rantell, R. Andrews, V. Gavalas and L. G. Bachas, Aligned multiwalled carbon nanotube membranes, *Science*, 303 (2004) 62.
- [18] M. Knudsen, Die Gesetze der Molekularströmung und der inneren Reibungsströmung der Gase durch Röhren, *Ann. Phys.*, 28 (1909) 75.
- [19] S. T. Hwang and K. Kammermeyer, *Membranes in Separations*, Krieger, Malabar, Florida, 1984.

- [20] Y. Yampolskii, I. Pinnau and B. D. Freeman, *Materials Science of Membranes for Gas and Vapor Separation*, John Wiley & Sons, Ltd, 2006.
- [21] T. C. Merkel, Z. He, I. Pinnau, B. D. Freeman, P. Meakin and A. J. Hill, Effect of nanoparticles on gas sorption and transport in poly(1-trimethylsilyl-1-propyne), *Macromolecules*, 36 (2003) 6844.
- [22] T. Stocker and D. Qin, *The physical science basis of climate change*, WMO and UNEP, 2008.
- [23] J. K. Holt, H. G. Park, Y. Wang, M. Stadermann, A. B. Artyukhin, C. P. Grigoropoulos, A. Noy and O. Bakajin, Fast mass transport through sub-2-nanometer carbon nanotubes, *Science*, 312 (2006) 1034.
- [24] H. Chen and D. S. Sholl, Predictions of selectivity and flux for CH₄/H₂ separations using single walled carbon nanotubes as membranes, *J. Membr. Sci.*, 269 (2006) 152.
- [25] M. Whitby and N. Quirke, Fluid flow in carbon nanotubes and nanopipes, *Nature Nanotechnol.*, 2 (2007) 87.
- [26] M. Whitby, L. Cagnon, M. Thanou and N. Quirke, Enhanced fluid flow through nanoscale carbon pipes, *Nano Letters*, 8 (2008) 2336.
- [27] J. Gilron and A. Soffer, Knudsen diffusion in microporous carbon membranes with molecular sieving character, *J. Membr. Sci.*, 209 (2002) 339.
- [28] M. C. Duke, S. J. Pas, A. J. Hill, Y. S. Lin and J. C. Diniz da Costa, Exposing the molecular sieving architecture of amorphous silica using positron annihilation spectroscopy, *Adv. Funct. Mater.*, 18 (2008) 1.
- [29] A. J. Burggraaf, Single gas permeation of thin zeolite (MFI) membranes: theory and analysis of experimental observations, *J. Membr. Sci.*, 155 (1999) 45.
- [30] D. Li and S. T. Hwang, Preparation and characterization of silicon based inorganic membrane for gas separation, *J. Membr. Sci.*, 59 (1991) 331.

- [31] T. C. Merkel, B. D. Freeman, R. J. Spontak, Z. He, I. Pinnau, P. Meakin and A. J. Hill, Ultrapermeable, reverse-selective nanocomposite membranes, *Science*, 296 (2002) 519.
- [32] H. B. Park, C. H. Jung, Y. M. Lee, A. J. Hill, S. J. Pas, S. T. Mudie, E. van Wagner, B. D. Freeman and D. J. Cookson, Polymers with cavities tuned for fast selective transport of small molecules and ions, *Science*, 318 (2007) 254.

List of symbols used in Chapter 3

PE	potential energy
η	atomic surface density
Φ	Lennard-Jones 6-12 potential energy function
dS	surface element
ρ	position within pore
σ	kinetic diameter
ε	well depth
F^{tot}	total force in the axial direction
F	hypergeometric function
d	theoretical pore size (between surface nuclei)
d^*	experimental pore size (d minus electron cloud thickness)
z	axis parallel with pore direction
Z	position of the gas molecules center on z -axis
W	suction energy
W_a	acceptance energy
Z_0	position along z -axis where force is equal to zero
W_0	initial kinetic energy of gas molecule before entering pore
Kn	Knudsen number
λ	mean free path

Chapter 4

Free volume and gas transport

4.1 Introduction

Tailoring the permeability and selectivity of polymeric materials for specific applications is a frequent task of the membrane researcher. To reduce experimental time and costs it is desirable to have reliable models for the prediction of physical properties such as permeability and diffusivity based on readily obtainable parameters. In this chapter a versatile predictive model is proposed that can be used in three ways:

- for a given free volume, permeability can be predicted;
- polymer structure can be better understood by evaluating the polymer in the context of the broad range to determine whether its free volume is isolated, interconnected, bi-continuous or percolated; and
- new types of polymers such as the recently reported thermally rearranged (TR) polymers [1] and polymers with intrinsic microporosity (PIM) [2] can be evaluated as to whether their free volume and permeability characteristics conform to other families of polymers described by this new model.

Currently the relationship between permeability P , diffusivity D , and free volume is typically modelled by the Doolittle relation,

$$P = A^* \exp\left[\frac{-B}{f}\right], \quad (4.1)$$

$$D = A \exp\left[\frac{-B}{f}\right], \quad (4.2)$$

where A and B are constants, A^* is the product of A and the solubility coefficient S , and f represents the various measures of free volume. The Doolittle relation fits the data within a limited range of free volume but breaks down for larger ranges of free volume.

This work aims to provide a global model that can describe gas diffusion in the wide range of polymers currently available, with fractional free volumes ranging from 10 to 35 %. This work starts where most models start, by empirically fitting an equation to the data,

$$P = \alpha^* \exp(\beta f), \quad (4.3)$$

$$D = \alpha \exp(\beta f), \quad (4.4)$$

where α and β are constants, α^* is the product of α and the solubility coefficient S . A fundamental explanation for this fit may come in future work; but for now the behaviour of the data is accurately described using this new relation and a postulation as to the fundamental significance of the model can be given.

The definitions of free volume used throughout this chapter are explained in Section 2.1.7 in detail and are briefly noted here. Free volume can be calculated by at least three methods: 1) as a fractional free volume (*FFV*) which is the ratio of free volume over total specific volume (inverse of density), where the free volume is the total specific volume minus the occupied volume calculated from Bondi's group contribution theory [3, 4], 2) as a gas-specific fractional free volume (*FFV_{gas}*) which is also the ratio of free volume over total volume where each part of the repeat unit is assigned a gas-specific occupied volume [5], and 3) as an accessible volume fraction (*AVF*) which is the ratio of accessible free volume over total volume where the accessible free volume for a particular gas is calculated via computer simulations [6-8].

4.2 Free volume, permeability, diffusivity and solubility

It is known that permeability P is the product of diffusivity D and solubility S , and it is generally accepted believed for light gases that the diffusivity varies a great deal more from polymer to polymer than solubility [5, 9]. The behaviour of the gas diffusion coefficient D can therefore be predicted by using the permeability results assuming solubility is constant. This assumption will be shown to be true for almost all polymers and all light gases. An exception is PIM with the higher adsorbing gases, namely, carbon dioxide, methane, nitrogen and oxygen.

4.2.1 Transport properties vs fractional free volume

Park and Paul's extensive permeability data consist of polymers with free volumes from 10 to 26 % free volume (using Bondi's group contribution method as opposed to Park

and Paul's modified Bondi's group contribution method). The Thran et al. [10] database consists of diffusivity values for most of the polymers in the Park and Paul's database and consequently solubility values are found (= permeability / diffusivity). To expand the data range, the high free volume polymers PTMSP, AF1600, AF2400, PMP and PTMSDPA having from 26% to 34% free volume [11-17] are included, listed in Table 4.1. The addition of new data provides the opportunity to test the ability of the model to

Table 4.1: Gas permeability, diffusivity and solubility of light gases within high free volume polymers.

Property	Ref.	Gases					
		H ₂	O ₂	N ₂	CH ₄	CO ₂	He
PTMSP							
Permeability	[12]	17000	9700	6300	15000	34000	6500
Diffusivity	[17]	29310	5640	4200	3600	4167	-
Solubility	[17]	0.58	1.72	1.50	4.17	8.16	-
AF1600							
Permeability	[16]	595	254	114	74.6	481	-
Diffusivity	[16]	-	273	144	60	133	-
Solubility	[16]	-	0.93	0.79	1.25	3.63	-
AF2400							
Permeability	[11]	2100	960	480	390	2200	-
Diffusivity	[16]	-	828	571	241	492	-
Solubility	[16]	-	1.16	0.84	1.62	4.47	-
PMP							
Permeability	[18]	5800	2700	1300	2900	11000	2600
Diffusivity	[18]	3500	-	-	562	-	-
Solubility	[18]	1.60	-	-	5.16	-	-
PTMSDPA							
Permeability	[12]	-	1200	-	-	-	-
PIM-1							
Permeability	[19]	3600	1300	340	430	6500	1500
Permeability	[14]	2332	786	238	360	3496	1061
Permeability	[2]	1300	370	92	125	2300	660
Diffusivity	[2]	1700	81	22	6.8	26	2700
Solubility	[2]	0.76	4.60	4.20	18.0	88.0	0.24
TR-1-450							
Permeability	[20]	4400	1100	280	150	4200	2650

Permeability units: [Barrers] (1 Barrer = 10^{-10} cm³ (STP) cm / cm².sec.cmHg)

Diffusivity units: [10⁻⁸ cm² / sec]

Solubility units: [10⁻² cm³ (STP) / cm³.cmHg]

fit the data over a larger range of fractional free volume as shown in Figure 4.1 and Figure 4.2. The new relation was empirically derived and is in the form $D = \alpha \exp(\beta f)$, where α and β are constants. Since $P = D.S$ an expression of the form $P = \alpha^* \exp(\beta f)$ was used to fit the permeability data, where α^* is the product of α and a solubility constant S . Figure 4.1 shows that the new expression fits the data much better than a Doolittle expression $P = A^* \exp(-B/f)$ for all gases. The fit involves one empirical adjustable parameter α^* as it is shown later that β is derived from the kinetic diameter of the particular light gas. Parameter values are listed for each gas in Table 4.2.

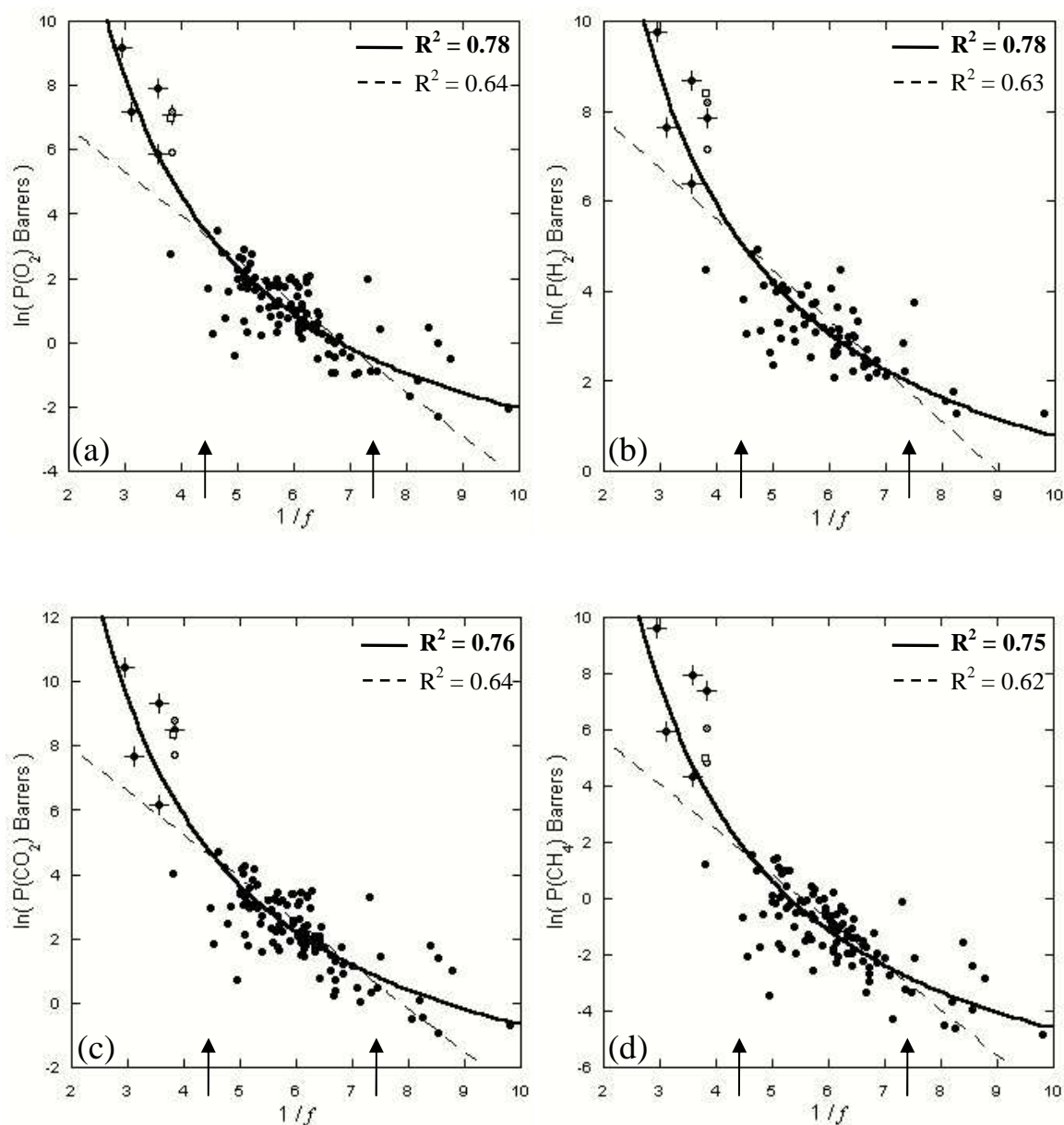


Figure 4.1 (continued to next page)

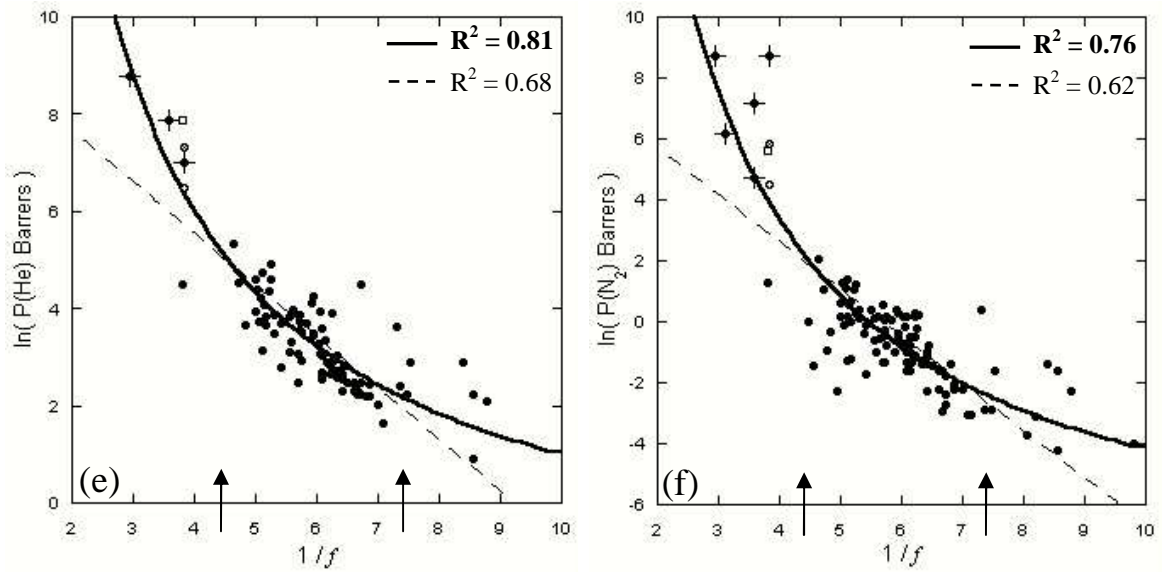


Figure 4.1: Permeability of light gases: (a) oxygen, (b) hydrogen, (c) carbon dioxide, (d) methane, (e) helium and (f) nitrogen, versus inverse fractional free volume $f = FFV$ (determined from Bondi's group contribution method) [5]. Dots with crosses represent high free volume polymers [11, 12, 14, 16-18]. Open square and circles represent TR-1-450 [1, 20] and PIM-1 [2, 19], respectively. Curves represent best fits of the Doolittle relation (dashed line) and the new relation (solid line). Arrows represent the prediction for pore interconnection and bi-continuity at 13.5% and 22.5% free volume, respectively from Hedstrom et al. [21]. Top right corner displays the least squares coefficients of determination for both curves.

Table 4.2: Best fit parameter values found by fitting the new relation to experimental permeability. New relation $P = \alpha^* \exp(\beta f)$.

Gases	α^* (10^{-4} Barrer)	β (dimensionless)
O ₂	15.54	44.17
H ₂	709.77	34.32
CO ₂	66.22	43.51
CH ₄	0.53	52.35
He	983.82	33.33
N ₂	1.02	50.22

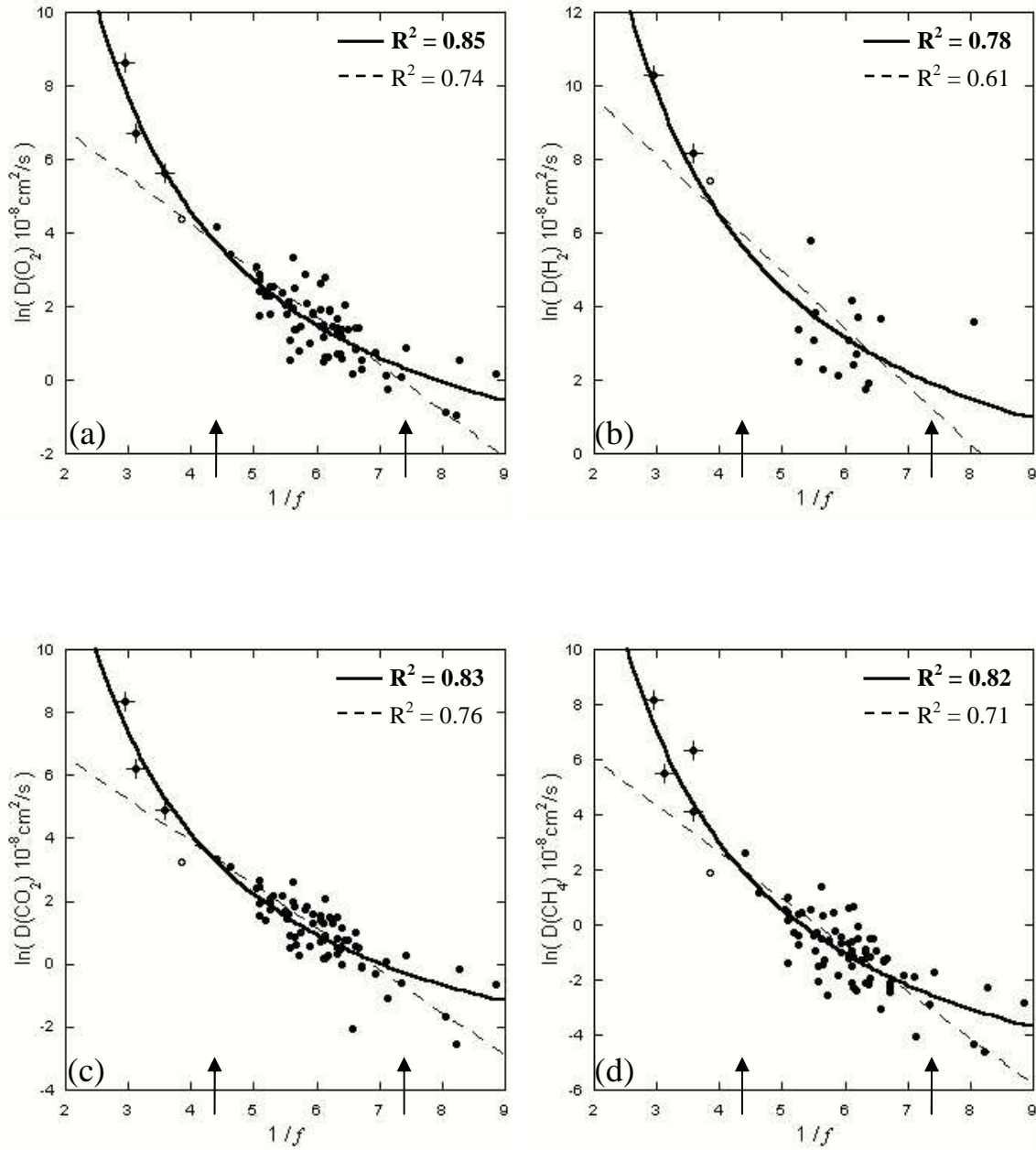


Figure 4.2 (continued to next page)

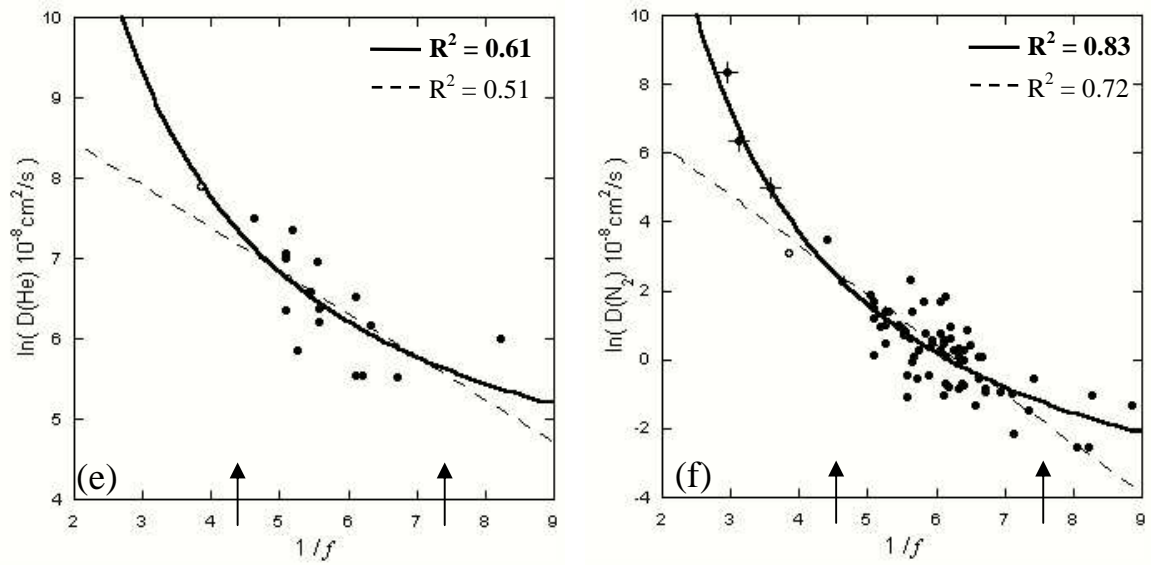


Figure 4.2: Diffusion coefficients of light gases: (a) oxygen, (b) hydrogen, (c) carbon dioxide, (d) methane, (e) helium and (f) nitrogen, versus inverse fractional free volume $f = FFV$ (determined from Bondi's group contribution method) [10]. Dots with crosses represent high free volume polymers [11, 12, 16-18]. Open circle represents PIM-1 [2]. Curves represent best fits of the Doolittle relation (dashed line) and the new relation (solid line). Arrows represent the prediction for pore interconnection and bi-continuity at 13.5% and 22.5% free volume, respectively from Hedstrom et al. [21]. Top right corner displays the least squares coefficients of determination for both curves.

Table 4.3: Best fit parameter values found by fitting the new relation to experimental diffusivity coefficients. New relation $D = \alpha \exp(\beta f)$.

Gases	α ($10^{-4} \text{cm}^2/\text{sec}$)	β (dimensionless)
O ₂	92.91	37.07
H ₂	308.10	39.88
CO ₂	42.89	38.42
CH ₄	1.14	48.31
He	226713	18.59
N ₂	11.25	42.01

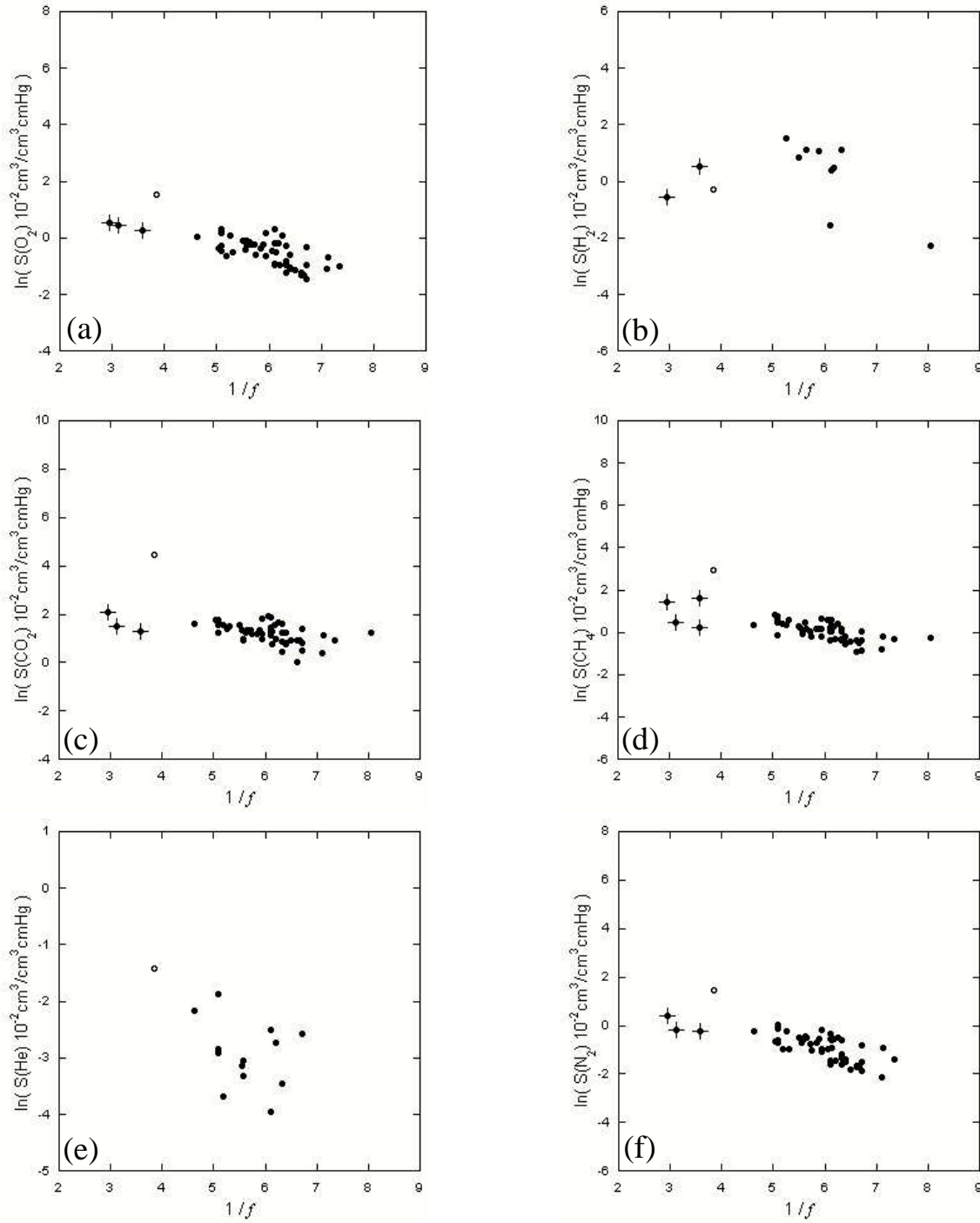


Figure 4.3: Solubility coefficients (= Permeability [5] / Diffusivity [10]) of light gases: (a) oxygen, (b) hydrogen, (c) carbon dioxide, (d) methane, (e) helium and (f) nitrogen, versus inverse fractional free volume $f = FFV$ (determined from Bondi's group contribution method). Dots with crosses represent high free volume polymers [11, 12, 16-18]. Open circle represents PIM-1 [2].

It is known that as the fractional free volume in polymers increases, the pores become interconnected and provide a flow through path for the permeating gas which

has commonly been identified with a pore flow diffusion process [18]. For example at 13.5% free volume pores become interconnected and at 22.5% free volume pores become bi-continuous for nanoporous methyl silsesquioxane (MSSQ) films according to MD simulations and SAXS experimental results [21]. These points have been marked by solid arrows in Figure 4.1 and Figure 4.2 and conveniently match the areas where the two model predictions begin to separate in behaviour. This deviation occurs when gas diffusion no longer is dependent on polymer chain motions, but the gas molecules now are free to move within the maze of connected pores (see schematic picture, Figure 4.4). Polymers with high free volume have been known as having two qualitatively different free volume phases: one composed of relatively small isolated holes similar to those in conventional polymers and one with mostly connected micropores which provide excellent diffusion path ways [13]. It is reasonable to believe that the new relation accommodates both of these processes so that it can be used for a range of polymers where the occupied space and free space vary widely.

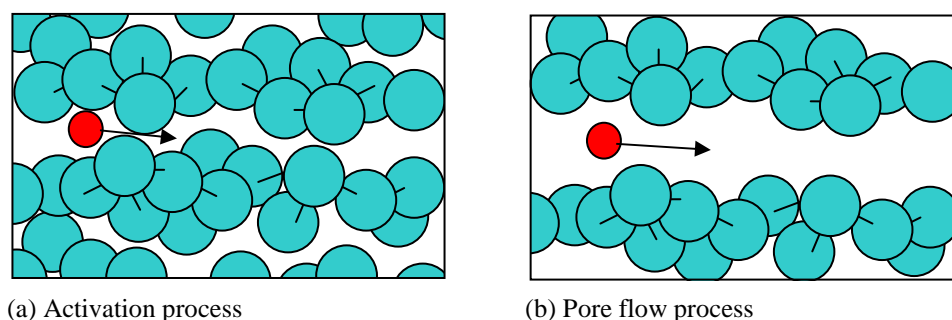


Figure 4.4: Schematic diagram of different diffusion processes within (a) closely packed conventional glassy polymer and (b) high free volume glassy polymer.

4.2.1.1 New classes of polymers

There is much interest of new classes of polymers with molecular sieving type structures that overcome the permeability-selectivity tradeoff providing membranes with both high permeabilities and high separation capabilities [22]. The model can be used to compare these new polymers with the wide range of existing polymers. Here the recently introduced thermally rearranged (TR) polymers [1, 20] and polymers of intrinsic microporosity (PIM) [2, 19] are considered, listed in Table 4.1. Figure 4.1 shows that the TR polymer TR-1-450 (open square) and the PIM polymer PIM-1 (open

circle) both sit within the range of the high free volume glassy polymers at the high permeability end of the curve. Both polymers are closest to the glassy acetylene based polymer PTMSDPA which has high free volume and high permeability and a relatively large pore size (0.75 nm) [8]. The pore sizes in TR-1-450 and PIM-1 have been reported as 0.75 nm and 1.05 nm, respectively [1, 14]. The pore size at which the diffusion mechanism in polymers changes from one governed by activation energy theory to one of Knudsen diffusion for light gases is estimated to be ≥ 1.4 nm [18], with the optimum range for molecular sieving selectivity estimated to be 0.75-1.0 nm [22]. These preliminary results indicate that the new relation can be used to model TR and PIM polymers as well as the ultra high free volume polymers, and that the model accommodates different diffusion processes.

PIM's are known to have high solubility values [2] which suggests that the high permeability is a result of high solubility rather than high diffusivity. This is true since the CO₂ solubility in PIM is 24 times greater than the average CO₂ solubility in conventional polymers while the CO₂ diffusivity is only 6.7 times greater than the average CO₂ diffusivity in conventional polymers, demonstrated in Figure 4.2 and Figure 4.3, and summarized in Table 4.4. This dependence on solubility, however, is not

Table 4.4: Comparison of CO₂ solubility, diffusivity and permeability enhancement ratios in high free volume polymers.

Polymer	Solubility		Diffusivity		Permeability	
	value	ratio	value	ratio	value	ratio
conventional*	3.6	1	3.86	1	14	1
PIM-1	88	24	26	6.7	2300	164
PTMSP	8.2	2.3	4167	1080	34000	2430

Ratio: High free volume property value / conventional property value

Permeability units: [Barrers] (1 Barrer = 10^{-10} cm³ (STP) cm / cm².sec.cmHg)

Diffusivity units: [10^{-8} cm² / sec]

Solubility units: [10^{-2} cm³ (STP) / cm³.cmHg]

*Geometric average of all available data for permeability (from ref. [5]), diffusivity (from ref. [10]) and solubility (= permeability / diffusivity) in conventional polymers

observed in other high free volume polymers where the large increase in permeability is due almost entirely to the increase in diffusivity, shown in Figure 4.2 and Figure 4.3. The new relation fits much better than the Doolittle relation and as expected is a better predictor for diffusivity than for permeability, with the exceptions of helium and

hydrogen most likely due to the lesser amount of available data. Best fit parameter values are listed in Table 4.3, found by fitting the new relation to experimental diffusivities and are commented on later with Figure 4.7. The PIM-1 diffusivity value is conveniently in good agreement with the new relation despite the high solubility. The conclusion for TR polymers can not be made until diffusivity and solubility data are made available.

4.2.2 Permeability vs gas-specific fractional free volume

Park and Paul's gas-specific modified fractional free volume FFV_{gas} was derived based on the assumption that permeability depends on free volume according to the Doolittle relation. It is interesting to observe that the new relation actually fits the modified data better than the Doolittle relation that Park and Paul chose to use, as seen in Figure 4.5.

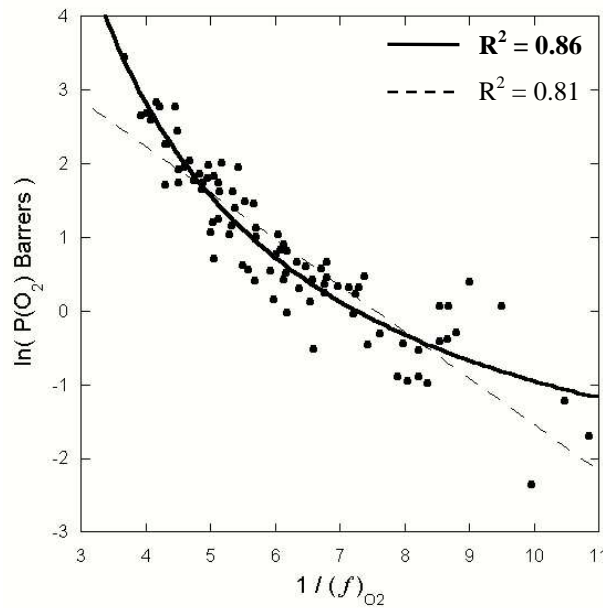


Figure 4.5: Permeability of oxygen versus inverse fractional free volume $f = FFV_{O_2}$ (determined from modified Bondi's group contribution method) [5]. Doolittle relation (dashed line) with $A^* = 116.04$ Barrers and $B = 0.620$. New relation (solid line) with $\alpha^* = 0.032$ Barrers and $\beta = 25.08$. Top right corner displays the least squares coefficients of determination for both curves.

This goodness of fit is particularly apparent in the high free volume range which is to be expected because at low free volume gas diffusion should follow an activation process and therefore the Doolittle expression should be appropriate in this region. Seeing that

the spread of the data is minimized using the modified Bondi expression (see Figure 4.5), it is anticipated that if the modified Bondi group contribution parameters were re-evaluated using the new relation in place of the Doolittle expression, and including the high free volume polymers, then the resultant deterministic relation will have less spread than Figure 4.1 and hence be a more effective predictor of permeability.

4.2.3 Diffusivity vs simulated gas-accessible free volume

Fractional free volume calculated using Bondi's group contribution method has been shown to not be the best measure of free volume for predicting diffusion results [13]. This is because Bondi's method is essentially similar to using a probe with a radius close to zero to determine free space as opposed to a gas molecule which will have a minimum radius larger than this [7]. Bondi's method will determine free space that is of such a small size that it is not accessible to any known gas. It has been shown that diffusivity is better correlated to accessible volume fraction (*AVF*) which can be determined using MD simulations such as those performed by Hofmann et al. [13] for oxygen in a range of polymers. Experimental data from Hofmann et al. for oxygen diffusivity and *AVF* for polymers with *FFV* ranging from 13% to 33% are shown in Figure 4.6. The data include polymers typically considered as ultra high permeability, e.g. PTMSP, AF2400, and AF1600 as well as polymers considered as conventional glassy polymers such as PTMSS (poly-p-trimethylsilylstyrene), PVTMS (polyvinyltrimethylsilane), and PPhSiDPA (poly(1-phenyl-2-(p-(triphenylsilyl) phenyl) acetylene). These data are compared with the new model and the Doolittle relation. Hoffman et al. commented on the large deviation of their results from the assumed Doolittle relation. It is shown here that the new model fits the data of Hoffman et al. [13] for high permeability and conventional polymers quite well.

A decade earlier Greenfield and Theodorou [6] had used computer simulations via energy minimization and Monte Carlo methods to illustrate that the percolation threshold is between 2% and 4% *AVF* for conventional glassy polymers such as atactic polypropylene. In other words, connectivity of pores that provide diffusion pathways from one side of the sample to the other begins to occur from the range 2 – 4% *AVF*. This range is shown by arrows in Figure 6 where 2 – 4% *AVF* is equivalent to ~25 – 31% *FFV* which is consistent with the free volume needed for bicontinuous porosity. Hofmann et al. [13] also showed a large change in oxygen diffusion at these free volume values. Therefore work done by Greenfield and Theodorou (1993), Hofmann et

al. (2003) and Hedstrom et al. (2004) agrees and indicates regions of free volume where the gas diffusion processes change from activation to pore flow transport. These results support the use of a model that accommodates the different flow regimes over a wide range of free volume.

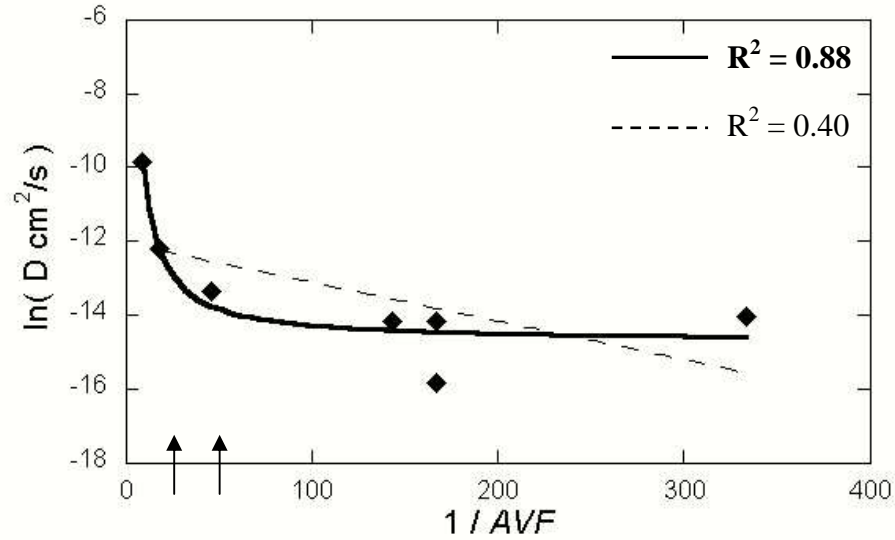


Figure 4.6: Experimental diffusion coefficients for oxygen (cm^2s^{-1}) versus inverse accessible volume fraction from Hofmann et al. [13]. Doolittle relation (dashed line) $D = A \exp(-B / AVF)$ with $A = 5.84 \times 10^{-6} \text{ cm}^2/\text{s}$ and $B = 0.0105$. New relation (solid line) $D = \alpha \exp(\beta AVF)$ with $\alpha = 4.02 \times 10^{-7} \text{ cm}^2/\text{s}$ and $\beta = 45.5$. Arrows represent the range at which the percolation threshold is reached according to Greenfield and Theodorou's [6] computer simulations.

4.3 Physical interpretation of new relation

Here a physical meaning of the new relation is postulated by comparing its form with the Doolittle relation. The new relation $D = \alpha \exp(\beta f)$, where α and β are constants, was empirically determined but can be shown to be very similar to the Doolittle relation when represented in this form,

$$D = \alpha' \exp(-\beta v_0 / (v_f + v_0)) \quad (4.5)$$

By using the definition of fractional free volume $f = v_f / (v_f + v_0)$, where v_f is the free volume and v_0 is the occupied volume, the equation becomes,

$$D = \alpha' \exp(\beta v_f / (v_f + v_0) - \beta) = \alpha \exp(\beta v_f / (v_f + v_0)) = \alpha \exp(\beta f) \quad (4.6)$$

Note that the difference in Equation 4.5 compared to the Doolittle equation is that the denominator is shifted to $(v_f + v_0)$ from v_f . In other words, an increase in occupied volume is capable of increasing diffusion. Although this result is counterintuitive, occupied volume may be increased by either increasing the volume of the polymer chains or by decreasing their mass. A decrease in polymer mass may contribute to an increase in polymer mobility. The numerator represents the effect which occupied volume has on diffusion where occupied volume is increased by a volume increase (as opposed to a mass decrease), resulting in a diffusion decrease. By combining the numerator with the denominator, an increase in occupied volume results in an overall decrease in diffusion, but at a lower rate than the Doolittle relation. Consequently, the new relation has the ability to follow the large increase in diffusion in high free volume polymers where occupied volume is usually increased along with free volume (eg. PSF, $f = 15\%$, $v_0 = 0.68$; PTMSP, $f = 34\%$, $v_0 = 0.92$). This suggests that the new relation more accurately predicts gas diffusion in a wide range of polymers where occupied volume varies from polymer to polymer in different ways (mass change and/or volume change).

4.4 Parameter values related to gas diameter

The constant α in the new relation is a pre-exponential empirical constant while β is found to be linearly dependent on the square of the particular gas kinetic diameter σ , shown in Figure 4.7. Figure 4.7(a) shows the β values determined from the permeability data and Figure 4.7(b) shows the β values determined from the diffusivity data. According to the theory outlined in this work the β values determined from both methods should match. The equations of best fit for (a) $\beta = 15.06(\pm 2.64) + 2.53(\pm 0.23)\sigma^2$ and (b) $\beta = 7.56(\pm 10.50) + 2.70(\pm 0.92)\sigma^2$ reasonably agree within the standard errors and the discrepancy could be the result of the lack of sufficient diffusivity data, especially for helium and hydrogen. In the same way, the constant B in the Doolittle relation is also linearly dependent on the square of the gas kinetic diameter where the equation for the best fit is $B = 0.51 + 0.03\sigma^2$ [23, 24]. This has been explained physically by the consideration of the hard sphere diffusion model where diffusion depends on the sphere's two dimensional area [25].

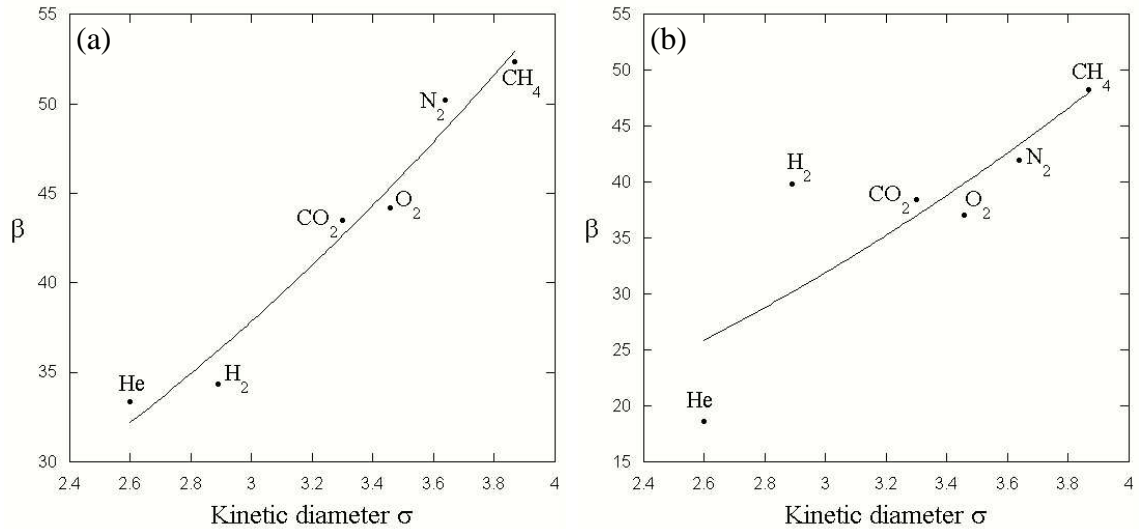


Figure 4.7: The dependence of β values found from fits to (a) permeability data and (b) diffusivity data, on kinetic diameter σ from Breck [26] for light gases. The method of least squares regression determined the best fit equations, (a) $\beta = 15.06 + 2.53 \sigma^2$ and (b) $\beta = 7.56 + 2.70 \sigma^2$.

4.5 Conclusion

A new relation was established between permeability/diffusivity and free volume to fulfil the need for a model that fits all the available data in the range of fractional free volume (10 to 35%) and permeability (0.1 to 9700 Barrer). This relation was empirically derived using Park and Paul's large database of 105 polymers with additional high free volume polymers where free volume was defined as fractional free volume with occupied volume calculated via Bondi's group contribution method. This relation also fitted Park and Paul's modified data with fractional free volume dependent on the permeating gas where occupied volume was calculated using a modified Bondi's group contribution method. Finally this new relation also fitted data from Hofmann et al. [13] for experimental diffusion coefficients with free volume defined as an accessible volume fraction specific to the permeating gas.

Using results from Hedstrom et al. [21] (MD simulations and SAXS) and Greenfield and Theodorou [6] (computer simulations) it was shown that as free volume increases to large amounts, pores become interconnected and eventually percolate through the polymer providing "diffusion highways" for the permeating gas to travel. This diffusion is no longer described by an activation process but depends on pore morphology, pore wall surface interaction and other factors. It was shown that the new

empirical relation deals with both processes and is good at modelling free volume change in a wide range of polymers.

It was shown that the new relation is not too fundamentally different from the popular Doolittle relation but that the denominator now includes occupied volume. A suggested reason was given that the better fit of the new relation may be attributed to the effect that occupied volume has on vacancy diffusion when polymer chains have a change in mass (increased/decreased mass results in a decreased/increased diffusion).

The new empirically derived relation for gas diffusion and free volume fits experimental data especially for the wide range of polymers, accommodates the transition of gas diffusion from an activation process to a free flow process and consequently is able to predict gas permeability from polymer to polymer and between vastly different families of polymers. In Chapter 6 of this thesis the new relation is shown to accurately model thin film physical aging in membranes.

References

- [1] H. B. Park, C. H. Jung, Y. M. Lee, A. J. Hill, S. J. Pas, S. T. Mudie, E. van Wagner, B. D. Freeman and D. J. Cookson, Polymers with cavities tuned for fast selective transport of small molecules and ions, *Science*, 318 (2007) 254.
- [2] P. M. Budd, K. J. Msayib, C. E. Tattershall, B. S. Ghanem, K. J. Reynolds, N. B. McKeown and D. Fritsch, Gas separation membranes from polymers of intrinsic microporosity, *J. Membr. Sci.*, 251 (2005) 263.
- [3] A. Bondi, van der Waals volumes and radii, *J. Phys. Chem.*, 68 (1964) 441.
- [4] D. VanKrevelen, *Properties of Polymers*, Elsevier, Amsterdam, The Netherlands, 1990.
- [5] J. Y. Park and D. R. Paul, Correlation and prediction of gas permeability in glassy polymer membrane materials via a modified free volume based group contribution method, *J. Membr. Sci.*, 125 (1997) 23.
- [6] M. L. Greenfield and D. N. Theodorou, Geometric analysis of diffusion pathways in glassy and melt atactic polypropylene, *Macromolecules*, 26 (1993) 5461.

- [7] D. Hofmann, M. Heuchel, Y. Yampolskii, V. Khotimskii and V. Shantarovich, Free volume distributions in ultrahigh and lower free volume polymers: Comparison between molecular modeling and positron lifetime studies, *Macromolecules*, 35 (2002) 2129.
- [8] X. Y. Wang, R. D. Raharjo, H. J. Lee, Y. Lu, B. D. Freeman and I. C. Sanchez, Molecular simulation and experimental study of substituted polyacetylenes: Fractional free volume, cavity size distributions and diffusion coefficients, *J. Phys. Chem. B.*, 110 (2006) 12666.
- [9] B. D. Freeman and A. J. Hill, *Structure and Properties of Glassy Polymers*, American Chemical Society, Washington, DC, 1998.
- [10] A. Thran, G. Kroll and F. Faupel, Correlation between fractional free volume and diffusivity of gas molecules in glassy polymers, *J. Polym. Sci., Part B: Polym. Phys.*, 37 (1999) 3344.
- [11] T. C. Merkel, V. Bondar, K. Nagai and B. D. Freeman, Hydrocarbon and perfluorocarbon gas sorption in poly(dimethylsiloxane), poly(1-trimethylsilyl-1-propyne), and copolymers of tetrafluoroethylene and 2,2-bis(trifluoromethyl)-4,5-difluoro-1,3-dioxole, *Macromolecules*, 32 (1999) 370.
- [12] L. G. Toy, K. Nagai, B. D. Freeman, I. Pinnau, Z. He, T. Masuda, M. Teraguchi and Y. P. Yampolskii, Pure-gas and vapor permeation and sorption properties of poly[1-phenyl-2-[p-(trimethylsilyl)phenyl]acetylene] (PTMSDPA), *Macromolecules*, 33 (2000) 2516.
- [13] D. Hofmann, M. Entrialgo-Castano, A. Lerbret, M. Heuchel and Y. Yampolskii, Molecular modeling investigation of free volume distributions in stiff chain polymers with conventional and ultrahigh free volume: Comparison between molecular modeling and positron lifetime studies, *Macromolecules*, 36 (2003) 8528.
- [14] C. L. Staiger, S. J. Pas, A. J. Hill and C. J. Cornelius, Gas separation, free volume distribution, and physical aging of a highly microporous spirobisindane polymer, *Chem. Mater.*, 20 (2008) 2606.

- [15] X. Y. Wang, K. M. Lee, Y. Lu, M. T. Stone, I. C. Sanchez and B. D. Freeman, Cavity size distributions in high free volume glassy polymers by molecular simulation, *Polymer*, 45 (2004) 3907.
- [16] A. Y. Alentiev, V. P. Shantarovich, T. C. Merkel, V. I. Bondar, B. D. Freeman and Y. P. Yampolskii, Gas and vapor sorption, permeation, and diffusion in glassy amorphous teflon AF1600, *Macromolecules*, 35 (2002) 9513.
- [17] T. C. Merkel, V. Bondar, K. Nagai and B. D. Freeman, Sorption and transport of hydrocarbon and perfluorocarbon gases in poly(1-trimethylsilyl-1-propyne), *J. Polym. Sci., Part B: Polym. Phys.*, 38 (2000) 273.
- [18] T. C. Merkel, Z. He, I. Pinnau, B. D. Freeman, P. Meakin and A. J. Hill, Effect of nanoparticles on gas sorption and transport in poly(1-trimethylsilyl-1-propyne), *Macromolecules*, 36 (2003) 6844.
- [19] S. Thomas, I. Pinnau, N. Du and M. D. Guiver, Pure- and mixed-gas permeation properties of a microporous spirobisindane-based ladder polymer (PIM-1), *J. Membr. Sci.*, 333 (2009) 125.
- [20] Y. M. Lee, ICOM Conference communication, (July 2008) <http://www.icom2008.org/lee.pdf>.
- [21] J. A. Hedstrom, M. F. Toney, E. Huang, H. C. Kim, W. Volksen, T. Magbitang and R. D. Miller, Pore morphologies in disordered nanoporous thin films, *Langmuir*, 20 (2004) 1535.
- [22] L. M. Robeson, The upper bound revisited, *J. Membr. Sci.*, 320 (2008) 390.
- [23] H. Lin and B. D. Freeman, Gas permeation and diffusion in cross-linked poly(ethylene glycol diacrylate), *Macromolecules*, 39 (2006) 3568.
- [24] Y. Yampolskii, I. Pinnau and B. D. Freeman, *Materials Science of Membranes for Gas and Vapor Separation*, John Wiley & Sons, Ltd, 2006.
- [25] M. H. Cohen and D. Turnbull, Molecular transport in liquids and glasses, *J. Chem. Phys.*, 31 (1959) 1164.

- [26] D. W. Breck, Zeolite Molecular Sieves: Structure, Chemistry, and Use, John Wiley & Sons, New York, 1973.

List of symbols used in Chapter 4

P	permeability
D	diffusivity
f	generalized free volume (including all definitions)
FFV	fractional free volume from Bondi's method
FFV_n	gas-specific fractional free volume from Park and Paul's method
AVF	accessible volume fraction from computational methods
R^2	least squares coefficient of determination
v_0	occupied volume
v_f	free volume
v	total specific volume

Part III

Gas storage

Chapter 5

Introduction to gas storage

5.1 Previous work

The ability to store gas is a much needed development for applications such as greenhouse gas capture, fuel preservation and fuel transportation. In this chapter storage systems for mobile applications, which are based on the physisorption mechanism, are compared to other storage methods. Further, the existing modelling approaches are reviewed, namely, geometry-based calculations, molecular simulations and ab-initio calculations.

5.1.1 Storage methods

The general goal for the transportation of gases is to fit large amounts of gas into a small space (measured by: weight of gas / volume of system) with a minimum increase in weight (measured by: weight of gas / weight of system) as safely and energetically efficient as possible [1]. The four general methods for gas storage are illustrated in Figure 5.1. The first method is to compress the gas using multi-stage high pressure equipment resulting in a tank of gas at pressures of up to 300 atm [2, 3]. Pressures as high as these may cause potential safety issues, and therefore there exist very high standards for the carefully engineered and expensive equipment for the safe storing and release of the gas [2, 4]. A second method is to cool the gas to its liquid phase, resulting in a tank of highly dense and cryogenic liquid [1, 2]. Although more amounts of gas can fit within the tank by liquification as compared to compression, the energy required to cool the gas into a liquid is an expense which needs to be avoided if at all possible. A third method is to store the gas in a chemically bonded state by the mechanism of chemisorption, in which the gas binds (usually covalently) to other elements forming a solid, liquid or gas [5, 6]. For example, hydrogen can be stored in a solid state as a metal

hydride (e.g. Alumane, AlH_3), or as a liquid state such as water (H_2O) or even as a methane gas (CH_4) [6, 7]. Large amounts of gas can be stored at close to ambient conditions using this method however large amounts of energy are required to bind the gas to the host elements and then also to break the bonds to release the gas. For example, it takes about 2.5 eV to split water into H_2 and O which is commonly performed by electrolysis [8]. The fourth method is to store the gas by the mechanism of physisorption by which gases become adsorbed onto a surface through van der Waals forces. This method is the most promising approach since a small amount of energy is required to store and release the gas. Further details of this method are given in the following section.

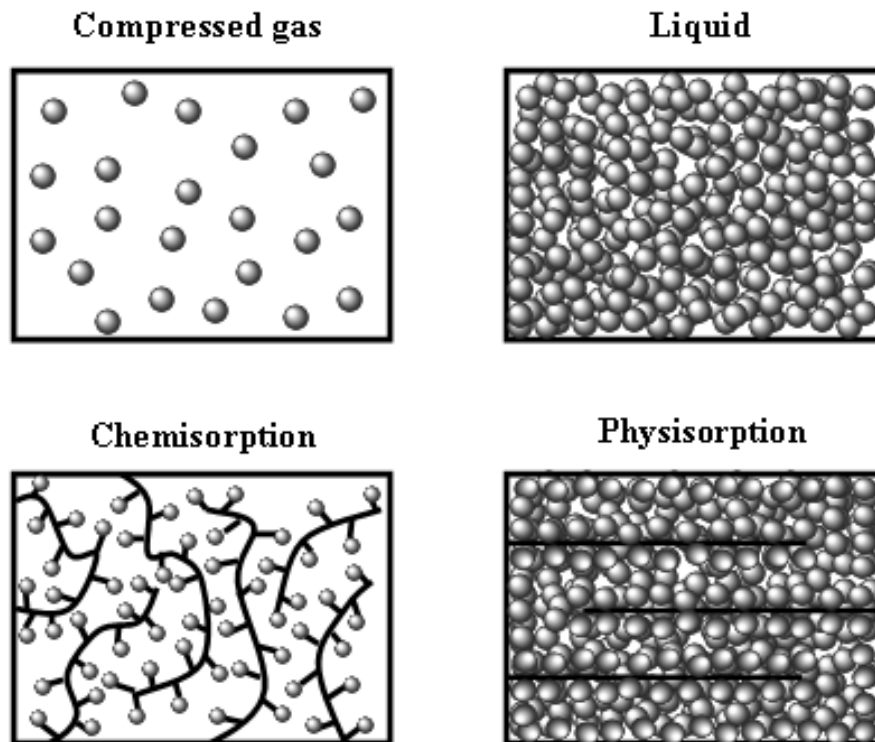


Figure 5.1: Four gas storage methods.

Figure 5.2 shows a comparison of the existing storage methods of hydrogen in terms of volumetric and gravimetric density. The methods utilizing the chemisorption mechanism include metal-hydrides (M-H_n) [1, 9], chemical storage (NaBH_4) [10], water (H_2O) [8], gasoline (C_mH_n) and diesel (C_mH_n) [11]. The methods utilizing the physisorption mechanism include metal-organic frameworks (MOFs) [12], carbon nanotubes (CNTs) [13], fibreglass, activated carbon (AC) [14] and polymers. The US

Department of Energy (DoE) has set future targets for vehicular hydrogen fuel systems which are currently only satisfied by gasoline and diesel [4], and all the other methods need to be improved to reach the DoE targets.

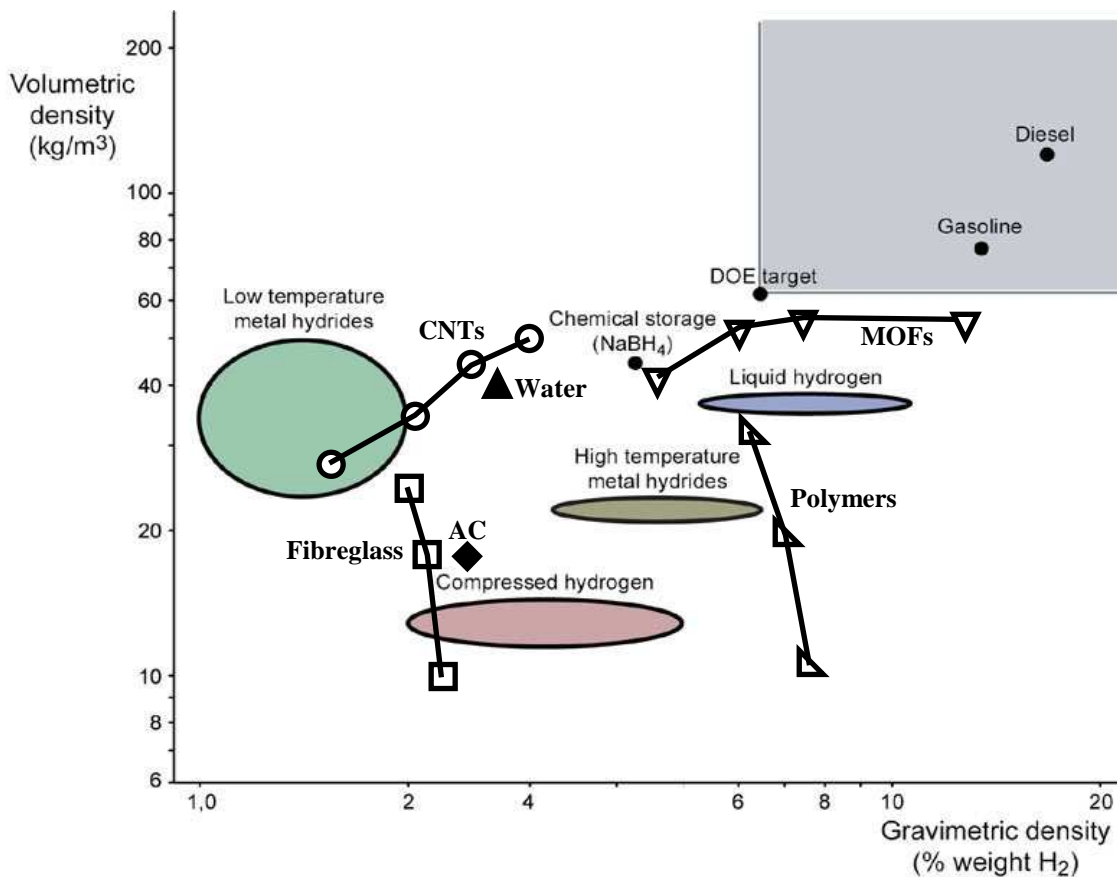


Figure 5.2: Storage methods for hydrogen as compared to the Department of Energy (DoE) target. Methods utilizing chemisorption include: metal-hydrides [1, 9], chemical storage [10] and water [8]. Methods utilizing physisorption include: carbon nanotubes (CNTs) [13, 15], fibreglass [15], activated carbon (AC) [14], metal-organic frameworks (MOFs) [12] and polymers [15]. Figure taken from Chemistry World [11] with additional data superimposed.

5.1.2 Physisorption

Physisorption is the process of gas molecules becoming adsorbed onto a surface due to attraction from the van der Waals forces. The potential energy between two atoms as a result of the van der Waals interactions which is well described by the Lennard-Jones function [16]. By integrating this function over a surface the potential energy between an atom and a surface can be calculated. For example the potential energy PE between

an atom and an infinite flat surface at a distance of ρ from the plane of surface nuclei can be shown to become

$$PE_{LJ} = 4\pi\eta\epsilon\sigma^2 \left[\frac{1}{5} \left(\frac{\sigma}{\rho} \right)^{10} - \frac{1}{2} \left(\frac{\sigma}{\rho} \right)^4 \right], \quad (5.1)$$

where η is the atomic density of the surface (i.e. number of atoms per unit surface area), σ is the kinetic diameter and ϵ is the well depth. This function contains a repulsive component that dominates at close distances and an attractive component that dominates at large distances, as demonstrated in Figure 5.3. If the attractive force is strong enough the gas molecules will bind to the surface and form dense liquid-like layers [5, 17].

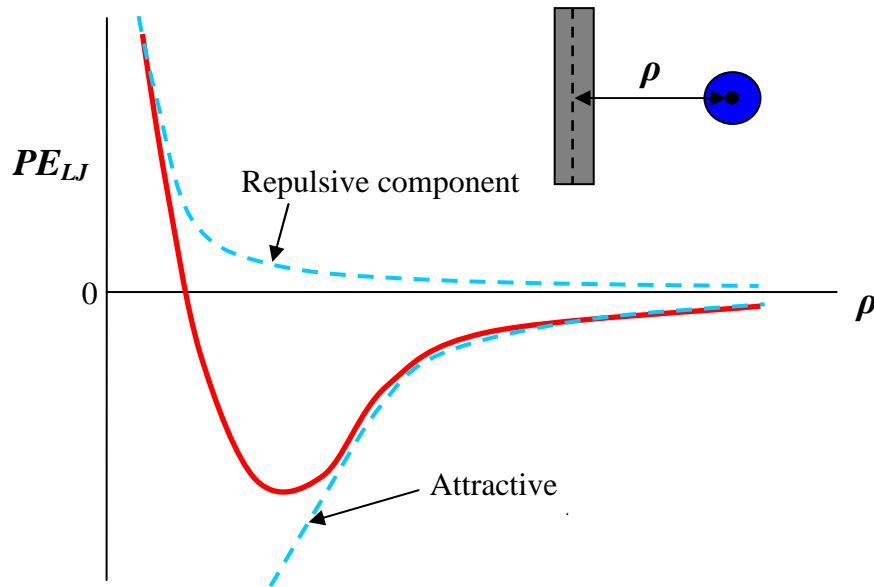


Figure 5.3: Lennard-Jones potential energy between atom and infinite flat surface at distance of ρ from the surface nuclei.

Langmuir equation

On assuming that a single layer is formed, the coverage can be adequately described by the Langmuir equation,

$$\theta = \frac{K_r p}{1 + K_r p}, \quad (5.2)$$

where θ is the fractional coverage (number of adsorption sites occupied / number of adsorption sites unoccupied), K_r is the equilibrium ratio of the rate of adsorption over the rate of desorption and p is the pressure.

BET equation

Assuming that multiple layers are formed, then the coverage can be described by the Brunauer, Emmett and Teller (BET) equation,

$$\frac{v_{cov}}{v_{mon}} = \frac{cz^*}{(1-z^*)\{1-(1-c)z^*\}}, \quad (5.3)$$

where v_{cov} is the volume of the adsorbed molecules, v_{mon} is the volume of a monolayer of adsorbed molecules, z^* is ratio of pressure p over the vapour pressure p^* and c is a constant relating to the heat of desorption $\Delta_{des}H$ and the heat of vaporization $\Delta_{vap}H$ in the following way,

$$c = \exp\left[\frac{\Delta_{des}H - \Delta_{vap}H}{RT}\right], \quad (5.4)$$

where R is the universal gas constant and T is temperature [17].

Heat of adsorption

An important factor influencing the uptake performance is the materials heat of adsorption, which is the energy difference between the bulk gas phase and the adsorbed phase, which is a measure reflecting the binding strength of the material. This can be enhanced by constructing the material out of elements that have strong interactions with the gas, arranging the surface such that the energy potentials overlap, and/or by creating surfaces with high curvature. The heat of adsorption $\Delta_{ad}H$ can be calculated from isotherm plots using the Clausius-Clapeyron equation derived from the van't Hoff equation [18],

$$\Delta_{ad}H = -\frac{RT_1T_2}{T_2 - T_1} \ln\left(\frac{p_2}{p_1}\right)_\theta, \quad (5.5)$$

where T_1 and T_2 are the temperatures that correspond to the gas pressures p_1 and p_2 , respectively, for an equal coverage θ . Alternatively, the heat of adsorption can be estimated from the Lennard-Jones potential energy function (Equation 5.1), as suggested by Everett and Powl [19],

$$\Delta_{ad}H = \left|PE_{LJ}^*\right| + \alpha_1 RT, \quad (5.6)$$

where PE_{LJ}^* is the depth of the potential minimum between the gas molecule and the surface, and α_1 (≈ 0.5) is the proportionality constant where $\alpha_1 RT$ is the energy contributed to the adsorbed phase due to the movement of the adsorbed molecules parallel to the surface. Other methods of predicting the heat of adsorption based on

molecular simulation work and ab-initio calculations are given in Sections 5.1.3.2 and 5.1.3.3, respectively.

By combining the Langmuir equation with the van't Hoff equation it has been shown that an optimal heat of adsorption $\Delta_{ad}H_{opt}$ can be calculated that maximizes the delivery for the operating temperature T , the storage pressure p_s and the delivery pressure p_d , as follows [20],

$$\Delta_{ad}H_{opt} = T\Delta S_o + \frac{RT}{2} \ln \left(\frac{p_s p_d}{p_o^2} \right), \quad (5.7)$$

where ΔS_o is the entropy change relative to the standard pressure p_o (1 atm). Similarly, an optimal operating temperature T_{opt} that maximizes delivery can be calculated for given heat of adsorption,

$$T_{opt} = \frac{\Delta_{ad}H}{\left[\Delta S_o + (R/2) \ln(p_s p_d / p_o^2) \right]}. \quad (5.8)$$

Surface area

From the Langmuir and BET equations it is clear that the amount of gas molecules adsorbed depends on the amount of available adsorption sites. Therefore the aim of a physisorption-based storage system is to create a material with an ultra high, accessible, internal surface area [21]. By considering a graphene sheet, Figure 5.4 demonstrates the increase in surface area as the sheet is split into fragments.

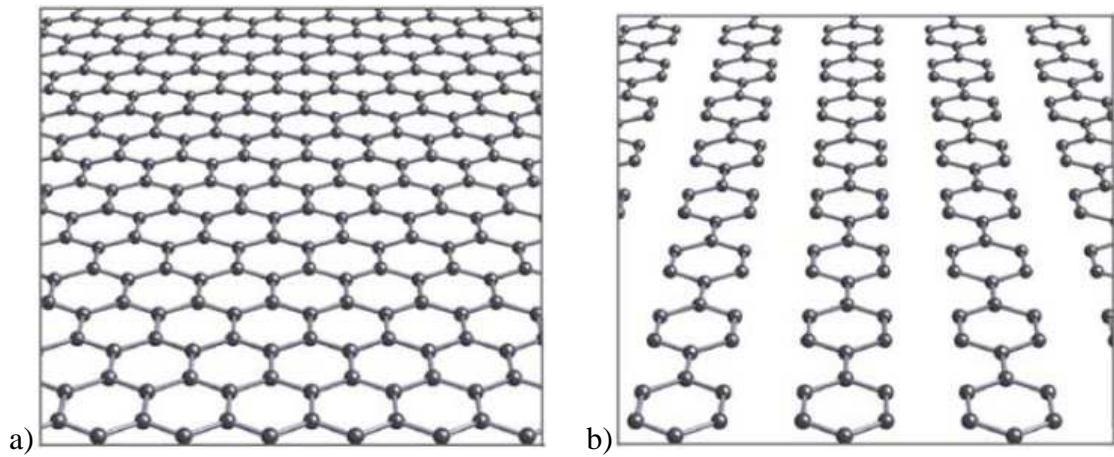


Figure 5.4 (continued to next page)

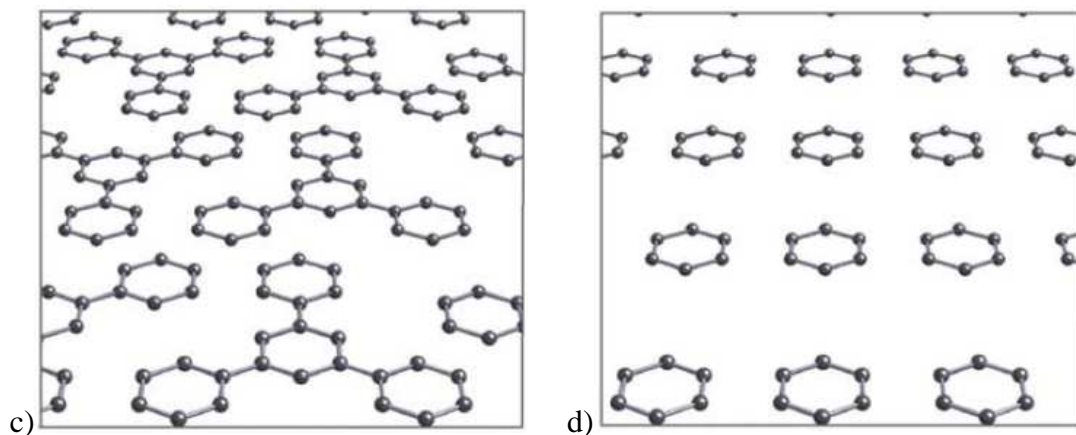


Figure 5.4: The surface area of graphite elements. a) graphene sheet 2965 m²/g, b) poly-p-linked six-membered rings 5683 m²/g, c) 1,3,5-linked six-membered rings 6200 m²/g and d) isolated six-membered rings 7745 m²/g. Taken from Chae et al. [21].

Excess adsorption

As the gas molecules enter the material, some are adsorbed onto the internal surface while others remain in the bulk gas phase distributed within the voids throughout the material. Due to the experimental techniques used to calculate the gas uptake it is necessary to define the total (or absolute) adsorption and the excess adsorption [22-24]. Total adsorption refers to the total amount of molecules within the material (adsorbed and non-adsorbed) N_{tot} while excess adsorption refers to the amount of molecules in excess N_{ex} of the hypothetical amount of molecules that would exist within the void in the bulk gas phase N_{bulk} , such that $N_{tot} = N_{ex} + N_{bulk}$, which is illustrated in Figure 5.5.

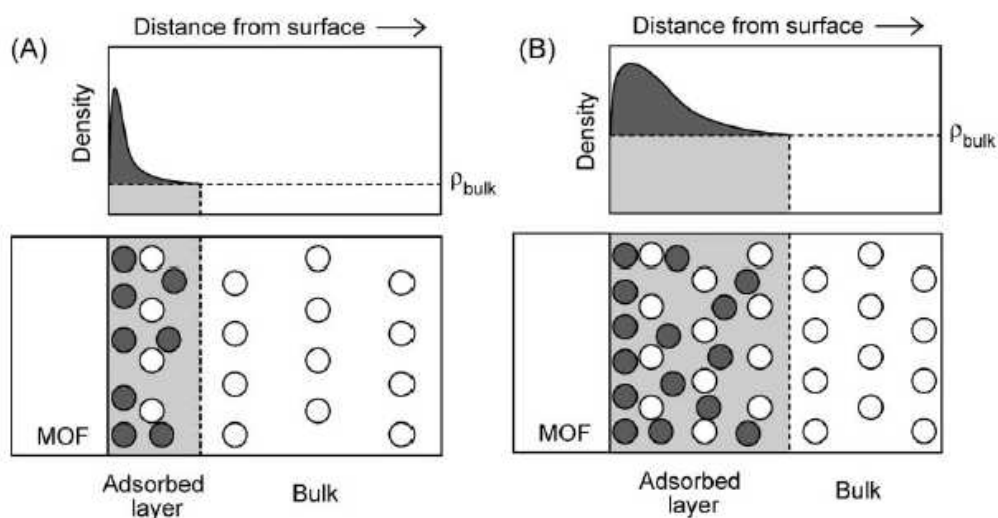


Figure 5.5 (continued to next page)

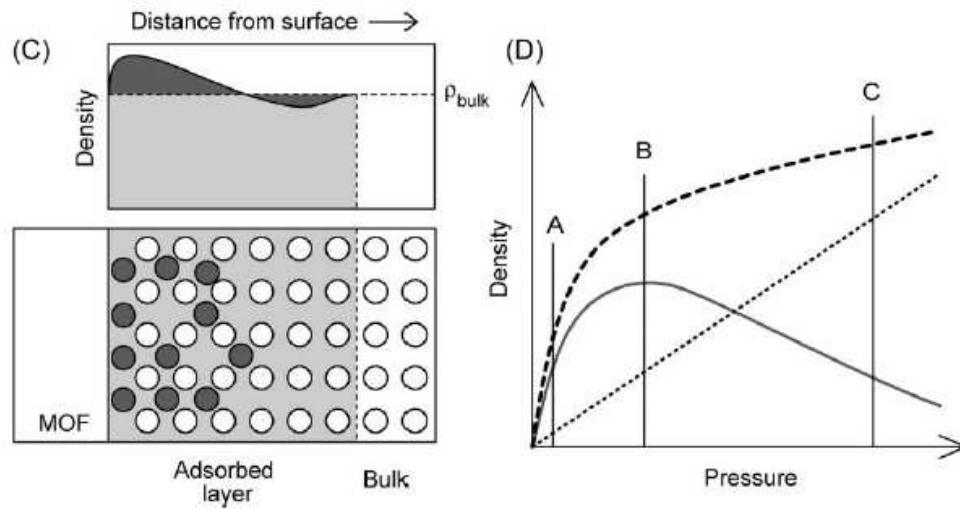


Figure 5.5: Density profiles for total amount of gas molecules upon the surface of a metal-organic framework (MOF). The total amount of gas molecules N_{tot} (A-C: all circles, D: dashed line) is demonstrated to be the addition of the amount of excess adsorbed molecules N_{ex} (A-C: coloured circles, D: solid line) and the amount of molecules that would exist within the space in the bulk gas phase N_{bulk} (A-C: empty circles, D: dotted line). Taken from Furukawa et al. [22].

5.1.3 Modelling approaches

The manufacturing and testing of adsorbents is costly and time-consuming, and therefore it is desirable to have simple models that might predict the storage performance within the proposed adsorbent [1]. Here three modeling approaches are summarized, namely, geometry-based calculations, molecular simulations and ab-initio calculations.

5.1.3.1 Geometry-based calculations

By assuming that the gas molecules are hard spheres, it is possible to estimate the maximum storage capacity of an adsorbent by considering the packing geometry upon the internal surface [13, 25]. Figure 5.6 demonstrates this approach applied to the packing of spheres upon a flat graphene sheet by assuming monolayer adsorption upon six-membered sites only (top), and alternatively by assuming no specific adsorption sites such that the adsorbed spheres stack together forming a triangular array (bottom). Similarly, the stacking of spheres along the surface of a cylinder has been considered to estimate the maximum storage capacity within tubes of different diameters, see Figure

5.7. Notice that there are critical diameters for which the stacking arrangement changes. For example, very small tubes will contain a single file arrangement, slightly larger tubes will contain a zig-zag configuration, larger tubes will contain a helix arrangement and even larger tubes will have a multiple helix arrangement.

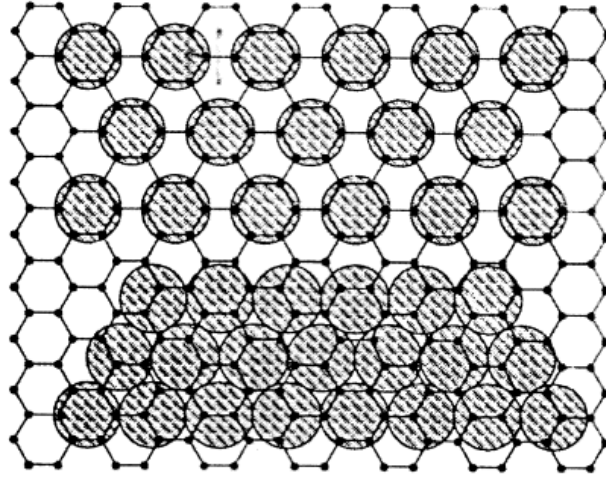


Figure 5.6: Stacking arrangement of a $\sqrt{3} \times \sqrt{3}$ commensurate (top) and an incommensurate (bottom) monolayer of spheres upon a graphite surface. Taken from Brown et al. [26].

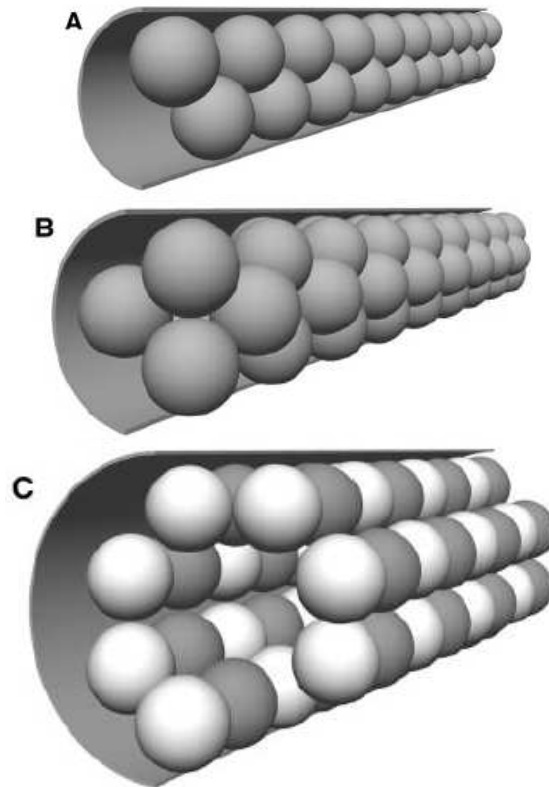


Figure 5.7: Stacking arrangements of spheres within tubes of different diameters. Taken from Michelson et al. [25].

This geometry-based approach is limited to simple surface geometries and will only provide a maximum storage capacity rather than a pressure and temperature dependent capacity. However, this approach is simple, fast to implement and does not require computer coding expertise.

5.1.3.2 Molecular simulations

Molecular simulation is probably the most commonly used modelling approach for gas storage applications. The simulation work in this area has been lead by groups such as, Snurr [27-30], Goddard [24, 31-33], Darkrim [34-36], Johnson [37-39] and Garberoglio [38, 40-42]. The majority of simulations are based on the Monte-Carlo algorithm which is outlined below [43, 44].

Firstly the atoms within the adsorbent structure are positioned within a fixed volume simulation box. Depending on the adsorbent, sometimes the structure is fixed using geometry considerations, other times, for more complicated structures, the structure first undergoes a series of energy minimization steps to ensure that the atoms are fixed in positions that closely reflect the actual physical structure. Either way, the structure of the adsorbent is then fixed and remains fixed throughout the rest of the simulation steps. The aim from this point is to simulate the behaviour of molecules within the simulation cell. This is achieved by executing certain steps including the creation, deletion, displacement and rotation of a gas molecule and then repeating these steps until equilibrium is achieved (usually on the order of millions of steps). In a creation step, the position of the new gas molecule is chosen randomly within the volume of the simulation box V_{box} and then the potential energy E of the new gas molecule is calculated using the Lennard-Jones function between neighbouring atoms. The step is then accepted with probability P or 1, whichever is smallest, where P is calculated as follows:

$$P = \exp\left(-\frac{E}{k_B T}\right) \frac{fV_{box}}{(N+1)k_B T} \quad (\text{creation}), \quad (5.9)$$

Where f is the gas phase fugacity and N is the total number of gas molecules within the box. Similarly, the deletion, displacement or rotation of a gas molecule is accepted with probability $\min(1, P)$, where P is calculated as follows:

$$P = \exp\left(\frac{E}{k_B T}\right) \frac{Nk_B T}{fV_{box}} \quad (\text{deletion}), \quad (5.10)$$

$$P = \exp\left(-\frac{E_1 - E_2}{RT}\right) \quad (\text{displacement or rotation}), \quad (5.11)$$

where E_1 and E_2 are the potential energies calculated before and after the step, respectively. After repeating the steps until equilibrium is reached, the average number of gas molecules N is calculated and then scaled according to the volumetric \bar{v} and gravimetric *wt. %* measures, thus

$$\bar{v} = \frac{N m_g}{V} \quad \text{and} \quad \text{wt. \%} = \frac{N m_g}{N m_g + M} \times 100, \quad (5.12)$$

where m_g is the molecular mass of an individual gas molecule and M is the mass of the adsorbent structure. Examples of simulations are shown in Figure 5.8.

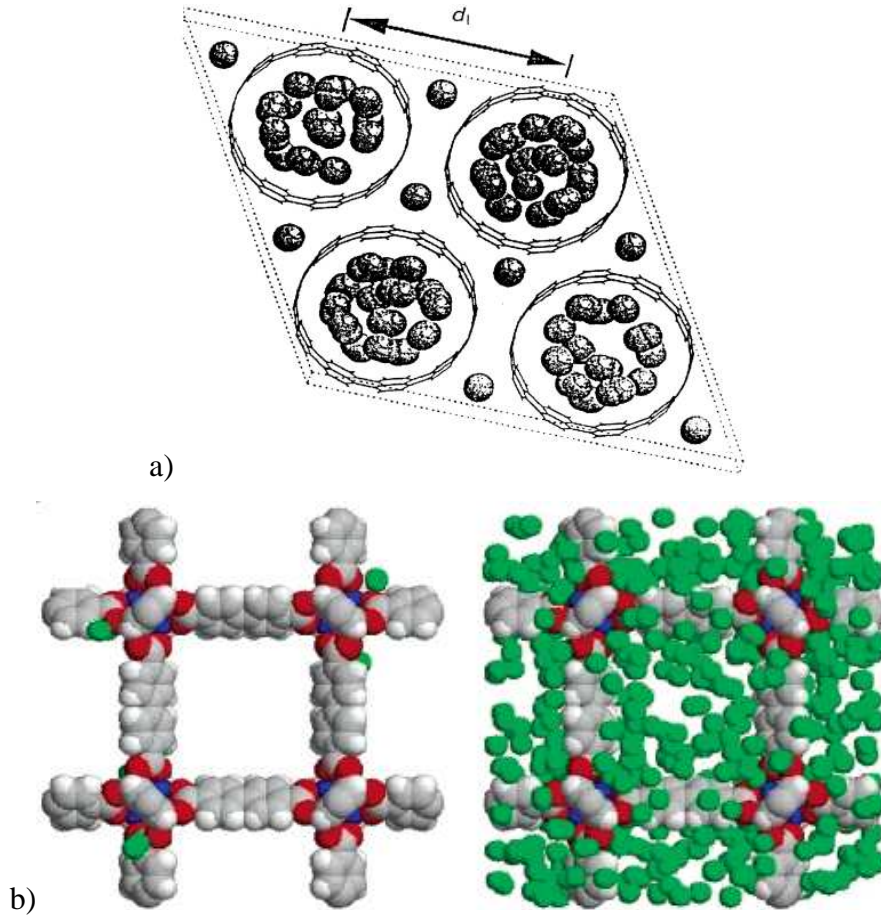


Figure 5.8: Molecular simulations. a) Hydrogen spheres within an array of carbon nanotubes, taken from Dresselhaus et al. [13], and b) Hydrogen spheres within a unit cell of a metal-organic framework at 0.1 (left) and 30 (right) bar, taken from Frost et al. [28].

This modelling approach provides a prediction for the total amount of molecules within the adsorbent. Since experiments provide amounts of excess adsorption as opposed to total (or absolute) adsorption, it is necessary to convert the simulated total adsorption to excess adsorption. A method has been provided by Myers and Monson [23], which is briefly outlined here. As previously explained in Section 5.1.2, with the assistance of Figure 5.5, the total number of molecules per unit volume within the adsorbent N_{tot} (from simulation) can be expressed as the sum of the excess adsorbed molecules N_{ex} (from experiment) and the hypothetical amount of molecules in the bulk gas phase N_{bulk} (from calculation), $N_{tot} = N_{ex} + N_{bulk}$. N_{bulk} may then be calculated as the product of the number density of the bulk gas ρ_{bulk} (from the Peng-Robinson equation of state) and the free volume within the adsorbent V_f , resulting in the expression

$$N_{tot} = N_{ex} + \rho_{bulk} V_f. \quad (5.13)$$

Currently the free volume V_f is calculated by integrating the potential energy of a helium atom PE_{He} throughout the entire volume V with r symbolically representing the three-dimensional coordinates,

$$V_f = \frac{1}{M} \int_V \exp\left[\frac{-PE_{He}(r)}{k_B T}\right] dr. \quad (5.14)$$

The molecular simulation approach has successfully matched many adsorption experiments and therefore has proven to be a good predictive tool for the testing of proposed adsorbents. Although this approach predicts adsorption performance much faster than the synthesis and experimental testing of the materials, it is still quite time-consuming and requires coding expertise. Further, the approach is restricted to a single case at a time and therefore is incapable of modelling the infinite amount of possible variations of structure, gas, temperature and pressure.

5.1.3.3 Ab-initio calculations

Ab-initio calculations involve the integration of various components based on first principles such as electron density, polarization and electrostatics [45]. This approach enables the prediction of the binding energies of the gas molecule to the adsorbent structure. This is useful for understanding the stability of certain adsorption scenarios and also for determining the specific adsorption sites that the gas molecule is likely to occupy [31, 46-56]. Figure 5.9 demonstrates an ab-initio study into the effect of transition-metals on the binding energies of hydrogen on a fullerene. Similarly, Figure

5.10 shows an ab-initio study of a lithium-coated nanotube and a lithium-coated peapod (nanotube with fullerenes inside) [55]. This approach does not consider statistical mechanics and therefore is incapable of modelling the randomness of actual adsorption but nevertheless is a good way of estimating the heat of adsorption and maximum capacity.

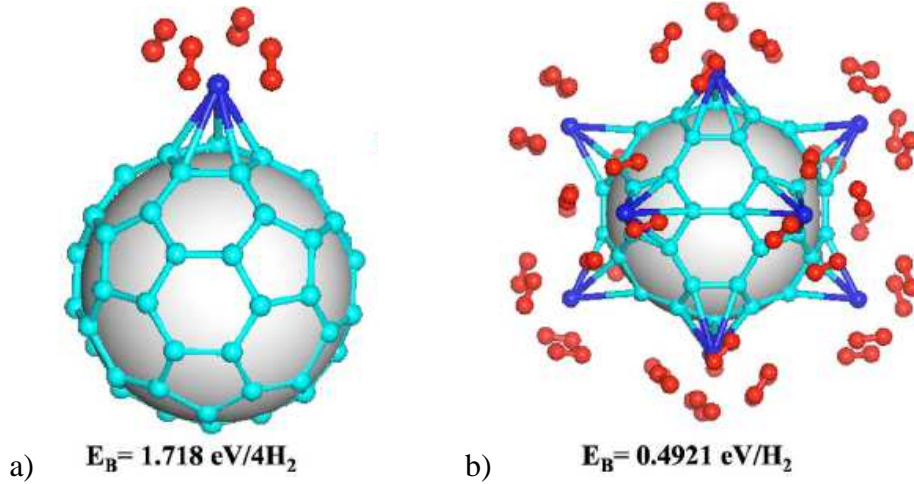


Figure 5.9: Ab-initio calculations for the binding energy E_B of hydrogen to a fullerene functionalized with a) 1 titanium atom and b) 12 titanium atoms, taken from Yildirim et al. [55].

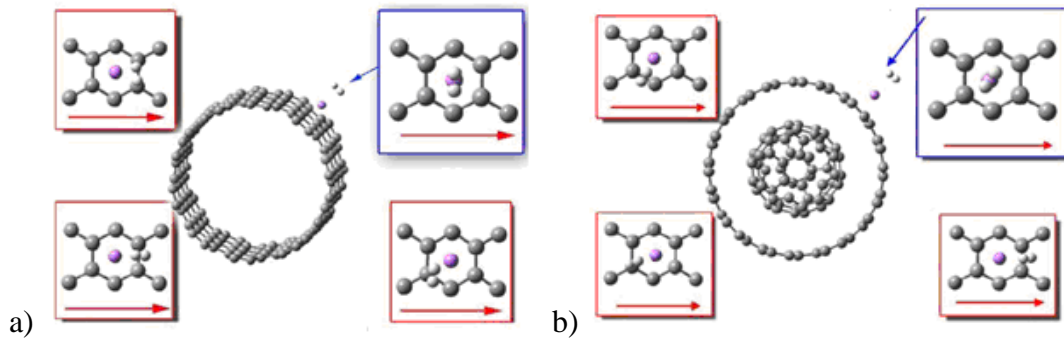


Figure 5.10: Ab-initio calculations for the binding energy E_B of hydrogen to a a) lithium-decorated carbon nanotube and b) lithium-decorated and fullerene-impregnated carbon nanotube. Taken from Chen et al. [57].

5.2 Thesis work overview

Chapter 6 presents a new approach for modelling gas adsorption, termed the TIMTAM approach (Topologically Integrated Mathematical Thermodynamic Adsorption Model), which combines components from the existing methods described above. The Lennard-

Jones potential energy function is integrated topologically throughout the material with parameter values derived from ab-initio calculations. From thermodynamic considerations the potential energy is then used to split the space within the material into two parts i) the space for which gas molecules are expected to remain in the bulk gas phase and ii) the space for which gas molecules are expected to translate to the adsorbed phase. Finally, the total amount of gas within the adsorbent is calculated from the corresponding equations of state. This enables the immediate prediction of adsorption performance without the need of coding expertise, and the effects from changes in temperature, pressure, cavity size, cavity shape and atomic composition can be readily explored. Additionally, the model is used to predict gas uptake within impregnated metal-organic frameworks and nanotubes in Chapters 7 and 8, respectively.

References

- [1] M. A. DeLuchi, Hydrogen vehicles: An evaluation of fuel storage, performance, safety, environmental impacts, and cost, *Int. J. Hydrogen Energy*, 14 (1989) 81.
- [2] G. D. Berry and S. M. Aceves, Onboard storage alternatives for hydrogen vehicles, *Energy Fuels*, 12 (1998) 49.
- [3] C. Cockroft, Perth's fuel cell bus trial 2004 - 2007: Final operation report to the department for planning and infrastructure, Murdoch University, Perth, 2008.
- [4] Multi-Year Research, Development and Demonstration Plan - Planned Program Activities for 2003-2010: Technical Plan; U.S. Department of Energy; <http://www.eere.energy.gov/hydrogenandfuelcells/mypp/pdfs/storage.pdf>.
- [5] A. C. Dillon and M. J. Heben, Hydrogen storage using carbon adsorbents: past, present and future, *Appl. Phys. A*, 72 (2001) 133.
- [6] T. Ichikawa, S. Isobe, N. Hanada and H. Fujii, Lithium nitride for reversible hydrogen storage, *J. Alloys Compd.*, 365 (2004) 271.
- [7] B. Sakintuna, F. Lamari-Darkrim and M. Hirscher, Metal hydride materials for solid hydrogen storage: A review, *Int. J. Hydrogen Energy*, 32 (2007) 1121.

- [8] O. Khaselev and J. A. Turner, A monolithic photovoltaic-photoelectrochemical device for hydrogen production via water splitting, *Science*, 280 (1998) 425.
- [9] A. T-Raissi and A. Sadhu, Systems study of metal hydride storage requirements, National Renewable Energy Laboratory, Golden, Colorado, 1994.
- [10] S. U. Jeong, R. K. Kim, E. A. Cho, H. J. Kim, S. W. Nam, I. H. Oh, S. A. Hong and S. H. Kim, A study on hydrogen generation from NaBH_4 solution using the high-performance Co-B catalyst, *J. Power Sources*, 144 (2005) 129.
- [11] R. van Noorden, Hydrogen storage targets out of reach, *Chemistry World*, 4 (10), Royal Society of Chemistry, 2007.
- [12] M. K. Thomas, Adsorption and desorption of hydrogen on metal-organic framework materials for storage application: comparison with other nanoporous materials, *Dalton Trans.*, (2009) 1487.
- [13] M. S. Dresselhaus, K. A. Williams and P. C. Eklund, Hydrogen adsorption in carbon materials, *MRS Bull*, 24 (1999) 45.
- [14] J. A. Schwarz, Final report for the tasks XC-1-1108-1 and XAE-3-13346-01, National Renewable Energy Laboratory, Golden, Colorado, 1994.
- [15] A. C. Dillon, K. M. Jones, T. A. Bekkedahl, C. H. Kiang, D. S. Bethune and M. J. Heben, Storage of hydrogen in single-walled carbon nanotubes, *Nature*, 386 (1997) 377.
- [16] J. E. Lennard-Jones, On the determination of molecular fields. II. From the equation of state of a gas, *Proc. R. Soc. A*, 106 (1924) 463.
- [17] P. W. Atkins, *Physical Chemistry*, Oxford University Press, Oxford, 1998.
- [18] B. Panella, M. Hirscher, H. Putter and U. Muller, Hydrogen adsorption in metal-organic frameworks: Cu-MOFs and Zn-MOFs compared, *Adv. Funct. Mater.*, 16 (2006) 520.

- [19] D. H. Everett and J. C. Powl, Adsorption in slit-like and cylindrical micropores in the henry's law region. A model for the microporosity of carbons, *J. Chem. Soc., Faraday Trans. 1*, 72 (1976) 619.
- [20] S. K. Bhatia and A. L. Myers, Optimum conditions for adsorptive storage, *Langmuir*, 22 (2006) 1688.
- [21] H. K. Chae, D. Y. Siberio-Perez, J. Kim, Y. Go, M. Eddaoudi, A. J. Matzger, M. O'Keeffe and O. M. Yaghi, A route to high surface area, porosity and inclusion of large molecules in crystals, *Nature*, 427 (2004) 523.
- [22] H. Furukawa, M. Miller and O. M. Yaghi, Independent verification of the saturation hydrogen uptake in MOF-177 and establishment of a benchmark for hydrogen adsorption in metal-organic frameworks, *J. Mater. Chem.*, 17 (2007) 3197.
- [23] A. L. Myers and P. A. Monson, Adsorption in porous materials at high pressure: Theory and experiment, *Langmuir*, 18 (2002) 10261.
- [24] S. S. Han, J. L. Mendoza-Cortes and W. A. Goddard III, Recent advances on simulation and theory of hydrogen storage in metal-organic frameworks and covalent organic frameworks, *Chem. Soc. Rev.*, 38 (2009) 1460.
- [25] W. Mickelson, S. Aloni, W.-Q. Han, J. Cumings and A. Zettl, Packing C60 in boron nitride nanotubes, *Science*, 300 (2003) 467.
- [26] S. D. M. Brown, G. Dresselhaus and M. S. Dresselhaus, Reversible hydrogen uptake in carbon-based materials, *Materials-Research-Society Symposium on Recent Advances in Catalytic Materials*, Boston, 497 (1997) 157.
- [27] T. Duren, L. Sarkisov, O. M. Yaghi and R. Q. Snurr, Design of new materials for methane storage, *Langmuir*, 20 (2004) 2683.
- [28] H. Frost, T. Duren and R. Q. Snurr, Effects of surface area, free volume, and heat of adsorption on hydrogen uptake in metal-organic frameworks, *J. Phys. Chem. B.*, 110 (2006) 9565.

- [29] H. Frost and R. Q. Snurr, Design requirements for metal-organic frameworks as hydrogen storage materials, *J. Phys. Chem. C.*, 111 (2007) 18794.
- [30] P. Ryan, L. J. Broadbelt and R. Q. Snurr, Is catenation beneficial for hydrogen storage in metal-organic frameworks?, *Chem. Commun.*, (2008) 4132.
- [31] S. S. Han and W. A. Goddard, High H₂ storage of hexagonal metal organic frameworks from first-principles-based grand canonical monte carlo simulations, *J. Phys. Chem. C.*, 112 (2008) 13431.
- [32] S. L. Mayo, B. D. Olafson and W. A. Goddard III, Dreiding: a generic force field for molecular simulations, *J. Phys. Chem.*, 94 (1990) 8897.
- [33] A. K. Rappe, C. J. Casewit, K. S. Colwell, W. A. Goddard and W. M. Skiff, Uff, a full periodic-table force-field for molecular mechanics and molecular-dynamics simulations, *J. Am. Chem. Soc.*, 114 (1992) 10024.
- [34] F. Darkrim and D. Levesque, Monte Carlo simulations of hydrogen adsorption in single-walled carbon nanotubes, *J. Chem. Phys.*, 109 (1998) 4981.
- [35] F. Darkrim and D. Levesque, High adsorptive property of opened carbon nanotubes at 77 K, *J. Phys. Chem. B.*, 104 (2000) 6773.
- [36] F. L. Darkrim, P. Malbrunot and G. P. Tartaglia, Review of hydrogen storage by adsorption in carbon nanotubes, *Int. J. Hydrogen Energy*, 27 (2002) 193.
- [37] Q. Y. Wang and J. K. Johnson, Molecular simulation of hydrogen adsorption in single-walled carbon nanotubes and idealized carbon slit pores, *J. Chem. Phys.*, 110 (1999) 577.
- [38] G. Garberoglio, A. I. Skoulidas and J. K. Johnson, Adsorption of gases in metal organic materials: Comparison of simulations and experiments, *J. Phys. Chem. B.*, 109 (2005) 13094.
- [39] V. V. Simonyan, P. Diep and J. K. Johnson, Molecular simulation of hydrogen adsorption in charged single-walled carbon nanotubes, *J. Chem. Phys.*, 111 (1999) 9778.

- [40] G. Garberoglio, Computer simulation of the adsorption of light gases in covalent organic frameworks, *Langmuir*, 23 (2007) 12154.
- [41] G. Garberoglio and R. Vallauri, Adsorption and diffusion of hydrogen and methane in 2D covalent organic frameworks, *Microporous Mesoporous Mater.*, 116 (2008) 540.
- [42] A. Skoulidas and G. Garberoglio, Computer simulation of hydrogen in metal organic frameworks, *J. Mol. Liq.*, 117 (2005) 43.
- [43] M. P. Allen and D. J. Tildesley, *Computer simulations of liquids*, Clarendon Press, Oxford, 1987.
- [44] D. Frenkel and B. Smit, *Understanding molecular simulation: From algorithms to applications*, Academic Press, San Diego, 2002.
- [45] R. M. Martin, *Electronic structure: Basic theory and practical methods*, Cambridge University Press, Cambridge, 2004.
- [46] P. N. Aukett, N. Quirke, S. Riddiford and S. R. Tennison, Methane adsorption on microporous carbons - A comparison of experiment, theory, and simulation, *Carbon*, 30 (1992) 913.
- [47] P. Dalach, H. Frost, R. Q. Snurr and D. E. Ellis, Enhanced hydrogen uptake and the electronic structure of lithium-doped metal-organic frameworks, *J. Phys. Chem. C.*, 112 (2008) 9278.
- [48] P. A. Gordon and R. B. Saeger, Molecular modeling of adsorptive energy storage: Hydrogen storage in single-walled carbon nanotubes, *Industrial & Engineering Chemistry Research*, 38 (1999) 4647.
- [49] M. Li, Y. Li, Z. Zhou, P. Shen and Z. Chen, Ca-coated boron fullerenes and nanotubes as superior hydrogen storage materials, *Nano Letters*, 9 (2009) 1944.
- [50] Y. Li, Z. Zhou, P. Shen, S. B. Zhang and Z. Chen, Computational studies on hydrogen storage in aluminum nitride nanowires/tubes, *Nanotechnology*, 20 (2009) 215701.

- [51] T. Mueller and G. Ceder, A density functional theory study of hydrogen adsorption in MOF-5, *J. Phys. Chem. B.*, 109 (2005) 17974.
- [52] L. Seung Mi and L. Young Hee, Hydrogen storage in single-walled carbon nanotubes, *Appl. Phys. Lett.*, 76 (2000) 2877.
- [53] Q. Wang, Q. Sun, P. Jena and Y. Kawazoe, Potential of AlN nanostructures as hydrogen storage materials, *ACS Nano*, 3 (2009) 621.
- [54] Q. Yang and C. Zhong, Understanding hydrogen adsorption in metal organic frameworks with open metal sites: A computational study, *J. Phys. Chem. B.*, 110 (2005) 655.
- [55] T. Yildirim, J. Iniguez and S. Ciraci, Molecular and dissociative adsorption of multiple hydrogen molecules on transition metal decorated C60, *Phys. Rev. B: Condens. Matter*, 72 (2005) 153403.
- [56] E. A. Ustinov, Modeling of N2 adsorption in MCM-41 materials: Hexagonal pores versus cylindrical pores, *Langmuir*, 25 (2009) 7450.
- [57] L. Chen, Y. Zhang, N. Koratkar, P. Jena and S. Nayak, First-principles study of interaction of molecular hydrogen with Li-doped carbon nanotube peapod structures, *Phys. Rev. B: Condens. Matter*, 77 (2008) 033405.

List of symbols used in Chapter 5

PE	potential energy
θ	fractional adsorption coverage
p	pressure
T	temperature
N_{tot}	total (absolute) amount of molecules absorbed ($=N_{ex} + N_{bulk}$)
N_{ex}	amount of molecules adsorbed in excess of bulk gas capacity
N_{bulk}	amount of molecules in bulk gas phase
P	probability function for Monte-Carlo steps

E	potential energy calculated for Monte-Carlo steps
\bar{v}	volumetric uptake (mass of gas over volume of adsorbent)
wt. %	gravimetric uptake (mass of gas over system mass)
m_g	mass of gas molecule
V	volume of simulation cell

Chapter 6

Gas adsorption model

6.1 Introduction

In this chapter a novel framework for the prediction of the gas storage capabilities for periodic porous materials is presented. The Topologically Integrated Mathematical Thermodynamic Adsorption Model (TIMTAM) combines surface potential energies with the classic thermodynamics of physisorption in a computationally inexpensive fashion. Experimental results from leading sorbent candidates such as metal-organic frameworks (MOFs), zeolites and carbon nanotubes have been used to verify the model, which closely describes the experimental outcomes. Furthermore, the effect of pore shape upon gas storage characteristics is explored with the TIMTAM routine.

6.2 Gas adsorption model

As a gas molecule approaches a surface, the interactions due to van der Waals forces, which are well described by the Lennard-Jones potential energy function, become dominant. This potential is known in this context as the potential energy for adsorption, found by integrating the atom-atom Lennard-Jones function over the surface. The formulation for the potential energy within three different cavity shapes is given below and further details are found in the references [1, 2].

Slit-shaped cavity:

$$PE_{slit}(\rho) = \pi\eta \left(-\frac{C_6}{2(\rho + d/2)^4} + \frac{C_{12}}{5(\rho + d/2)^{10}} \right) + \pi\eta \left(-\frac{C_6}{2(d/2 - \rho)^4} + \frac{C_{12}}{5(d/2 - \rho)^{10}} \right). \quad (6.1)$$

Cylindrical cavity:

$$PE_{cyl}(\rho) = \eta(-C_6 H_{cyl}[3] + C_{12} H_{cyl}[6])$$

$$H_{cyl}[k] = \frac{2\pi^2 d^2}{(d)^{2k} (2k-2)!} \sum_{j=0}^{\infty} \left(\frac{\rho^j (2k+2j-2)!}{(2d)^j j! (k+j-1)!} \right)^2. \quad (6.2)$$

Spherical cavity:

$$PE_{sph}(\rho) = \eta(-C_6 H_{sph}[6] + C_{12} H_{sph}[12]),$$

$$H_{sph}[k] = \frac{\pi d}{\rho(2-k)} \left(\frac{1}{(\rho + d/2)^{k-2}} - \frac{1}{(\rho - d/2)^{k-2}} \right). \quad (6.3)$$

ρ is the distance of the gas molecule from the cavity center, d represents the cavity size (distance between nuclei) and η is the atomic surface density of the cavity wall. C_6 and C_{12} are the attractive and repulsive constants, respectively, defined as $C_k = 4\varepsilon\sigma^k$ (σ is the kinetic diameter and ε is the well depth). Potential energy maps are shown within each cavity in Figure 6.1. The potential minimum is deepest within cavities with higher curvature where the gas is closer to more surface atoms. Note that this potential is independent of both temperature and pressure. The kinetic energy of the gas in the bulk phase relative to the size of the potential energy for adsorption determines the probability that surface adsorption of a gas molecule will occur at a specified temperature.

Usually the values of the kinetic energy of a gas molecule KE_{gas} and the potential energy for adsorption $PE_{surface}$ are similar and hence there exists a fusion between the adsorbed and bulk phases, as shown in Figure 6.2. Generally speaking, if $KE_{gas} < PE_{surface}$ then surface adsorption occurs. Following this, the probability of adsorption can be derived from the Arrhenius equation which incorporates the average kinetic energy RT , where R is the universal gas constant and T is temperature. The probability that a molecule at a distance ρ from the cavity center will be adsorbed can be expressed as

$$P_{ad}(\rho) = 1 - \exp\left(\frac{-|PE(\rho)|}{RT}\right), \quad (6.4)$$

where $\exp(-|PE|/RT)$ is the probability that $KE_{\text{gas}} > PE_{\text{surface}}$, i.e. the probability that a gas molecule is in the bulk phase. The probability of adsorption is plotted in Figure 6.2 showing the dependence of temperature and distance from the surface.

The total free volume V_f within a cavity is defined here as the volume for which the potential energy is less than zero. In other words, the boundaries for this free volume are located where the potential energy for adsorption is zero at the distance ρ_0 from the center of the cavity in Figure 6.1, and also demonstrated in Figure 6.2 where the volume occupied by the surface is shaded. This total free volume will be the sum of the volume free for adsorption V_{ad} and the volume free for bulk gas V_{bulk} . The volume free for adsorption is found by integrating the probability of adsorption over the total free volume as follows,

$$V_{ad} = \int_{V_f} P_{ad}(\rho) d\rho. \quad (6.5)$$

Similarly, the volume free for bulk gas is calculated as

$$V_{bulk} = \int_{V_f} [1 - P_{ad}(\rho)] d\rho. \quad (6.6)$$

The final step in the model is to calculate the actual number of gas molecules within the total free volume at a certain temperature and pressure. Equations of state are commonly used for this purpose [3-5]. Here an appropriate equation of state is established for the adsorbed phase which is in a similar form to the Dieterici equation of state [4, 6]. The common concept is that the kinetic energy between molecules is reduced due to attractive intermolecular interactions. Dieterici included the interactions between particles in a liquid while here the interactions with the cavity wall are included. This means that the average kinetic energy between molecules is reduced during the transition from the bulk gas phase to the adsorbed phase, allowing molecules to sit closer together and therefore to exist in a denser form. The heat of adsorption is a good measure to describe the amount of energy lost upon adsorption. A reasonable approximation to the heat of adsorption Q is given by Everett and Powl [7] as $Q = |PE_{\min}| + \alpha_1 RT$, where PE_{\min} is the depth of the potential minimum between the gas molecule and the cavity wall, and α_1 (≈ 0.5) is the proportionality constant where $\alpha_1 RT$ is the energy contributed to the adsorbed phase due to the movement of the adsorbed molecules parallel to the cavity surface. Similarly, in this work the heat of adsorption is defined as

$$Q = |\omega PE_{\min} + (1 - \omega) PE_{\text{cent}}| + \alpha_1 RT, \quad (6.7)$$

where ω represents the weighted contribution of the potential minimum PE_{\min} and the potential at the center PE_{cent} of the cavity. Accordingly, the equation of state for the adsorbed phase is expressed as

$$p(V_{ad} / n_{ad} - v_0) = RT \exp(-Q / RT), \quad (6.8)$$

where n_{ad} is the total number of molecules in the adsorbed phase, p is pressure and v_0 is the occupied volume of closely packed gas molecules. n_{ad} is not to be confused with the excess amount N_{ex} used frequently in the literature [8]. N_{ex} is defined as the amount of molecules in excess of the theoretical amount of molecules that the cavity would contain in the bulk gas phase. While n_{ad} is the actual amount of molecules in adsorbed phase.

The total amount of gas molecules in the bulk gas phase n_{bulk} is found by solving the simplified van der Waals equation of state,

$$p(V_{bulk} / n_{bulk} - v_0) = RT. \quad (6.9)$$

After the total amount of molecules are found ($n = n_{ad} + n_{bulk}$), the gravimetric uptake is calculated in the following way,

$$wt.\% = \frac{nm}{(nm + M)} \times 100, \quad (6.10)$$

where m is the mass of a gas molecule and M is the mass of the cavity wall (shown in Figure 6.1). In addition, the volumetric uptake is calculated as,

$$\bar{v} = \frac{nm}{V}, \quad (6.11)$$

where V is the total volume of the cavity including the free volume and occupied volume (shown in Figure 6.1).

Figure 6.2 demonstrates the effect of temperature and pressure from the underlying concepts of the TIMTAM approach. To summarize, the potential energy for adsorption is calculated within the cavity which is used to determine the temperature dependent probability of adsorption throughout the cavity. By integrating the probability of adsorption over the free volume, the volume free for adsorption is found and in the same way, the volume free for bulk phase is also found. Finally, temperature and pressure dependent equations of state are used to determine the quantity of gas molecules in each phase within the cavity.

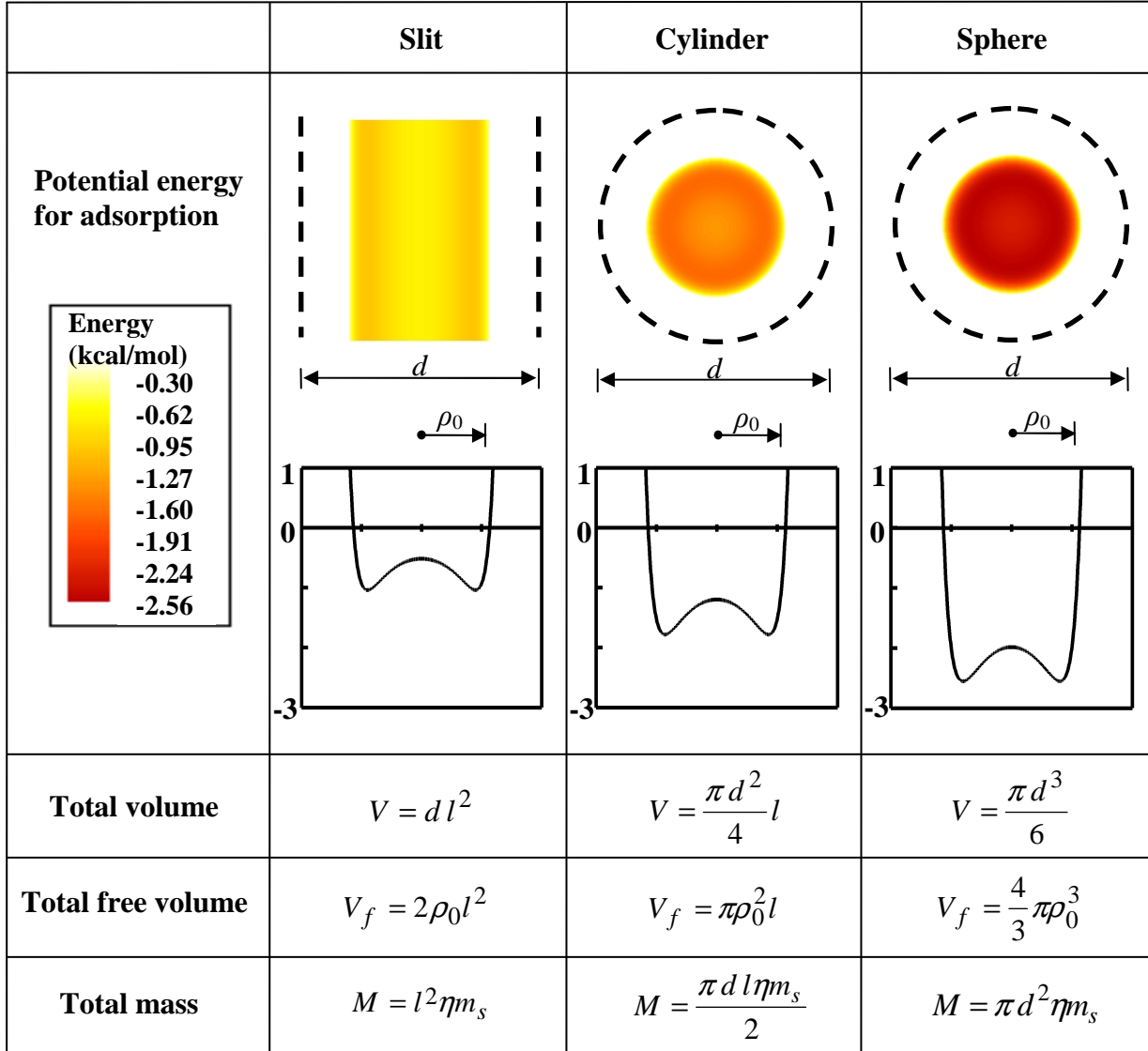


Figure 6.1: Potential energy for adsorption, total volume and free volume within slit-shaped, cylindrical and spherical cavities. l is the arbitrary length of a section of cavity and m_s is the molecular mass of the surface atoms.

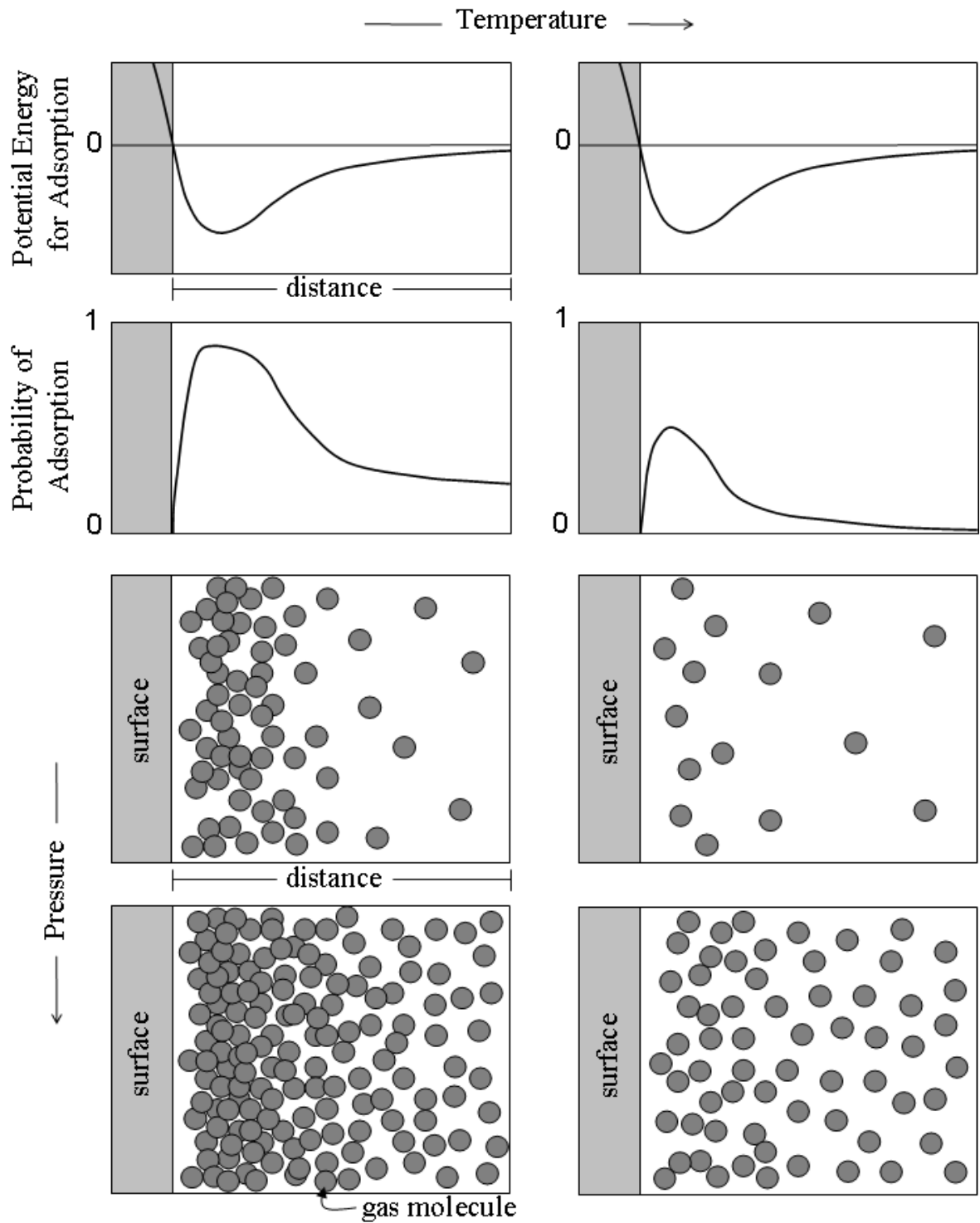


Figure 6.2: Schematic illustration of the new adsorption model, TIMTAM, using the potential energy for adsorption to determine the probability of adsorption resulting in the overall uptake at certain temperature and pressure.

6.3 Comparison with experimental results

To demonstrate the TIMTAM capacity to accurately predict adsorption performance within a range of porous absorbents the following results are reproduced: MD simulations for hydrogen uptake within carbon slits and carbon nanotubes by Rzepka et al. [5], experimental results for methane uptake in carbon slits by Aukett et al. [9], MD simulations for hydrogen uptake within Metal-Organic Frameworks (MOFs) by Ryan et al. [10], and experimental results for hydrogen uptake within MOFs by Kaye et al. [11].

Comparison with existing simulation results is a good test of the model since more often than not all the variables are known, as opposed to experimental results which are difficult experiments to perform accurately. Rzepka et al. [5] have simulated the gravimetric and volumetric hydrogen uptake in carbon slits and carbon nanotubes of various sizes d at various pressures and temperatures. Here the same parameter values are used, listed in Table 6.1. Further, the TIMTAM formulation is found to provide a good fit with $\omega = 0.8$ and $\alpha_1 = 0.16$. This means that the potential minimum is a stronger factor contributing to the energy in the adsorbed phase and there is little movement of the adsorbed molecules parallel to the surface. Figure 6.3 and Figure 6.4 show excellent fits of the model with the simulation results for gravimetric and volumetric uptake for slits and nanotubes. Despite the simplicity, it is clear that the model captures the essential characteristics of the simulation results.

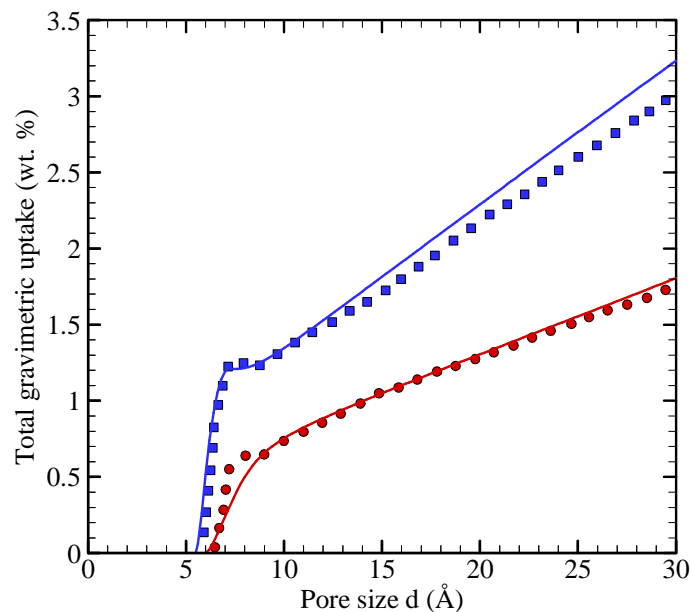


Figure 6.3 (continued to next page)

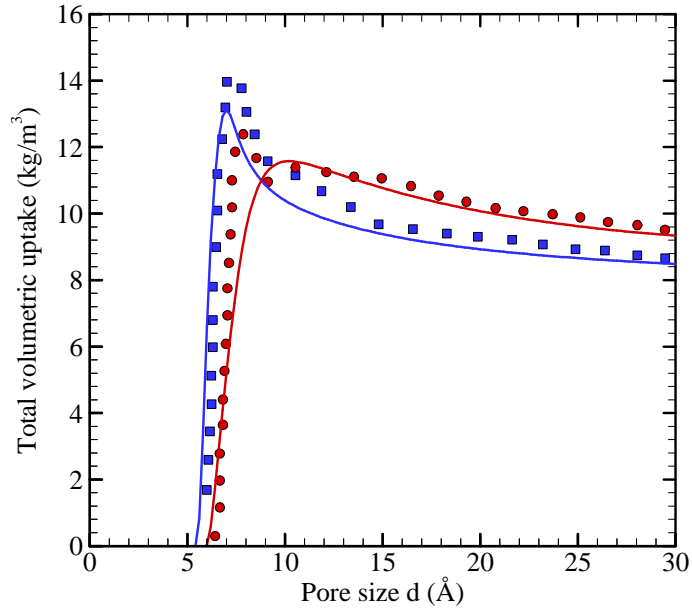


Figure 6.3: TIMTAM fit (solid lines) to simulation results for hydrogen gravimetric (above) and volumetric (below) uptake within carbon slits (blue squares) and carbon nanotubes (red circles) of different pore sizes d at 300 K and 98.7 atm, data from Rzepka et al. [5].

Rzepka et al. [5] noted that the small peaks in the uptake correspond to pores in which an individual hydrogen molecule can just fit. Since the model utilizes a continuum perspective it is difficult to mimic the uptake of an individual molecule accurately. However, the pore size for this situation is very close to the pore size in which the potential is at a minimum and therefore the model is often capable of mimicking the peak uptake especially within the slit-shaped cavities, see Figure 6.3.

The model also reproduced the experimental methane uptake within activated carbon AX21 which is believed to contain slit-shaped pores with an average size d of 22 Å, see Figure 6.5. An excellent fit is observed and the parameter values are listed in Table 6.1.

Since the leading hydrogen storage materials are the MOFs it is important that the model is capable of describing their uptake performance. Here the isorecticular MOF-1 (IRMOF-1) composed of a cubic grid structure is approximated by a composition of spherical cavities. The framework atoms zinc, oxygen, carbon and hydrogen, denoted by the subscripts $i = 1, 2, 3$ and 4, are assumed to be evenly distributed on the surface of the spherical cavity at radii $d/2$. Therefore the potential energy for adsorption within the cavity can be estimated as

$$PE_{MOF}(\rho) = \sum_{i=1}^4 PE_{sph,i}(\rho), \quad (6.12)$$

where the parameters in Equation 5.3 are given by $\eta = \sum_{i=1}^4 \eta_i$ and $C_k = \sum_{i=1}^4 C_i^k$. The

Lennard-Jones parameter values are taken from the Dreiding force field calculations [12] and listed in Table 6.1 along with all the other parameter values used. The cavity size d for the MOF is found from fits to the simulation and experimental results. However, a good approximation for the cavity radius is $d/2 = \sqrt{6} d^*/4$, where d^* is the diameter of the largest van der Waals sphere inside the cavity, as determined by Eddaoudi et al. [13] for each MOF in the series IRMOF- n ($n = 1..16$). Despite the geometrical approximation the TIMTAM results agree well with the simulation and experimental results, see Figure 6.6.

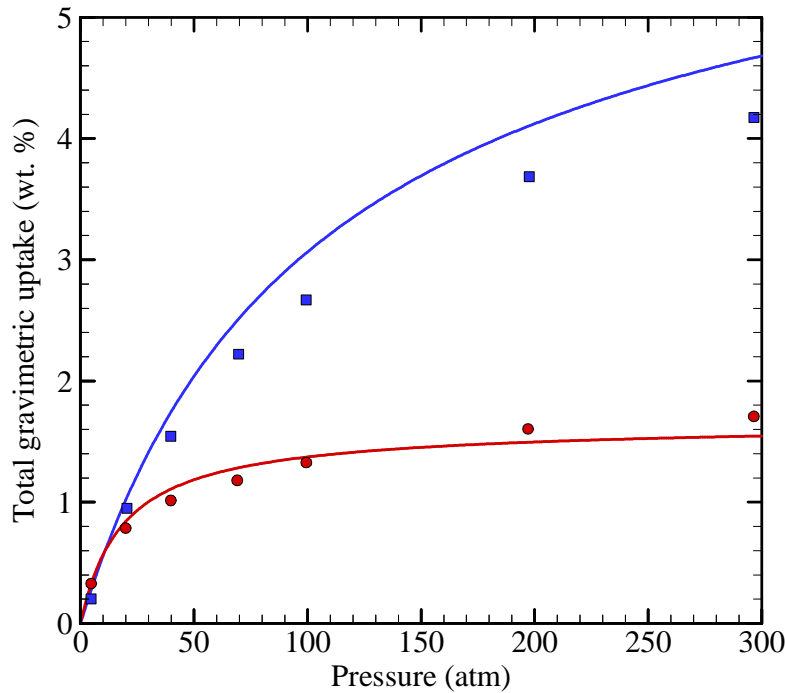


Figure 6.4 (continued to next page)

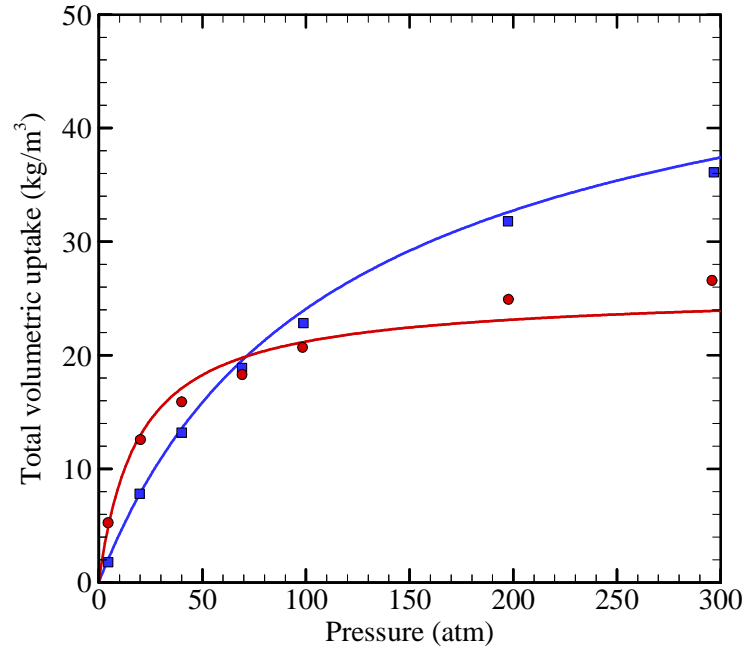


Figure 6.4: TIMTAM fit (solid lines) to simulation results for hydrogen gravimetric (above) and volumetric (below) uptake within carbon slits (blue squares) and carbon nanotubes (red circles) of pore size 10 \AA at different pressures and 200 K, data from Rzepka et al. [5].

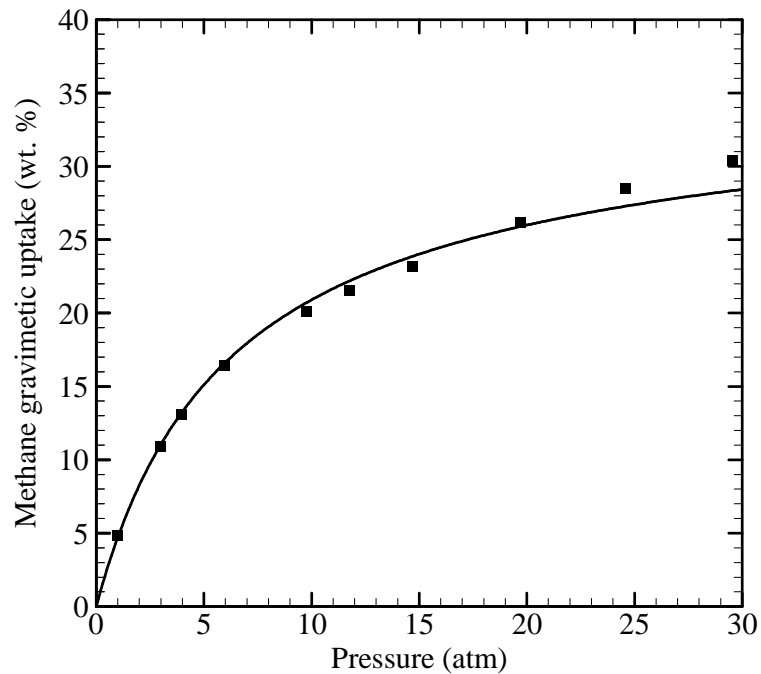


Figure 6.5: TIMTAM fit (solid black line) to experimental methane uptake (black squares) [9] within activated carbon AX21 with an average slit-shaped pore size of 22 \AA .

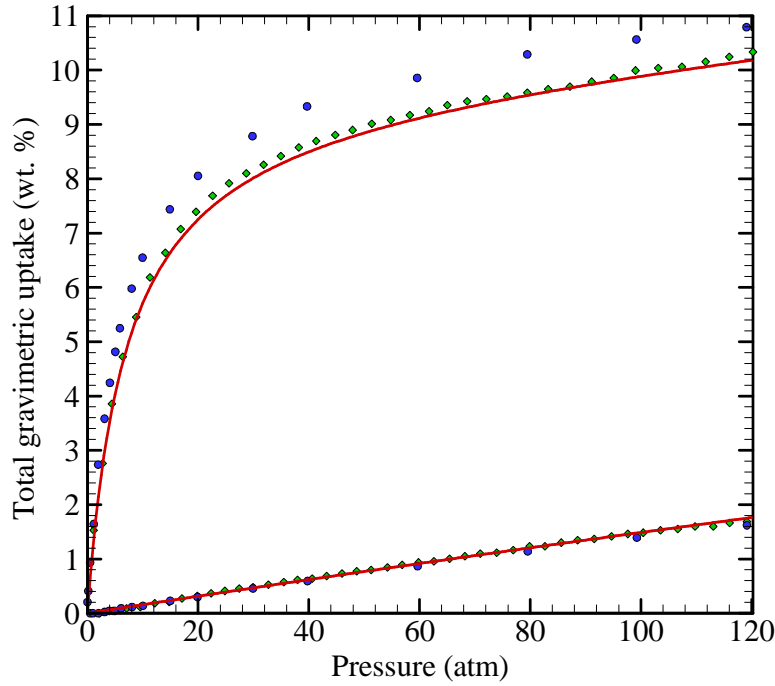


Figure 6.6: TIMTAM fit (solid red lines) of total hydrogen uptake to experimental results (green diamonds) [11] and simulation results (blue circles) [10] for IRMOF-1 at 77 (upper curve) and 298 (lower curve) K.

Table 6.1: Parameter values used to reproduce the data from the literature. Additionally, the occupied volume of compressed hydrogen $v_0 = 0.0156$ L/mol and of methane $v_0 = 0.043$ L/mol (calculated from critical parameters).

Data from literature	Gas-adsorbent	Kinetic diameter σ (Å)	Well depth ϵ/k_B (K)	Surface density η (No. / Å ²)	ω	α_1
Hydrogen uptake Carbon nanotubes and carbon slits Rzepka et al. [5]	H ₂ -C:	3.19	30.5	0.382	0.80	0.16
Methane uptake Carbon slits Aukett et al. [9]	CH ₄ -C:	3.64	84.19	0.382	0.55	0.22
Hydrogen uptake IRMOF-1 Kaye et al. [11]	H ₂ -C:	3.22	41.90	0.064	1	0.90
	H ₂ -O:	3.00	42.05	0.070		
	H ₂ -H:	2.91	16.76	0.032		
	H ₂ -Zn:	3.50	31.89	0.021		

6.4 Predictions of the model

An advantage of the TIMTAM approach is that it provides a way of exploring the numerical landscape of factors controlling adsorption. Pore size, free volume, system mass, heat of adsorption, temperature and pressure all play a crucial role in determining gas storage outcomes. Figure 6.7 demonstrates the effect of pressure within carbon slits, tubes and spheres of dimension 10 \AA and at temperature 243 K . The same parameter values used by Rzepka et al. [5] are used here. An important note is that the cavity shape with the highest hydrogen uptake depends on the pressure which means that the appropriate cavity shape is to be chosen according to the known operating pressure. This observation is more noticeable from the volumetric uptake. Frost et al. [14] provide an explanation for this in that at low pressures the heat of adsorption is the dominant factor while at higher pressures the free volume becomes the dominant factor. The heat of adsorption is greatest in spherical cavities and lowest in slit-shaped cavities, while free volume is greatest in slit-shaped cavities and lowest in spherical cavities. Therefore the observation is a result of the shifting trade off between the heat of adsorption and free volume at various pressures.

As there are many possible combinations of temperature, pressure and pore size, Figure 6.8 and Figure 6.9 show the gravimetric and volumetric uptake within carbon slits, tubes and spheres of varying pore sizes at four distinct pressures and temperatures. Slit-shaped cavities outperform the other shaped cavities in gravimetric uptake due mainly to the higher volume to mass ratio. However, the cavity shape delivering the highest volumetric uptake depends on cavity size, temperature and pressure. At small pore sizes the gas uptake is restricted by the free volume available in each cavity shape. At large pore sizes the volumetric uptake tends toward that of compressed gas (no adsorbent), slit-shaped cavities approach this limit first followed by cylindrical cavities and spherical cavities. This is because the pore surfaces with higher curvature (higher heat of adsorption) cause denser adsorption layers to form along the surface which keeps the uptake higher than that of compressed gas until pores become larger where curvature decreases and the ratio of surface adsorption to bulk gas decreases.

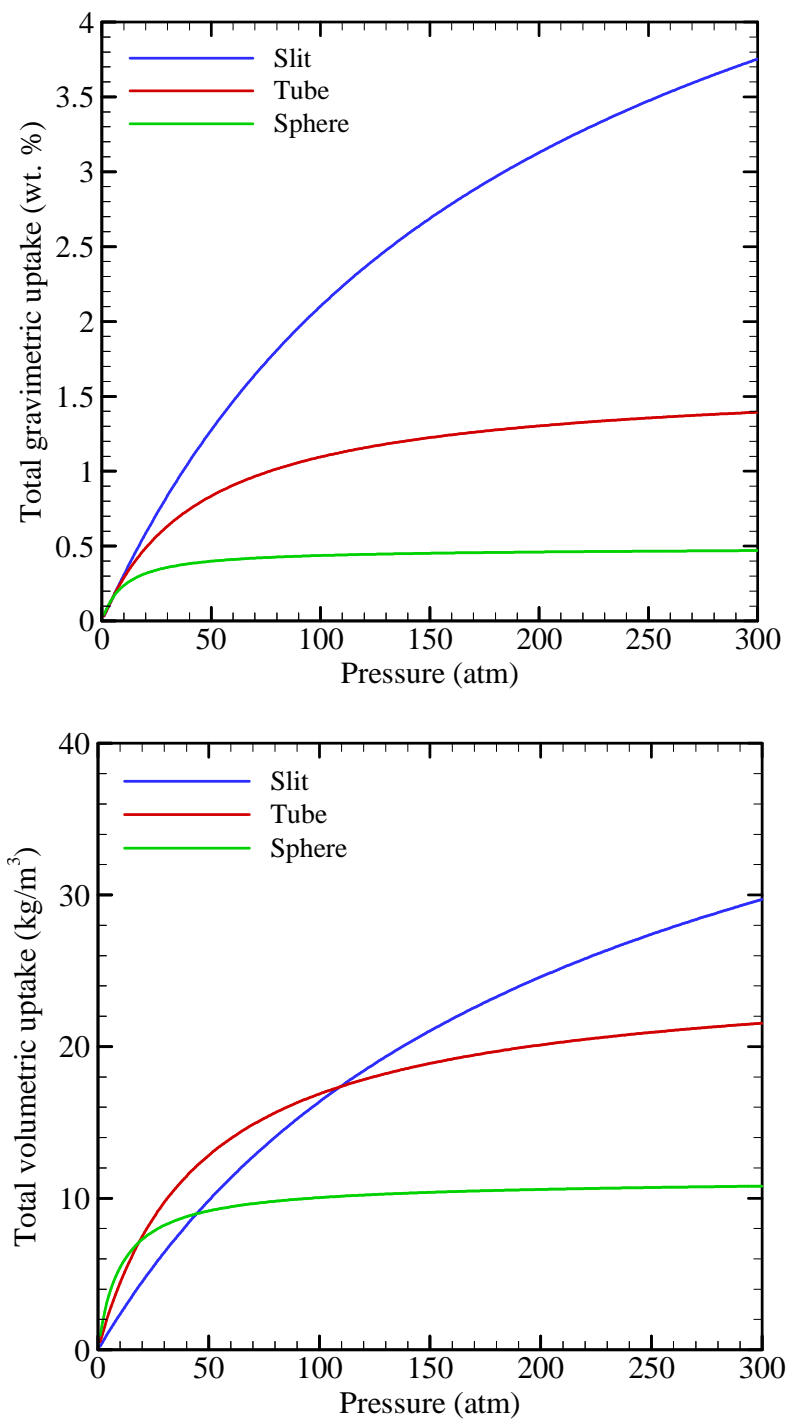


Figure 6.7: TIMTAM results for total hydrogen gravimetric (above) and volumetric (below) uptake within carbon slits (blue lines), tubes (red lines) and spheres (green lines) with dimension 10 \AA and at temperature 243 K .

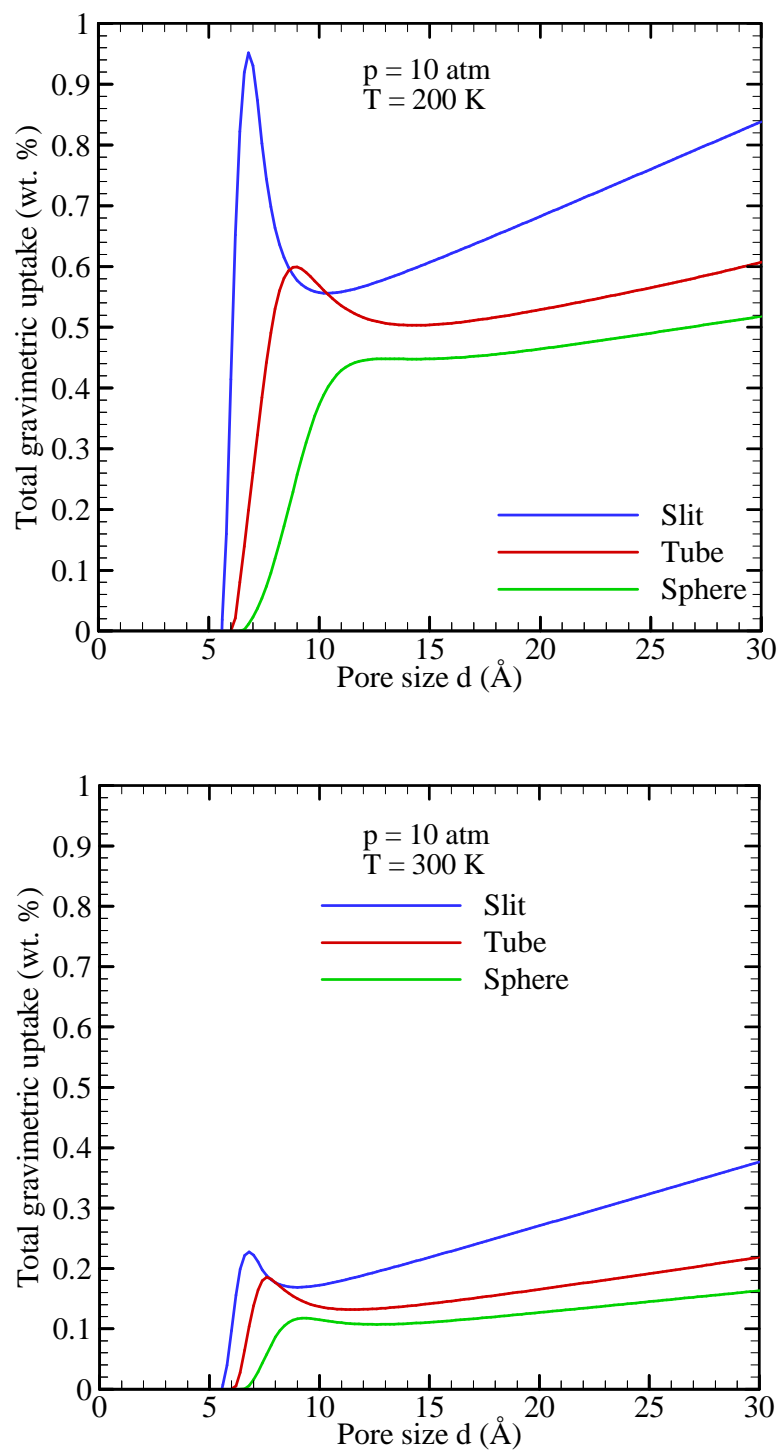


Figure 6.8 (continued to next page)

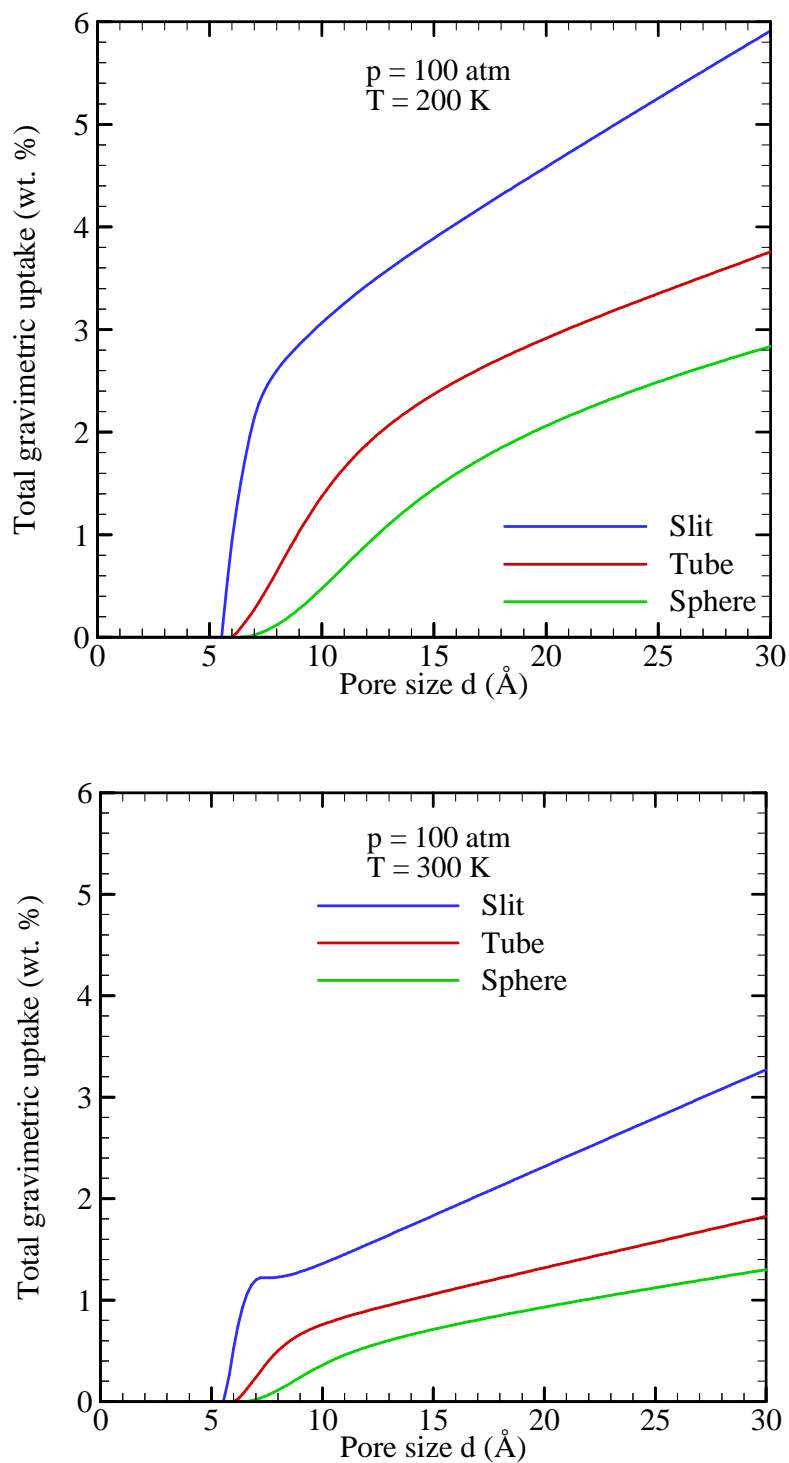


Figure 6.8: TIMTAM results for total gravimetric hydrogen uptake within carbon slits (blue lines), tubes (red lines) and spheres (green lines) with varying pore sizes at four distinct pressures and temperatures.

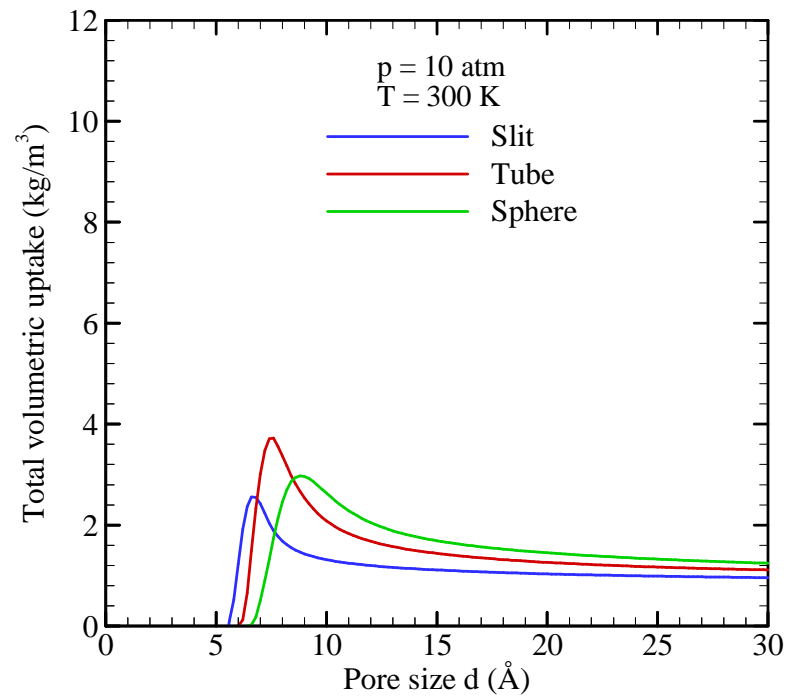
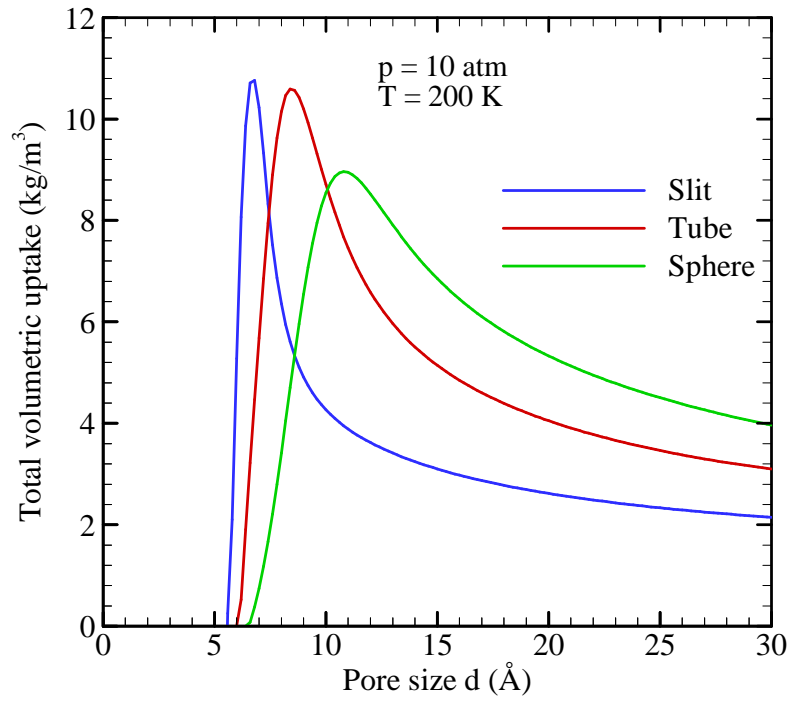


Figure 6.9 (continued to next page)

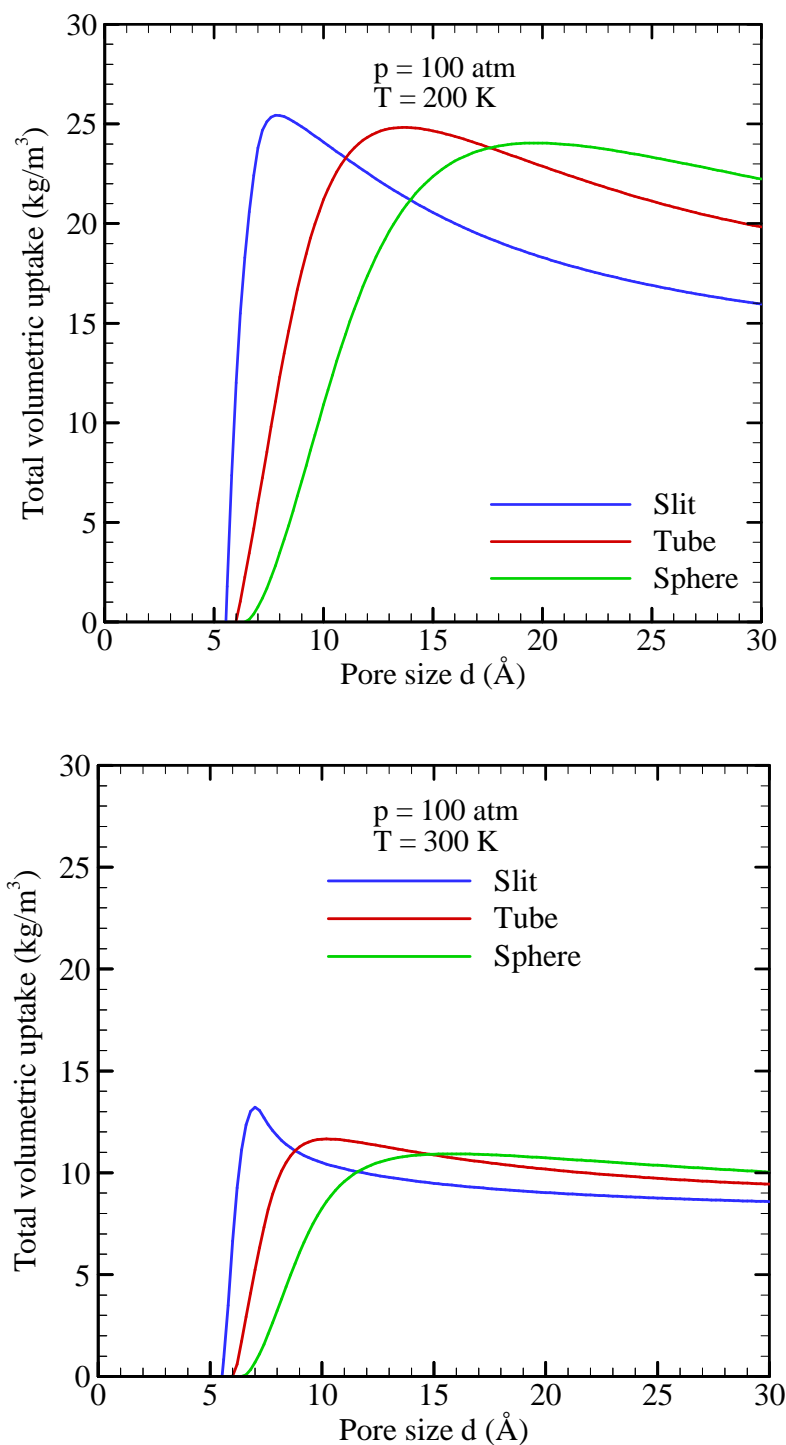


Figure 6.9: TIMTAM results for total volumetric hydrogen uptake within carbon slits (blue lines), tubes (red lines) and spheres (green lines) with varying pore sizes at four distinct pressures and temperatures.

Overall TIMTAM encompasses many characteristics observed in the gas adsorption phenomenon including the following: The amount of molecules in adsorbed and bulk gas phase increases with decreasing temperature and increasing pressure; The amount of

molecules in adsorbed phase increases with increasing heat of adsorption; Heat of adsorption is proportional to the magnitude of potential energy for adsorption which increases with increasing surface curvature and increasing well depth of surface atoms, and is maximum at a critical pore size; Gravimetric uptake increases with decreasing surface mass. Therefore, the TIMTAM approach is an excellent tool to guide the material design for gas storage applications.

6.5 Conclusion

The TIMTAM formulation is established for predicting gas storage within slit-shaped, cylindrical and spherical cavities, and is found to agree with available simulation and experimental data. The transparency of the model provides insight into the adsorption phenomenon and allows the analysis of each critical factor governing storage performance. Here the effects of pore size, free volume, heat of adsorption, system mass, pressure and temperature are investigated, offering the guidelines for tailoring absorbent materials for desired gas storage applications.

Further extensions of the model may include the potential of neighbouring gas molecules causing the total potential to be dependent on number of molecules. Differently shaped cavities may be investigated via TIMTAM by numerically integrating the potential throughout the cavity.

References

- [1] B. J. Cox, N. Thamwattana and J. M. Hill, Orientation of spheroidal fullerenes inside carbon nanotubes with potential applications as memory devices in nano-computing, *J. Phys. A: Math. Theor.*, 41 (2008) 27.
- [2] T. A. Hilder and J. M. Hill, Continuous versus discrete for interacting carbon nanostructures, *J. Phys. A: Math. Theor.*, 40 (2007) 3851.
- [3] A. L. Myers, Equation of state for adsorption of gases and their mixtures in porous materials, *Adsorpt.-J. Int. Adsorpt. Soc.*, 9 (2003) 9.
- [4] R. J. Sadus, Equations of state for fluids: The Dieterici approach revisited, *J. Chem. Phys.*, 115 (2001) 1460.

- [5] M. Rzepka, P. Lamp and M. Casa-Lillo, Physisorption of hydrogen on microporous carbon and carbon nanotubes, *J. Phys. Chem. B.*, 102 (1998) 10894.
- [6] C. Dieterici, *Anns. Phys. Chem. Wiedemanns Ann.*, 69 (1899) 685.
- [7] D. H. Everett and J. C. Powl, Adsorption in slit-like and cylindrical micropores in the henry's law region. A model for the microporosity of carbons, *J. Chem. Soc., Faraday Trans. 1*, 72 (1976) 619.
- [8] H. Furukawa, M. Miller and O. M. Yaghi, Independent verification of the saturation hydrogen uptake in MOF-177 and establishment of a benchmark for hydrogen adsorption in metal-organic frameworks, *J. Mater. Chem.*, 17 (2007) 3197.
- [9] P. N. Aukett, N. Quirke, S. Riddiford and S. R. Tennison, Methane adsorption on microporous carbons - A comparison of experiment, theory, and simulation, *Carbon*, 30 (1992) 913.
- [10] P. Ryan, L. J. Broadbelt and R. Q. Snurr, Is catenation beneficial for hydrogen storage in metal-organic frameworks?, *Chem. Commun.*, (2008) 4132.
- [11] S. S. Kaye, A. Dailly, O. M. Yaghi and J. R. Long, Impact of preparation and handling on the hydrogen storage properties of $\text{Zn}_4\text{O}(\text{1,4-benzenedicarboxylate})_3$ (MOF-5), *J. Am. Chem. Soc.*, 129 (2007) 14176.
- [12] S. L. Mayo, B. D. Olafson and W. A. Goddard III, Dreiding: a generic force field for molecular simulations, *J. Phys. Chem.*, 94 (1990) 8897.
- [13] M. Eddaoudi, J. Kim, N. Rosi, D. Vodak, J. Wachter, M. O'Keeffe and O. M. Yaghi, Systematic design of pore size and functionality in isorecticular MOFs and their application in methane storage, *Science*, 295 (2002) 469.
- [14] H. Frost, T. Duren and R. Q. Snurr, Effects of surface area, free volume, and heat of adsorption on hydrogen uptake in metal-organic frameworks, *J. Phys. Chem. B.*, 110 (2006) 9565.

List of symbols used in Chapter 6

PE	potential energy
ρ	distance from center of pore
C_6, C_{12}	attractive and repulsive Lennard-Jones constants ($C_k = 4\epsilon\sigma^k$)
σ	kinetic diameter
ϵ	well depth
η	atomic surface density
d	pore size (between surface nuclei)
KE	kinetic energy of gas molecule
T	temperature
R	universal gas constant
P_{ad}	probability of molecule in adsorbed phase
P_{bulk}	probability of molecule in bulk gas phase
V_{ad}	volume free for adsorption
V_{bulk}	volume free for bulk gas
V_f	free volume within adsorbent ($=V_{ad} + V_{bulk}$)
Q	heat of adsorption
ω	weight fraction
p	pressure
v_0	occupied volume of closely packed gas molecules
n_{ad}	number of molecules in adsorbed phase
n_{bulk}	number of molecules in bulk gas phase
n	total number of molecule stored ($= n_{ad} + n_{bulk}$)
m	mass of individual gas molecule
M	mass of adsorbent

m_s	mass of individual surface elements
d^*	diameter of metal-organic framework estimated by Eddaoudi et al.
l	arbitrary pore length
V	total volume of unit cell
ρ_0	position at which $PE = 0$
\bar{v}	volumetric uptake (mass of gas over volume of adsorbent)
wt. %	gravimetric uptake (mass of gas over system mass)

Chapter 7

Impregnated metal-organic frameworks

7.1 Introduction

In this chapter the adsorption model outlined in Chapter 6 is used to analyze a new concept for methane and hydrogen storage materials involving the incorporation of magnesium-decorated fullerenes within Metal-Organic Frameworks (MOFs), see Figure 7.1. Impregnation of MOF pores with magnesium-decorated fullerenes, denoted as Mg-C₆₀ @ MOF, places exposed metal sites with high heats of adsorption into intimate contact with large surface area MOF structures. Perhaps surprisingly, given the void space occupied by C₆₀, this impregnation delivers remarkable gas uptake, according to the model, which predicts exceptional performance for the Mg-C₆₀ @ MOF family of materials. These predictions include a volumetric methane uptake of 265 v/v, the highest reported value for any material, which significantly exceeds the US Department of Energy (DoE) target of 180 v/v. The model also predicts a very high hydrogen adsorption enthalpy of 11 kJ/mol with relatively little decrease as a function of H₂ filling. This value is close to the calculated optimum value of 15.1 kJ/mol, and is achieved concurrently with saturation hydrogen uptake in large amounts at pressures under 10 atm.

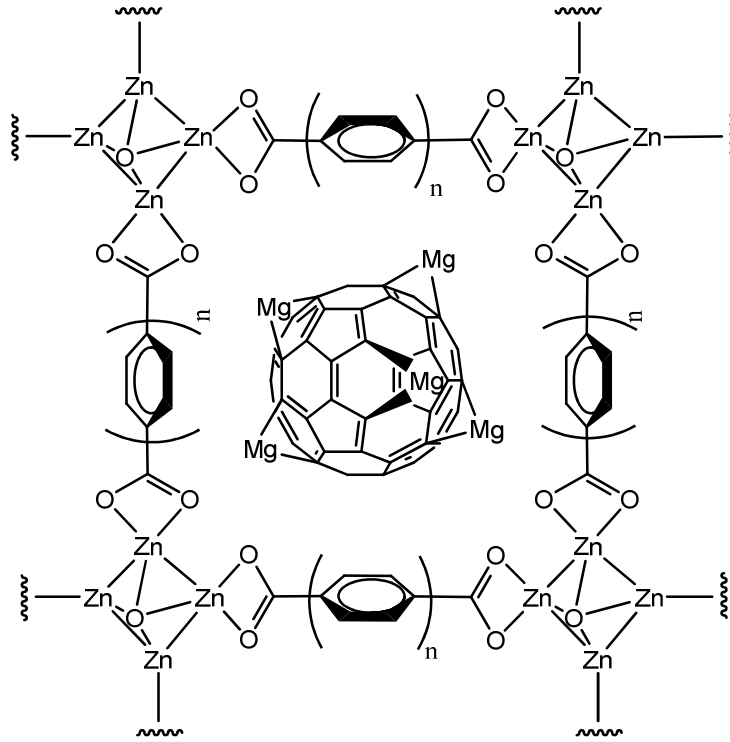


Figure 7.1: Schematic representation for the recently proposed material $\text{Mg-C}_{60} @ \text{MOF}$ showing a MOF cavity impregnated with magnesium decorated C_{60} .

7.2 Method

The MOF cavity structure is approximated to enable the development of a potential energy function, which is then used to predict various important adsorption results such as the average potential energy for adsorption, volume free for adsorption, heat of adsorption and adsorbate (gas) uptake. A similar approach has been used previously to explore the optimization of porosity and chemistry for material performance, including successful determination of the adsorption of fullerenes onto the inside wall of carbon nanotubes [1] and the gas separation regimes within cylindrical pore channels [2, 3].

The TIMTAM approach taken here is an approximation which begins by assuming that the iso-reticular MOF (IRMOF) structure is composed of spherically shaped cavities such that the cavity surface, defined at radius r_1 , consists of the framework atoms, namely zinc, oxygen, carbon and hydrogen indexed as $i = 1, 2, 3, 4$, respectively. These atoms are averaged over the cavity surface creating a homogeneous layer onto which a gas molecule can adsorb. This approximation enables the development of a potential energy function between a gas molecule and the cavity surface based on the 6-12 Lennard-Jones potential assuming a spherical geometry,

$$PE_{MOF}(\rho) = \sum_{i=1}^4 (-E_{6,i} + E_{12,i}), \quad (7.1)$$

$$E_{k,i} = \frac{2C_{k,i}\eta_i\pi r_l}{\rho(2-k)} \left(\frac{1}{(\rho+r_l)^{k-2}} - \frac{1}{(\rho-r_l)^{k-2}} \right), \quad (7.2)$$

where $C_{k,i} = 4\varepsilon_i\sigma_i^k$; ε_i and σ_i are the well depth and the kinetic diameter, respectively, found by using the Berthelot-Lorentz mixing rules between the gas molecule and atom i on the cavity surface. Further, η_i is the atomic surface density of atom i within the cavity surface at radius r_l (see Figure 7.3), and ρ is the distance between the gas molecule and the center of the cavity. Dreiding [4] force field values are used for the framework atoms and experimentally determined values are used for hydrogen [5] and methane [6], found in Table 7.1.

The effect of the insertion of decorated C_{60} fullerenes into the MOF cavity can be studied by including the potential energy of the interaction between the gas molecule and the surface of the fullerene. The interaction between an atom and a fullerene has been formulated by Cox et al. [7]. Here this formulation is extended to consider fullerenes which are functionalized with magnesium atoms, where functionalization is by 10 magnesium atoms, which is equal to the number of phenanthrene subunit bridging sites. The van der Waals interaction energy becomes

$$PE_{Mg_{10}C_{60}}(\rho) = \sum_{j=1}^2 (-E_{6,j} + E_{12,j}) \quad (7.3)$$

$$E_{k,j} = \frac{2C_{k,j}\eta_j\pi b}{\rho(2-k)} \left(\frac{1}{(\rho+b)^{k-2}} - \frac{1}{(\rho-b)^{k-2}} \right), \quad (7.4)$$

where $C_{n,j} = 4\varepsilon_j\sigma_j^n$, b is the radius of a fullerene and here $j = 1,2$ represents carbon and magnesium, respectively. By assuming that the fullerene is located in the center of the cavity a combination of both expressions ($PE(\rho) = PE_{MOF}(\rho) + PE_{Mg_{10}C_{60}}(\rho)$) enables a prediction of the potential energy distribution throughout the cavity. For undecorated fullerenes the terms corresponding to $j = 2$ are simply omitted.

The framework surface atomic densities for carbon and hydrogen in the series of IRMOF-n structures are approximately constant since the number of ligand atoms increases with increasing cavity radius. The number of zinc and oxygen atoms remains constant in the IRMOF-n structures and therefore surface atomic densities depend on

cavity radius, as shown in Table 7.2. Fullerene properties are listed in Table 7.3. Each cavity is formed by 8 vertices of zinc and oxygen, and 12 ligands of carbon and hydrogen. Taking into account that each vertex connects with 8 cavities and each ligand connects with 4 cavities, an average molecular mass per cavity can be found, given in Table 7.4.

In reality the fullerenes will be randomly but evenly distributed throughout the porous network as demonstrated in recent molecular simulation work [8]. It is most likely that the fullerene is to assume a position close to the cavity wall, rather than centrally located as shown in Figure 7.3. However, as can be seen from Figure 7.2, the actual hydrogen uptake as calculated from assuming a central location is a very close approximation to that of an offset fullerene.

Table 7.1: Lennard-Jones parameter values for framework atoms from Dreiding [4] and gas molecules from experiments. [5, 6]

Adsorbate / Adsorbent	Kinetic diameter $\sigma(\text{\AA})$	Well depth $\varepsilon/k_B(\text{K})$
C	3.47	47.86
O	3.03	48.19
H	2.85	7.65
Zn	4.04	27.70
Mg ^a	4.36	156.00
H ₂	2.96	36.70
CH ₄	3.73	148.00

^a Dreiding force field values for aluminum are used here for magnesium, suggested by Aicken et al. [9].

Table 7.2: Cavity atomic surface density.

Framework atom	Atomic density of cavity wall $\eta_{\text{adsorbent}} (\text{no. atoms} / \text{\AA}^2)$
C	no. C atoms / $4\pi r_l^2 \approx 0.089$
H	no. H atoms / $4\pi r_l^2 \approx 0.045$
Zn	$32 / 4\pi r_l^2$
O	$104 / 4\pi r_l^2$

Table 7.3: Fullerene properties.

Properties	Values
C ₆₀ radius	3.55 \AA
C ₆₀ mass	720.64 g/mol
Mg ₁₀ -C ₆₀ mass	960.69 g/mol
C ₆₀ surface density	0.379 (no. C atoms / \AA ²)
Mg ₁₀ -C ₆₀ surface density	0.063 (no. Mg atoms / \AA ²)

Table 7.4: Adsorbent molecular mass per cavity and adsorbate molecular mass.

Adsorbent / Adsorbate	Molecular mass (g mol^{-1})
IRMOF-1	769.79
IRMOF-8	920.04
IRMOF-10	998.15
IRMOF-16	1226.44
IRMOF-n	$\approx 1.35\pi r_1^2 + 469.51$
C_{60} @ IRMOF-n	$\approx 1.35\pi r_1^2 + 1190.15$
$\text{Mg}_{10}\text{-C}_{60}$ @ IRMOF-n	$\approx 1.35\pi r_1^2 + 1433.20$
H_2	2.02
CH_4	16.04

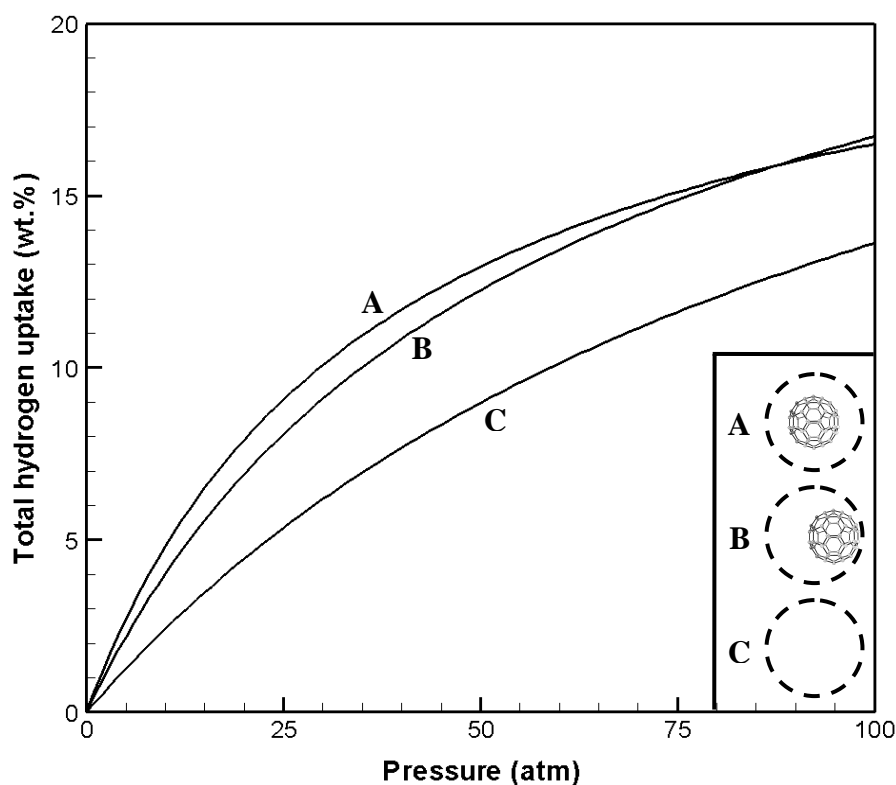


Figure 7.2: Comparison of total hydrogen uptake predictions inside a hypothetical carbon sphere with radius 12 \AA at 77 K . Inset displays the three cases: A) Centered C_{60} , B) Offset C_{60} , and C) Empty cavity.

If the kinetic energy of the gas molecule, $|KE_{\text{gas}}|$, is less than the potential energy of the interaction between the gas molecule and the framework, $|PE_{\text{MOF}}|$, then the gas molecule will be adsorbed. Conversely, if $|KE_{\text{gas}}| > |PE_{\text{MOF}}|$ the gas molecule will remain in the bulk phase. Hence the probability of the molecule remaining as bulk gas is given by $\exp[-|PE|/RT]$ and the probability of the gas molecule adsorbing is given by

$1 - \exp[-|PE|/RT]$. The cavity free volume may then be split into two: the volume in which gas molecules are adsorbed:

$$V_{ad} = \int_{\rho_0}^{\rho_1} 4\pi\rho^2 (1 - \exp[-|PE(\rho)|/RT]) d\rho, \quad (7.5)$$

And that in which they remain as bulk gas:

$$V_{bulk} = \int_{\rho_0}^{\rho_1} 4\pi\rho^2 (\exp[-|PE(\rho)|/RT]) d\rho, \quad (7.6)$$

where R is the universal gas constant and T is temperature. There are various ways of defining the total cavity free volume and here it is defined as the total space within the cavity for which the potential energy is negative. The radial boundaries of this space are indicated by ρ_0 and ρ_1 in Figure 7.3 and Figure 7.6A, where ρ_0 is equal to zero in the absence of a fullerene. An alternative definition of the total cavity free volume could be the total space within the cavity for which the potential energy is less than the average kinetic energy of the bulk gas phase RT . In this case ρ_0 and ρ_1 would be temperature dependent satisfying $PE(\rho_0) = PE(\rho_1) = RT$. In this work the former definition is used where ρ_0 and ρ_1 are independent of temperature, however, calculations show that the latter definition determines a total cavity free volume increase of 3.5 % at a temperature of 298 K, although, this only results in a hydrogen uptake increase of 0.01 wt. %. Note that the total cavity free volume is equal to the sum of the volume free for adsorption and the volume free for bulk gas ($V_f = V_{ad} + V_{bulk}$). It is believed that these expressions are crucial to determining adsorption performance, since the adsorbate is stored more densely in the adsorbed state than in the bulk gas state. The adsorbate uptake is derived by combining the volume free for adsorption and that for non-adsorption, or bulk gas, with the appropriate corresponding equations of state. The simplified van der Waals equation of state is used for determining the number of molecules n_{bulk} in the bulk gas state,

$$p(V_{bulk} / n_{bulk} - v_0) = RT, \quad (7.7)$$

where p is the pressure and v_0 is the occupied volume of densely packed gas molecules calculated from critical parameters. The equation of state used to find the number of molecules in the adsorbed state n_{ad} is a modified version of the Dieterici equation of state [10],

$$p(V_{ad} / n_{ad} - v_0) = RT\alpha \exp\left[-|\overline{PE}| / RT\right], \quad (7.8)$$

where \overline{PE} is the average potential energy for adsorption and α is an empirical constant. The average potential energy for adsorption is calculated by integrating the potential energy function $PE(\rho)$ over the total cavity free volume. This equation of state allows the kinetic energy between the adsorbate molecules to decrease as the adsorption energy increases. The total uptake can be calculated as the weight percentage in the following way,

$$wt.\% = \frac{nm}{nm + M} \times 100, \quad (7.9)$$

where n is the total number of molecules within the cavity ($= n_{ad} + n_{bulk}$), m is the mass of a gas molecule and M is the mass of the adsorbent per cavity.

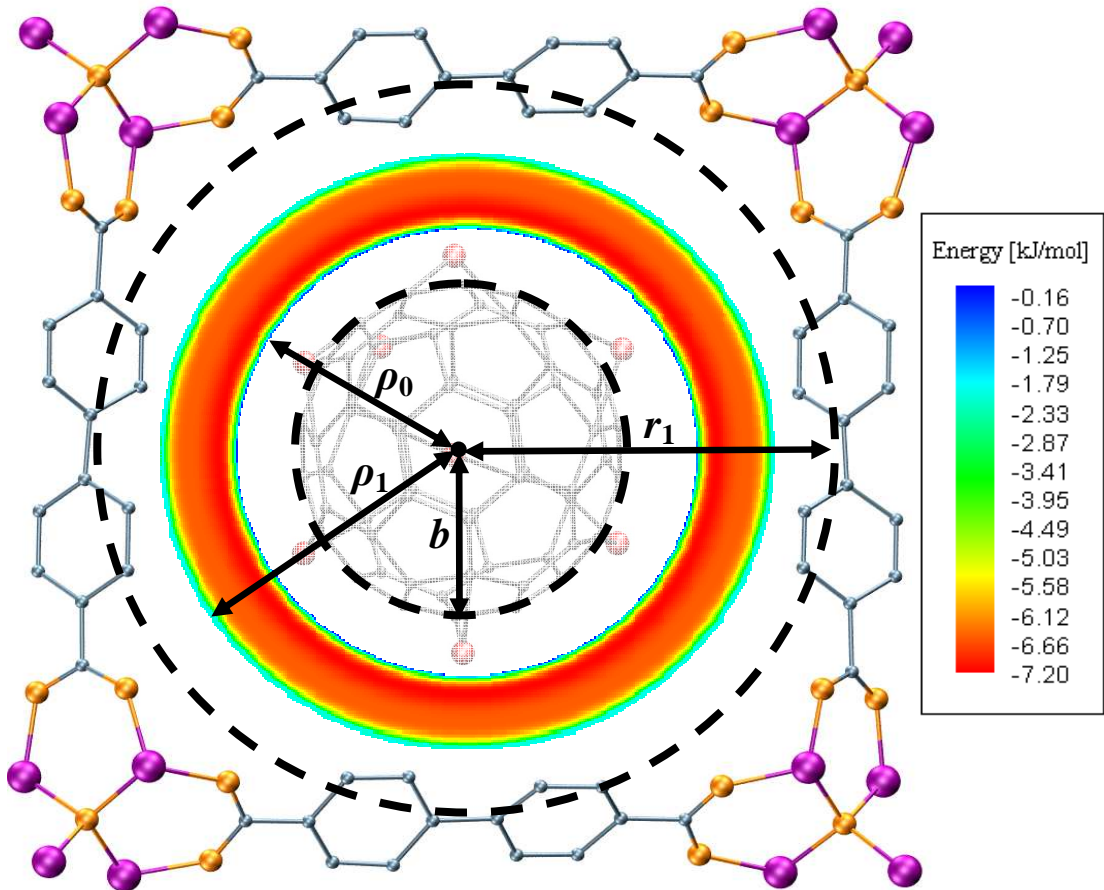


Figure 7.3: Potential energy for hydrogen adsorption within the free volume of Mg-C₆₀ @ MOF.

7.3 Comparison with experimental and simulation data

In the modelling of the likely gas storage performance for the proposed material, it is crucial that the modelling output be verified against other experimental and simulation results for MOFs, in order to provide confidence in the accuracy of the predictions made. The difficulty of the sample preparation and measurement has led to varying reported experimental results, and simulation results also vary according to the different methods and the different parameter values adopted [11]. Therefore, a sample set consisting of conservative uptake values [12-15] has been selected and used to calculate the empirical constant α . Consequently, the empirical constant α is set to 0.35, see Figure 7.4, Figure 7.5 and Table 7.5. In addition, it is found that a good approximation

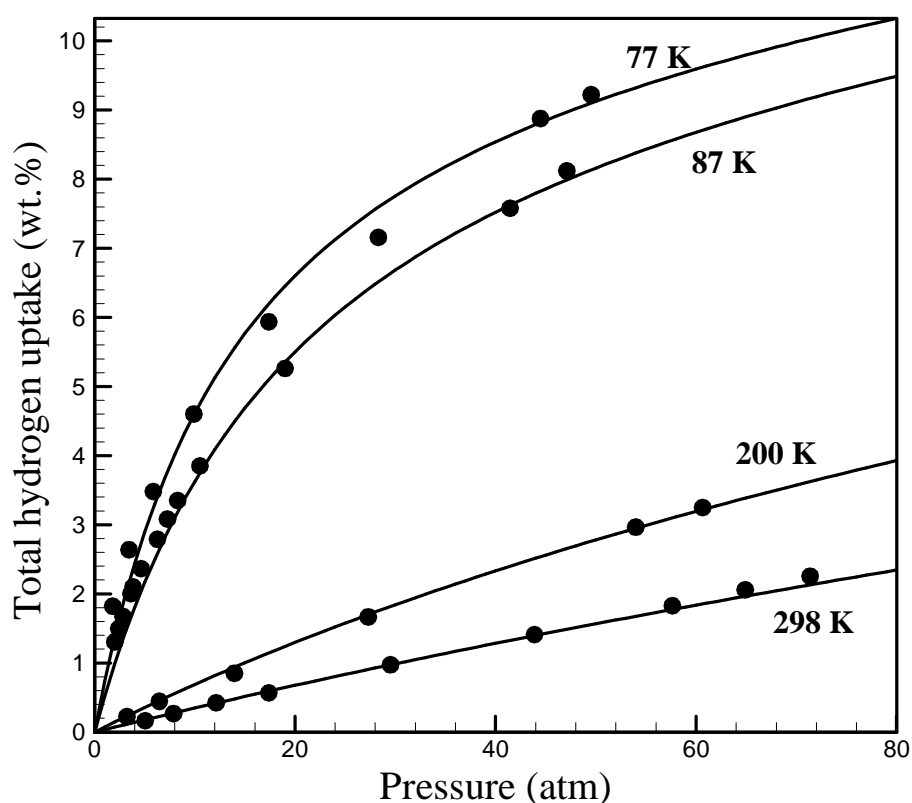


Figure 7.4: TIMTAM fit (solid lines) to Panella et al. [12] experimental results (filled circles) for total hydrogen uptake by IRMOF-1 at 77 K, 87 K, 200 K and 298 K. Panella et al. [12] measure the excess number of adsorbed molecules, reported as a quantity N_{ex} which was converted to total (absolute) adsorption n by the formula: $n = N_{\text{ex}} + V_f \rho_g$, where ρ_g is the bulk gas density [16].

for the cavity radius is $r_1 = \sqrt{3/2} r^*$ where r^* is the fixed radius determined by Eddaoudi et al. [17] which represents the radius of the largest van der Waals sphere that fits into the cavity without touching the framework atoms. These particular experimental and simulation results are chosen for model validation since the data available encompass a wide range of temperatures, pressures and cavity sizes. The model accurately portrays the observed effects of temperature, pressure and cavity size on the adsorbate uptake and is consequently capable of predicting the effect of impregnated fullerenes within the MOF structure.

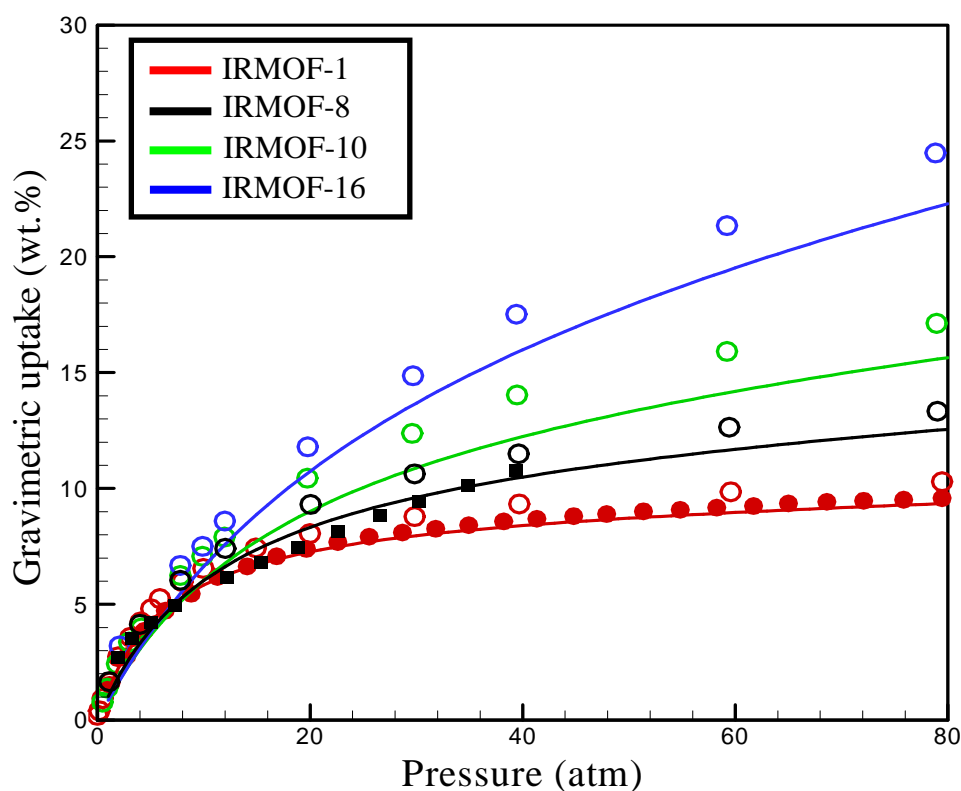


Figure 7.5: TIMTAM fit (solid lines) for total hydrogen uptake to experimental results for IRMOF-1 [14] (filled circles) and IRMOF-8 [18] (filled squares), Monte Carlo simulation results (unfilled circles) for IRMOF-1 [13], -10, and -16 [15] at 77K. Average systematic deviation $\approx 9\%$.

Table 7.5: Parameter values for α and cavity radius r_1 found from fits to experimental and simulation results, with ρ_1 calculated such that $PE(\rho_1) = 0$. Fixed cavity radius r^* from Eddaoudi et al. [17] and cavity radius approximation $r_1 = \sqrt{3/2} r^*$.

Exp. and Sim. results	α (fitted)	r_1 (Å) (fitted)	ρ_1 (Å) (calc.)	r^* (Å) (fixed)	$r_1 = \sqrt{3/2} r^*$ (Å) (approximation)
Panella et al. [12] IRMOF-1	0.43	11.45	8.70	9.25	11.32
Ryan et al. [13] IRMOF-1	0.28	10.78	8.03	9.25	11.32
Kaye et al. [14] IRMOF-1	0.28	10.78	8.03	9.25	11.32
Frost et al. [15] IRMOF-8	0.28	12.74	10.00	10.70	13.10
Ryan et al. [13] IRMOF-10	0.28	14.45	11.70	12.25	15.00
Ryan et al. [13] IRMOF-16	0.28	18.25	15.50	14.40	17.64

7.4 Model prediction of impregnated MOF structures

One of the major benefits expected from the impregnation of MOF structures is the surface potential energy overlap from the fullerene ‘guest’ with that of the MOF ‘host’ across the remaining free volume. This overlap could increase both the adsorption strength and the total amount of gas that is adsorbed in a dense fashion, as opposed to simply filling the pores in a lower density gaseous form. Figure 7.6 demonstrates these effects in three discrete cases, by varying r_I , the MOF cavity radius at which the framework atoms are approximately located.

When r_I is small (Figure 7.6A), the overlap of potential energies is strong, and under these conditions the material tends to engender gas adsorption at high enthalpies, but this is offset by a reduction in the free volume which is available for adsorption (Figure 7.7). Large values of r_I reduce the potential energy overlap (Figure 7.6C), but for intermediate r_I there exists a region where potential energy enhancement can be achieved while still maintaining a substantial amount of free volume (Figure 7.6B). In all cases it is clear that Mg-C₆₀ @ MOF has a superior performance over C₆₀ @ MOF and unfilled MOF.

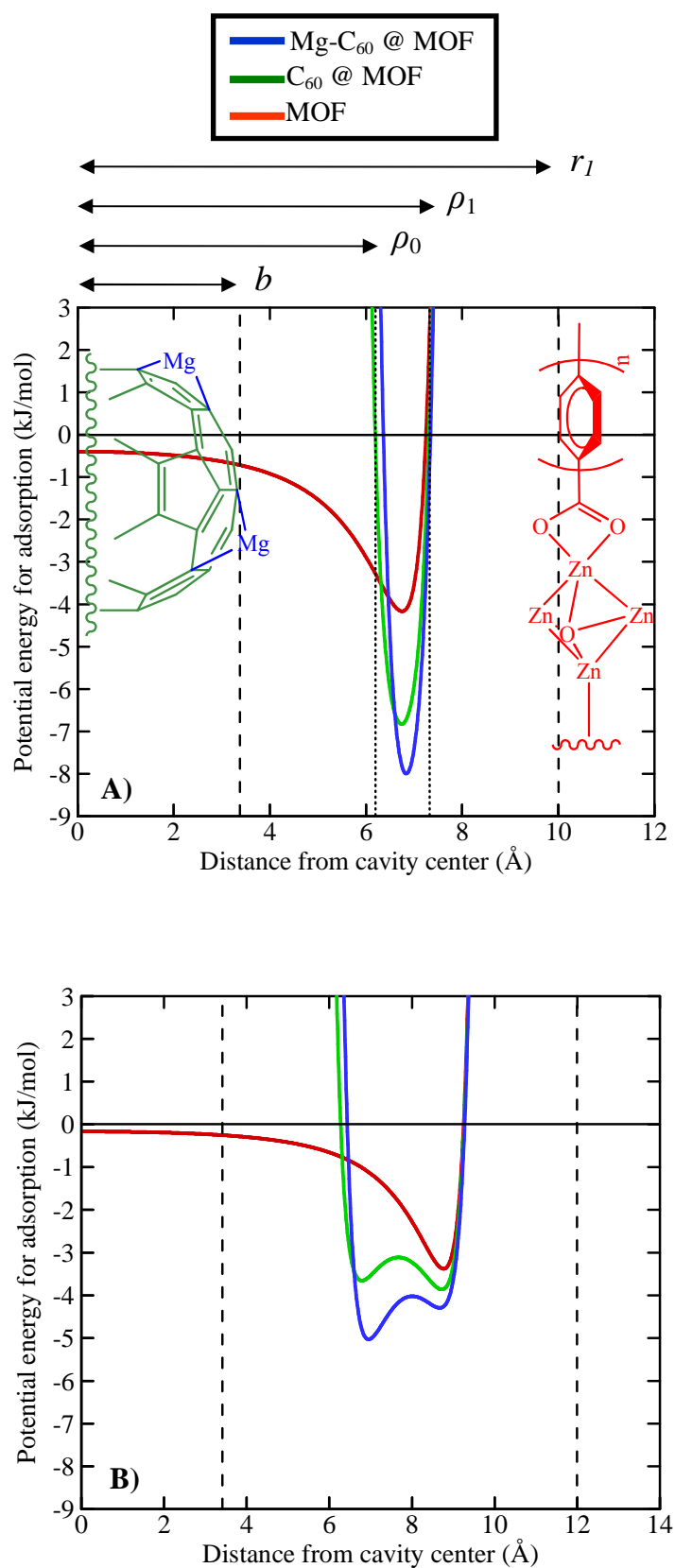


Figure 7.6 (continued to next page)

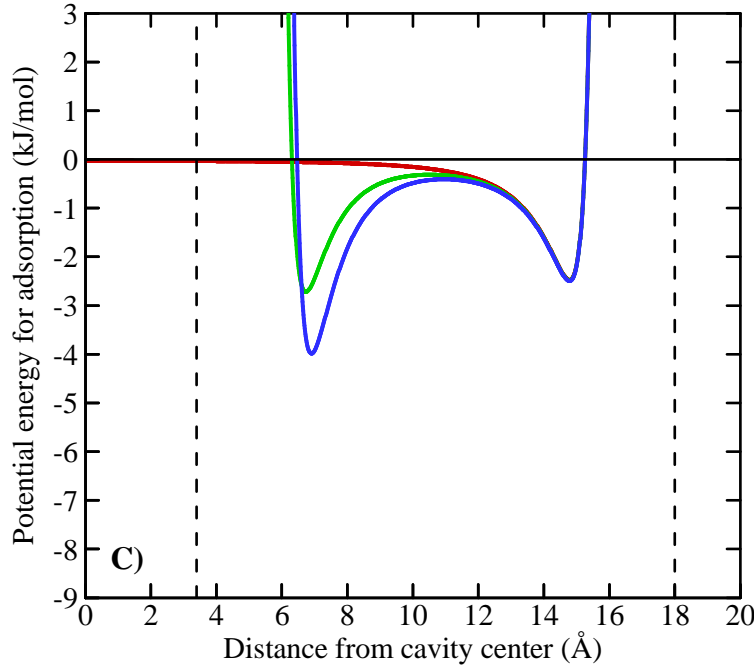


Figure 7.6: Profile of potential energy for adsorption within MOFs with cavity radii r_1 of A) 10 Å, B) 12 Å and C) 18 Å. Unfilled MOF (red), C_{60} @ MOF (green) and $Mg_{10}-C_{60}$ @ MOF (blue). Cavity surface at radius r_1 , fullerene surface at radius b , and free volume boundaries at ρ_0 and ρ_1 for $Mg-C_{60}$ @ MOF are labelled on Figure 7.6A for clarity.

Fractional free volume for adsorption (V_{ad}/V) is one of the major factors governing gas storage within porous materials, where V is given by $4/3\pi r_1^3$. It represents that proportion of volume within the MOF where gases will exist in the dense adsorbed state, as opposed to the bulk gaseous state. Figure 7.7 demonstrates that up to 44 % of the volume within $Mg-C_{60}$ @ MOF is able to accommodate both hydrogen and methane in the densely adsorbed state, which is about 10 % more than that for empty MOF structures. In the case of both adsorbing gases, the optimal cavity radius increases at lower temperatures (CH_4 17Å / 298K, 21Å / 77K ; H_2 13Å / 298K, 16Å / 77K). This is because at lower temperatures it is possible for gas molecules to be in the adsorbed state at larger distances from the adsorbent's surface, creating multiple adsorption layers, and thus larger cavities are required to reach the optimal capacity.

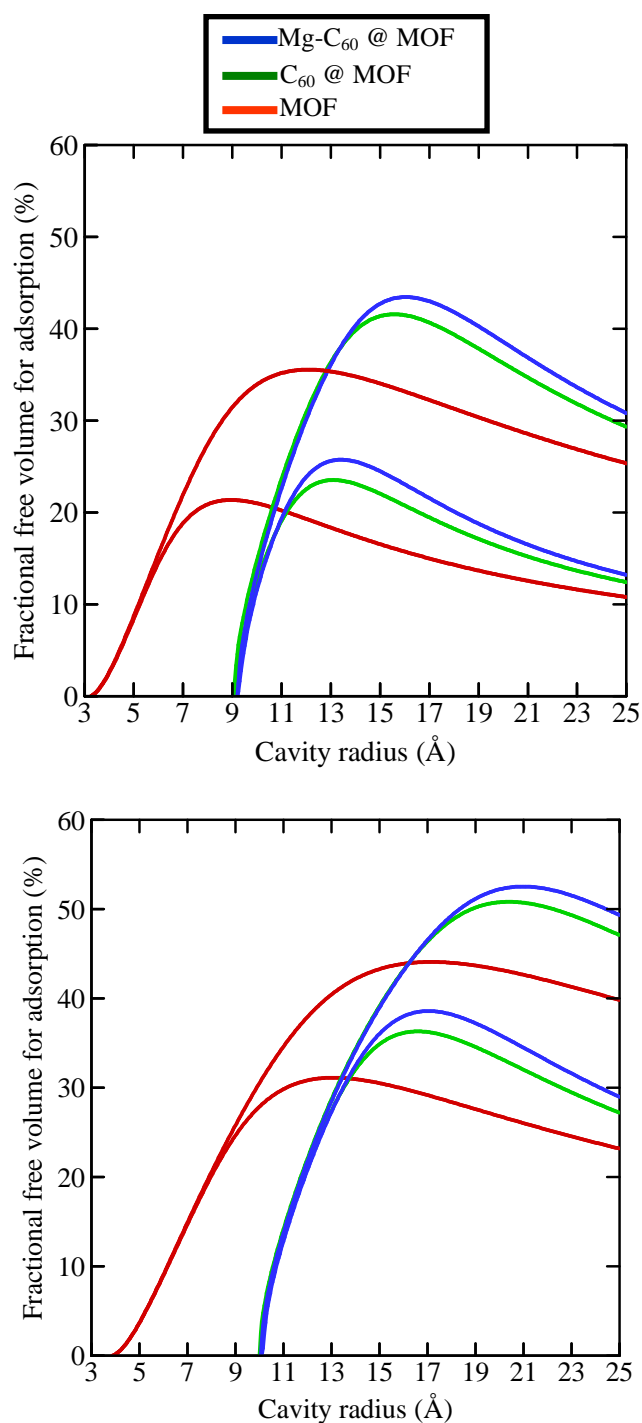


Figure 7.7: Fractional free volume for adsorption (V_{ad} / V) at 298 K (lower curves) and 77 K (upper curves) for hydrogen (top) and methane (bottom) as a function of cavity radius r_I .

Tuning the heat of adsorption within hydrogen storage materials represents perhaps one of the greatest challenges facing those concerned with the viability of hydrogen powered transport. Most physisorbent materials operate well below the 15.1 kJ/mol

proposed as necessary for room temperature operation [19, 20]. Since it is possible to overlap surface potential energies through pore impregnation (Figure 7.7), some enhancement in the measured heat of adsorption is expected, as calculated through van't Hoff plots (using Equation 5.5), and shown in Figure 7.8.

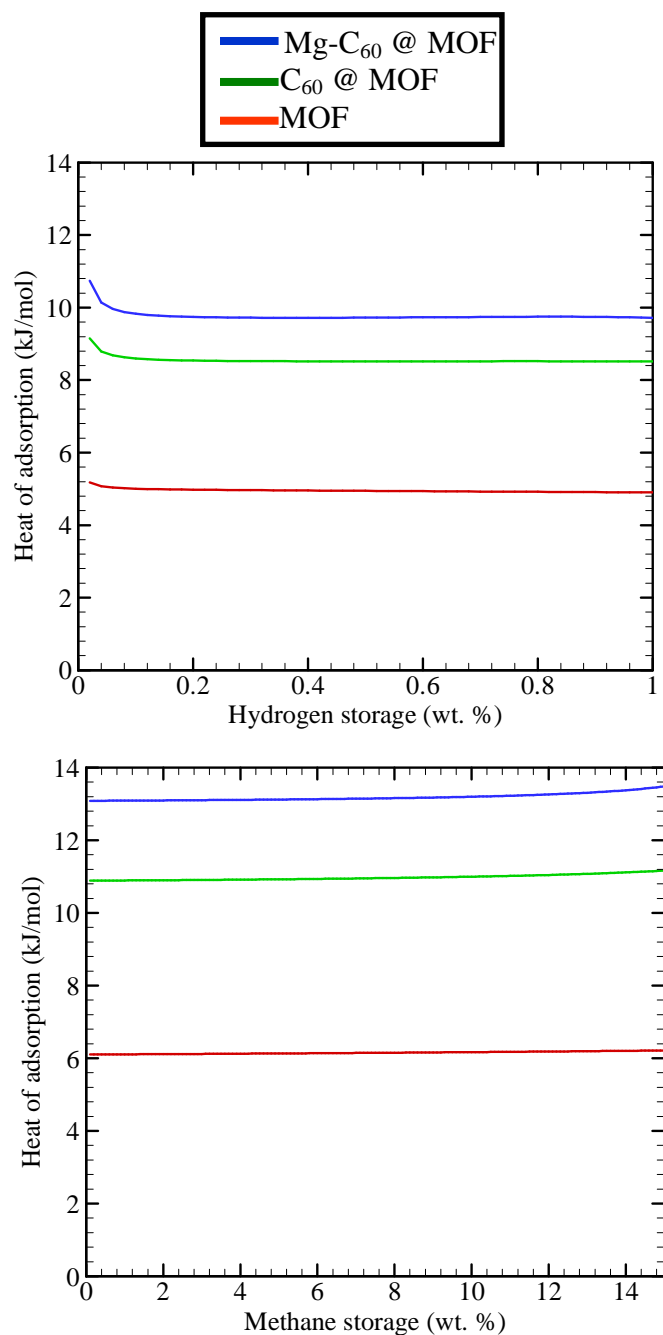


Figure 7.8: Heat of adsorption within IRMOF-8 for hydrogen (top) and methane (bottom). IRMOF-8 was chosen for this specific case as the cavity size approaches the optimal value which is determined from Figure 7.7.

The increase in the heat of adsorption observed through the fullerene impregnation is appreciable. The calculations conservatively predict a heat of adsorption of 11 kJ/mol for Mg-C₆₀ @ IRMOF-8. This value is slightly lower than for very recently reported materials which have heats of adsorption as high as 12.5 kJ/mol for Cu/Zn mixed metal frameworks [21] or 13.5 kJ/mol for frameworks with exposed Ni²⁺ sites [22]. However, the heavier metals with a more dense overall structure would be likely to render these materials less capable of significant weight percentage gas uptake. Moreover the optimum cavity radius is much smaller in these materials, 6 Å, while in the present materials the space available for adsorption of H₂ is much greater, and is calculated to be optimum at the much larger r_I radius of 13 Å (Figure 7.7). Higher enthalpies for Mg-C₆₀ @ MOF would also be attainable at smaller r_I values, but at the expense of the overall gas uptake capacity. Typically the heat of adsorption decreases with increased H₂ loading, as weak interactions between hydrogen atoms begin to dominate, but as shown here impregnated MOFs provide the required surface interactions to overcome this problem.

The relative increase in the adsorption heat for methane uptake is even more marked than that for hydrogen, with Mg-C₆₀ @ MOF providing an enhancement of over 100 %. As shown in Figure 7.8, the calculated value, 13.5 kJ/mol, is close to that required for an ideal methane storage material [19].

The hydrogen uptake (calculated from Equation 7.9 at low pressures), shown in Figure 7.9, demonstrates substantial enhancement under these conditions, with H₂ uptake as high as 7.6 wt. % at just 10 atm for Mg-C₆₀ @ MOF-10. Further development of this strategy may remove the need for high pressure vessels.

The effect of fullerene impregnation on methane storage is even more pronounced. The gravimetric values demonstrated in Figure 7.10 may be compared to the US DoE volumetric figure of merit of 180 v/v for adsorbed natural gas storage [23, 24]. As shown in Figure 7.11, both bare and decorated fullerenes produce substantial increases in the predicted methane uptake values when impregnated in MOFs. The material Mg-C₆₀ @ IRMOF-8 has the highest predicted methane uptake of 265 v/v, presumably due to the increase in heat of adsorption.

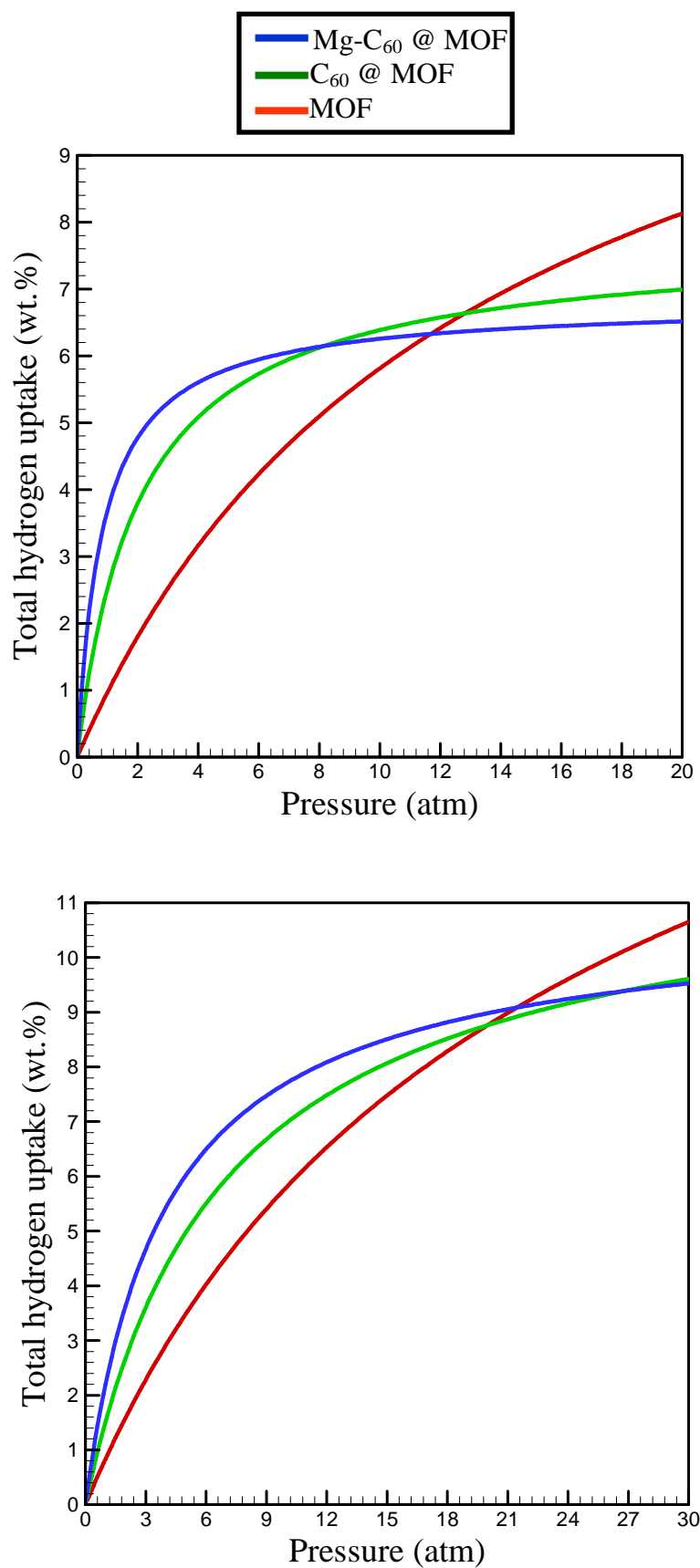


Figure 7.9: Modelling of total hydrogen storage (wt. %) within IRMOF-8 (left) and IRMOF-10 (right) at 77K.

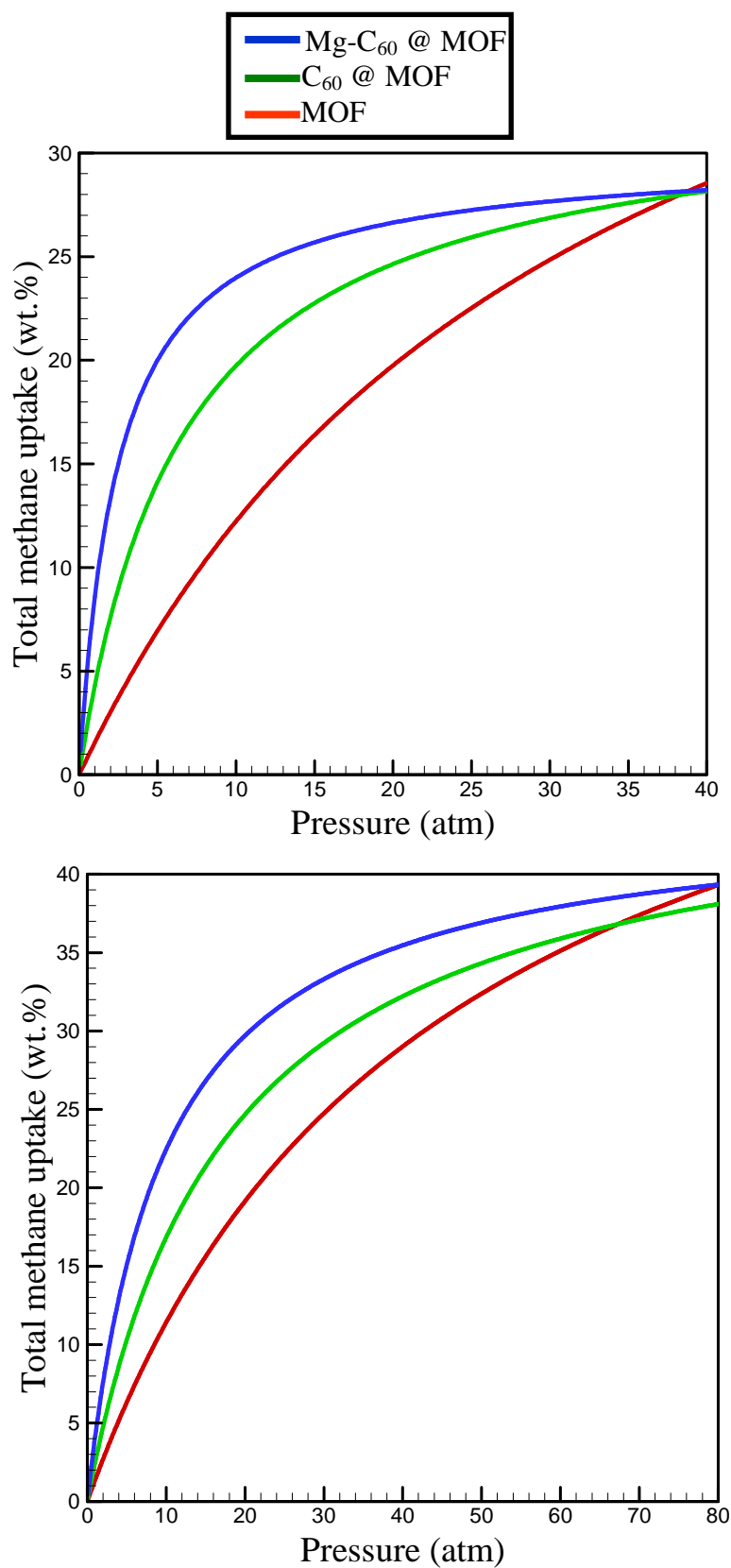


Figure 7.10: Modelling of total methane uptake (wt. %) within IRMOF-8 (left) and IRMOF-10 (right) at 298K.

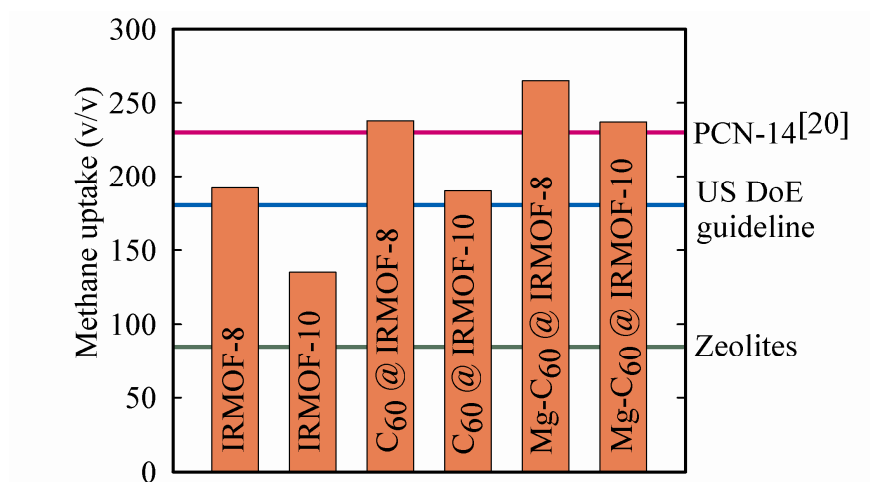


Figure 7.11: Predicted methane uptake performance for impregnated MOFs at 35 atm and 298 K.

7.5 Conclusion

Here in this chapter a new concept for hydrogen and methane storage materials was modelled using the new approach, TIMTAM. The specific example of metal-organic frameworks impregnated with magnesium-decorated fullerenes has been analyzed. Perhaps surprisingly, capacity was found to increase despite an apparent loss of free volume related to pore filling by fullerenes. The increase in capacity was related to the tunability of pore sizes in conjunction with a drastic increase in adsorption enthalpy. The TIMTAM approach was designed to be deliberately conservative to ensure that the results display a high degree of verisimilitude, so that the actual physical materials may possibly display an even higher performance. Moreover, TIMTAM is verified using published experimental results. The predicted properties include methane uptake of 265 v/v, which is the highest reported value for any material, exceeding the US DoE target by a remarkable 47 %. In addition, the model predicts one of the highest reported physisorption hydrogen adsorption heats of 11 kJ/mol, which does not diminish with increased hydrogen loading.

References

- [1] B. J. Cox, N. Thamwattana and J. M. Hill, Orientation of spheroidal fullerenes inside carbon nanotubes with potential applications as memory devices in nano-computing, *J. Phys. A: Math. Theor.*, 41 (2008) 27.
- [2] R. S. A. de Lange, K. Keizer and A. J. Burggraaf, Analysis and theory of gas transport in microporous sol-gel derived ceramic membranes, *J. Membr. Sci.*, 104 (1995) 81.
- [3] A. W. Thornton, T. Hilder, A. J. Hill and J. M. Hill, Predicting gas diffusion regime within pores of different size, shape and composition, *J. Membr. Sci.*, 336 (2009) 101.
- [4] S. L. Mayo, B. D. Olafson and W. A. Goddard III, Dreiding: a generic force field for molecular simulations, *J. Phys. Chem.*, 94 (1990) 8897.
- [5] A. Michels, W. Degraaff and C. A. Tenseldam, Virial coefficients of hydrogen and deuterium at temperatures between -175 degrees C and +150 degrees C. Conclusions from the second virial coefficient with regards to the intermolecular potential, *Physica*, 26 (1960) 393.
- [6] G. C. Maitland, M. Rigby, E. B. Smith and W. A. Wakeham, *Intermolecular Forces*, Claredon Press, Oxford, U.K., 1981.
- [7] B. J. Cox, N. Thamwattana and J. M. Hill, Mechanics of atoms and fullerenes in single-walled carbon nanotubes. I. Acceptance and suction energies, *Proc. R. Soc. A*, 463 (2007) 461.
- [8] S. S. Han, J. L. Mendoza-Cortes and W. A. Goddard III, Recent advances on simulation and theory of hydrogen storage in metal-organic frameworks and covalent organic frameworks, *Chem. Soc. Rev.*, 38 (2009) 1460.
- [9] M. A. Aicken, I. S. Bell, P. V. Coveney and W. Jones, Simulation of layered double hydroxide intercalates, *Adv. Mater.*, 9 (1997) 496.
- [10] C. Dieterici, *Ann. Phys. Chem. Wiedemanns Ann.*, 69 (1899) 685.

- [11] M. K. Thomas, Adsorption and desorption of hydrogen on metal-organic framework materials for storage application: comparison with other nanoporous materials, *Dalton Trans.*, (2009) 1487.
- [12] B. Panella, M. Hirscher, H. Putter and U. Muller, Hydrogen adsorption in metal-organic frameworks: Cu-MOFs and Zn-MOFs compared, *Adv. Funct. Mater.*, 16 (2006) 520.
- [13] P. Ryan, L. J. Broadbelt and R. Q. Snurr, Is catenation beneficial for hydrogen storage in metal-organic frameworks?, *Chem. Commun.*, (2008) 4132.
- [14] S. S. Kaye, A. Dailly, O. M. Yaghi and J. R. Long, Impact of preparation and handling on the hydrogen storage properties of $\text{Zn}_4\text{O}(\text{1,4-benzenedicarboxylate})_3$ (MOF-5), *J. Am. Chem. Soc.*, 129 (2007) 14176.
- [15] H. Frost, T. Duren and R. Q. Snurr, Effects of surface area, free volume, and heat of adsorption on hydrogen uptake in metal-organic frameworks, *J. Phys. Chem. B.*, 110 (2006) 9565.
- [16] H. Furukawa, M. Miller and O. M. Yaghi, Independent verification of the saturation hydrogen uptake in MOF-177 and establishment of a benchmark for hydrogen adsorption in metal-organic frameworks, *J. Mater. Chem.*, 17 (2007) 3197.
- [17] M. Eddaoudi, J. Kim, N. Rosi, D. Vodak, J. Wachter, M. O'Keeffe and O. M. Yaghi, Systematic design of pore size and functionality in isorecticular MOFs and their application in methane storage, *Science*, 295 (2002) 469.
- [18] A. Dailly, J. J. Vajo and C. C. Ahn, Saturation of hydrogen sorption in Zn benzenedicarboxylate and Zn naphthalenedicarboxylate, *J. Phys. Chem. B*, 110 (2006) 1099.
- [19] S. K. Bhatia and A. L. Myers, Optimum conditions for adsorptive storage, *Langmuir*, 22 (2006) 1688.
- [20] P. G. Menon, Adsorption at high pressures, *Chem. Rev.*, 68 (1968) 277.

- [21] B. Chen, X. Zhao, A. Putkham, K. Hong, E. B. Lobkovsky, E. J. Hurtado, A. J. Fletcher and K. M. Thomas, Surface interactions and quantum kinetic molecular sieving for H-2 and D-2 adsorption on a mixed metal-organic framework material, *J. Am. Chem. Soc.*, 130 (2008) 6411.
- [22] J. G. Vitillo, L. Regli, S. Chavan, G. Ricchiardi, G. Spoto, P. D. C. Dietzel, S. Bordiga and A. Zecchina, Role of exposed metal sites in hydrogen storage in MOFs, *J. Am. Chem. Soc.*, 130 (2008) 8386.
- [23] D. Lozano-Castelló, J. Alcañiz-Monge, M. A. de la Casa-Lillo, D. Cazorla-Amorós and A. Linares-Solano, Advances in the study of methane storage in porous carbonaceous materials, *Fuel*, 81 (2002) 1777.
- [24] R. Ma, Y. Bando and T. Sato, Controlled synthesis of BN nanotubes, nanobamboos, and nanocables, *Adv. Mater.*, 14 (2002) 366.

List of symbols used in Chapter 7

PE	potential energy
ρ	distance from center of pore
C_6, C_{12}	attractive and repulsive Lennard-Jones constants ($C_k = 4\epsilon\sigma^k$)
σ	kinetic diameter
ϵ	well depth
η	atomic surface density
r_1	radial location of surface atoms
b	radius of fullerene
KE	kinetic energy of gas molecule
T	temperature
R	universal gas constant
V_{ad}	volume free for adsorption
V_{bulk}	volume free for bulk gas

V_f	free volume within adsorbent ($=V_{ad} + V_{bulk}$)
Q	heat of adsorption
p	pressure
v_0	occupied volume of closely packed gas molecules
n_{ad}	number of molecules in adsorbed phase
n_{bulk}	number of molecules in bulk gas phase
n	total number of molecule stored ($= n_{ad} + n_{bulk}$)
m	mass of individual gas molecule
M	mass of adsorbent
r_1^*	radius of metal-organic framework estimated by Eddaoudi et al.
V	total volume of unit cell
ρ_0, ρ_1	positions at which $PE = 0$
\bar{v}	volumetric uptake (mass of gas over volume of adsorbent)
wt. %	gravimetric uptake (mass of gas over system mass)

Chapter 8

Nanotubes

8.1 Introduction

Here the viability of nanotubes as potential adsorbents for hydrogen storage applications is investigated by adopting the new thermodynamic approach (TIMTAM), established in Chapter 6. The effects of the tube size and composition have been explored with respect to the hydrogen uptake and adsorption energy, and optimal compositions and structures are proposed. In particular, inorganic nanotubes exhibit the greatest potential for high enthalpy adsorption, leading to the possibility of increased operating temperatures.

8.1.1 Hydrogen storage requirements

With the hydrogen electro-chemical cell powered automobile as a focus, the US Department of Energy (DoE) has set the benchmark for 2010 that the hydrogen storage system must achieve a gravimetric uptake of 0.06 (kg H₂ / kg system) and a volumetric uptake of 0.045 (kg H₂ / L system), and for 2015 a gravimetric uptake of 0.09 (kg H₂ / kg system) and a volumetric uptake of 0.081 (kg H₂ / L system) [1-3]. The requirements further constrict the operating pressure to 100 atm and operating temperature within 243-323 K by 2010 (233-333 K by 2015) [1]. Basically, the challenge is to fit enough hydrogen inside a tank that is small and light enough for a vehicle to travel at least 300 miles (483 km).

8.1.2 Storage methods

The storage requirements can be achieved by the compressed gas method at pressures of about 350 atm, but that is a safety concern for public roads and there are a few problems with refuelling according to the Ecobus operational report from a 3-year trial throughout

Australia [4]. Adsorbents are porous materials capable of storing hydrogen in a highly dense phase at ambient conditions by mechanism of physisorption or chemisorption. Physisorption takes advantage of the high continuous surface areas while chemisorption takes advantage of the available high enthalpy site-specific locations within the adsorbent.

The optimal adsorption enthalpy to enhance the storage and release process has been predicted to be 15.1 kJ/mol [5] which chemisorbents well exceed requiring vast temperature ranges for adsorption and desorption to occur [2, 6]. In addition, chemisorbents' uptake capacities are limited to their number of adsorption sites and hence physisorption based systems are favourable in this respect and are the focus of this study.

8.1.3 Nanotubes: Properties and synthesis

Among the many physisorbents striving to meet the requirements there are the popular nanotube-based materials, mainly because of their open tunnel-like pores which are highly accessible to hydrogen [7, 8]. Since the discovery of the carbon nanotubes' ability to store hydrogen there has been much work into enhancing the storage capacity by methods such as, tailoring tube size, forming different structures and shapes, functionalizing the surface and many others [8-11]. It is clear from experiments and simulations that carbon simply does not interact strongly enough with hydrogen to create high adsorption close to ambient conditions [11]. Therefore, other atoms that have stronger van der Waals potential energies (characterized by well depth) need to be included in the structure which is why the metal-organic frameworks (MOFs) are currently the leading hydrogen adsorbents [12, 13].

While MOFs expose their metal sites resulting in binding energies of about 2 kJ/mol per H₂ [14], inorganic nanotubes are capable of exposing their metal (or metalloid) sites even more than MOFs resulting in binding of energies of up to 20 kJ/mol per H₂ [15, 16]. Additionally, nanotubes provide ultra-fast gas diffusion pathways which could possibly speed the adsorption/desorption process [17, 18] and hence inorganic nanotubes are excellent adsorbent candidates.

Since the synthesis of carbon nanotubes [19], there has been much work in creating nanotubes out of non-carbonic elements, for example Zhang and Zhang have reviewed the following tubes, AlN, SiO₂, BN, InP, ZnO, GaN and ZnS [20]. Boron nitride nanotubes can be synthesized by arc-discharge [21], chemical vapour deposition (CVD)

[22], laser ablation [23], carbon-thermal reduction synthesis [24] carbon nanotube- and template-confined methods [25, 26], pyrolysis method [27] and ball milling [28]. The other nanotubes are synthesized by different methods such as: epitaxial casting [29] for single-crystal gallium nitride nanotubes; vapour phase synthesis [30] for aluminium nitride nanotubes; VLS (vapour-liquid-solid) laser ablation [31] for indium phosphorus nanotubes; thermal oxidation-etching [32] for silica nanotubes; organogel template [33], unconstrained solution growth [34] and templateless nanoparticle growth [35] for titanium oxide nanotubes; and microwave plasma system [36], thermal reduction [37] and vapour phase [38] for zinc oxide nanotubes. The primary interest of this work is to theoretically test the storage performance of these tubes and determine the characteristics needed to satisfy the DOE requirements by considering tube size, potential energy for adsorption (well depth) and material mass.

8.2 Method

Complete details of the model are found in Chapter 6 while a brief description is provided in this section. Overall, the method uses the van der Waals interactions to determine the space within the material in which hydrogen will either be in adsorbed phase or bulk gas phase. Equations of states are then employed to calculate the total number of hydrogen molecules in each state.

Firstly, the van der Waals interaction between the hydrogen molecule and the tube wall is calculated using a continuum approach where the atoms making up the tube wall are smeared across a continuous surface. From the 6-12 Lennard-Jones potential energy function, the total interaction energy between the hydrogen molecule and the tube can be expressed as

$$PE(\rho) = \eta(-C_6 H_3 + C_{12} H_6),$$

$$H_k = \frac{2\pi^2 d^2}{(d)^{2k} (2k-2)!} \sum_{i=0}^{\infty} \left(\frac{\rho^i (2k+2i-2)!}{(2d)^i i! (k+i-1)!} \right)^2, \quad (8.1)$$

where d is the tube diameter (between surface nuclei), ρ is the radial distance from tube center, and C_6 and C_{12} are the attractive and repulsive Lennard Jones constants represented as $C_k = 4\epsilon\sigma^k$ (σ is the kinetic diameter and ϵ is the well depth). The van der Waals parameter values are available from a variety of sources including the Universal Force Field (UFF) [39], DREIDING [40] and Poling et al. [41] database. The most

favourable database for this application has been the UFF and parameter values are given in Table 8.1 using Lorentz-Berthlot mixing rules for the interaction between hydrogen and the nanotube atoms. The resulting potential energy is demonstrated in Figure 8.1 for a single nanotube with various tube sizes. A contour view of this example is given in Figure 8.2.

By knowing the potential energy between a gas molecule and the tube wall the free volume for adsorption may be determined,

$$V_{ad} = \int_0^{\rho_0} 2\pi\rho l \{1 - \exp[-|PE(\rho)|/RT]\} d\rho, \quad (8.2)$$

and the free volume for bulk gas,

$$V_{bulk} = \int_0^{\rho_0} 2\pi\rho l \{\exp[-|PE(\rho)|/RT]\} d\rho, \quad (8.3)$$

where ρ_0 is the radial position at which the potential energy is equal to zero, R is the universal gas constant ($= 5.1894861 \times 10^{19}$ eV K⁻¹mol⁻¹), T is temperature (K) and l is the arbitrary tube length.

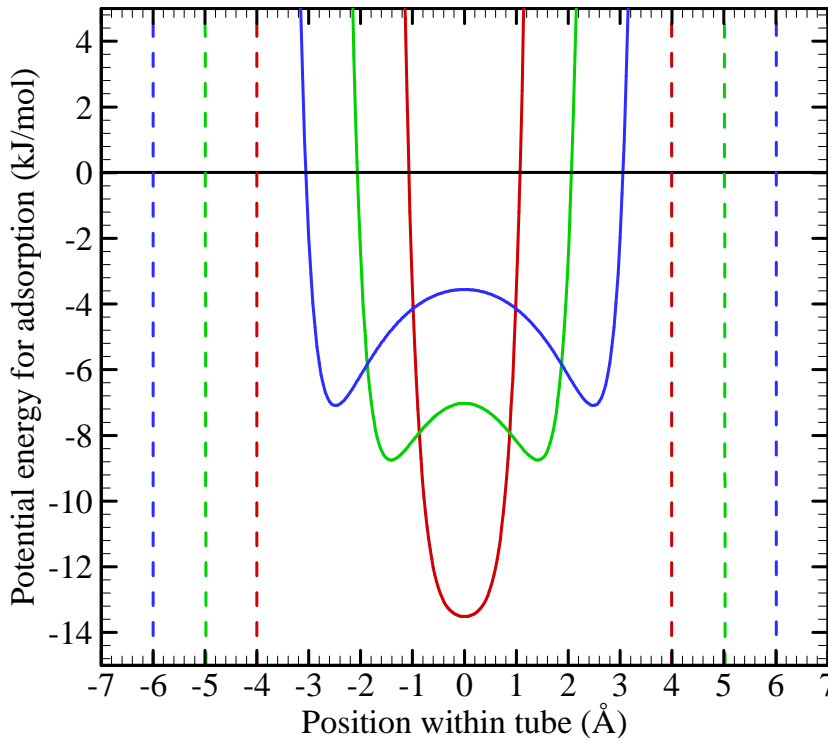


Figure 8.1: Potential energy for adsorption within carbon nanotubes of diameters; $d = 8$ (red lines), 10 (green lines) and 12 (blue lines) Å. Dashed lines represent the position of the surface nuclei.

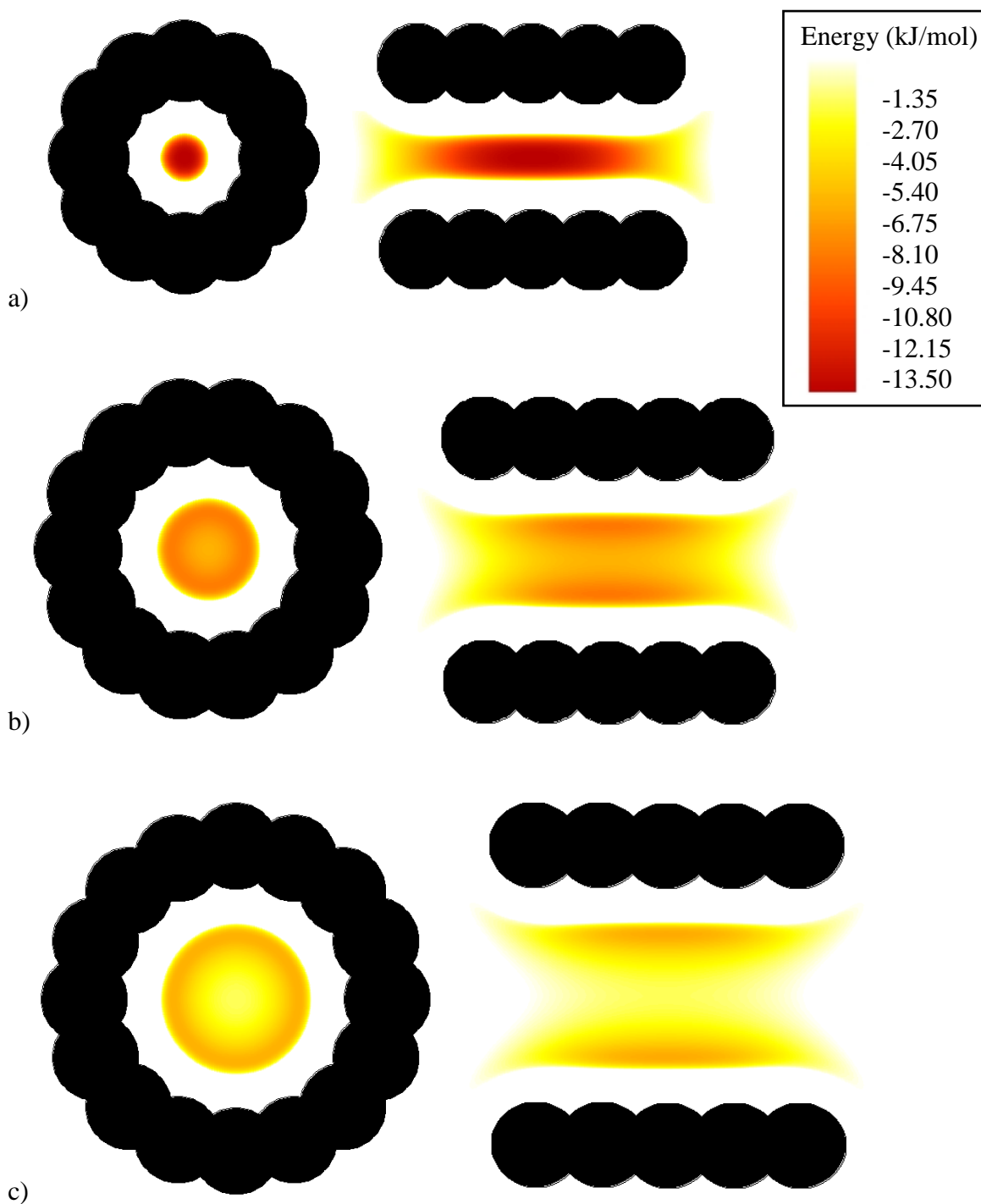


Figure 8.2: Contour plot of potential energy for adsorption within carbon nanotubes of diameters; a) 8, b) 10 and c) 12 Å.

Table 8.1: Parameter values used in this chapter. The kinetic diameter σ between H_2 and the nanotube element X is approximated as 3.3 \AA , and the surface atomic density η is approximated as 0.38 No./\AA^2 (in reality σ and η vary for different nanotubes but does not influence uptake as much as changes in well depth).

Element X	X - H_2 well depth $\varepsilon / k_B \text{ (K)}$	Mass (g/mol)
C	56.16	12.01
O	42.45	16.00
N	45.53	14.01
Al	123.17	26.98
Si	109.89	28.09
B	73.54	10.81
Zn	61.04	65.38
S	90.73	32.07
Ga	111.66	69.82
In	134.15	114.80
P	95.72	30.97
Bi	124.75	208.98

Note that the total free volume, defined as $V_f = \pi \rho_0^2 l$, within the nanotube is equal to the sum of the volume free for adsorption and the volume free for bulk gas ($V_f = V_{ad} + V_{bulk}$). Figure 8.3 depicts the fractional free volume for adsorption (V_{ad} / V) within a carbon nanotube at temperatures 77 and 298 K, with the total volume defined as $V = \pi d^2 l$. This is a very important property to consider since the amount of adsorbed

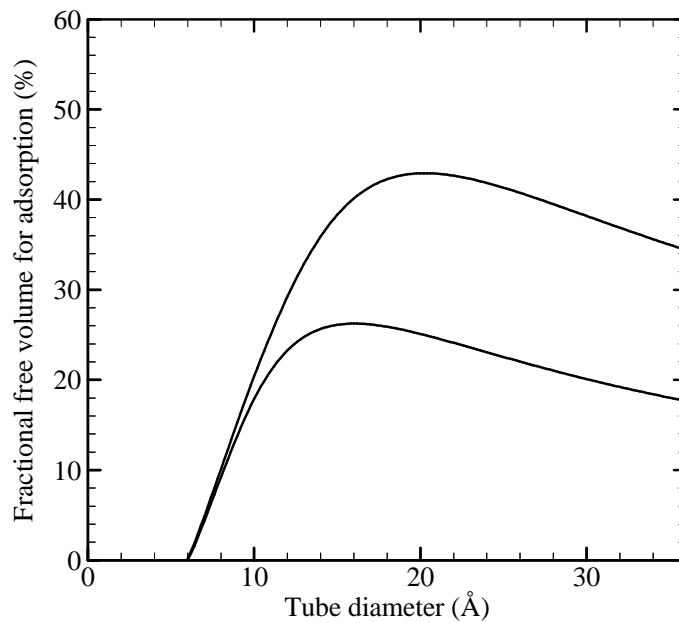


Figure 8.3: Fractional volume for adsorption within a carbon nanotube at temperatures 77 (higher curve) and 298 K (lower curve).

molecules is maximized when there is more space within the material for which the gas will be in adsorbed phase. This is predicted to be maximized at a tube size of 16 and 21 Å which match excellently with the optimal sizes predicted by Dillon et al. [7] of 16.3 and 20 Å.

The actual number of molecules within the nanotube can be predicted by using the appropriate equation of state for each phase. A simplified van der Waals equation of state is used to calculate the number of molecules in the bulk gas phase expressed as

$$p(V_{bulk} / n_{bulk} - v_0) = RT, \quad (8.4)$$

where p is pressure, n_{bulk} is the number of adsorbate molecules in the bulk gas phase per nanotube and v_0 represents the occupied volume of the adsorbate calculated from critical parameters (set to 0.0136 L/mol). Similarly, the number of molecules in adsorbed phase is calculated from a modified Dieterici equation of state,

$$p(V_{ad} / n_{ad} - v_0) = \alpha RT \exp\left(-\left|\overline{PE}\right| / RT\right), \quad (8.5)$$

where n_{ad} is the number of molecules in adsorbed phase per nanotube, \overline{PE} is the average potential energy for adsorption and α is an empirical factor dependent on the mobility parallel to the surface (set to 0.85). As the binding energy of adsorption gets stronger the collision energy between adsorbate molecules lessens causing the molecules to store closer together in a highly dense fashion. Once the total number of molecules are found ($n = n_{ad} + n_{bulk}$), the gravimetric uptake can be calculated in the following way,

$$wt.\% = \frac{nm}{(nm + M/2)}, \quad (8.6)$$

where m is the mass of an adsorbate molecule (kg/mol) and M is the mass of the nanotube (kg/mol). Note that the mass of the nanotube is halved (same as work by Rzepka et al. [42]) since this study is only interested in analyzing the inside of the nanotube where the higher uptake results are obtained. The full consideration of interstitial gaps between the nanotube array is discussed at the end of this section. The volumetric uptake is calculated as

$$\bar{v} = \frac{nm}{V}, \quad (8.7)$$

where V is the nanotube volume (L). An example of the uptake isotherms for hydrogen within a carbon nanotube is given in Figure 8.4. The isotherm trends match closely to

those predicted by Rzepka et al. [42] and are in relative agreement with the range of experimental results summarized in review work by Cheng et al. [8].

This study is only interested in analyzing the inside of the nanotube. In reality there are interstitial gaps between the arrangement of nanotubes which usually are in a triangle or square packing array. The fact that nanotubes are in contact with each other is a disadvantage to the system because there is wasted space where hydrogen can not stick onto the complete outside surface of each tube. In addition, concave surfaces have much stronger adsorption energies than convex surfaces, meaning that the insides of the tubes are the more favourable parts of the nanotube system. If there were a method to separate the nanotube array such that the tubes complete outside surface were accessible to hydrogen then the total adsorption uptake could possibly reach as high as the inside-only results. Therefore, the results could be in excess of actual adsorption results, provided that the available van der Waals parameters are accurate for this application.

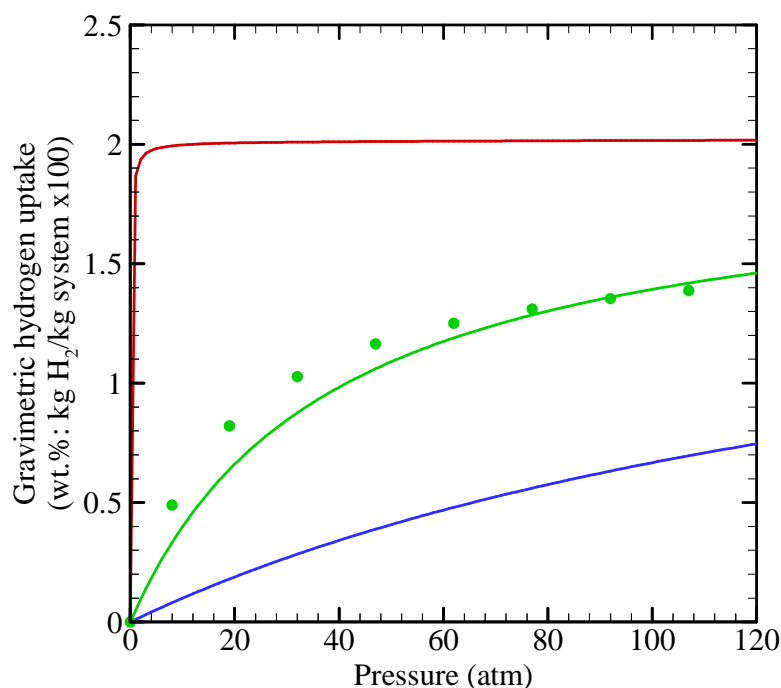


Figure 8.4 (*continued to next page*)

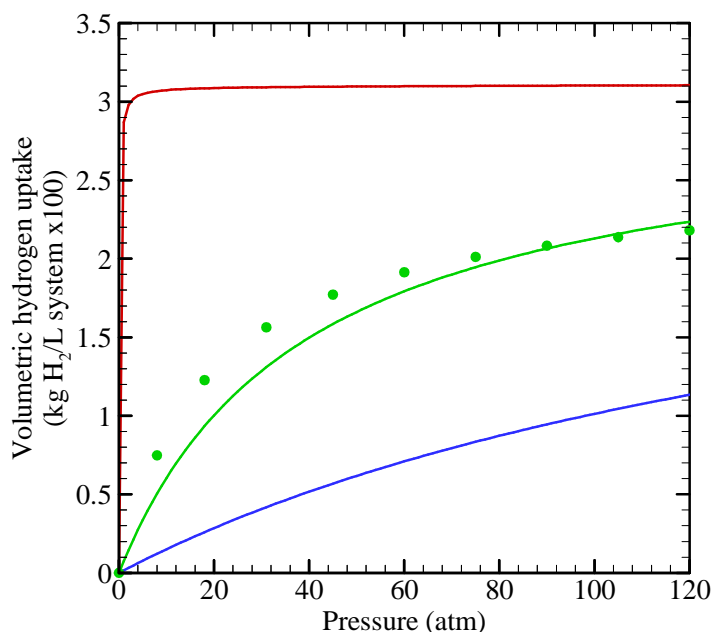


Figure 8.4: Predictions of gravimetric (top) and volumetric (bottom) hydrogen uptake isotherms in a carbon nanotube of diameter 10 Å at temperatures 77 (red lines), 200 (green lines) and 300 (blue lines) K. Simulations results (green circles) from Rzepka et al. [42] at 77 K.

8.3 Model prediction of nanotubes

It has been shown experimentally that carbon nanotubes are far behind in the race for the ultimate hydrogen storage material because of the weak interaction energy between hydrogen and carbon. However it is possible that nanotubes made out of non-carbonic elements could be capable of achieving high uptake results. Each element has a different adsorption energy (well depth) and mass, two major characteristics important for achieving high gravimetric storage results. The formulations outlined in Chapter 6 allow the direct exploration of how the characteristics well depth, mass and tube size can be tailored to reach the DoE requirements and, therefore, determine whether any existing elements are capable of reaching these requirements.

First the hydrogen uptake is investigated with varying well depth within tubes of diameters 10, 15, and 20 Å, and with identical mass of 10 g/mol, demonstrated in Figure 8.5. The atmosphere conditions are set as the DoE requirements for 2010. According to the gravimetric uptake results, the 2010 goal may be reached with a nanotube of diameter 20 Å and composed of an element with a mass of 15 g/mol and well depth of 230 K. It is clear that there is an upper bound limit for each tube size where the

maximum number of hydrogen molecules can fit inside the tube. Dresselhaus et al. [43] predicted by geometrical considerations that the maximum amount of hydrogen molecules that could fit inside a (10,10) nanotube (diameter of 13.6 Å) was equivalent to 4 wt. % which matches excellently with the model results in Figure 8.5 (this is comparable since the mass of carbon is close to 15 g/mol). The results in Figure 8.5 demonstrate that the volumetric uptake DoE goals are more attainable than the gravimetric requirements. One advantage is that the volumetric uptake does not depend on material mass where it is difficult to find elements with high adsorption energies that also have a low mass.

Gravimetric uptake with varying well depth within tubes of mass 10, 20, and 30 g/mol is investigated; see Figure 8.6, with identical pore diameter of 16 Å. The drop in uptake as mass increases is remarkable, indicating that tubes created from light atoms have a great advantage over heavier tubes. As before there is an upperbound, this time determined by mass. This demonstrates that even when there is an identical number of hydrogen stored in the tubes, the difference in mass drastically changes the final gravimetric uptake.

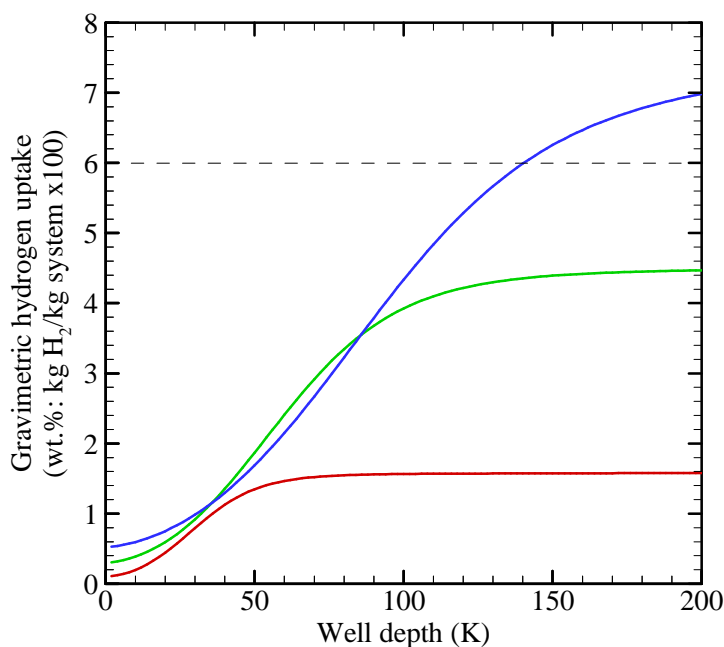


Figure 8.5 (continued to next page)

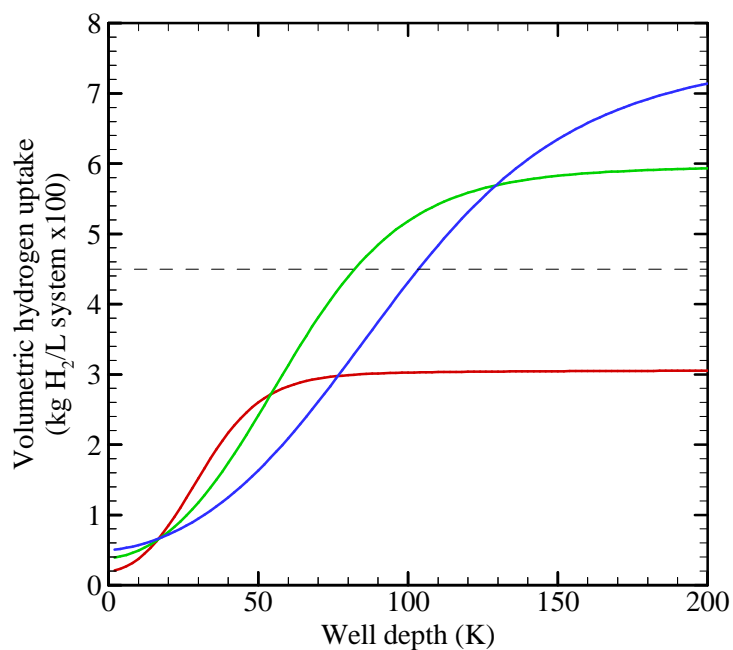


Figure 8.5: Prediction of hydrogen gravimetric (top) and volumetric (bottom) uptake in nanotubes with diameters 10 (red), 15 (green), and 20 (blue) Å with a mass of 15 g/mol in operating conditions: temperature = 243 K and pressure = 100 atm (DoE requirement for 2010). Dotted lines represent the 2010 DoE target.

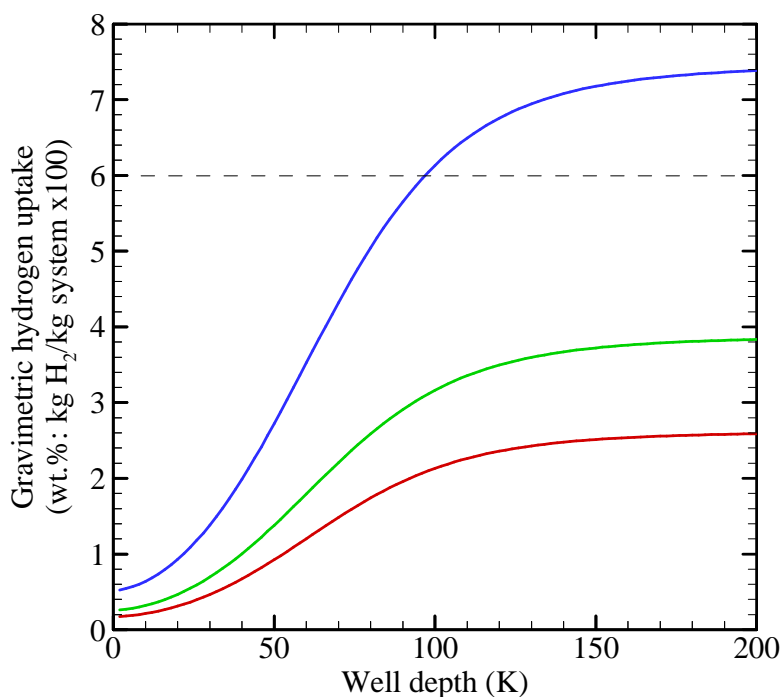


Figure 8.6: Prediction of hydrogen gravimetric uptake in nanotubes with mass 10, 20, and 30 g/mol with diameter of 16 Å in operating conditions: temperature = 243 K and pressure = 100 atm (DoE requirement for 2010). Dotted line represents the 2010 goal.

The final investigation includes the testing of the performance of non-carbonic nanotubes, namely, AlN, SiO₂, BN, InP, ZnO, GaN and ZnS in Figure 8.7,

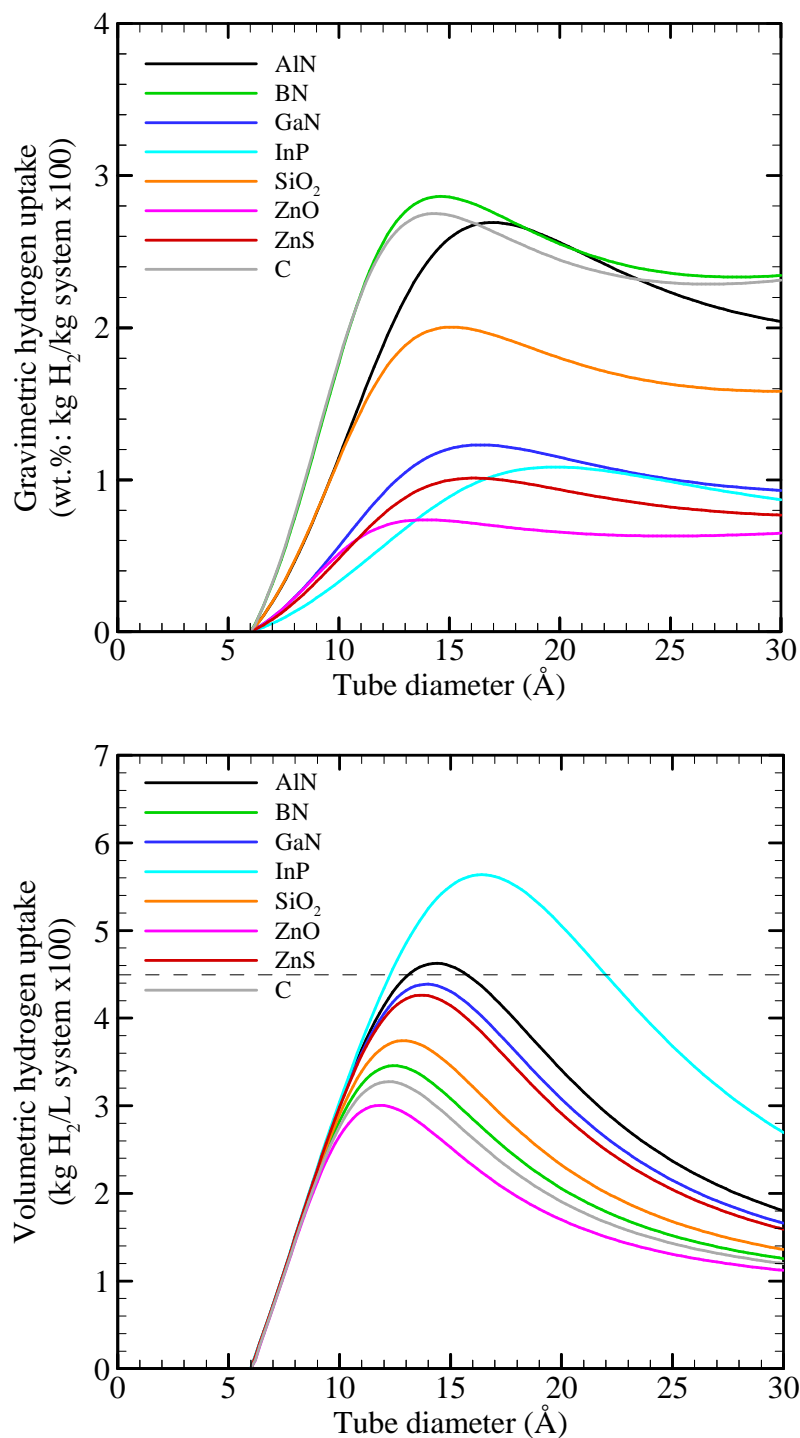


Figure 8.7: Prediction of hydrogen gravimetric (top) and volumetric (bottom) uptake in nanotubes in operating conditions: temperature = 243 K and pressure = 100 atm (DOE requirement for 2010). Dotted line represents the 2010 goal.

manufactured by Zhang and Zhang [20]. Since the well depth and mass (found in Table 8.1) are set, the only varying parameter available is the tube size. The volumetric targets are met for an InP tube of diameter 11.5 – 22 Å and an AlN tube of diameter 12.5 – 16 Å while the gravimetric uptake predictions fall short of the targets. The boron nitride tube is the highest performing for gravimetric uptake because of its strong van der Waals well depth and relatively light mass.

8.4 Conclusion

Hydrogen uptake predictions were made with the TIMTAM approach where factors such as, adsorption energy, tube size and tube mass were investigated. The study showed some intuitive trends that provide insight into the tube characteristics needed to achieve the DoE goals. Gravimetric uptake showed to be the more difficult adsorption measure to achieve with aluminium nitride and boron nitride tubes performing the highest but still below the DoE targets. The volumetric uptake 2010 target is achieved within the indium phosphide and aluminium nitride tubes with maximum uptake occurring for tube diameters of 15 and 17 Å, respectively. Overall, the complete DoE requirements are almost achievable and the hydrogen storage may be maximized by tuning the nanotube properties with the guidance of this study.

References

- [1] Multi-Year Research, Development and Demonstration Plan - Planned Program Activities for 2003-2010: Technical Plan; U.S. Department of Energy; <http://www.eere.energy.gov/hydrogenandfuelcells/mypp/pdfs/storage.pdf>.
- [2] E. M. Gray, Hydrogen storage - status and prospects, *Adv. Appl. Ceram.*, 106 (2007) 25.
- [3] L. Schlapbach and A. Züttel, Hydrogen-storage materials for mobile applications, *Nature*, 414 (2001) 353.
- [4] C. Cockroft, Perth's fuel cell bus trial 2004 - 2007: Final operation report to the department for planning and infrastructure, Murdoch University, Perth, 2008.

- [5] S. K. Bhatia and A. L. Myers, Optimum conditions for adsorptive storage, *Langmuir*, 22 (2006) 1688.
- [6] P. Chen, Z. Xiong, J. Luo, J. Lin and K. L. Tan, Interaction of hydrogen with metal nitrides and imides, *Nature*, 420 (2002) 302.
- [7] A. C. Dillon, K. M. Jones, T. A. Bekkedahl, C. H. Kiang, D. S. Bethune and M. J. Heben, Storage of hydrogen in single-walled carbon nanotubes, *Nature*, 386 (1997) 377.
- [8] H.-M. Cheng, Q.-H. Yang and C. Liu, Hydrogen storage in carbon nanotubes, *Carbon*, 39 (2001) 1447.
- [9] T. Yildirim, J. Iniguez and S. Ciraci, Molecular and dissociative adsorption of multiple hydrogen molecules on transition metal decorated C₆₀, *Phys. Rev. B: Condens. Matter*, 72 (2005) 153403.
- [10] L. Chen, Y. Zhang, N. Koratkar, P. Jena and S. Nayak, First-principles study of interaction of molecular hydrogen with Li-doped carbon nanotube peapod structures, *Phys. Rev. B: Condens. Matter*, 77 (2008) 033405.
- [11] F. L. Darkrim, P. Malbrunot and G. P. Tartaglia, Review of hydrogen storage by adsorption in carbon nanotubes, *Int. J. Hydrogen Energy*, 27 (2002) 193.
- [12] J. G. Vitillo, L. Regli, S. Chavan, G. Ricchiardi, G. Spoto, P. D. C. Dietzel, S. Bordiga and A. Zecchina, *J. Am. Chem. Soc.*, 130 (2008) 8386.
- [13] M. K. Thomas, Adsorption and desorption of hydrogen on metal-organic framework materials for storage application: comparison with other nanoporous materials, *Dalton Trans.*, (2009) 1487.
- [14] T. Mueller and G. Ceder, A density functional theory study of hydrogen adsorption in MOF-5, *J. Phys. Chem. B.*, 109 (2005) 17974.
- [15] Y. Li, Z. Zhou, P. Shen, S. B. Zhang and Z. Chen, Computational studies on hydrogen storage in aluminium nitride nanowires/tubes, *Nanotechnology*, 20 (2009) 215701.

- [16] Q. Wang, Q. Sun, P. Jena and Y. Kawazoe, Potential of AlN nanostructures as hydrogen storage materials, *ACS Nano*, 3 (2009) 621.
- [17] J. K. Holt, H. G. Park, Y. Wang, M. Stadermann, A. B. Artyukhin, C. P. Grigoropoulos, A. Noy and O. Bakajin, Fast mass transport through sub-2-nanometer carbon nanotubes, *Science*, 312 (2006) 1034.
- [18] B. J. Hinds, N. Chopra, T. Rantell, R. Andrews, V. Gavalas and L. G. Bachas, Aligned multiwalled carbon nanotube membranes, *Science*, 303 (2004) 62.
- [19] S. Iijima, Helical microtubules of graphitic carbon, *Nature*, 354 (1991) 56.
- [20] L. Zhang and Y. Zhang, Recent results in the preparation of non-carbonic nanotubes, *Physics (Wuli)*, 34 (2005) 191.
- [21] N. G. Chopra, R. J. Luyken, K. Cherrey, V. H. Crespi, M. L. Cohen, S. G. Louie and A. Zettl, Boron nitride nanotubes, *Science*, 269 (1995) 966.
- [22] R. Ma, Y. Bando and T. Sato, Controlled synthesis of BN nanotubes, nanobamboos, and nanocables, *Adv. Mater.*, 14 (2002) 366.
- [23] T. Laude and Y. Matsui, Long ropes of boron nitride nanotubes grown by a continuous laser heating, *Appl. Phys. Lett.*, 76 (2000) 3239.
- [24] V. Pokropivny, V. V. Skorokhod, G. S. Oleinik, A. V. Kurdyumov, T. S. Bartnitskaya, A. V. Pokropivny, A. G. Sisonyuk and D. M. Scheichenko, Boron nitride analogs of fullerenes (the fulborenes), nanotubes, and fullerites (the fulborenites), *J. Solid State Chem.*, 154 (2000) 214.
- [25] W. Han, Y. Bando, K. Kurashima and T. Sato, Synthesis of boron nitride nanotubes from carbon nanotubes by a substitution reaction, *Appl. Phys. Lett.*, 73 (1998) 3085.
- [26] K. B. Shelimov and M. Moskovits, Composite nanostructures based on template-grown boron nitride nanotubes, *Chem. Mater.*, 12 (2000) 250.
- [27] O. R. Lourie, C. R. Jones, B. M. Bartlett, P. C. Gibbons, R. S. Ruoff and W. E. Buhro, CVD growth of boron nitride nanotubes, *Chem. Mater.*, 12 (2000) 1808.

- [28] Y. Chen, J. F. Gerald, J. S. Williams and S. Bulcock, Synthesis of boron nitride nanotubes at low temperatures using reactive ball mining, *Chem. Phys. Lett.*, 299 (1999) 260.
- [29] J. Goldberger, R. He, Y. Zhang, S. Lee, H. Yan, H.-J. Choi and P. Yang, Single-crystal gallium nitride nanotubes, *Nature*, 422 (2003) 599.
- [30] Q. Wu, Z. Hu, X. Wang, Y. Lu, X. Chen, H. Xu and Y. Chen, Synthesis and characterization of faceted hexagonal aluminium nitride nanotubes *J. Am. Chem. Soc.*, 125 (2003) 10176.
- [31] E. P. A. M. Bakkers and M. A. Verheijen, Synthesis of InP nanotubes, *J. Am. Chem. Soc.*, 125 (2003) 3440.
- [32] R. Fan, Y. Wu, D. Li, M. Yue, A. Majumdar and P. Yang, Fabrication of silica nanotube arrays from vertical silicon nanowire templates, *J. Am. Chem. Soc.*, 125 (2003) 5254.
- [33] J. H. Jung, H. Kobayashi, K. J. C. van Bommel, S. Shinkai and T. Shimizu, Creation of novel helical ribbon and double-layered nanotube TiO₂ structures using an organogel template, *Chem. Mater.*, 14 (2002) 1445.
- [34] S. M. Liu, L. M. Gan, L. H. Liu, W. D. Zhang and H. C. Zeng, Synthesis of single-crystalline TiO₂ nanotubes, *Chem. Mater.*, 14 (2002) 1391.
- [35] Z. R. Tian, J. A. Voigt, J. L. Liu, B. McKenzie and H. Xu, Large oriented arrays and continuous films of TiO₂-based nanotubes, *J. Am. Chem. Soc.*, 125 (2003) 12384.
- [36] X.-H. Zhang, S.-Y. Xie, Z.-Y. Jiang, X. Zhang, Z.-Q. Tian, Z.-X. Xie, R.-B. Huang and L.-S. Zheng, Rational design and fabrication of ZnO nanotubes from nanowire templates in a microwave plasma system, *J. Phys. Chem. B.*, 107 (2003) 10114.
- [37] J. Q. Hu, X. M. Mang, C. S. Lee and S. T. Lee, Thermal reduction route to the fabrication of coaxial Zn/ZnO nanocables and ZnO nanotubes, *Chem. Mater.*, 15 (2003) 305.

- [38] Y. J. Xing, Z. H. Xi, Z. Q. Xue, X. D. Zhang and J. H. Song, Optical properties of the ZnO nanotubes synthesised via vapor phase growth, *Appl. Phys. Lett.*, 83 (2003) 1689.
- [39] A. K. Rappe, C. J. Casewit, K. S. Colwell, W. A. Goddard and W. M. Skiff, Uff, a full periodic-table force-field for molecular mechanics and molecular-dynamics simulations, *J. Am. Chem. Soc.*, 114 (1992) 10024.
- [40] S. L. Mayo, B. D. Olafson and W. A. Goddard III, Dreiding: a generic force field for molecular simulations, *J. Phys. Chem.*, 94 (1990) 8897.
- [41] B. E. Poling, J. M. Prausnitz and J. O. O'Connell, *The Properties of Gases and Liquids*, McGraw-Hill, New York, 2001.
- [42] M. Rzepka, P. Lamp and M. Casa-Lillo, Physisorption of hydrogen on microporous carbon and carbon nanotubes, *J. Phys. Chem. B.*, 102 (1998) 10894.
- [43] M. S. Dresselhaus, K. A. Williams and P. C. Eklund, Hydrogen adsorption in carbon materials, *MRS Bull*, 24 (1999) 45.

List of symbols used in Chapter 8

PE	potential energy
ρ	distance from center of nanotube
C_6, C_{12}	attractive and repulsive Lennard-Jones constants ($C_k = 4\epsilon\sigma^k$)
σ	kinetic diameter
ϵ	well depth
η	atomic surface density
d	diameter of nanotube
T	temperature
R	universal gas constant
V_{ad}	volume free for adsorption

V_{bulk}	volume free for bulk gas
V_f	free volume within adsorbent ($=V_{ad} + V_{bulk}$)
p	pressure
v_0	occupied volume of closely packed gas molecules
n_{ad}	number of molecules in adsorbed phase
n_{bulk}	number of molecules in bulk gas phase
n	total number of molecule stored ($= n_{ad} + n_{bulk}$)
m	mass of individual gas molecule
M	mass of adsorbent
l	length of nanotube
V	total volume of nanotube
ρ_0	position at which $PE = 0$
\bar{v}	volumetric uptake (mass of gas over volume of adsorbent)
wt. %	gravimetric uptake (mass of gas over system mass)

Part IV

Physical aging in polymers

Chapter 9

Introduction to physical aging

9.1 Previous work

The leading membrane for industrial gas separation is the glassy polymer membrane. Glassy membranes are in a non-equilibrium state below their glass temperature T_g . A usual aging experiment is to quench the polymer from a temperature above the glass transition temperature T_g to a temperature below T_g causing the polymer to be in a non-equilibrium state. Over time the molecules within the polymer move toward equilibrium, with a consequent increase in density, and decrease in both free volume and molecular mobility, see Figure 9.1. This process is known as physical aging and affects many mechanical, physical, structural, and electrical properties, and more importantly gas separation and storage properties. Reviews of non-equilibrium behaviour and physical aging can be found in Tant and Wilkes [1], Struik [2] and Hutchinson [3]. Models that accurately describe the physical aging process are important for the prediction of the polymers performance over time and to provide some physical insight to guide possible preventions of aging. In this chapter existing models of physical aging are reviewed.

The usual measure of physical aging is the change of specific volume V (volume/mass) over time which is generally modelled as the departure from equilibrium δ , see Figure 9.1. A successful model needs to accurately describe the initial departure from equilibrium δ_0 and the gradual relaxation to equilibrium which are dependent on many factors such as the temperature, the quench rate and the sample thickness.

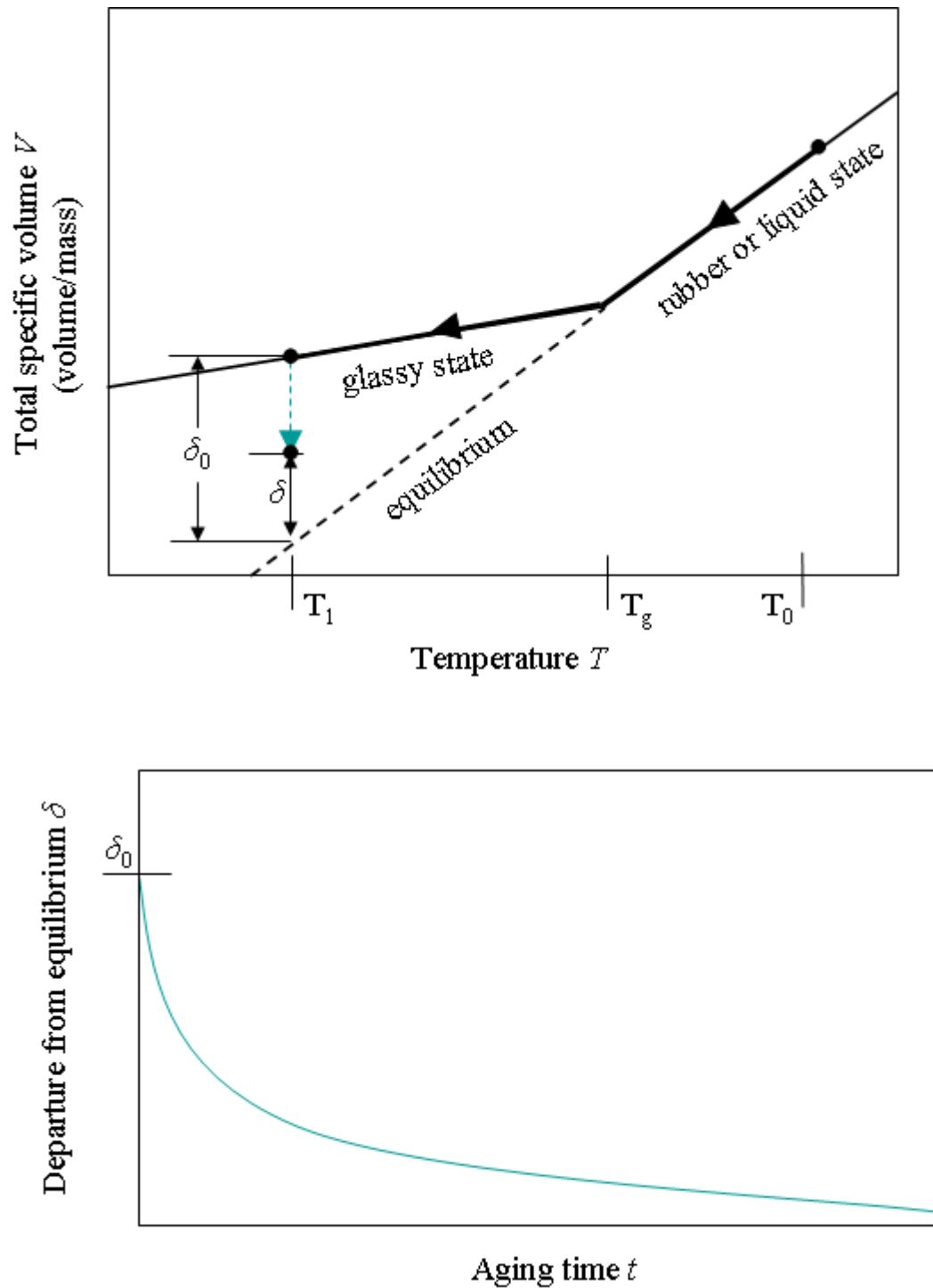


Figure 9.1: Diagrams of the physical aging process after a quench from T_0 (above T_g) to T_1 (below T_g).

9.1.1 Kovacs Model

Kovacs [4] who performed a large range of experiments initially proposed the first-order equation,

$$\frac{d\delta}{dt} = -\frac{\delta}{\tau}, \quad (9.1)$$

to match the experimental data where τ is known as the relaxation time. Equation 9.1 has become the basis for other physical aging models such as the Struik model [2], the KAHR model [5] and the constitutive kinetic equation [6-12].

9.1.2 Struik Model

Struik [2] built on Kovacs' theory of isothermal volume relaxation (Equation 9.1) by defining a relation for the relaxation time as follows,

$$\ln \tau = \ln \tau_{\infty} - \gamma \delta, \quad (9.2)$$

where γ is a constant, and τ_{∞} is the value of τ at equilibrium. The combination of this relation with Equation 9.1 yields the following first-order differential equation,

$$\frac{d\delta}{dt} = -\frac{\delta}{\tau_{\infty} \exp(-\gamma \delta)}, \quad (9.3)$$

which can be solved to yield the implicit solution,

$$E_1(-\gamma \delta) - E_1(-\gamma \delta_0) = \frac{t}{\tau_{\infty}}, \quad (9.4)$$

where δ_0 is the initial departure from equilibrium and $E_1(x)$ is the exponential integral,

$$E_1(x) = \int_x^{\infty} \frac{\exp(-u)}{u} du. \quad (9.5)$$

The Struik model has been used to successfully model aging data [13, 14], examples are shown in Figure 9.2. In addition, it has been shown that the parameters correlate to temperature and thickness by Huang, Wang and Paul [13], see Figure 9.3. Therefore, by extrapolating these fits (linear and polynomial) one can predict the aging properties with differing temperature and sample thickness.

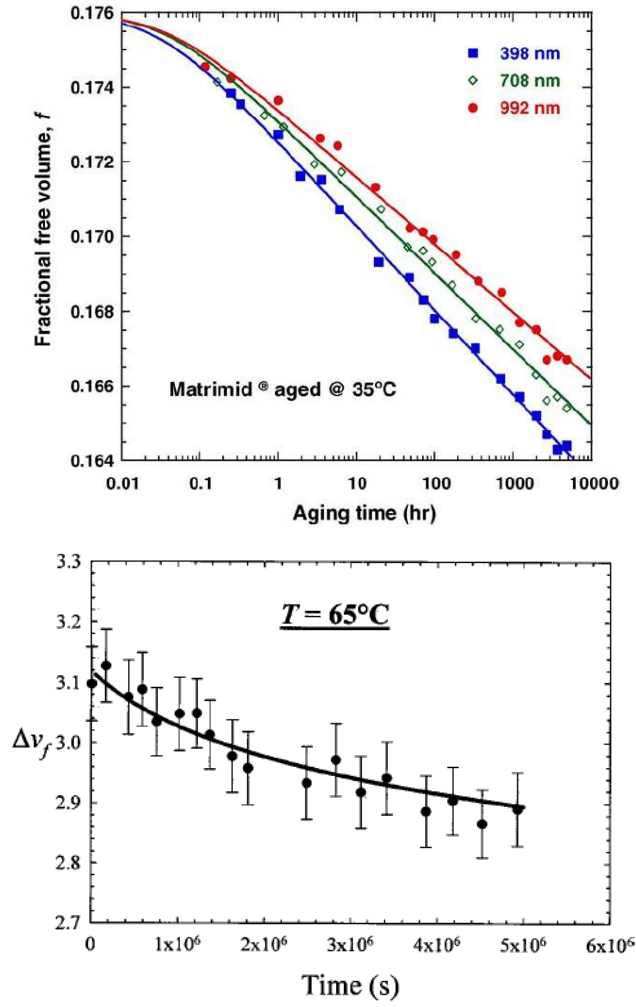


Figure 9.2: The Struik model fitted to various aging data. Taken from Huang et al. [13] (top) and from Cangialosi et al. [15] (bottom).

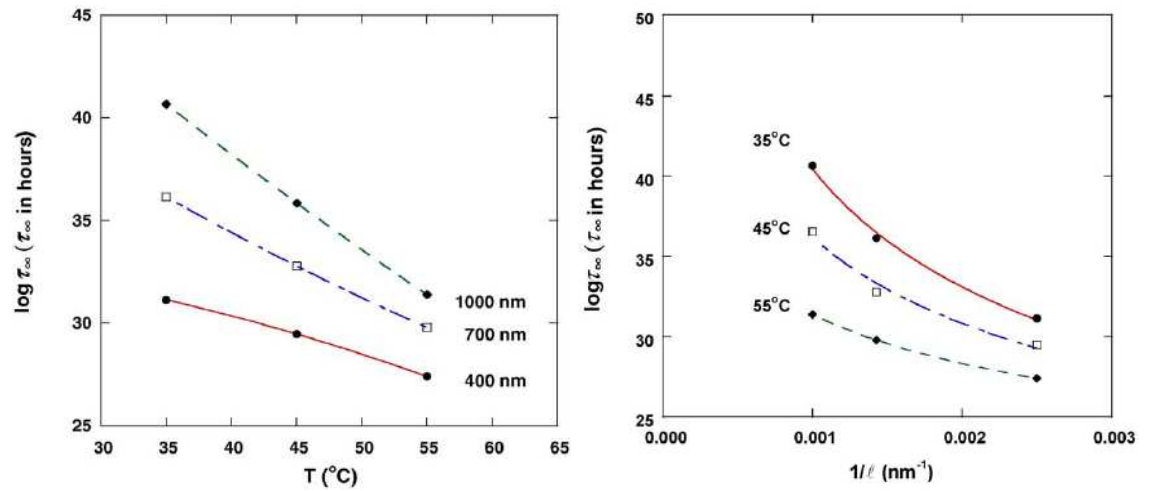


Figure 9.3 (continued to next page)

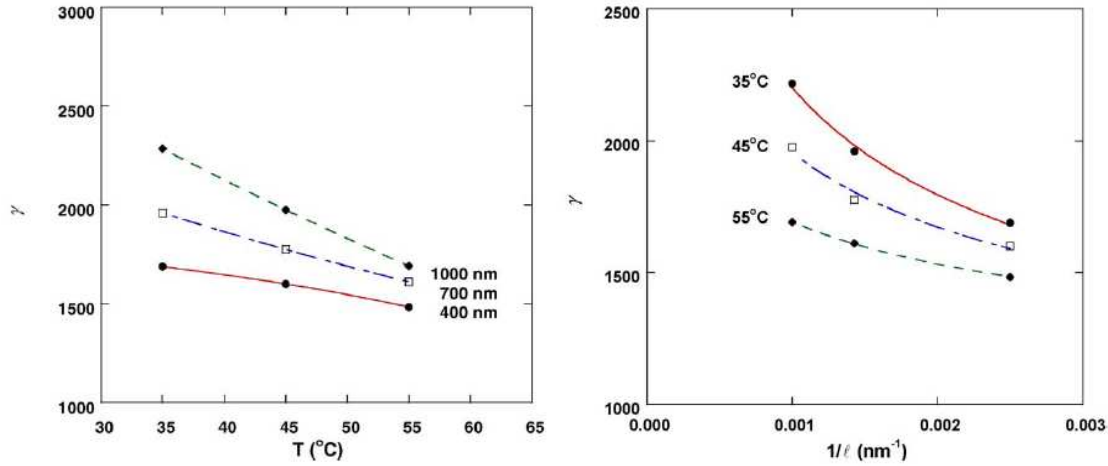


Figure 9.3: Relationships between the parameters of the Struik model and temperature and film thickness. Taken from Huang et al. [13].

9.1.3 Constitutive kinetic equation

With the Kovacs' equation as the basis, the dependence of the relaxation time was found to rely on the temperature and the structure pioneered by Tool [16], Narayanaswamy [17], Rekhson [6], Moynihan et al. [7] and Hodge et al. [8-12]. Although it was originally expressed in terms of the fictive temperature, here it is expressed in terms of the departure from equilibrium δ ,

$$\frac{d\delta}{dt} = -\frac{\delta}{\tau(T, \delta)}, \quad (9.6)$$

$$\tau(T, \delta) = \tau_r \exp[-\theta(T - T_r)] \exp[-(1-x)\theta\delta / \Delta\alpha_T],$$

where τ_r is the relaxation time in equilibrium at the reference temperature T_r , θ is a material constant and x is a partition parameter ($0 \leq x \leq 1$) which determines the contributions of temperature (T) and structure (δ) to the relaxation time $\tau(T, \delta)$. Finally, $\Delta\alpha_T$ is the difference between the thermal expansion coefficients in the liquid and glassy state. This form of the constitutive kinetic equation was developed by Kovacs, Aklonis, Hutchinson and Ramos (KAHR) [5] which is the basis for the KAHR model, see Section 9.1.4. Equation 9.6 allows the modelling of a single relaxation unit and can also be used to model the relaxation of a material which is believed to be the contribution of many relaxation units. One method of achieving this is by causing the total relaxation time τ to depend on the distribution of relaxation times (corresponding to the many relaxation units) expressed continuously with a stretched exponential function,

$$\phi(t) = \exp[-(t/\tau)^\beta], \quad (9.7)$$

developed by Kohlrausch [18], Williams and Watts [19], where β ($0 \leq \beta \leq 1$) is inversely proportional to the width of the distribution and where $\beta = 1$ represents a single relaxation unit (a solution to Equation 9.1). An alternative approach to incorporating the distribution of relaxation units is offered by Kovacs, Aklonis, Hutchinson and Ramos [5], as outlined in the following section.

9.1.4 Kovacs, Aklonis, Hutchinson and Ramos (KAHR) model

The KAHR model considers the total relaxation of the material as the sum of a discrete number (N) of relaxation units where the total departure from equilibrium δ can be derived from the following system of equations,

$$\delta = \sum_{i=1}^N \delta_i, \quad (9.8)$$

$$\frac{d\delta_i}{dt} = -\frac{\delta_i}{\tau_i(T, \delta)}, \quad (9.9)$$

$$\tau_i(T, \delta) = \tau_{i,r} \exp[-\theta(T - T_r)] \exp[-(1-x)\theta\delta / \Delta\alpha_T], \quad (9.10)$$

where the parameters are as defined above in Section 9.1.3 and the subscript i refers to an individual relaxation unit. Initially, each relaxation unit contributes a fraction of g_i to

the total departure from equilibrium, i.e. $\delta_i(0) = g_i \delta(0)$, where $\sum_{i=1}^N g_i = 1$. Further, each

relaxation unit is assigned an equilibrium relaxation time $\tau_{i,r}$ causing each relaxation unit to relax at different rates. Figure 9.4 demonstrates an example of how each relaxation unit δ_i and their corresponding relaxation times τ_i change after each time step (a-d). For this example, each relaxation unit contributes the same amount of departure from equilibrium, i.e. $g_i = 1/N$. The relaxation unit corresponding to $i = 1$ has the lowest relaxation time and therefore relaxes the fastest to equilibrium. It has been suggested that the distribution of relaxation units could possibly represent the distribution of free volume elements, measurable by techniques such as PALS or photochromic spectroscopy.

The KAHR model has the capacity to model the relaxation (contraction) after a temperature quench and also an expansion after a temperature rise, as demonstrated for various temperature jumps ΔT in Figure 9.5. An advantage of the KAHR model is in its

transparency in that the relaxation of each unit can be observed throughout the aging process.

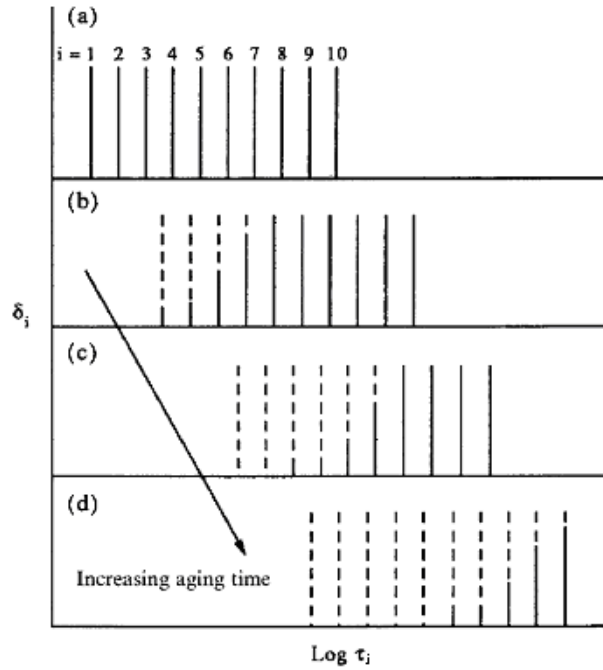


Figure 9.4: Schematic example of how each relaxation unit's contribution δ_i changes over time with the corresponding relaxation times τ_i . Taken from Hutchinson. [3].

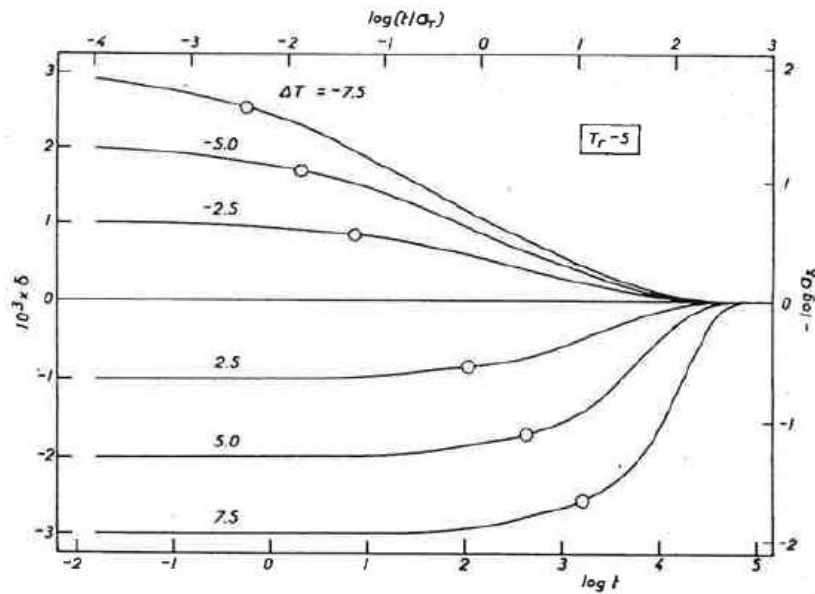


Figure 9.5: KAHR model predictions of the relaxation (contraction) process after a temperature quench $\Delta T < 0$ and the expansion process after a temperature rise $\Delta T > 0$.

9.1.5 Dorkenoo and Pfromm model

Physical aging has been shown to depend on the membrane thickness and therefore a model that explains and predicts this phenomena is highly desirable. Dorkenoo and Pfromm [20] developed a thickness-dependent physical aging model that is based on several well known functions arising from works such as Doolittle [21], Cohen and Turnbull [22], Kovacs [4] and Keddie et al. [23]. The important component of the model is the thickness-dependent glass transition temperature [23] expressed as

$$T_g(l) = T_{g0} \left[1 - \left(\frac{a_0}{l} \right)^{b_0} \right], \quad (9.11)$$

where l is the sample thickness, T_{g0} is the glass transition temperature of a thick film, and a_0 and b_0 are adjustable parameters. The physical consequence of this dependence is demonstrated in Figure 9.6, where the initial departure from equilibrium depends on the film thickness. With permeability P as the chosen aging property the following model was developed,

$$P = P_0 \exp \left(- \frac{\beta}{S(x) - S_0} \right), \quad (9.12)$$

$$S(x) = F_0(x) + \gamma F_1(x) + \gamma^2 F_2(x) + \gamma^3 F_3(x) + O(\gamma^4), \quad (9.13)$$

$$F_0(x) = S(0)e^{-x}, \quad (9.14)$$

$$F_1(x) = S(0)e^{-x} \ln \left(\frac{S_0 - S(0)e^{-x}}{S_0 - S(0)} \right), \quad (9.15)$$

$$F_2(x) = S(0)e^{-x} \left\{ - \frac{S_0^2(1 - e^{-x})}{[4S_0 - S(0)][4S_0 - S(0)e^{-x}]} - \frac{1}{2} \ln \left(\frac{S_0 - S(0)e^{-x}}{S_0 - S(0)} \right) + \frac{1}{2} \ln^2 \left(\frac{S_0 - S(0)e^{-x}}{S_0 - S(0)} \right) \right\} \quad (9.16)$$

$$F_3(x) = S(0)e^{-x} \left\{ \frac{S_0 S(0)(1 - e^{-x})}{S_0 - S(0)e^{-x}} \left[\frac{S(0)e^{-x}}{[4S_0 - S(0)][4S_0 - S(0)e^{-x}]} \right] - \frac{S_0 S(0)(1 - e^{-x})}{[4S_0 - S(0)]^2 [4S_0 - S(0)e^{-x}]} \right\}$$

$$\begin{aligned}
& + \ln \left(\frac{S_0 - S(0)e^{-x}}{S_0 - S(0)} \right) \left[-\frac{1}{6} + \frac{S(0)e^{-x} [S_0 - 2S(0)e^{-x}]}{2[S_0 - S(0)e^{-x}]^2} \right] \\
& + \frac{S_0^2(1 - e^{-x})}{[4S_0 - S(0)]^2 [4S_0 - S(0)e^{-x}]} \\
& + \ln^2 \left(\frac{S_0 - S(0)e^{-x}}{S_0 - S(0)} \right) \left[\frac{S_0^2 - S_0 S(0)e^{-x} + S(0)^2 e^{-2x}}{2[S_0 - S(0)e^{-x}]} \right] \\
& - \frac{1}{6} \ln^3 \left(\frac{S_0 - S(0)e^{-x}}{S_0 - S(0)} \right) \Bigg\}, \tag{9.17}
\end{aligned}$$

$$x = \frac{t}{\exp \left[\frac{E_h [T_g(l) - T]}{R T T_g(l)} - \frac{\left(\frac{b_1}{f_g} \right) (T - T_g(l))}{\left(\frac{f_g}{\alpha_g} \right) + T - T_g(l)} \right] \tau_g}, \tag{9.18}$$

$$S_0 = v_0 - v_\infty \quad \text{and} \quad \gamma = \frac{b_1 v_\infty}{v_\infty - v_0}, \tag{9.19}$$

where v_0 is the occupied volume, v_∞ is the equilibrium volume, E_h is the activation energy for the movement of defects, and P_0 , β , b_1 , f_g , τ_g and α_g are constants. This model has been successfully fitted to permeability aging data; an example of this is shown in Figure 9.7. However, because of its complex form and its many adjustable parameters the model has not been widely adopted.

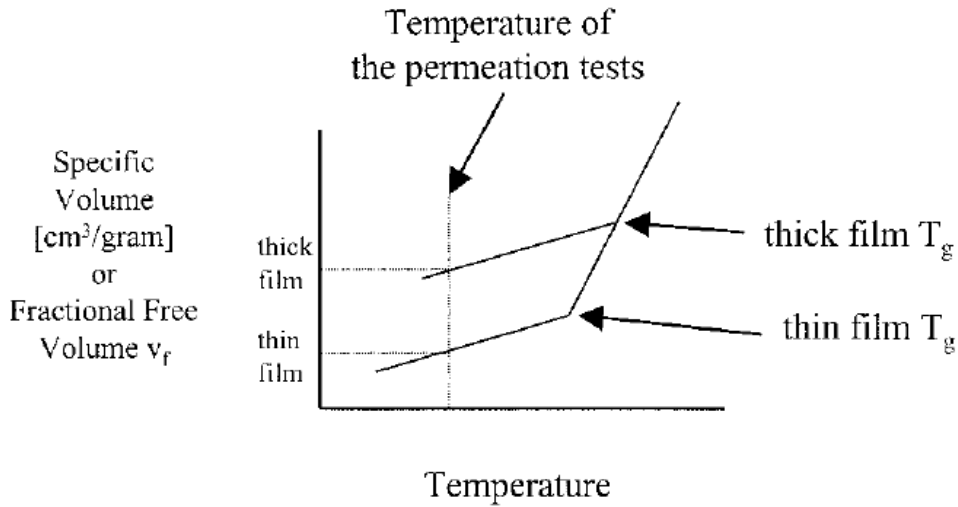


Figure 9.6: Schematic of the thickness-dependent glass transition temperature. Taken from Dorkenoo and Pfromm [20].

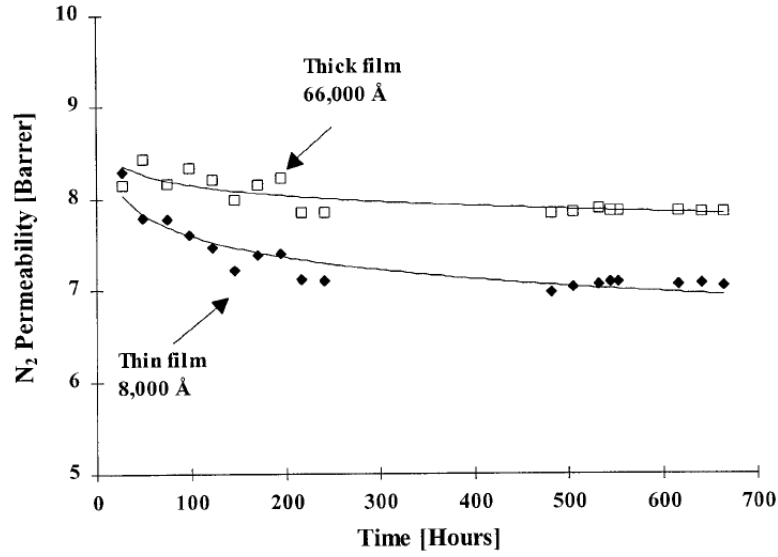


Figure 9.7: Dorkenoo and Pfromm model fit to experimental N_2 permeability results for a thin and thick film during the aging time. Taken from Dorkenoo and Pfromm [20].

9.1.6 Zhou, Chung, Wang and Goh (ZCWG) model

An alternative thickness-dependent aging model has been established by Zhou et al. [24] based upon chain mobility equations, free volume theory and a newly proposed empirical thickness-dependent component. The derivation begins by using Park and Paul's [25] expression for permeability with respect to fractional free volume (FFV),

$$P = A_1 \exp(-B_1 / FFV), \quad (9.20)$$

where A_1 and B_1 are constants for a particular gas. According to free volume theory [2, 21, 22, 26-28] the chain mobility can be expressed as,

$$\ln M = A_2 - \frac{k(T)}{FFV^\gamma} + \phi(T), \quad (9.21)$$

where A_2 is a constant, $k(T)$ is a non-increasing function of temperature, γ is a positive exponent and $\phi(T)$ is an increasing function of temperature. Finally, Struik and Kovacs [2, 4] suggested that the mobility is proportional to the reciprocal of the aging time in the following way,

$$M \propto \frac{B_2}{t}, \quad (9.22)$$

where B_2 is a constant and t is the aging time. By setting γ equal to unity which was empirically determined by Doolittle [29], Turnbull, and Cohen [27], Equations 9.20-9.22 are combined to create the ZCWG equation,

$$\ln P = A + B(T) \ln t, \quad (9.23)$$

where A is a constant and $B(T)$ is a function of temperature which is also shown to be heavily dependent on the sample thickness l and therefore an empirical equation was proposed of the form

$$B(T) = a - b \ln(1/l^2), \quad (9.24)$$

where a and b are constants. An example of the ZCWG model which is used to fit permeability aging data is shown in Figure 9.8. This model is easier to use than the other models but there are too many adjustable parameters and the model has not been widely verified by use in the literature. Additionally, it is unable to mimic the cross over behaviour of thin films $< 1 \mu\text{m}$ found in Huang and Paul's [30] experiments.

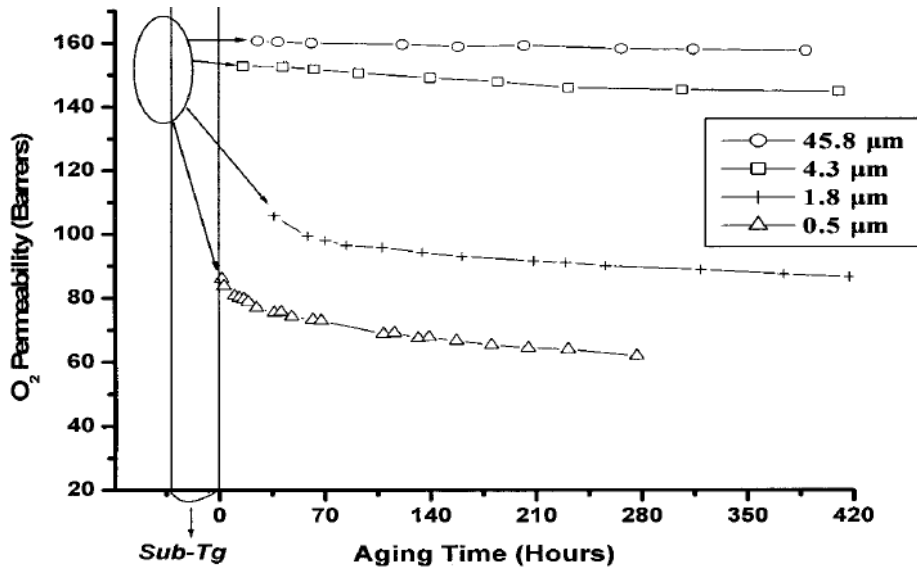


Figure 9.8: The ZCWG model fit to experimental O_2 permeability results during aging time. Taken from Zhou et al. [24].

9.1.7 Curro, Lagasse and Simha (CLS) vacancy diffusion model

Alfrey et al. [31] first suggested that during aging, vacancies were diffusing to or from the external surface where they would be annihilated or created. This diffusion process can be described by the well-known partial differential equation for one-dimensional diffusion,

$$\frac{\partial f}{\partial t} = \frac{\partial}{\partial x} \left(D \frac{\partial f}{\partial x} \right), \quad (9.25)$$

where $f = f(x,t)$ is the fractional free volume at position x and at time t , and D is the diffusion coefficient (or diffusivity), schematically shown in Figure 9.9. Curro, Lagasse and Simha (CLS) [32] used Equation 9.25 with the diffusion coefficient in the form of the Doolittle relation,

$$D = D_r \exp\left[-B\left(f^{-1} - f_r^{-1}\right)\right], \quad (9.26)$$

where B is a material constant, and D_r is the diffusivity and f_r is the fractional free volume at the reference temperature. This model was shown to match the KAHR model results [4, 5] for the aging of polyvinylacetate (PVAc), shown in Figure 9.10.

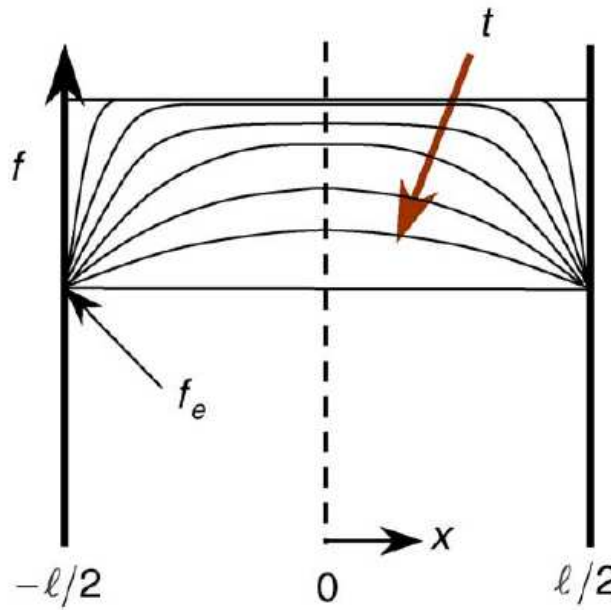


Figure 9.9: Schematic of the fractional free volume relaxation towards equilibrium f_e within a membrane of thickness l . Taken from Huang et al. [13].

CLS found that the model did not match the data if the assumption that the vacancies diffuse to the external surface was held. CLS suggested three alternative mechanisms which may occur simultaneously with vacancy diffusion. These three are lattice contraction, internal annihilation of vacancies, and density fluctuations. McCaig et al. [33] combined the vacancy diffusion model with a lattice contraction component to successfully model aging data within films of thicknesses from 0.25 to 33 μm , reviewed in the following section.

The CLS vacancy diffusion model is a simple model that provides a conceptual explanation for the physical aging phenomena. However, vacancy diffusion to the external surface does not explain all the experimental data and therefore the model needs to be modified or combined with other aging mechanisms.

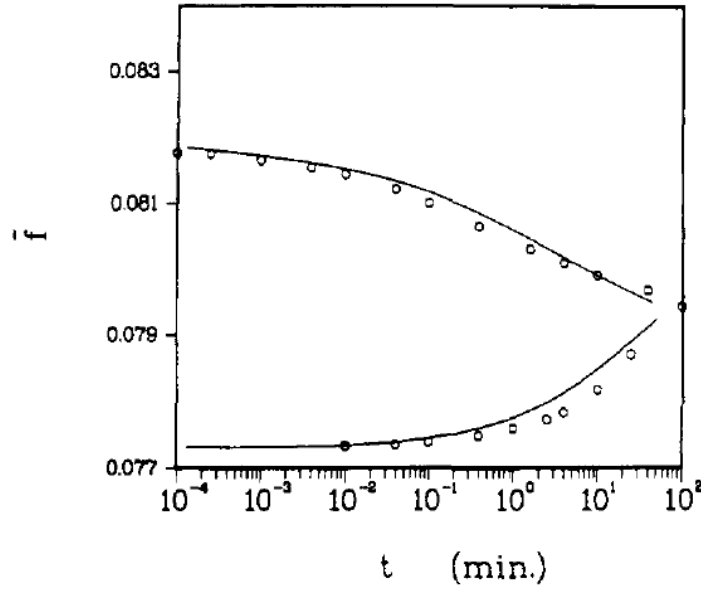


Figure 9.10: The CLS vacancy diffusion model (curves) and the KAHR model results (circles) for the relaxation and expansion in average fractional free volume within PVAc. Taken from Curro et al. [32].

9.1.8 McCaig, Paul and Barlow (MPB) dual mechanism model

McCaig et al. [33, 34] performed oxygen permeability experiments after an immediate quench with films of thickness ranging from 0.25 to 33 μm , and found that the vacancy diffusion mechanism alone was incapable of modelling the data. Therefore, a lattice contraction component was included to form a dual mechanism model which is labelled here as the MPB model, illustrated in Figure 9.11. The total fractional free volume is expressed as

$$f = f_i - \Delta f_{LC} - \Delta f_D, \quad (9.27)$$

where f_i is the initial fractional free volume, $\Delta f_{LC} (= f_i - f_{LC}^*)$ is the amount of free volume lost due to lattice contraction and $\Delta f_D (= f_i - f_D)$ is the amount of free volume lost due to vacancy diffusion. The lattice contraction free volume is modelled according to the Hirai and Eyring [35] equation,

$$f_{LC}^* = f_g + (f_i - f_g) e^{-t/\tau}, \quad (9.28)$$

where f_g is the fractional free volume at the glass transition temperature and τ is a relaxation time. As in the previous section, the vacancy diffusion free volume is modelled according to the differential equation,

$$\frac{\partial f_D}{\partial t} = \frac{\partial}{\partial x} \left(D \frac{\partial f_D}{\partial x} \right), \quad (9.29)$$

where D is the diffusion coefficient as defined by the Doolittle expression (Equation 9.26).

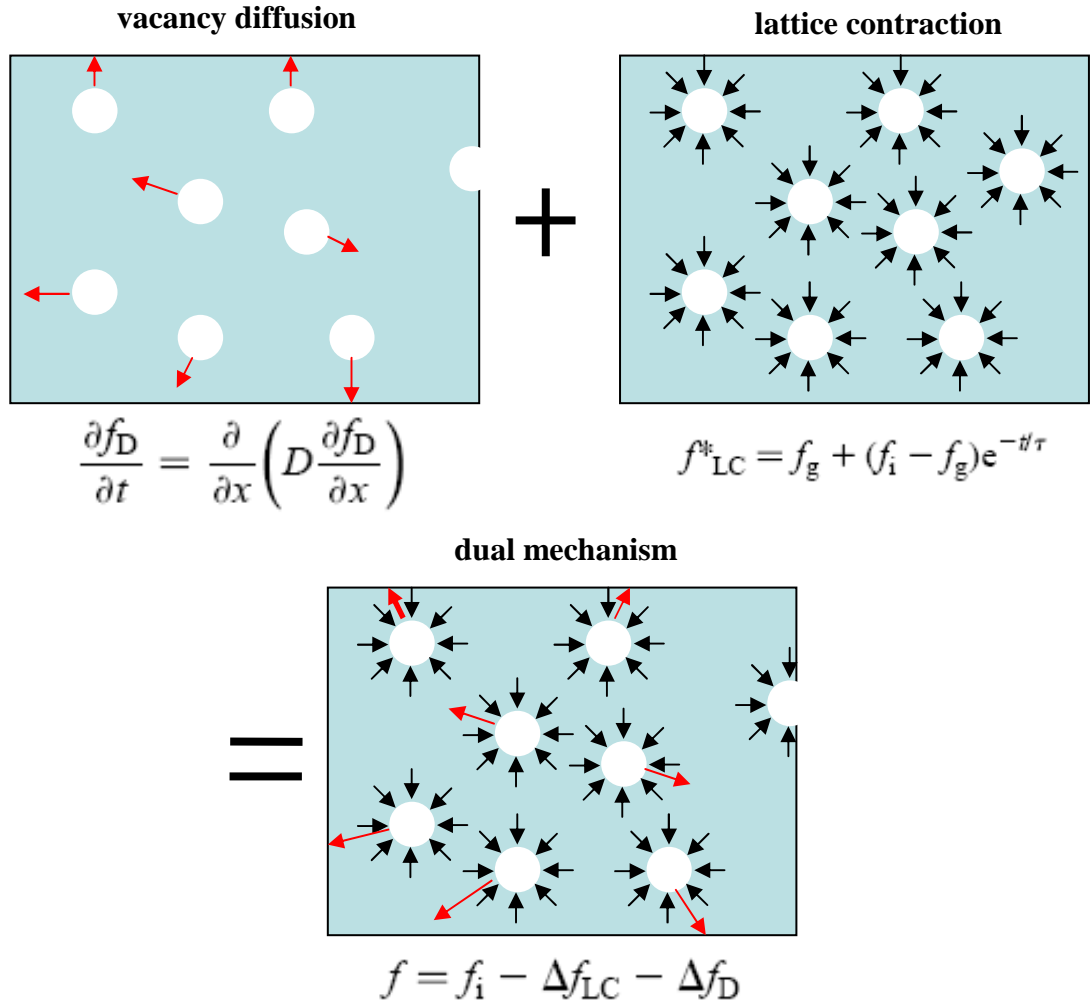


Figure 9.11: MPB dual vacancy diffusion and lattice contraction model.

The MPB dual mechanism model successfully followed the decreasing trend of permeability during the aging time and provided some insight into the physical aging process, see Figure 9.12. According to the model, the aging of the thicker films ($l > 2.5 \mu\text{m}$) is primarily due to the lattice contraction component, because of the large distances that the internal vacancies have to travel to reach the external surface causing vacancies to decrease in size before annihilation at the edges. While the aging of the thinner films ($l < 2.5 \mu\text{m}$) is mainly due to the vacancy diffusion component, since vacancies

disappear at the surface much quicker because of the shorter travelling distance. This intuitive model is satisfactory for these experiments but was incapable of modelling other aging experiments by the same group [30]. Therefore, a modified model that explains all the experimental results is highly desirable.

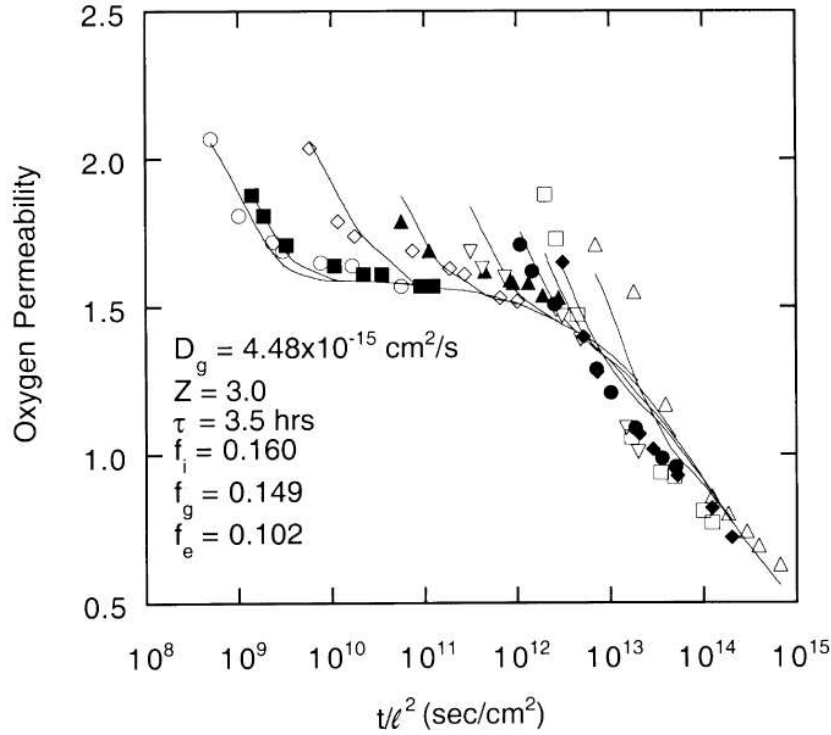


Figure 9.12: The MPB dual mechanism model (curves) fitted to experimental O_2 permeability data within films of thicknesses (\circ) 33 μm , (\blacksquare) 28 μm , (\diamond) 9.7 μm , (\blacktriangle) 4.4 μm , (∇) 1.85 μm , (\bullet) 0.99 μm , (\square) 0.74 μm , (\blacklozenge) 0.58 μm and (\triangle) 0.25 μm .

9.2 Thesis work overview

In Chapter 10 the CLS vacancy diffusion model with an alternative diffusion coefficient to the Doolittle relation (found in Chapter 4 [36]) is presented which gives rise to a new Empirically-derived Vacancy Diffusion (EVD) model. This EVD model is an approximate analytical solution that satisfies the vacancy diffusion equation (Equation 9.24), and the initial and boundary conditions. An analytical solution allows the user to fit and predict data without having to numerically solve complex partial differential equations as is the case for the current CLS, KAHR and MPB models. Determination of the best fit parameters is easily found through a least squares algorithm when an analytical solution is available. This new approach offers significant advantage given that there is presently no method to determine the best fit parameters when fitting a

numerical solution to data, according to the best of our knowledge. Furthermore, physical aging data [30] for thin films ($< 1\ \mu\text{m}$) are accurately described by the model, indicating that the vacancy diffusion mechanism is dominant in these films. However, thick films ($> 1\ \mu\text{m}$) are not described by the model and hence vacancy diffusion to the external surface is not the dominant aging mechanism. Finally, the new vacancy diffusion model is combined with the new gas diffusion model to investigate the transport process with in an aging polymer sample during the uptake and release of gas.

References

- [1] M. R. Tant and G. L. Wilkes, An overview of the non-equilibrium behavior of polymer glasses, *Polym. Eng. Sci.*, 21 (1981) 874.
- [2] L. C. E. Struik, *Physical Aging in Amorphous Polymers and other Materials*, Elsevier, Amsterdam, 1978.
- [3] J. M. Hutchinson, Physical aging of polymers, *Prog. Polym. Sci.*, 20 (1995) 703.
- [4] A. J. Kovacs, *Fortschr. Hochpolym. Forsch. (Adv. in Polym. Sci.)*, 3 (1964) 394.
- [5] A. J. Kovacs, J. J. Aklonis, J. M. Hutchinson and A. R. Ramos, Isobaric volume and enthalpy recovery of glasses. II. A transparent multiparameter theory, *J. Polym. Sci., Polym. Phys. Ed.*, 17 (1979) 1097.
- [6] S. M. Rekhson, A. V. Bulaeva and O. V. Mazurin, *Izv. Akad. Nauk. SSR., Neorg. Mater.*, 7 (1971) 714.
- [7] M. A. DeBolt, A. J. Easteal, R. B. Macedo and C. T. Moynihan, Analysis of structural relaxation in glass using rate heating data, *J. Am. Ceram. Soc.*, 59 (1976) 16.
- [8] I. M. Hodge, Effects of annealing and prior history on enthalpy relaxation in glassy-polymers. 4. Comparison of 5 polymers, *Macromolecules*, 16 (1983) 898.
- [9] I. M. Hodge, Effects of annealing and prior history on enthalpy relaxation in glassy-polymers. 3. Experimental and modeling studies of polystyrene, *Macromolecules*, 16 (1983) 371.

- [10] I. M. Hodge, Effects of annealing and prior history on enthalpy relaxation in glassy-polymers. 6. Adam-gibbs formulation of nonlinearity, *Macromolecules*, 20 (1987) 2897.
- [11] I. M. Hodge and A. R. Berens, Effects of annealing and prior history on enthalpy relaxation in glassy-polymers. 2. Mathematical-modeling, *Macromolecules*, 15 (1982) 762.
- [12] I. M. Hodge and A. R. Berens, Effects of annealing and prior history on enthalpy relaxation in glassy-polymers. 5. Mathematical-modeling of nonthermal preaging perturbations, *Macromolecules*, 18 (1985) 1980.
- [13] Y. Huang, X. Wang and D. R. Paul, Physical aging of thin glassy polymer films: Free volume interpretation, *J. Membr. Sci.*, 277 (2006) 219.
- [14] D. Cangialosi, M. Wubbenhorst, J. Groenewold, E. Mendes and S. J. Picken, Diffusion mechanism for physical aging of polycarbonate far below the glass transition temperature studied by means of dielectric spectroscopy, *J. Non-Cryst. Solids*, 351 (2005) 2605.
- [15] D. Cangialosi, M. Wubbenhorst, H. Schut, A. Van Veen and S. J. Picken, Dynamics of polycarbonate far below the glass transition temperature: A positron annihilation lifetime study, *Phys. Rev. B: Condens. Matter*, 69 (2004) 134206.
- [16] A. M. Tool, Relation between inelastic deformability and thermal expansion of glass in its annealing range, *J. Am. Ceram. Soc.*, 29 (1946) 240.
- [17] O. S. Narayanaswamy, Model of structural relaxation in glass, *J. Am. Chem. Soc.*, 54 (1971) 491.
- [18] F. Kohlrausch, *Annalen der Physik und Chemie*, 128 (1866) 1.
- [19] G. Williams and D. C. Watts, Non-symmetrical dielectric relaxation behaviour arising from a simple empirical decay function, *Trans. Faraday Soc.*, 66 (1970) 80.

- [20] K. D. Dorkenoo and P. H. Pfromm, Experimental evidence and theoretical analysis of physical aging in thin and thick amorphous glassy polymer films, *J. Polym. Sci., Part B: Polym. Phys.*, 37 (1999) 2239.
- [21] A. K. Doolittle, Studies in newtonian flow. II. The dependence of the viscosity of liquids on free-space, *J. Appl. Phys.*, 22 (1951) 1471.
- [22] M. H. Cohen and D. Turnbull, Molecular transport in liquids and glasses, *J. Chem. Phys.*, 31 (1959) 1164.
- [23] J. L. Keddie, R. A. L. Jones and R. A. Cory, Size-dependent depression of the glass transition temperature in polymer films, *Europhys. Lett.*, 27 (1994) 59.
- [24] C. Zhou, T.-S. Chung, R. Wang and S. H. Goh, A governing equation of physical aging of thick and thin fluoropolyimide films *J. Appl. Polym. Sci.*, 92 (2004) 1758.
- [25] J. Y. Park and D. R. Paul, Correlation and prediction of gas permeability in glassy polymer membrane materials via a modified free volume based group contribution method, *J. Membr. Sci.*, 125 (1997) 23.
- [26] M. L. Williams, R. F. Landel and J. D. Ferry, The temperature dependence of relaxation mechanisms in amorphous polymers and other glass-forming liquids, *J. Am. Chem. Soc.*, 77 (1955) 3701.
- [27] D. Turnbull and M. H. Cohen, Free-volume model of amorphous phase - Glass transition, *J. Chem. Phys.*, 34 (1961) 120.
- [28] R. E. Robertson, Theory of plasticity of glassy polymers, *J. Chem. Phys.*, 44 (1966) 3950.
- [29] A. K. Doolittle, Studies in newtonian flow. I. The dependance of the viscosity of liquids on temperature, *J. Appl. Phys.*, 22 (1951) 1031.
- [30] Y. Huang and D. R. Paul, Physical aging of thin glassy polymer films monitored by gas permeability, *Polymer*, 45 (2004) 8377.

- [31] T. Alfrey, G. Goldfinger and H. Mark, The apparent second-order transition point of polystyrene, *J. Appl. Phys.*, 14 (1943) 700.
- [32] J. G. Curro, R. R. Lagasse and R. Simha, Diffusion model for volume recovery in glasses, *Macromolecules*, 15 (1982) 1621.
- [33] M. S. McCaig, D. R. Paul and J. W. Barlow, Effect of film thickness on the changes in gas permeability of a glassy polyarylate due to physical aging, Part II. Mathematical model, *Polymer*, 41 (2000) 639.
- [34] M. S. McCaig and D. R. Paul, Effect of film thickness on the changes in gas permeability of a glassy polyarylate due to physical aging Part I. Experimental observations, *Polymer*, 41 (2000) 629.
- [35] N. Hirai and H. Eyring, Bulk viscosity of liquids, *J. Appl. Phys.*, 29 (1958) 810.
- [36] A. W. Thornton, K. M. Nairn, A. J. Hill, J. M. Hill and Y. Huang, New relation between diffusion and free volume: II. Predicting vacancy diffusion, *J. Membr. Sci.*, 338 (2009) 38.

List of symbols used in Chapter 9

T_g	glass transition temperature
δ_0	initial departure from equilibrium
δ	departure from equilibrium
T_0, T_1	temperatures at which the sample is quenched from and to
t	aging time
τ	relaxation time parameter
l	sample thickness
T_r	reference temperature
$\Delta\alpha_T$	difference between thermal expansion coefficients
ΔT	temperature jump
T_{g0}	glass transition temperature of thick film

P	permeability
F_i	functions for the Dorkenoo and Pfromm model
FFV	fractional free volume
M	mobility of polymer chains
f	generalized free volume (various definitions)
f_D	free volume for vacancy diffusion
f_{LC}	free volume for lattice contraction
f_i	initial free volume
f_g	free volume at glass transition temperature
D	diffusivity (diffusion coefficient)

Chapter 10

Vacancy diffusion model

10.1 Introduction

It has been suggested that physical aging is a result of vacancies (cavities, holes or pores) travelling to the external surface where they disappear and therefore can cause an increase in density. The Doolittle relation $D = A \exp(-B/f)$ where f is the fractional free volume and A and B are constants, has been used in previous work to describe the diffusion coefficient D (diffusivity) for vacancy transport. In Chapter 4 a new empirically determined relation has been suggested as an alternative to the Doolittle relation, and this new relation has been shown to accurately model gas permeability data over a wide range of polymeric free volume. This new relation takes the form $D = \alpha \exp(\beta f)$ with α and β as constants. Here it is shown that when the Doolittle relation is replaced with the new relation an exact analytical solution exists to the differential equation that governs the fractional free volume behaviour throughout the sample during physical aging leading to an Empirically-determined Vacancy Diffusion (EVD) model for physical aging. An approximate analytical solution based on the exact solution is then compared to experimental data and other popular models such as the Kovacs, Aklonis, Hutchinson and Ramos (KAHR) phenomenological model and the Curro, Lagasse and Simha (CLS) vacancy diffusion model. This EVD model is also combined with a lattice contraction model to form a dual lattice contraction and vacancy diffusion model which is compared with McCaig, Paul and Barlow's (MPB) experimental results, showing a good correlation. Further support for the new EVD model is revealed by its similarity with the early established constitutive kinetic equation. Previous aging models are complicated and difficult to implement, therefore, a model that is easy to implement and physically meaningful such as this EVD model is highly sought after. An application of the model reveals that vacancy diffusion to the

external surface is the dominant aging mechanism within polysulfone thin films ($< 1 \mu\text{m}$), but not within the thick films ($> 1 \mu\text{m}$). Additionally, the model is used to predict the gas transport within an aging polymer.

10.2 New empirically-derived vacancy diffusion model

First the one dimensional diffusion equation which CLS and MPB used is solved with the new empirically derived diffusion coefficient [1] for vacancies in the form,

$$D = \alpha \exp(\beta f_D), \quad (10.1)$$

where D is the diffusion coefficient, α and β are constants, and f_D is the fractional free volume governed by vacancy diffusion such that $f_0 - f_D$ is the free volume lost to the surface by diffusion, where f_0 is the initial fractional free volume. The one dimensional vacancy diffusion equation can be created,

$$\frac{\partial f_D}{\partial t} = \frac{\partial}{\partial x} \left(D \frac{\partial f_D}{\partial x} \right). \quad (10.2)$$

where t is time and x is the position across the sample. For this equation, an exact solution is available by the method of separation ($f(x,t)=Q(x)+R(t)$) accomplished by Polyanin and Zaitsev [2],

$$f_D(x,t) = \ln \left(\frac{c_1 + c_2 x - c_3 x^2}{c_4 + 2\alpha c_3 t} \right) / \beta, \quad (10.3)$$

where c_1 to c_4 are constants. Equation 10.3 is the EVD equation for the one dimensional problem. Here this solution is manipulated so as to fit initial and boundary conditions of a typical aging experiment where a sample is heated above the glass transition temperature T_g and is then rapidly cooled to a temperature below T_g . The sample has an initial fractional free volume of f_0 and gradually approaches towards an equilibrium fractional free volume of f_e , as illustrated in Figure 9.9. Initial and boundary conditions are given as

$$f_D(x,0) = f_0, \quad f_D(\pm l/2,t) = f_e + (f_0 - f_g) \quad \text{and} \quad \partial f_D(0,t)/\partial x = 0, \quad (10.4)$$

where f_g is the fractional free volume at the glass transition temperature and $x = 0$ is the middle of the slab with thickness l . The no flux boundary condition at the center of the sample causes the constant c_2 to become zero. Unfortunately it is not possible to determine the remaining constants such that the initial and boundary conditions are satisfied. However, there is a modified form of this solution found by allowing c_1 , c_3

and c_4 to depend on f , x , and t , which results in an approximate solution that does satisfy initial and boundary conditions,

$$f_D(x, t) = f_0 + \ln \left(\frac{8\alpha \exp(\beta(f_e + f_0 - f_g))t + l^2 - 4x^2}{8\alpha \exp(\beta f_0)t + l^2 - 4x^2} \right) / \beta. \quad (10.5)$$

The above approximate analytical solution is formally based on an exact solution of the governing partial differential Equation 10.2 and is essentially the new EVD model. However, for the exact solution it is not possible to satisfy all the initial and boundary conditions, and therefore the above approximate solution is proposed as one which is similar in mathematical structure to an exact solution, but it is constrained to satisfy all the given initial and boundary data. In fact, numerical results indicate that the above approximate solution is very accurate except at the edges at small times. The average fractional free volume within the sample is given by

$$\bar{f}_D(t) = \sum_{k=0}^K \frac{f\left(\frac{kl}{2K}, t\right)}{K+1}, \quad (10.6)$$

where K is the total number of intervals used to calculate the average fractional free volume while k is the summation parameter where $k = 0$ represents the center of the sample and $k = K$ represents the edge of the sample (in this work $K = 100$). This average fractional free volume may be combined with a lattice contraction component based on the work of Hirai and Eyring [3] where fractional free volume decreases during aging according to

$$f_{LC}(t) = f_g + (f_0 - f_g) \exp(-t/\tau), \quad (10.7)$$

where f_{LC} is the fractional free volume governed by lattice contraction such that $f_0 - f_{LC}$ is the free volume lost due to lattice contraction, f_g is the fractional free volume for the glassy or “bulk” state demonstrated in figure 2 of reference [4] and τ is a material relaxation time. This component is assumed to be independent of sample thickness while the vacancy diffusion component depends on the sample thickness as vacancies have further to travel in a thicker sample to escape at the surface.

Once the final total fractional free volume is determined, given as

$$f(t) = \bar{f}_D(t) + f_{LC}(t) - f_0, \quad (10.8)$$

it is then converted to permeability by the new relation $P(t) = a^* \exp(b f(t))$. a^* and b are chosen to be 0.008 and 35.2 respectively to match experimental results of oxygen

permeation through PVAc so that $P = 2.33$ when $f_0 = 0.160$ and $P = 1.58$ when $f_g = 0.149$, values from reference [4].

10.3 Comparison with results in the literature

10.3.1 Comparison with MPB

Experimental permeability results were obtained by MPB [4] during aging for up to 1000 hours. Results for polyarylate films with thicknesses 33, 28, 9.7, 4.4, 1.85, 0.99, 0.74, 0.58 and 0.25 μm are plotted in Figure 10.1. Also included in the figure is the dual

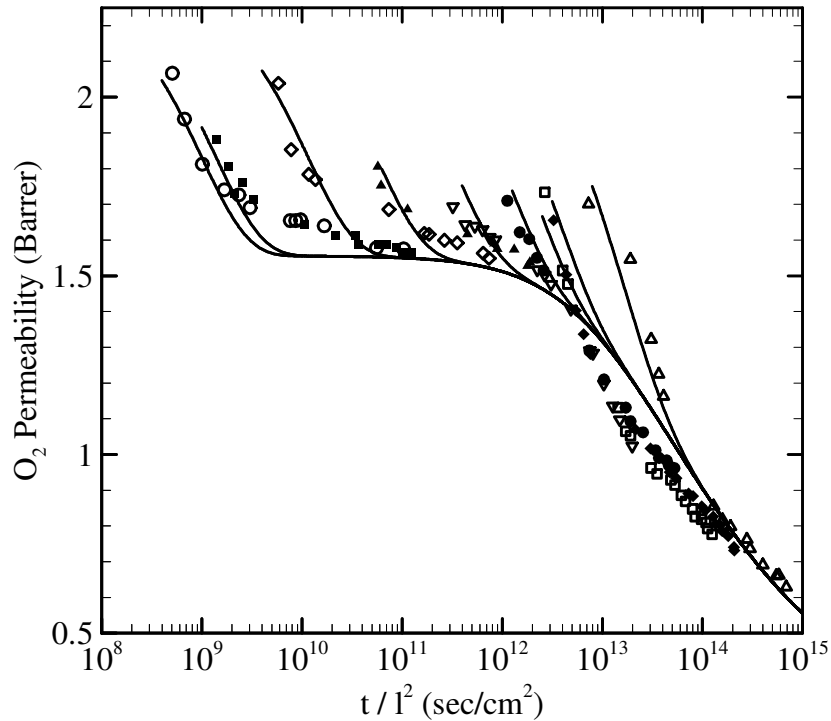


Figure 10.1: Experimental oxygen permeability data for BPA-BnzDCA films with thicknesses (\circ) 33 μm , (\blacksquare) 28 μm , (\diamond) 9.7 μm , (\blacktriangle) 4.4 μm , (∇) 1.85 μm , (\bullet) 0.99 μm , (\square) 0.74 μm , (\blacklozenge) 0.58 μm and (\triangle) 0.25 μm fitted with the dual mechanism model (lines).

mechanism model where the vacancy diffusion part is replaced with the new EVD model, with $\alpha = 3.5 \times 10^{-21} \text{ cm}^2 \text{ s}^{-1}$, $\beta = 150$, $\tau = 3.5$ hours, $f_0 = 0.160$, $f_g = 0.149$ and $f_e = 0.102$. The fit is reasonably good and is almost identical to the original numerical solution of MPB. Note that this procedure is to demonstrate the ability to replace the previous model based on the Doolittle relation with the new EVD model and does not

prove the reliability of the dual mechanism model for predicting permeability during aging.

10.3.2 Comparison with CLS

Secondly the model is compared with the CLS model [5]. The CLS model was the first use of the Doolittle relation for vacancy diffusion in a physical aging model. The CLS model fitted estimates of experimental volume recovery results for poly(vinyl acetate) from the KAHR phenomenological theory. Spherical geometry was assumed by CLS and therefore the diffusion equation becomes

$$\frac{\partial f}{\partial t} = \frac{1}{r^2} \frac{\partial}{\partial r} \left(r^2 D \frac{\partial f}{\partial r} \right), \quad (10.9)$$

$$D = \alpha \exp(\beta f),$$

where r is the radius of a spherical sample and f is fractional free volume. Again by using the method of separation an exact solution is also available in the form

$$f(r, t) = \ln \left(\frac{\frac{c_1 \beta r^2}{6\alpha} - \frac{\beta c_2}{r} + c_3}{-c_1 \beta t + c_4} \right) / \beta. \quad (10.10)$$

Once again this solution is manipulated to satisfy the initial and boundary conditions,

$$f(r, 0) = f_0, \quad f(l, t) = f_e \quad \text{and} \quad \partial f(0, t) / \partial r = 0. \quad (10.11)$$

l now represents the radius of the sample. However, CLS believed that volume recovery is sample-thickness independent and therefore the radius length of the sample l was scaled out of the equation. This can be done by scaling the length parameter l into a characteristic time $\tau = l^2/\alpha$. The following approximate analytical solution is almost identical to the one dimensional solution and also varies from a full numerical solution of the boundary value problem at small times,

$$f(r, t) = f_0 + \ln \left(\frac{6\alpha \exp(\beta f_e) t + l^2 - r^2}{6\alpha \exp(\beta f_0) t + l^2 - r^2} \right) / \beta. \quad (10.12)$$

The above approximate solution is the EVD equation for the free volume distribution in a spherically shaped sample. For large times the above solution provides a very accurate approximation to the numerical result. Figure 10.2 shows comparison of the KAHR phenomenological model (circles), CLS vacancy diffusion model (solid lines) and the newly proposed EVD model (dashed lines) for average fractional free volume during volume recovery of poly(vinyl acetate). Some experimental results (crosses) are

included from Kovacs, Stratton and Ferry (KSF) [6] where specific volume is converted to fractional free volume using the Bondi group contribution method where occupied volume is calculated to be $0.7988 \text{ cm}^3/\text{g}$. The T_g of poly(vinyl acetate) is 36°C . The upper symbols/lines correspond to a sample equilibrated at 40°C and cooled to 35°C at $t = 0$. The lower symbols/lines correspond to a sample equilibrated at 30°C and heated

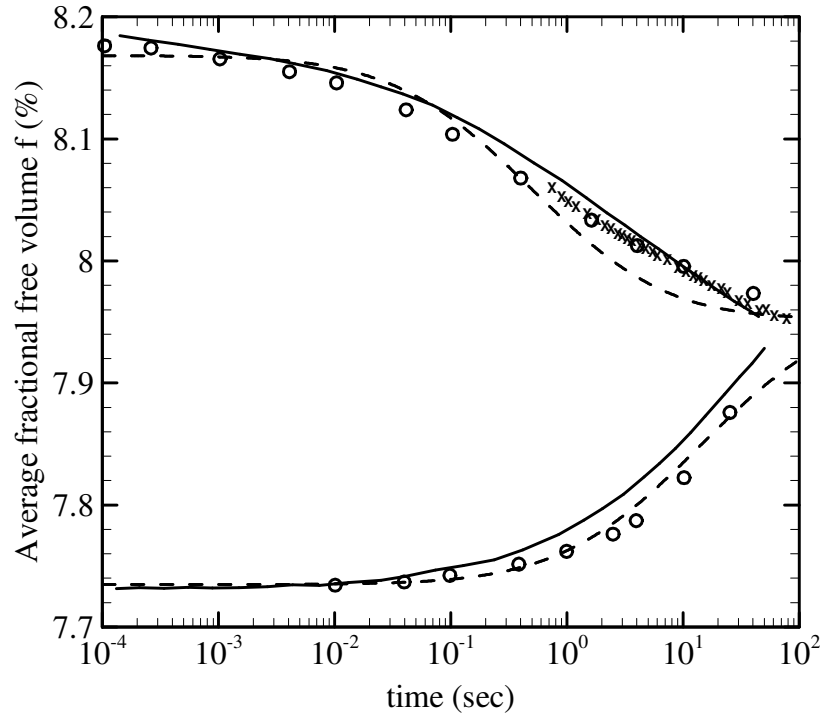


Figure 10.2: Average fractional free volume predicted by the KAHHR model (circles), CLS model (solid lines) and the new EVD model (dashed lines) with $\alpha = 3 \times 10^{-54} \text{ cm}^2 \text{ s}^{-1}$ and $\beta = 1500$. KSF [6] experimental data points included (crosses). The upper symbols/lines correspond to a sample equilibrated at 40°C and brought to 35°C at $t = 0$. The lower symbols/lines correspond to a sample equilibrated at 30°C and brought to 35°C at $t = 0$.

to 35°C at $t = 0$. The new EVD model agrees well with the KAHHR results and is a good replacement for the diffusion model used by CLS. Note that this example is for a sample aging very close to the glass transition temperature therefore there is not a very large amount of difference between initial and equilibrated free volume. Although the new model is capable of fitting this type of experiment its real advantage is modelling aging after a large temperature jump where the free volume is far from equilibrium, this is

because the diffusion coefficient has been shown to fit data best over a large range of free volume [1]. This small departure from equilibrium explains the very small and large values determined for the parameters a and b , respectively.

10.3.3 Comparison with constitutive kinetic equation

This new EVD model is similar to the early established constitutive kinetic equation,

$$\frac{d\delta}{dt} = -\frac{\delta}{\tau(T, \delta)}, \quad (10.13)$$

$$\tau(T, \delta) = \tau_r \exp[-\theta(T - T_r)] \exp[-(1-x)\theta\delta / \Delta\alpha_T],$$

where δ is the departure from equilibrium which can be expressed as $(f - f_e)$. $\tau(T, \delta)$ is known as the relaxation time dependent on temperature T and distance from equilibrium δ . τ_r is the relaxation time in equilibrium at reference temperature T_r . θ is a material constant and x is a partition parameter ($0 \leq x \leq 1$) which determines the contributions of temperature (T) and structure (δ) to the relaxation time $\tau(T, \delta)$. Finally $\Delta\alpha_T$ is the difference between the thermal expansion coefficients in the liquid and glass state. This form of the constitutive kinetic equation was developed by Kovacs, Aklonis, Hutchinson and Ramos (KAHR) [7]. It is founded upon earlier pioneering work of Rehson [8], Moynihan et al. [9], and Hodge et al. [10-15] and is the basis for the KAHR phenomenological model. An excellent review of these works and physical aging of polymers in general is written by Hutchinson [16].

By substitution and simplification this constitutive equation can be expressed as

$$\frac{df}{dt} = -\tau_\infty^{-1} \exp(\gamma \Delta f) \Delta f, \quad (10.14)$$

where Δf is equivalent to the departure from equilibrium $\delta = (f - f_e)$ with constants

$$\tau_\infty^{-1} = \tau_r^{-1} \exp[\theta(T - T_r)] \text{ and } \gamma = (1-x)\theta / \Delta\alpha_T. \quad (10.15)$$

Apart from the obvious dependence on the exponential of fractional free volume f , a stronger similarity is found by approximating the EVD equation using a finite difference method which approximates the sample width into three steps (the center $f(0, t) = f(t)$ and the edges $f(l, t) = f_e$ and $f(-l, t) = f_e$ of the sample). This means that there is only one discrete relaxation unit as opposed to a continuous distribution of relaxation parts throughout the sample. The approximation is performed as follows,

$$\frac{\partial f}{\partial t} = \frac{\partial}{\partial x} \left(\alpha \exp(\beta f) \frac{\partial f}{\partial x} \right)$$

$$\begin{aligned}
&= \alpha \exp(\beta f) \frac{\partial^2 f}{\partial x^2} + \alpha \beta \exp(\beta f) \left(\frac{\partial f}{\partial x} \right)^2 \\
&\approx \alpha \exp(\beta f(0, t)) \left(\frac{f(l, t) - 2f(0, t) + f(-l, t)}{l^2} \right) + \alpha \beta \exp(\beta f(0, t)) \left(\frac{f(l, t) - f(0, t)}{l} \right)^2 \\
&= \frac{\alpha \exp(\beta f(t))}{l^2} \left[-2(f(t) - f_e) + \beta(f(t) - f_e)^2 \right] \\
&= -2 \frac{\alpha \exp(\beta f_e)}{l^2} \exp(\beta \Delta f) [\Delta f - \beta/2 (\Delta f)^2]
\end{aligned} \tag{10.16}$$

When Δf is small $(\Delta f)^2 \approx 0$ the approximated EVD equation becomes identical to the original constitutive kinetic equation with constants,

$$\alpha = \frac{l^2}{2\tau_r} \exp(\theta(T - T_r)) \exp(-(1-x)\theta_f / \Delta\alpha_T) \tag{10.17}$$

and $\beta = (1-x)\theta / \Delta\alpha_T$.

Coincidentally it is pointed out by Kovacs [17] that the constitutive equation is most accurate within a narrow temperature interval which is equivalent to a small departure from equilibrium Δf .

It is important to note that both the KAHR model and the EVD model actually use a distribution of relaxation parts rather than a single discrete part. The relaxation parts of the KAHR model have been suggested to represent the distribution of hole sizes [16] where each hole size decreases in quantity according to the kinetic equation which could possibly be tested by positron annihilation lifetime spectroscopy (PALS) experiments [18]. In contrast the parts of the EVD model represent a spatial distribution of free volume throughout the depth of the sample which could possibly be tested by a positron beam that provides a free volume depth profile [19]. However, the core basis of these models is very similar as demonstrated above.

10.4 Model applied to thin film aging

This new EVD model, which is easier to implement, since it is a simple analytical equation, will provide the opportunity for experimental data to be modelled and predicted without having to numerically solve complicated differential equations. This ease of use will also help the testing of the vacancy diffusion explanation for physical aging. For example previously it was shown that it was necessary to include a lattice

contraction component to fit MPB's experimental data and this was done without having to numerically solve the governing partial differential equation. An additional example is given here where the model is applied to experimental permeability data within thin films to test whether the observed physical aging is a result of vacancies diffusing to the external surface. The logic behind the test is that if the physical aging can be described by the vacancy diffusion model in which the length scale is that of the sample thickness then it is confirmed that vacancy diffusion is the dominant mechanism governing physical aging.

Huang and Paul's experimental results for oxygen permeability through polysulfone (PSF) films of thicknesses from 413 nm to 61.2 μm during aging [20] are used as an example of this test. Equation 10.5 is used with the length scale l set as the macroscopic sample thickness and all other parameters varied to attain the best fit. As seen in Figure 10.3, the model fits the thin samples ($l < 1000$ nm) well but is unable to

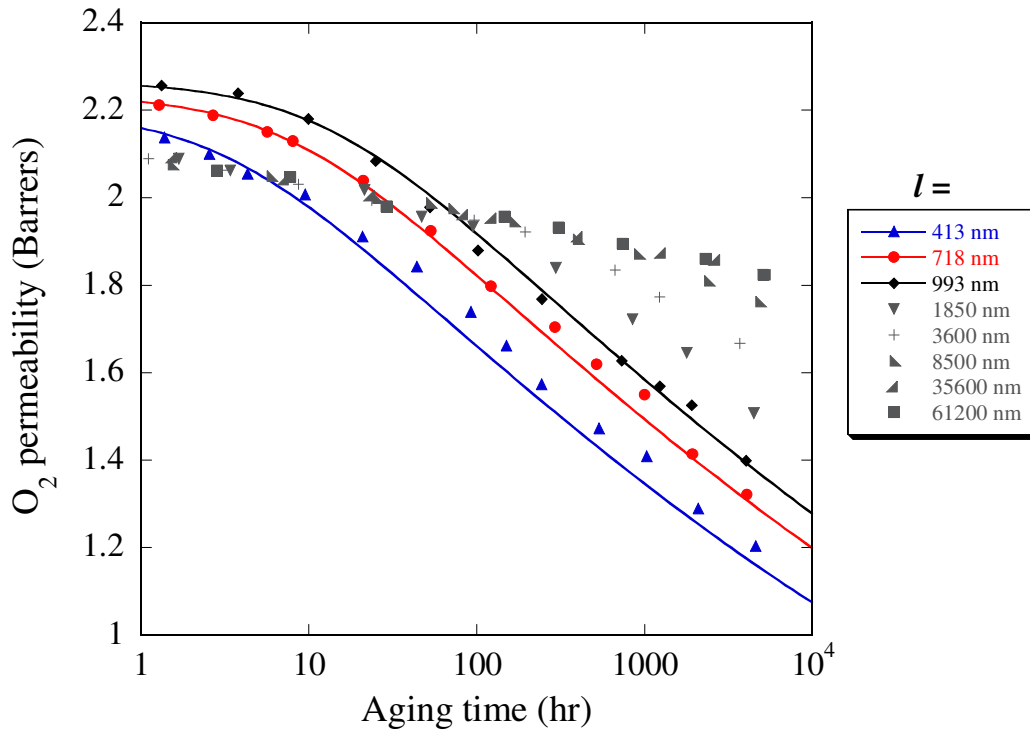


Figure 10.3: Experimental oxygen permeability of PSF films as a function of aging time. The new EVD model (solid lines) with $\alpha = 10^{-24.1} \text{ nm}^2 \cdot \text{h}^{-1}$, $\beta = 400$, $f_0 = 16.2 \%$ and $f_e = 13.5 \%$.

fit the thick samples ($l > 1000$ nm). Consequently the model invokes the conclusion that vacancy diffusion to the external surface explains the majority of the physical aging effects within these thin films, however, another aging mechanism must be included to explain the aging in the thick films. This other aging mechanism is not known since the addition of the lattice contraction component, used earlier, did not describe these experimental results.

10.5 Model predictions of transport in aging polymer (store and release application)

As shown above, a vacancy diffusion coefficient of the form

$$D_v = \alpha_v \exp(\beta_v f), \quad (10.18)$$

allows the partial differential equation that governs vacancy diffusion to be analytically solved. By defining a gas diffusion coefficient of the same form

$$D_g = \alpha_g \exp(\beta_g f), \quad (10.19)$$

analytical expressions are found for the system of partial differential equations that govern gas diffusion throughout the sample, shown below. These solutions provide an excellent model (or tool) for investigating many transport and adsorption applications. In this section the model is used to investigate the store and release process of a gas within an aging polymer.

By assuming that the fractional free volume within a polymer decreases as a result of vacancy diffusion (according to Equation 10.18) and that the gas diffuses through the available free volume (according to Equation 10.19), the simple coupled partial differential equations can be formed,

$$\frac{\partial f}{\partial t} = \frac{\partial}{\partial x} \left(\alpha_v \exp(\beta_v f) \frac{\partial f}{\partial x} \right), \quad (10.20)$$

$$\frac{\partial C}{\partial t} = \frac{\partial}{\partial x} \left(\alpha_g \exp(\beta_g f) \frac{\partial C}{\partial x} \right), \quad (10.21)$$

where $C = C(x, t)$ is the concentration of the gas within the available free volume at position x and at time t . Equations 10.20 and 10.21 can be solved using the separation of variables method in which solutions are assumed to take the form

$$f(x, t) = Q(x) + R(t), \quad (10.22)$$

$$C(x, t) = S(x) + T(t). \quad (10.23)$$

By substituting these into Equations 10.20 and 10.21 we have,

$$R'(t) = a_v e^{\beta_v(Q(x)+R(t))} \beta_v (Q'(x))^2 + \alpha_v e^{\beta_v(Q(x)+R(t))} Q''(x), \quad (10.24)$$

$$T'(t) = \alpha_g e^{\beta_g(Q(x)+R(t))} \beta_g Q'(x) S'(x) + \alpha_g e^{\beta_g(Q(x)+R(t))} S''(x) \quad (10.25)$$

By rearranging Equations 10.24 and 10.25 the variables can be separated to form the following four equations,

$$R'(t) e^{-\beta_v R(t)} = \lambda_1, \quad (10.26)$$

$$\alpha_v e^{\beta_v Q(x)} (\beta_v (Q'(x))^2 + Q''(x)) = \lambda_1, \quad (10.27)$$

$$T'(t) e^{-\beta_g R(t)} = \lambda_2, \quad (10.28)$$

$$\alpha_g e^{\beta_g Q(x)} (\beta_g Q'(x) S'(x) + S''(x)) = \lambda_2. \quad (10.29)$$

By solving these four equations the following solutions can be obtained,

$$Q(x) = \ln(c_1 + c_2 x - c_3 x^2) / \beta_v, \quad (10.30)$$

$$R(t) = -\ln(c_4 + 2\alpha_v c_3 t) / \beta_v, \quad (10.31)$$

$$S(x) = \int \frac{1}{\alpha_g} (\lambda_2 x + c_5 \alpha_g) (c_1 + c_2 x - c_3 x^2)^{\left(\frac{\beta_g}{\beta_v}\right)} dx + c_6, \quad (10.32)$$

$$T(t) = \frac{\beta_v (c_4 + 2\alpha_v c_3 t)^{\left(\frac{\beta_g}{\beta_v} + 1\right)} \lambda_2}{2\alpha_v c_3 (\beta_v - \beta_g)} + c_7. \quad (10.33)$$

where c_i ($i = 1..7$) are constants. These constants depend on the initial and boundary conditions for the appropriate application. Here the storage and release of a gas is investigated and therefore the initial and boundary conditions for the fractional free volume are

$$f(x,0) = f_0 \text{ and } f(\pm l, t) = f_e, \quad (10.34)$$

where f_0 is the initial fractional free volume, f_e is the equilibrium fractional free volume at the edges of the sample and $2l$ is the sample thickness (center at $x = 0$). The initial and boundary conditions for the gas concentration are

$$C(x,0) = C_0 \text{ and } C(\pm l, t) = C_e, \quad (10.35)$$

where C_0 is the initial gas concentration within the polymer and C_e is the equilibrium gas concentration in the environment surrounding the polymer. These conditions can be used to model the uptake of gas into the sample ($C_0 < C_e$) or the release of gas from the

sample ($C_0 > C_e$). The exact solution has been manipulated to satisfy the boundary conditions, providing the following solution for the fractional free volume

$$f(x, t) = Q(x) + R(t) = f_0 + \ln \left(\frac{2\alpha_v e^{\beta_v f_e t + l^2 - x^2}}{2\alpha_v e^{\beta_v f_0 t + l^2 - x^2}} \right) / \beta_v. \quad (10.36)$$

Note that the aging of the polymer does not depend on the gas concentration. It is found that this approximate solution is very accurate except at the edge of the sample at short times. The solution for $C(x, t)$ was found and is provided in the appendix due to its length. Although the solution for $C(x, t)$ is very large, it is made up of simple functions which provide quick results with any mathematical software.

Here the polymer sample is assumed to initially have a fractional free volume of 30 % (f_0) and will eventually relax to an equilibrium fractional free volume of 20 % (f_e). For the storing process, the gas concentration within the sample is initially zero (C_0) with an outside concentration of 50 vol. % (C_e), and vice-versa for the release process ($C_0 = 50$ vol. % and $C_e = 0$). Additionally, the sample thickness is 2 cm ($l = 1$ cm) and the other parameters are assigned the following values: $\alpha_v = 1 \times 10^{-5} \text{ cm}^2 \text{ s}^{-1}$, $\beta_v = 30$, $\alpha_g = 93 \times 10^{-4} \text{ cm}^2 \text{ s}^{-1}$ and $\beta_g = 37$. The total volume percent concentration within the sample is calculated as $C_{\text{tot}}(x, t) = C(x, t) f(x, t)$, since $C(x, t)$ is the concentration within the available free volume and $f(x, t)$ is the ratio of the free volume over the total volume of the sample.

The model provides quick and easy predictions of the fractional free volume profile (Figure 10.4), gas uptake profile (Figure 10.5) and gas release profile (Figure 10.6) within the polymer sample. These predictions are very useful for calculating the uptake and delivery rates and additionally provide insight into the effect of physical aging. If the free volume within the sample could be controlled then the uptake and delivery rates could be controlled and these equations would determine the necessary free volumes for specified operation rates. Other applications of the model include gas separation membranes, polymer coatings for corrosion protection, polymer packages for food preservation and many others.

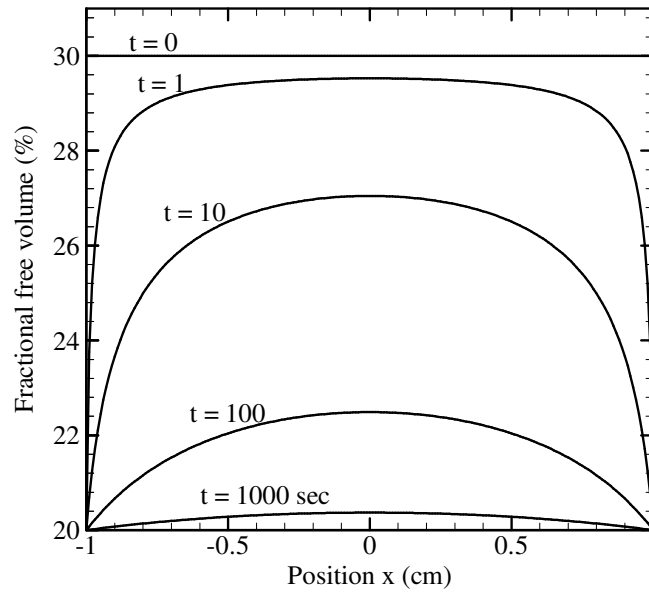


Figure 10.4: Fractional free volume profile predictions within a polymer sample at times t .

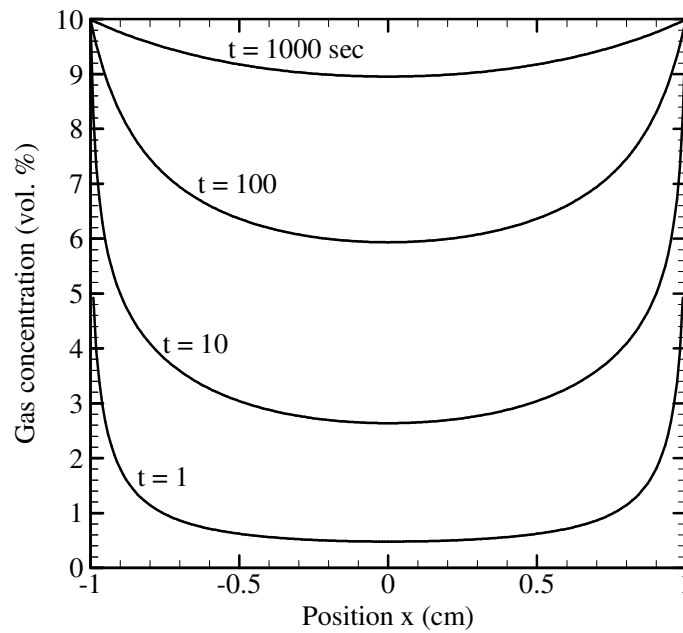


Figure 10.5: Gas uptake profile predictions within a polymer sample at times t .

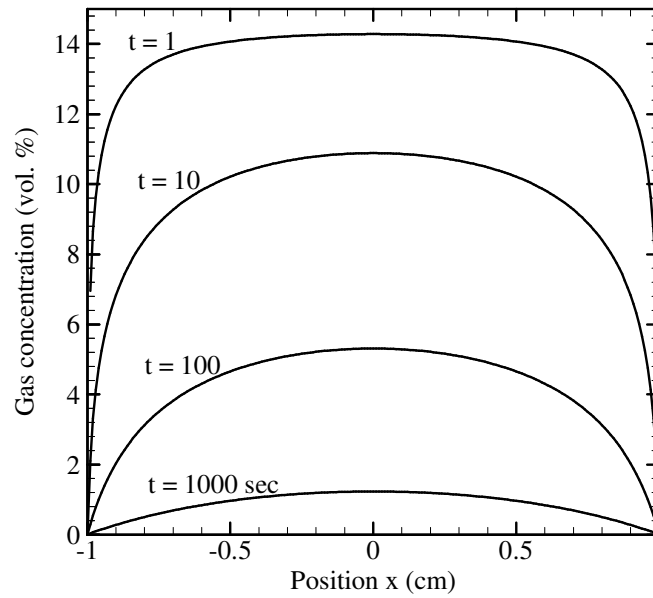


Figure 10.6: Gas release profile predictions within a polymer sample at times t .

10.6 Conclusion

Previously the Doolittle relation has been used to describe a variety of properties and processes within polymers such as viscosity, mobility, fluidity, and particle diffusion. Another use of the Doolittle relation was established by CLS where the Doolittle equation was used to predict the diffusion coefficient for vacancies in a vacancy diffusion physical aging model. With this in mind the diffusion coefficient in the vacancy diffusion aging model is replaced with the new relation, established in Chapter 4 [1], that provided an exact analytical solution. This new EVD model matched experimental results and compared well with other models such as the KAHR phenomenological model and the CLS vacancy diffusion model.

Further support for the EVD model was given by revealing the essential similarity with the early established constitutive kinetic equation. This kinetic equation has been used as a basis for many models including the KAHR model, and at a fundamental level the new EVD model is very similar.

The usefulness of the model was demonstrated in testing whether the vacancy diffusion mechanism could explain the physical aging effects in films ranging in thickness from 400 nm to 60 μm . According to the fit, the vacancy diffusion concept could explain the aging phenomena within the thin films ($< 1 \mu\text{m}$) but failed to describe the aging behaviour within the thick films ($> 1 \mu\text{m}$), implying that an additional

mechanism may be responsible for aging within the thick films. Additionally, the model was shown to be a useful tool for observing the gas concentration profile within an polymer sample during the store and release process.

In summary the new empirically derived relation [1] between diffusion and free volume allows an exact solution to the one dimensional vacancy diffusion equation giving rise to a new analytical EVD model for the diffusion of vacancies which compares well with experimental results and other popular models.

References

- [1] A. W. Thornton, K. M. Nairn, A. J. Hill and J. M. Hill, New relation between diffusion and free volume: I. Predicting gas diffusion, *J. Membr. Sci.*, 338 (2009) 29.
- [2] A. D. Polyanin and V. F. Zaitsev, *Handbook of Nonlinear Partial Differential Equations*, Chapman & Hall /CRC, 2004.
- [3] N. Hirai and H. Eyring, Bulk viscosity of liquids, *J. Appl. Phys.*, 29 (1958) 810.
- [4] M. S. McCaig, D. R. Paul and J. W. Barlow, Effect of film thickness on the changes in gas permeability of a glassy polyarylate due to physical aging, Part II. Mathematical model, *Polymer*, 41 (2000) 639.
- [5] J. G. Curro, R. R. Lagasse and R. Simha, Diffusion model for volume recovery in glasses, *Macromolecules*, 15 (1982) 1621.
- [6] A. J. Kovacs, R. A. Stratton and J. D. Ferry, Dynamic mechanical properties of polyvinyl acetate in shear in the glass transition temperature range, *J. Phys. Chem.*, 67 (1963) 152.
- [7] A. J. Kovacs, J. J. Aklonis, J. M. Hutchinson and A. R. Ramos, Isobaric volume and enthalpy recovery of glasses. II. A transparent multiparameter theory, *J. Polym. Sci., Polym. Phys. Ed.*, 17 (1979) 1097.
- [8] S. M. Rekhson, A. V. Bulaeva and O. V. Mazurin, *Izv. Akad. Nauk. SSR., Neorg. Mater.*, 7 (1971) 714.

- [9] M. A. DeBolt, A. J. Eastale, R. B. Macedo and C. T. Moynihan, Analysis of structural relaxation in glass using rate heating data, *J. Am. Ceram. Soc.*, 59 (1976) 16.
- [10] I. M. Hodge, Effects of annealing and prior history on enthalpy relaxation in glassy-polymers. 4. Comparison of 5 polymers, *Macromolecules*, 16 (1983) 898.
- [11] I. M. Hodge, Effects of annealing and prior history on enthalpy relaxation in glassy-polymers. 3. Experimental and modeling studies of polystyrene, *Macromolecules*, 16 (1983) 371.
- [12] I. M. Hodge, Effects of annealing and prior history on enthalpy relaxation in glassy-polymers. 6. Adam-Gibbs formulation of nonlinearity, *Macromolecules*, 20 (1987) 2897.
- [13] I. M. Hodge and A. R. Berens, Effects of annealing and prior history on enthalpy relaxation in glassy-polymers. 2. Mathematical-modeling, *Macromolecules*, 15 (1982) 762.
- [14] I. M. Hodge and A. R. Berens, Effects of annealing and prior history on enthalpy relaxation in glassy-polymers. 5. Mathematical-modeling of nonthermal preaging perturbations, *Macromolecules*, 18 (1985) 1980.
- [15] A. R. Berens and I. M. Hodge, Effects of annealing and prior history on enthalpy relaxation in glassy-polymers. 1. Experimental-study on polyvinyl-chloride, *Macromolecules*, 15 (1982) 756.
- [16] J. M. Hutchinson, Physical aging of polymers, *Prog. Polym. Sci.*, 20 (1995) 703.
- [17] A. J. Kovacs, *Fortschr. Hochpolym. Forsch. (Adv. in Polym. Sci.)*, 3 (1964) 394.
- [18] A. J. Hill, P. L. Jones, J. H. Lind and G. W. Pearsall, A positron annihilation lifetime study of isothermal structural relaxation in bisphenol-A polycarbonate, *J. Polym. Sci., Part A: Polym. Chem.*, 26 (1988) 1541.
- [19] C. He, T. Suzuki, E. Hamada, H. Kobayashi, K. Kondo, V. P. Shantarovich and Y. Ito, Characterization of polymer films using a slow positron beam, *Mater. Res. Innovations*, 7 (2003) 37.

- [20] Y. Huang and D. R. Paul, Physical aging of thin glassy polymer films monitored by gas permeability, *Polymer*, 45 (2004) 8377.

List of symbols used in Chapter 10

P	permeability
D	diffusivity
S	solubility
f	represents the generalized free volume (for various definitions)
FFV	fractional free volume from Bondi's method
FFV_n	gas-specific fractional free volume from Park and Paul's method
f_D	free volume for vacancy diffusion
f_{LC}	free volume for lattice contraction
f_0	initial free volume
f_e	equilibrium free volume
f_g	free volume at glass transition temperature
x	position within sample
l	sample thickness
t	time
τ	relaxation time parameter
r	radial position within the sample
C	gas concentration
C_0	initial gas concentration
C_e	equilibrium gas concentration (concentration surrounding sample)

Part V

Conclusion

Chapter 11

Concluding remarks and future directions

11.1 Summary

In this thesis, new mathematical models have been presented to analyse, describe and predict the physical phenomena that govern the following three processes:

- (i) gas separation;
- (ii) gas storage; and
- (iii) physical aging in polymers.

Materials that efficiently separate and store gases are composed of angstrom and nano-sized pores which can be tailored to control and enhance their performance. The technique of applied mathematical modelling has been adopted to gain insight into the behaviour of gases within different porous networks which has lead to the development of new models and conceptual frameworks that might guide material design. Moreover, polymers that currently dominate the gas separation industry are composed of dynamic porous networks that may collapse over time due to the physical aging process, for which a new model has been developed that accurately describes the process. The main advantages of these new mathematical models as compared to the computational models, are their simplicity, speed of calculation, and overall ability to facilitate a more complete understanding of the processes.

11.1.1 Gas separation

Gases are separated as a consequence of their different transport rates through a porous material referred to as the membrane. In this thesis two new models have been

developed that determine the gas transport rates by considering various material properties.

Firstly, a nano-scale approach was taken by considering the individual pore shape, size and composition. The interactions between the gas and the pore surface were formulated, and this formulation provides insight into the behaviour of the gas. This information led to the development of precise decision criteria that can be used to predict the dominant transport regime. In addition, the model predicted a new transport regime, termed suction diffusion, by which the gas is “sucked” through the pore like a nano-scale worm hole due to the favourable gas-pore interactions within almost frictionless environments. Further, the model predictions which are readily calculated, agree with experimental and simulation results.

Secondly, a macro-scale approach was taken by considering the bulk material property, free volume. An extensive collection of permeability, diffusivity, solubility and free volume data for available polymers, revealed a new relationship for which a new empirical model has been developed that accurately encompasses all the data. The new model is shown to follow the large increase in permeability (diffusivity) at the critical amounts of free volume for which pores become interconnected and bi-continuous. In addition, new types of polymers are evaluated using the model to determine whether their free volume and permeability characteristics conform to other families of polymers. The practical utility of this model is that it can be used as an efficient tool for predicting transport properties in the wide range of available polymers, and it is based only on one readily obtainable material characteristic, free volume.

11.1.2 Gas storage

Gases may be stored densely within adsorbent materials containing porous networks in which the gases enter and adsorb onto the available internal surface. The interactions between the gas and the pore surface were integrated throughout pores of different size, shape and composition to determine the binding energies. This information was combined with fundamental thermodynamic theory to form a new mathematical adsorption model that predicts the amount of gas stored within the adsorbent material at chosen temperatures and pressures. The new model was found to agree with available experimental and simulation results. Further, the new model was used to investigate the potential gas storage performance within nanotubes and metal-organic frameworks impregnated with various nanostructures. Again the new mathematical model produces

essentially the same characteristics that the simulation studies deliver but is easier and faster to implement and can be readily applied to a wider range of cases.

11.1.3 Physical aging in polymers

Polymers are widely used as membranes, adsorbents, films and coatings. Due to their dynamic structure polymers are subject to physical aging, a relaxation process by which the internal porous network tends to collapse and consequently cause a change in the transport properties. In this thesis a new model was presented based on the vacancy diffusion mechanism in the form of analytical equations which agree with experimental data. The model was used to explain the aging process within ultra thin films and was combined with gas transport theory to predict the gas concentration profile within an aging polymer.

11.2 Final comments

The technique of applied mathematical modelling has been adopted to successfully develop models and conceptual frameworks to:

- provide understanding of the physical phenomena of gas separation and storage;
- provide guidelines for tailoring porosity;
- characterize novel materials; and
- ultimately accelerate the development of clean alternative fuel technologies.

11.3 Future directions

Possible extensions of the work presented in this thesis are suggested here. The transport and adsorption models presented in Chapters 2 and 6 could be used to investigate any molecules of interest including water, proteins, drugs, ions, viruses or acids, and can easily consider electrostatic effects by adding Coulomb's equation to the potential energy functions. Further, more complex cavity shapes could be investigated including hour-glasses, funnels, spheroids, cubes or rectangles.

It would also be interesting if the model presented in Chapter 3 could be extended to membranes which have a distribution of pores, bearing in mind that the pores might be distributed in many different ways. For example, Figure 11.1 shows four membranes with an identical pore size distribution but with the pores arranged differently. The question arises as to how the flux would differ for each membrane?

Another useful study might be to try and relate the free volume within polymers with the connectivity of pores. This has been investigated using a computer simulation approach, but an analytical equation relating these properties would be a very useful tool. The percolation threshold has been found by various computational methods indicating the amount of free volume for which a connected path exists. But the question arises as to how the diffusion depends on connectivity when the amount of free volume is below or above the percolation threshold?

Factors that have not been considered in the models presented here for gas transport through polymer membranes include cohesive energy density, chain vibrations, chain length, chain mass, temperature and gas concentration. Future work could include the formulation of a more complete universal gas transport model for which these factors would need to be incorporated.

The physical aging in polymers was shown in Chapter 10 to be governed by vacancy diffusion within films thinner than 1000 nm. It would be interesting to see whether the vacancy diffusion model could match the free volume profile within these films during aging, measured possibly by a positron beam. Additionally, positron annihilation lifetime spectroscopy has the ability to measure pore size and number and therefore it would be useful to test whether the dual mechanism model can describe the loss in number (vacancy diffusion) and loss in size (lattice contraction).

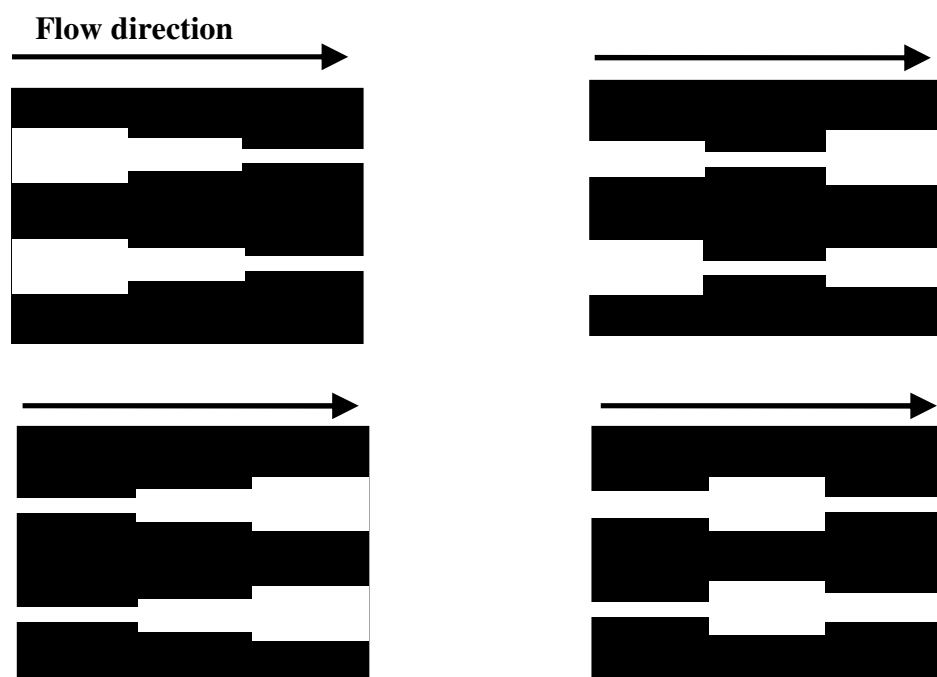


Figure 11.1: Membranes with identical pore size distributions but with different arrangements.

Appendix

Solution for the gas concentration with an aging polymer for Section 10.5.

$$C(x,t) =$$

$$\begin{aligned} & -\frac{1}{2} Bl \left(e^{(-Bl (\ln(-2Ala(-1+e^{(Bl(f0-fe))}))(Ce-C0)(b-Bl)) / (-2AlBltae^{(f0b+feBl)} \right. \\ & \quad + 2AlBltae^{(feb+Blf0)} - (l-x)(l+x)(-Al(b-Bl)e^{(feBl)} + Al(b-Bl)e^{(Blf0)} + Bl e^{(f0b)a})) + feBl \\ & \quad + f0b)/b) - 2Al e^{(-Bl (\ln(-2Ala(-1+e^{(Bl(f0-fe))}))(Ce-C0)(b-Bl)) / (-2AlBltae^{(f0b+feBl)} \\ & \quad + 2AlBltae^{(feb+Blf0)} - (l-x)(l+x)(-Al(b-Bl)e^{(feBl)} + Al(b-Bl)e^{(Blf0)} + Bl e^{(f0b)a})) + feBl \\ & \quad \left. \left(-\frac{b}{Bl} + 1 \right) \right. \\ & \quad \left. + f0b)/b) (-e^{(feBl)} + e^{(Blf0)}) t / (-2 e^{(feBl)} Al t + x^2 - l^2) \right) \\ & \quad (-2 e^{(feBl)} Al t + x^2 - l^2) / (Al e^{(-Bl (\ln(-2Ala(-1+e^{(Bl(f0-fe))}))(Ce-C0)(b-Bl)) / (\\ & \quad -2AlBltae^{(f0b+feBl)} + 2AlBltae^{(feb+Blf0)} \\ & \quad - (l-x)(l+x)(-Al(b-Bl)e^{(feBl)} + Al(b-Bl)e^{(Blf0)} + Bl e^{(f0b)a})) + feBl + f0b)/b) \\ & \quad (-e^{(feBl)} + e^{(Blf0)}) (-b + Bl)) + 1 + \left(2 (-e^{(f0b+feBl)} + e^{(f0(b+Bl))}) (Ce - C0) Al \right. \\ & \quad (b - Bl) (2AlBltae^{(f0b+feBl)} - 2AlBltae^{(feb+Blf0)} \\ & \quad + (x-l)(-Bl e^{(f0b)a} + Al(e^{(feBl)} - e^{(Blf0)})(b-Bl))(l+x)) \ln(\\ & \quad 2AlBltae^{(f0b+feBl)} - 2AlBltae^{(feb+Blf0)} \\ & \quad + (l-x)(l+x)(-Al(b-Bl)e^{(feBl)} + Al(b-Bl)e^{(Blf0)} + Bl e^{(f0b)a})) + (\\ & \quad 2AlBlata(-1+Ce)e^{(f0b+feBl)} - 2BlataAl t (C0-1)e^{(feb+Blf0)} \\ & \quad - Bl a (x-l)(l+x)(-1+Ce)e^{(f0b)} \\ & \quad + (x^2(-1+Ce) - (C0-1)l^2) Al(b-Bl)(e^{(feBl)} - e^{(Blf0)})) \\ & \quad \left. (-Bl e^{(f0b)a} + Al(e^{(feBl)} - e^{(Blf0)})(b-Bl))(e^{(Blf0)})^{\left(\frac{b}{Bl}\right)} \right) \Bigg) / \left((\right. \\ & \quad 2AlBltae^{(f0b+feBl)} - 2AlBltae^{(feb+Blf0)} \\ & \quad + (x-l)(-Bl e^{(f0b)a} + Al(e^{(feBl)} - e^{(Blf0)})(b-Bl))(l+x)) \\ & \quad \left. (-Bl e^{(f0b)a} + Al(e^{(feBl)} - e^{(Blf0)})(b-Bl))(e^{(Blf0)})^{\left(\frac{b}{Bl}\right)} \right) \Bigg) \end{aligned}$$

List of author's publications

Journal articles

- A. W. Thornton, A. J. Hill, K. M. Nairn and J. M. Hill, Predicting particle transport through an aging polymer using vacancy diffusion, *Current Applied Physics*, 8 (2008) 501.
- A. W. Thornton, T. Hilder, A. J. Hill and J. M. Hill, Predicting gas diffusion regime within pores of different size, shape and composition, *Journal of Membrane Science*, 336 (2009) 101.
- A. W. Thornton, K. M. Nairn, A. J. Hill and J. M. Hill, New relation between diffusion and free volume: I. Predicting gas diffusion, *Journal of Membrane Science*, 338 (2009) 29.
- A. W. Thornton, K. M. Nairn, A. J. Hill, J. M. Hill and Y. Huang, New relation between diffusion and free volume: II. Predicting vacancy diffusion, *Journal of Membrane Science*, 338 (2009) 38.
- A. W. Thornton, K. M. Nairn, J. M. Hill, A. J. Hill and M. R. Hill, Metal-Organic Frameworks Impregnated with Magnesium-Decorated Fullerenes for Methane and Hydrogen Storage, *Journal of the American Chemical Society*, 131 (2009) 10662.
- A. W. Thornton and J. M. Hill, Modelling hydrogen adsorption within spherical, cylindrical and slit-shaped cavities, *Advanced Materials and Nanotechnology: Proceedings of the International Conference (AMN-4)*, Dunedin (New Zealand), 1151 (2009) 181.

Submitted manuscripts

- A. W. Thornton, K. M. Nairn, R. K. F. Lee, A. J. Hill, J. M. Hill and M. R. Hill, Investigation into the viability of nanotubes for hydrogen storage, *Langmuir*, (submitted 2009).
- A. W. Thornton, K. M. Nairn, A. J. Hill, J. M. Hill and M. R. Hill, TIMTAM: A new gas adsorption model based on fundamental thermodynamic principles, *New Journal of Physics*, (submitted 2009).